

Lecture Notes in Electrical Engineering 999

Girolamo Di Francia
Corrado Di Natale *Editors*

Sensors and Microsystems

Proceedings of AISEM 2022

 Springer

Lecture Notes in Electrical Engineering

Volume 999

Series Editors

Leopoldo Angrisani, Department of Electrical and Information Technologies Engineering, University of Napoli Federico II, Naples, Italy

Marco Arteaga, Departament de Control y Robótica, Universidad Nacional Autónoma de México, Coyoacán, Mexico

Bijaya Ketan Panigrahi, Electrical Engineering, Indian Institute of Technology Delhi, New Delhi, Delhi, India

Samarjit Chakraborty, Fakultät für Elektrotechnik und Informationstechnik, TU München, Munich, Germany

Jiming Chen, Zhejiang University, Hangzhou, Zhejiang, China

Shanben Chen, Materials Science and Engineering, Shanghai Jiao Tong University, Shanghai, China

Tan Kay Chen, Department of Electrical and Computer Engineering, National University of Singapore, Singapore, Singapore

Rüdiger Dillmann, Humanoids and Intelligent Systems Laboratory, Karlsruhe Institute for Technology, Karlsruhe, Germany

Haibin Duan, Beijing University of Aeronautics and Astronautics, Beijing, China

Gianluigi Ferrari, Università di Parma, Parma, Italy

Manuel Ferre, Centre for Automation and Robotics CAR (UPM-CSIC), Universidad Politécnica de Madrid, Madrid, Spain

Sandra Hirche, Department of Electrical Engineering and Information Science, Technische Universität München, Munich, Germany

Faryar Jabbari, Department of Mechanical and Aerospace Engineering, University of California, Irvine, CA, USA

Limin Jia, State Key Laboratory of Rail Traffic Control and Safety, Beijing Jiaotong University, Beijing, China

Janusz Kacprzyk, Systems Research Institute, Polish Academy of Sciences, Warsaw, Poland

Alaa Khamis, German University in Egypt El Tagamoa El Khames, New Cairo City, Egypt

Torsten Kroeger, Stanford University, Stanford, CA, USA

Yong Li, Hunan University, Changsha, Hunan, China

Qilian Liang, Department of Electrical Engineering, University of Texas at Arlington, Arlington, TX, USA

Ferran Martín, Departament d'Enginyeria Electrònica, Universitat Autònoma de Barcelona, Bellaterra, Barcelona, Spain

Tan Cher Ming, College of Engineering, Nanyang Technological University, Singapore, Singapore

Wolfgang Minker, Institute of Information Technology, University of Ulm, Ulm, Germany

Pradeep Misra, Department of Electrical Engineering, Wright State University, Dayton, OH, USA

Sebastian Möller, Quality and Usability Laboratory, TU Berlin, Berlin, Germany

Subhas Mukhopadhyay, School of Engineering and Advanced Technology, Massey University, Palmerston North, Manawatu-Wanganui, New Zealand

Cun-Zheng Ning, Electrical Engineering, Arizona State University, Tempe, AZ, USA

Toyoaki Nishida, Graduate School of Informatics, Kyoto University, Kyoto, Japan

Luca Oneto, Department of Informatics, Bioengineering, Robotics and Systems Engineering, University of Genova, Genova, Genova, Italy

Federica Pascucci, Dipartimento di Ingegneria, Università degli Studi Roma Tre, Roma, Italy

Yong Qin, State Key Laboratory of Rail Traffic Control and Safety, Beijing Jiaotong University, Beijing, China

Gan Woon Seng, School of Electrical and Electronic Engineering, Nanyang Technological University, Singapore, Singapore

Joachim Speidel, Institute of Telecommunications, Universität Stuttgart, Stuttgart, Germany

Germano Veiga, Campus da FEUP, INESC Porto, Porto, Portugal

Haitao Wu, Academy of Opto-electronics, Chinese Academy of Sciences, Beijing, China

Walter Zamboni, DIEM—Università degli studi di Salerno, Fisciano, Salerno, Italy

Junjie James Zhang, Charlotte, NC, USA

The book series *Lecture Notes in Electrical Engineering* (LNEE) publishes the latest developments in Electrical Engineering—quickly, informally and in high quality. While original research reported in proceedings and monographs has traditionally formed the core of LNEE, we also encourage authors to submit books devoted to supporting student education and professional training in the various fields and applications areas of electrical engineering. The series cover classical and emerging topics concerning:

- Communication Engineering, Information Theory and Networks
- Electronics Engineering and Microelectronics
- Signal, Image and Speech Processing
- Wireless and Mobile Communication
- Circuits and Systems
- Energy Systems, Power Electronics and Electrical Machines
- Electro-optical Engineering
- Instrumentation Engineering
- Avionics Engineering
- Control Systems
- Internet-of-Things and Cybersecurity
- Biomedical Devices, MEMS and NEMS

For general information about this book series, comments or suggestions, please contact leontina.dicecco@springer.com.

To submit a proposal or request further information, please contact the Publishing Editor in your country:

China

Jasmine Dou, Editor (jasmine.dou@springer.com)

India, Japan, Rest of Asia

Swati Meherishi, Editorial Director (Swati.Meherishi@springer.com)

Southeast Asia, Australia, New Zealand

Ramesh Nath Premnath, Editor (ramesh.premnath@springernature.com)

USA, Canada

Michael Luby, Senior Editor (michael.luby@springer.com)

All other Countries

Leontina Di Cecco, Senior Editor (leontina.dicecco@springer.com)

**** This series is indexed by EI Compendex and Scopus databases. ****

More information about this series at <https://link.springer.com/bookseries/7818>

Girolamo Di Francia · Corrado Di Natale
Editors

Sensors and Microsystems

Proceedings of AISEM 2022

 Springer

Editors

Girolamo Di Francia
ENEA
Portici, Italy

Corrado Di Natale
Department of Electronic Engineering
University of Rome Tor Vergata
Rome, Italy

ISSN 1876-1100

ISSN 1876-1119 (electronic)

Lecture Notes in Electrical Engineering

ISBN 978-3-031-25705-6

ISBN 978-3-031-25706-3 (eBook)

<https://doi.org/10.1007/978-3-031-25706-3>

© The Editor(s) (if applicable) and The Author(s), under exclusive license
to Springer Nature Switzerland AG 2023

This work is subject to copyright. All rights are solely and exclusively licensed by the Publisher, whether the whole or part of the material is concerned, specifically the rights of translation, reprinting, reuse of illustrations, recitation, broadcasting, reproduction on microfilms or in any other physical way, and transmission or information storage and retrieval, electronic adaptation, computer software, or by similar or dissimilar methodology now known or hereafter developed.

The use of general descriptive names, registered names, trademarks, service marks, etc. in this publication does not imply, even in the absence of a specific statement, that such names are exempt from the relevant protective laws and regulations and therefore free for general use.

The publisher, the authors, and the editors are safe to assume that the advice and information in this book are believed to be true and accurate at the date of publication. Neither the publisher nor the authors or the editors give a warranty, expressed or implied, with respect to the material contained herein or for any errors or omissions that may have been made. The publisher remains neutral with regard to jurisdictional claims in published maps and institutional affiliations.

This Springer imprint is published by the registered company Springer Nature Switzerland AG
The registered company address is: Gewerbestrasse 11, 6330 Cham, Switzerland

Preface

This book collects some of the papers presented at the XXI Italian Conference on Sensors and Microsystems. The conference was held on-line on 10th and 11th February 2022.

The conference was held during the last phase of the pandemics, and it was an occasion for the sensors community to meet again and to restart the research activities. Pandemics strongly affected the research; during lockdown, most of the laboratories were closed, so it is amazing that even in this harsh condition, the research actually did not stop, and researchers have been able to pursue their activities.

The number of papers in this edition of the proceedings of the Italian Conference on Sensors and Microsystems is conspicuously smaller respect to the other editions, nonetheless, we believe it is a demonstration that the research on sensors never stops even in difficult circumstances. Thus, it is a sign of recognition of the resilience of those that even in these conditions produced results, and it is a promise that once full operativity is restored, the research on sensors and related technology will return to flourish.

Our thanks to the members of the AISEM steering committee for their commitment and to the company *Athena Consulting srl* for providing the excellent technical support that made possible the conference.

Girolamo Di Francia
Corrado Di Natale

Associazione Italiana Sensori E Microsistemi



www.aisem.eu

Steering Committee

Bruno Ando'	University of Catania
Dario Compagnone	University of Teramo
Elisabetta Comini	University of Brescia
Sabrina Conoci	University of Messina
Francesco Baldini	CNR–Institute of Applied Physics, Firenze
Giovanni Betta	University of Cassino
Girolamo Di Francia	ENEA-Portici
Corrado Di Natale (Chairperson)	University of Rome Tor Vergata
Vittorio Ferrari	University of Brescia
Leandro Lorenzelli	Foundation Bruno Kessler, Trento
Giovanna Marrazza	University of Firenze
Anna Grazia Mignani	CNR Institute of Applied Physics, Firenze
Giovanni Neri	University of Messina
Pietro Siciliano	CNR–Institute of Microelectronics and Microsystems, Lecce

Contents

Albumin-Based Optical and Electrochemical Biosensors for PFAS Detection: A Comparison	1
G. Moro, F. Chiavaioli, P. Zubiato, I. Del Villar, F. Baldini, K. De Wael, L. M. Moretto, and A. Giannetti	
Coronavirus Label-Free Immunosensor: Preliminary Results	16
R. Cancelliere, Laura Micheli, E. Suffredini, S. Bellucci, G. Betta, L. Ferrigno, A. Maffucci, and G. Miele	
Characterization of Temperature Distribution in Microfluidic Chip for DNA Amplification	22
Nicola Lovecchio, Francesca Costantini, Martina Orsatti, Lorenzo Iannascoli, Augusto Nascetti, Giampiero de Cesare, and Domenico Caputo	
Compliant Multi-hinge Microgripper for Biomanipulation: Microbeads Grasping Feasibility Study	28
Alessio Buzzin, Andrea Veroli, Federica Vurchio, Pietro Ursi, Andrea Scorza, Salvatore Andrea Sciuto, Giampiero de Cesare, and Nicola Pio Belfiore	
Investigation on the Sensing Properties at Room Temperature of a Graphene/SnO₂ Nanocomposite Towards CO₂	34
Maria Lucia Miglietta, Brigida Alfano, Tiziana Polichetti, Ettore Massera, Fausta Loffredo, Fulvia Villani, Anna De Girolamo Del Mauro, and Paola Delli Veneri	
3D-Printed Face Mask with Integrated Sensors as Protective and Monitoring Tool	40
Silvia Casalnuovo, Alessio Buzzin, Antonio Mastrandrea, Ivan Mazzetta, Marcello Barbirotta, Lorenzo Iannascoli, Augusto Nascetti, Giampiero de Cesare, Donatella Puglisi, and Domenico Caputo	

Capacitive Gas Sensors with Porphyrinoids Coated SiO₂ Hybrid Nanoparticles	46
Mounika Mudiganti, Gabriele Magna, Lorena Di Zazzo, Roberto Paolesse, and Corrado Di Natale	
Detection of Volatile Organic Compounds by Using a Nanoporous Zeolite Layer	53
G. Oliva, A. S. Fiorillo, and S. A. Pullano	
Role of IR and UV-Vis Spectroscopies Combined with Electrical Measurements in Materials Relevant for Gas Sensing	58
Ambra Fioravanti, Sara Morandi, Stefano Lettieri, Michele Sacerdoti, Pietro Marani, and Maria Cristina Carotta	
A High Accuracy QCM Based Sensing System for in Water Ammonia Monitoring	64
Ada Fort, Anna Lo Grasso, Elia Landi, Marco Mugnaini, Enza Panzardi, Valerio Vignoli, Luigi Talarico, Marco Consumi, and Agnese Magnani	
A Portable Electrochemical Platform for Cobalt Detection In-Field	71
Giulia Selvolini, Matteo Nuzzo, Bianca Melean, Magdolna Casian, Oana Hosu, Cecilia Cristea, and Giovanna Marrazza	
Ethanol and Glucose Determination by DCFC Working in Batch or Flow Mode	77
Mauro Tomassetti, Mauro Castrucci, Emanuele Dell'Aglio, Luigi Campanella, Riccardo Pezzilli, and Corrado Di Natale	
Voltammetric Determination of H₂O₂ Using a GC-LDH-Proline Catalytic Sensor	83
Mauro Tomassetti, Riccardo Pezzilli, Giuseppe Prestopino, Pier Gianni Medaglia, and Corrado Di Natale	
Colorimetry by a Smartphone	88
Leonardo Ciaccheri, Barbara Adinolfi, Andrea A. Mencaglia, and Anna G. Mignani	
Nafion-Based Chipless RFID Humidity Sensor for Smart Tag Applications	94
Giada Marchi, Viviana Mulloni, Massimo Donelli, and Leandro Lorenzelli	
Metal Nanoparticles on Board of Low-Cost Devices for Optical Sensing	100
Annalisa Scroccarello, Filippo Silveri, Flavio Della Pelle, and Dario Compagnone	
Soiling Detection Investigation in Solar Irradiance Sensors Systems . . .	111
Elena Esposito, Gianni Leanza, and Girolamo Di Francia	

Actively Controlled Synchronized-Switch Harvesting on Inductor for Piezoelectric Transducers 118
 Laura Landi, Cinzia Tamburini, and Aldo Romani

LoRa-Based Wireless Sensor Network System for Aquatic Elements and Flood Early Warning Monitoring 124
 Mattia Ragnoli, Gianluca Barile, Alfiero Leoni, Giuseppe Ferri, Andrea Pelliccione, Vincenzo Stornelli, and Dina Del Tosto

Quartz Crystal Microbalance Study in Controlled Environment for Particulate Matter Sensing 129
 Ettore Massera, Luigi Barretta, Maria Lucia Miglietta, Brigida Alfano, and Tiziana Polichetti

3D-Printed Capacitive Accelerometers 135
 Massimo Scarsella, Gianluca Barile, Laura Iacoboni, Stefano Ricci, Vincenzo Stornelli, and Giuseppe Ferri

A Novel Sensor Node for Smart Personal Protective Equipment 141
 Fabrizio Formisano, Antonio Del Giudice, Michele Dellutri, Girolamo Di Francia, Giuseppe Loffredo, Armando Picardi, and Stefano Salvatori

Radar Sensor System for Unobtrusive Level Monitoring of Granular Solids Stored in Silos 147
 Marco Zini, Marco Baù, Fabio Scubla, Matteo Loda, Giuseppe Stefini, Alessandro Nastro, Marco Ferrari, and Vittorio Ferrari

Fusion Analysis of a Palmprint-Hand Geometry Multimodal Ultrasound Recognition System 153
 Monica Micucci and Antonio Iula

Algorithm for Velocity Estimation in a Multivariable Motion Sensor . . . 160
 Federico Mazzoli, Davide Alghisi, and Vittorio Ferrari

Analysis of Logic Schemes for the Optical Implementation of Pointwise Operations in Gated Recurrent Unit Cells 167
 Badrul Alam, Andrea Ceschini, Antonello Rosato, Massimo Panella, and Rita Asquini

Deep Learning for a Comprehensive Transformer Fault Detection Through Vibrational Data 174
 Valerio Ruconci, Letizia De Maria, Daniele Bartalesi, Bau Valecillos, Simone Garatti, and Sergio Bittanti

PM Sensor Based on Piezoelectric MEMS: Mock Up 180
 L. Barretta and F. Foncellino

**Assessment of Piezoelectric Properties on Prototype
BZT-BCT Devices** 186
Rossana Scaldasferri, Luigi Barretta, Paolo Aprea, Valeria Casuscelli,
Paola Sabrina Barbato, and Domenico Caputo

**Smart Internet of Things (IoT) System for Construction
Sites Monitoring** 192
Davide Colaiuda, Gianluca Barile, Eleonora Laurini, Andrea Pelliccione,
Pierluigi De Berardinis, Vincenzo Stornelli, and Giuseppe Ferri

Author Index 199



Albumin-Based Optical and Electrochemical Biosensors for PFAS Detection: A Comparison

G. Moro^{1,2,3}, F. Chiavaioli⁴, P. Zubiato⁵, I. Del Villar^{5,6}, F. Baldini⁴, K. De Wael^{2,3},
L. M. Moretto¹, and A. Giannetti⁴(✉)

¹ Department of Molecular Sciences and Nanosystems, Ca' Foscari University of Venice, Via Torino 155, 30172 Mestre, Italy

² AXES Research Group, University of Antwerp, Groenenborgerlaan 171, 2020 Antwerp, Belgium

³ NanoLab Center of Excellence, University of Antwerp, Groenenborgerlaan 171, 2020 Antwerp, Belgium

⁴ Institute of Applied Physics "Nello Carrara", National Research Council of Italy (CNR), 50019 Sesto Fiorentino, Firenze, Italy
a.giannetti@ifac.cnr.it

⁵ Electrical and Electronic Engineering Department, Public University of Navarra, 31006 Pamplona, Spain

⁶ Institute of Smart Cities (ISC), Public University of Navarra, 31006 Pamplona, Spain

Abstract. The widespread industrial use of per- and polyfluoroalkyl substances (PFAS) have engendered the release of these manmade chemicals in the environment with harmful effects on animal and human health. To monitor PFAS levels in drinking waters, sensitive and versatile sensing strategies are urgently required. Since many perfluoroalkyl carboxylic acids, such as perfluorooctanoic acid (PFOA), are fatty acid-mimic, delipidated human serum albumin (HSA) can be applied as biorecognition element for the design of novel PFAS sensors. Here, two albumin-based biosensing strategies are described and compared: *i*) a lossy mode resonance (LMR) fiber optic one and *ii*) an impedimetric portable one developed on screen-printed electrodes. In both biosensing platforms, HSA was covalently immobilized via EDC/NHS chemistry using the carboxylic moieties of the polymeric layers previously deposited at the transducer surface. Afterwards, the conformational changes related to the formation of HSA/PFOA complex were followed considering: *i*) the LMR spectral shifts for the optical platform and *ii*) the changes of absolute impedance for the impedimetric one. The performance and future developments of both PFOA biosensors are discussed.

Keywords: Lossy mode resonance (LMR) fiber optic · Per- and polyfluoroalkyl substances (PFAS) · Perfluorooctanoic acid (PFOA) · Delipidated human serum albumin (HSA) · D-shaped fiber optics · Biosensor

1 Introduction

Per- and polyfluoroalkyl substances (PFAS) are synthetic compounds, which have been created in the early 40s to answer the needs of the construction industry as well as

electronics, food packaging, household, textile manufacturers [1]. Their ground-breaking capacity to resist extreme conditions (i.e., high temperatures and corrosion) and their lipophobic/hydrophobic behaviour are of great importance for industrial applications. However, these properties are also responsible for the hazardous effects of PFAS, their toxicity and persistence in the environment [2]. PFAS contamination and its long-term effects need to be carefully monitored to safeguard overexposed populations and our ecosystem [3–5]. To this aim, the levels of such forever chemicals in environmental matrices (mainly water and soil) and biological fluids (plasma) have to be constantly monitored. Chromatographic and mass spectrometry-based hyphenated techniques play a key role in the quantification of PFAS in environmental matrices [6, 7]. However, their applicability in frequent, large-scale monitoring plans is not affordable, thus, other analytical tools are needed to map PFAS contamination, study their long-term effects and act locally to reduce their levels [8]. These screening methods should evolve fast to follow the *endless* growth of PFAS family due to the fact that manufacturers keep on introducing new compounds to respond to the restrictions imposed by national and local governments [9].

Since PFAS were traced in human plasma, several multi-analytical studies focused on elucidating the interactions of PFAS in complex with serum proteins [10–12]. Perfluorooctanoic acid (PFOA) was observed to form 4:1 stable complexes with delipidated human serum albumin (HSA) with one high-affinity site ($K_D = 0.35 \mu\text{M}$) and three low-affinity sites ($K_D = 27 \mu\text{M}$), as shown in Fig. 1a [11]. The molecular basis of the intermolecular interactions among PFOA molecules and FAs binding site underlined that PFOA structure (with its carboxylic head followed by a fluorinated C8 tail) can mimic long-chain FAs [13–15]. Daems *et al.* [12] confirmed the stability of HSA upon PFOA additions showing that delipidated albumin binds a larger number of PFOA molecules compared to the untreated protein. Furthermore, SEC-SAXS measurements were performed on HSA and PFOA:HSA showing a meaningful change in the radius of gyration after PFOA binding. This difference (about 0.8 \AA) shows that PFOA:HSA complexes assumed a more compact shape in respect to unbound HSA [16]. In conclusion, PFOA binding was found to alter HSA conformation and affect its physiological functions. These high affinity interactions helped explaining PFAS toxicity, but suggest also the possibility to apply HSA in PFAS biosensing and to take advantage from its conformation change to develop new PFOA screening methods (using indirect detection strategies) [12, 17].

The recent literature offers a rich toolbox of experimental data, sensor design protocols and characterisation techniques for albumin application in optical and electrochemical biosensors. Albumin-based electrochemical, optical and surface-plasmon resonance (SPR) sensors were successfully applied in the detection of metal ions [18, 19], small molecules [20] as well as larger analytes, such as antigens [19], over the last decade. Albumin, especially bovine serum albumin, is a well-known blocking agent able to prevent nonspecific adsorption phenomena in DNA/RNA sensors and immunosensors [21, 22]. Lately, albumin was largely applied in hybridized materials and in the formation of monolayers for probe carriers in DNA biosensors [23, 24]. The stability of albumin in biosensing platforms was investigated considering variables such as temperature, light

radiations, etc. [25]. Albumin is often combined with impedimetric affinity-based sensors, where the bioreceptor is first immobilised on the electrode surface, detecting the protein-target interaction as a localized change in the electrode/solution interface [26].

Fiber optic (FO)-based sensors rely on different strategies to allow the interaction of light traveling inside a FO with the surrounding environment where target-receptor recognition event takes place [27, 28]. The deposition of thin films, micro or nanocoatings, as optical materials has led to the development of SPR sensors as well as lossy mode resonance (LMR) sensors [29, 30]. In these sensors, the spectral position of the resonance, expressed in wavelength (λ), is sensitive to the refractive index (RI) and film thickness (surface sensitivity) as well as the RI of FO-surrounding medium (bulk sensitivity) [31]. By applying a layer sensitive to the analyte on top of the nanocoating, it is possible to correlate the changes in the resonance wavelength with the analyte concentration [32]. In LMR sensing, working with D-shaped optical fibers (also called side-polished) allowed to enlarge the evanescent field and, as a consequence, to record narrower resonances compared to uncladded optical fibers improving the surface sensitivity and figure of merit. To maximise the sensitivity in LMR sensing, the waveguide modes need to be coupled with a particular lossy mode of the semiconductor nanocoating with optimal film thickness [29]. The control of the nanocoating thickness play a key role in LMR-based sensors, as described by Del Villar *et al.* [33]. Several metallic oxides were tested and the one that showed the highest RI sensitivity was tin dioxide (SnO_{2-x}) [34, 35]. Despite the versatility of LMR-platforms in label-free biosensing, their capability to detect small molecules is extremely limited due to the non-chromogenic/fluorescent nature of the analyte (in this case a labelled-based approach must be used as single molecule array methodology [36]) or its low molecular weight. So far, this challenge was addressed by implementing the instrumentation and methodologies in use, including immobilisation steps or receptors, as overviewed by Peltomaa *et al.* [37]. LMR-sensors for small-molecules detection need to be further investigated keeping in mind that LMR-devices have several advantages over the well-established SPR-based ones, such as: *i*) easy tunability of the LMR wavelength in the optical spectrum as a function of the coating thickness, *ii*) more versatility of the material used as coating (metal-oxides or polymers with respect to noble metals), *iii*) possibility of exciting both polarization states of light and *iv*) capability of multiple LMR generation above all.

Electrochemical impedance spectroscopy (EIS) is a sensitive techniques which enables characterizing the changes at a transducer interface and wide variety of physicochemical properties [38]. Impedimetric sensors were applied in both labelled and label-free detection strategies for the determination of small-molecules as well as large biomolecules and cells [39]. EIS-based indirect detection sensing strategies provide high performance but their applicability in real matrices is often limited by non-specific adsorption phenomena [17]. These physisorption phenomena can be limited by including several washing and rinsing steps or protecting the electrode surface with a suitable polymeric layer [40, 41]. Once designed a suitable architecture, impedimetric sensors can be miniaturized, combined with portable devices, microfluidic systems, etc. [42, 43]. These integrated devices were largely applied in the single-substance or multiplexed screening of PFAS, as recently reviewed [44, 45]. For instance, Cheng *et al.* combined a

mesoporous metal–organic framework within a microfluidic setup correlating increasing analyte concentrations with the increase in impedance [46]. However, the use of bioreceptor in PFAS impedimetric sensing was not extended to proteins, so far.

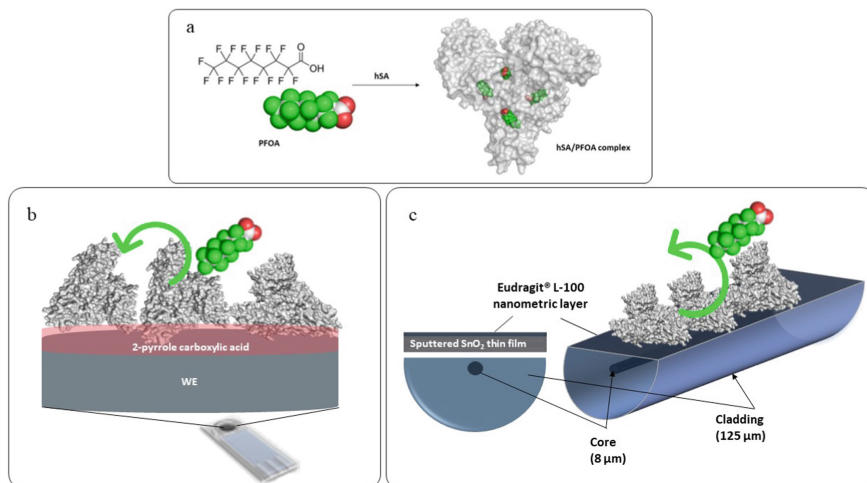


Fig. 1. Structure of the PFOA:HSA complex (a). Schematic representation of the albumin-based sensing strategies designed for PFOA detection and compared in this work: (b) impedimetric portable sensors and (c) D-shaper fiber optic platform. In both architectures the transducer (working electrode, WE, or D-shaped fiber surface) were modified with polymeric layers rich in COOH free moieties (2-pyrrole carboxylic acid and Eudragit L-100, respectively). These layers were optimized for the covalent immobilization of HSA biorecognition layer.

In this work, the two albumin-based biosensing strategies described in Fig. 1 are compared: *i*) a lossy mode resonance (LMR) fiber optic one [47] and *ii*) an impedimetric portable one designed on screen-printed electrodes [16]. In both biosensing platforms, HSA was covalently immobilized via EDC/NHS chemistry using the carboxylic moieties of a polymeric layer previously deposited at the transducer surface. Afterwards, the conformational changes related to the formation of HSA/PFOA complex were followed considering the LMR spectral shifts for the optical platform and the changes of absolute impedance for the impedimetric one. The performance and future developments of both PFOA biosensors are discussed.

2 Materials and Methods

2.1 Reagents and Materials

Pyrrole-2-carboxylic acid (99%) (Py-2-COOH), perfluorooctanoic acid (PFOA, 96%), perfluorooctanesulfonic acid potassium salt (PFOS, 98%), 2,3,3,3-tetrafluoro-2-(heptafluoropropoxy)-propanoate ammonium salt (HFPO-DA), haemoglobin (Hb, purity > 98%), ovalbumin (OVA, purity > 98%), potassium ferro(II/III)cyanide

and hydroxylamine ($[\text{Fe}(\text{CN})_6]^{3-/4-}$) were purchased from Sigma Aldrich Ltd (Belgium). 1-ethyl-3-(3-dimethylamino) propyl carbodiimide hydrochloride (EDC) and N-hydroxysulfosuccinimide (NHS) were purchased from TCI (Europe).

The 0.1 M phosphate buffer saline (PBS) pH 7.4 with 0.01 NaCl was prepared by mixing stock solutions of 0.1 M NaH_2PO_4 and 0.1 M Na_2HPO_4 , purchased from Sigma Aldrich. Solutions were prepared using MilliQ water ($R > 18 \text{ M}\Omega \text{ cm}$). Highly purified delipidated human serum albumin (HSA) obtained following the protocol reported in [11].

D-shaped fiber samples were purchased from Phoenix Photonics Ltd (Birchington, UK). Tin oxide target (SnO_{2-x}) with 99.99% purity, purchased from ZhongNuo Advanced Material Technology Co. (Beijing, China), was applied for the nanocoating deposition. UV-polymerizing optical adhesive (NOA 68), Norland Products Inc. (East Windsor, NJ, US) was used for glueing the FO into a thermo-stabilized microfluidic system. Methacrylic acid/methacrylate copolymer, commercially known as Eudragit L100, was purchased from Evonik Degussa GmbH (Dusseldorf, Germany). Graphite screen-printed electrodes (G-SPE) were purchased by Metrohm (Antwerp, Belgium).

2.2 Optical Biosensor: Preparation and Preliminary Tests

The FOs were prepared by deposition of tin oxide nanocoating on D-shaped fibers, consisting of a standard single-mode fiber (i.e., Corning SMF-28e) with a side-polished region, as previously described by Zubiate *et al.* [48]. The SnO_{2-x} nanocoating deposition is carried out at the polished surface of the fiber and its thickness ranging from 150 nm to 180 nm [35], as required from the excitation of LMR [49].

An ad-hoc experimental setup shown in Fig. 2 was assembled to monitor the transmission spectrum of the fiber during the biosensing tests. The setup included: *i*) a broadband multi-LED light source (SLD-1310/1430/1550/1690; FiberLabs, Inc., Saitama, Japan), which enables guiding the light through the fiber, *ii*) an optical spectrum analyser (OSA, Anritsu MS9030A-MS9701B; Kanagawa, Japan) to monitor the LMR in the range from 1250 to 1700 nm, *iii*) a FO in-line polarizer and *iv*) a polarization controller, which permits to tune the polarization state of light (transverse electric, TE, or transverse magnetic, TM). After the deposition process, the fiber was placed inside a thermo-stabilised microfluidic system, previously described by Trono *et al.* [50] and Chiavaioli *et al.* [51].

The sensitive portion of the SnO_{2-x} nanocoated D-shaped fibers was modified with Eudragit L100 by dipping the fiber for 1 min in a solution of 0.04% (w/v) of the polymer in ethanol [35, 48]. The polymeric layer rich in carboxylic moieties was dried at room temperature for 15 min to assure its complete reticulation. Afterwards, the carboxylic groups were activated with EDC/NHS (2 mM/5 mM, respectively) by a solution injected at $25 \mu\text{L min}^{-1}$ for 30 min. Then, a 1 mg mL^{-1} solution of HSA was injected at a flow rate of $10 \mu\text{L min}^{-1}$. This step was followed by a washing step in PBS running buffer at a flow rate of $250 \mu\text{L min}^{-1}$ for 10 min. All solutions mentioned were freshly prepared in PBS pH 7.4. The assays were performed injecting increasing concentrations of PFOA at a flow rate of $25 \mu\text{L min}^{-1}$. Washing steps were performed with PBS after each PFOA injection, at a flow rate of $250 \mu\text{L min}^{-1}$ for 10–20 min when the steady-state condition was reached.

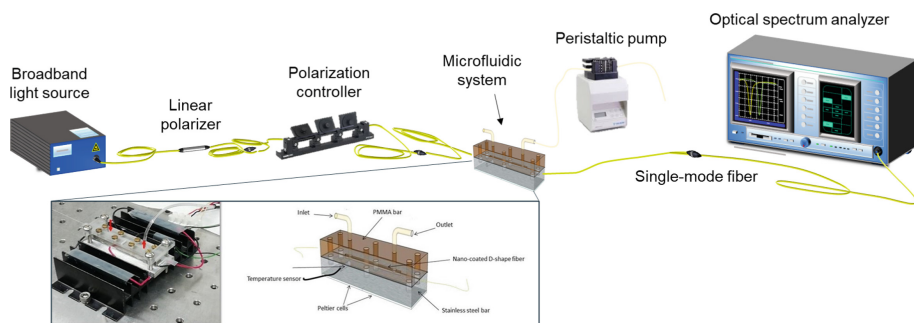


Fig. 2. Schematic of the main components of the experimental setup in use with details of the microfluidic system.

2.3 Impedimetric Biosensor: Preparation and Preliminary Tests

Disposable graphite screen-printed electrodes (G-SPE) consisting of a graphite working (diameter of 4 mm) and counter electrode and a silver pseudo reference were first modified with a polymeric layer. The electropolymerisation of 10 mM Py-2-COOH was performed by CV, using the following parameters: a potential window between 0.3 V and + 1.2 V, at different scan rates (25, 50, 100 mV s^{-1}) and number of cycles (5, 10, 20) in 0.1 M SDS. Afterwards, HSA was immobilised via EDC/NHS chemistry. To activate the carboxylic moieties, 20 μL of an equimolar solution (0.07 M) of EDC/NHS in MilliQ water were incubated at the working electrode (WE) for about 20 min. During the incubation step the G-SPE were stored at 4 $^{\circ}\text{C}$. The solution was then washed away and 30 μL of 2 mg mL^{-1} HSA in PBS pH 7.4 were let in contact with the WE for other 30 min. Albumin-modified G-SPE (described in Fig. 3) were rinsed with PBS to remove protein excess and the unreacted carboxylic moieties were blocked incubating 20 μL of 1 M hydroxylamine for 20 min at 4 $^{\circ}\text{C}$.

EIS measurements were recorded in 0.1 M PBS, pH 7.4 with 2 mM $[\text{Fe}(\text{CN})_6]^{3-/4-}$, in the frequency range between 0.1 M Hz and 0.1 Hz, with 0.01 V amplitude and bias potential determined by open circuit potential. The EIS data were verified for linearity with the Kramers-Kronig transformation and analysed using ZView 2 [52, 53]. Except where otherwise stated, all the potentials are referred to silver pseudo reference electrode. All electrochemical experiments were performed at room temperature. EIS and cyclic voltammetry (CV) measurements were performed using an Autolab potentiostat/galvanostat (PGSTAT 302N, ECOCHEMIE, The Netherlands) controlled by NOVA 1.1 software. The modified electrode (HSA-Py-2-COOH-G-SPE) was incubated with 20 mL of PFOA solution at different concentrations for 20 min at room temperature. After, the electrode was rinsed with 500 μL of phosphate buffer and EIS spectra were acquired in 80 μL of 2 mM $[\text{Fe}(\text{CN})_6]^{3-/4-}$ in 0.1 M phosphate buffer. The calibration plot was built in the concentration range between 100 nM and 5 mM. The relevant analytical parameter ΔZ is defined as the difference in absolute impedance values, acquired at 10 Hz, between the HSA-Py2-COOH-G-SPE and after the incubation with PFOA. All measurements were performed in triplicates, unless otherwise indicated.

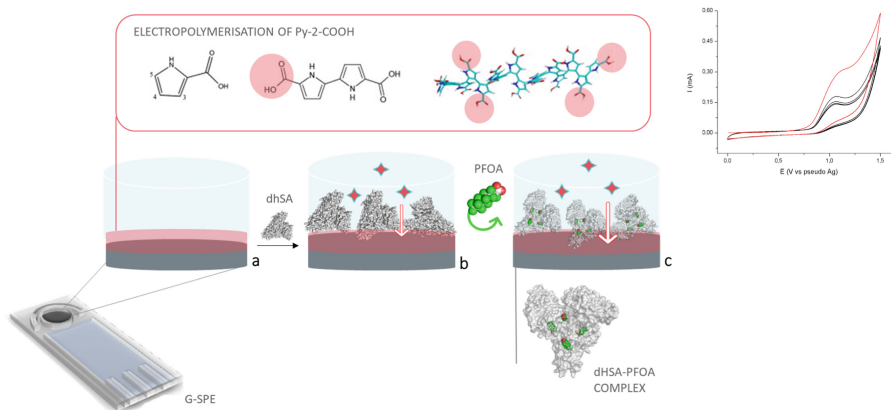


Fig. 3. Schematic representation of the screen-printed impedimetric sensor designed for PFOA detection. (a) The WE is modified with Py-2-COOH: the monomer, dimer and linear polymer are showed in the figure inset to show the distribution of the free carboxylic moieties. The polymer electropolymerisation was followed by CV (first cycle in red in the voltammograms reported). (b) HSA immobilization and the biorecognition layer characterization in presence of the redox probe were performed prior to target incubation (c).

2.4 Scanning Electron Microscopy Imaging

The surface of the FO after functionalisation with the biorecognition layer and incubation with increasing PFOA concentrations was characterised with scanning electron microscope (SEM): a Gaia 3 Tescan FIB-SEM; Tescan Orsay Holding (Brno- Kohoutovice, Czech Republic) equipped with an in-lens detector at 3 kV and an aperture diameter of 30 μm . The images of fiber morphology were collected using secondary electrons (SE) at 5.0 kV with a magnification of 19.6 kx. The elemental composition of the FO samples, both longitudinal and transversal cross-section, was investigated via X-ray microanalysis system (EDAX; Octane Elect EDS system; AMETEK, US) comparing the results obtained at nude and modified FOs.

The modified and bare G-SPE morphology was also characterized by SEM. The images were acquired with a Field Emission Gun – Environmental Scanning Electron Microscope equipped with an Energy Dispersive X-Ray detector (FEI Quanta 250, USA).

3 Results and Discussion

3.1 Optical LMR-Based Biosensing: Preliminary Results

The covalent immobilization of HSA biosensing layer onto the fiber via EDC/NHS chemistry was first optimized as described in [47]. The flat surface of the D-shaped fiber portion was analyzed via SEM-EDS to check the morphology and the elemental composition of the region, as showed in Fig. 4a. The biofilm (colored in green for sake of clarity in Fig. 4a) showed an average thickness of about 200 ± 15 nm. It comprises the biological layer anchored at the polymeric one (*biorecognition layer*) and tin dioxide nanocoating

(*LMR-exciting layer*). The stability of the modification protocol was assessed incubating different concentration of PFOA and considering the changes in the sensorgram: even with a very low concentration of PFOA (0.156 ng mL^{-1}) a clear LMR shift was observed after following the modification protocol described in Sect. 2.2. Afterwards, the biosensor performance was tested in real-time incubating three different concentrations of PFOA ranging from 0.156 ng mL^{-1} to 1.56 ng mL^{-1} and 15.6 ng mL^{-1} . The PFOA spiked PBS solutions at increasing concentrations were injected using the peristaltic pump, within the microfluidic system where the functionalized FO was previously located.

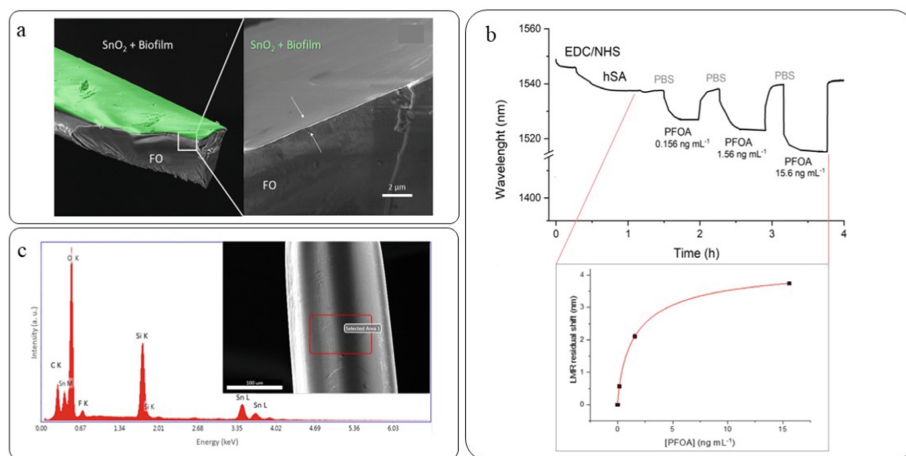


Fig. 4. (a) SEM images of the modified FO in the longitudinal (left) and cross-sectional (right) views. Details of the D-shaped region of the fiber with the modified surface (colored in green) and of the interface between the silica fiber (FO) and the SnO_{2-x} nanocoating are shown. (b) Example of sensorgram of the real-time monitoring of the biosensor modification and incubation of increasing concentrations of PFOA with the calibration curve fitted with a Langmuir adsorption isotherm (bottom inset). (c) SEM-EDS analysis of the FO after PFOA incubation showing the presence of fluorine residues on the FO surface.

Each sample incubation was followed by an intermediate washing step with PBS as well, to prevent nonspecific binding and/or analyte aggregation, as described in Sect. 2.2. All these steps are summarized in the exemplificative sensorgram of Fig. 4b with the trend of LMR shift vs PFOA concentration. These preliminary experimental data were fitted with a Langmuir adsorption isotherm making use of Hill equation; this latter was previously applied in LMR-based biosensors [48]. In this case study, the use of this equation is justified by the fact that it can model a reversible association, such as PFOA:HSA complex formation, giving information about the degree of interaction. These first screening was followed by regeneration trials using hydroxylamine (1 mM solution injected at $25 \mu\text{L min}^{-1}$ for 15 to 30 min). Unfortunately, this step resulted in a strong red shift and led to the destabilisation of the biorecognition layer. Other alternatives need to be tested to regenerate this highly sensitive platform and improve its applicability in real sample analysis. Since PFOA:HSA is highly stable, it is difficult to

design a regeneration protocol able to operate the selective removal of the analyte (via competition mechanism or playing on PFOA affinity for organic solvents). However, even a one-step removal of the entire biofilm would be instrumental to limit the costs of these sensing strategy.

The presence of PFOA at the modified FO after incubation was indirectly verified by SEM-EDS. As showed in Fig. 4c, it was possible to observe the presence of fluorine (3.72 wt%) due to PFOA binding to HSA. The data provide an additional proof of HSA capacity to complex PFOA and preconcentrate the analyte at the fiber surface undergoing measurable changes.

3.2 Impedimetric Biosensing: Preliminary Results

The design of the sensing platform was previously optimized [16]. The EIS signal changes upon incubation of spiked samples with increasing PFOA concentrations were evaluated directly from the Bode phase plots (instead of analysing the equivalent electrochemical circuit parameters after fitting the Nyquist plots), as exemplified in Fig. 5a. From the analysis of HSA-Py-2-COOH-G-SPE (blue dots), two peaks, with Θ_{\max} at 1 and 10 Hz, were observed: each corresponding to a different kinetic processes [54]. Both peaks appear after the Py-2-COOH electropolymerisation, but only the process II at 10 Hz is affected after PFOA incubation with an increase in the phase value. Therefore, the changes in terms of ΔZ were plotted against different PFAS concentrations and the calibration curves in Fig. 5b were obtained. Here, ΔZ is defined as the difference between the Z value of the HSA modified electrode at 10 Hz and the same value recorded after incubation with different PFOA solutions. PFAS concentrations in the range from 100 nM to 5 μM were tested, corresponding to 41 ng mL^{-1} to 2.07 $\mu\text{g mL}^{-1}$ for PFOA. Other PFAS were selected to: *i*) test another fluorinated substance with the same chain length of PFOA and a different head group (PFOS) and *ii*) test a shorter-chain PFAS with a carboxylic group (HFPO-DA). The results show clearly that the properties of the electro/solution interface are altered by both the PFAS (PFOS and HFPO-DA) and the blank (buffer solution). With buffer solution additions, the ΔZ ranged from 7 to 15 (grey area) and no trend was observed, as expected for a blank. The signal for 41 ng mL^{-1} (100 nM) of PFOA falls below the threshold value ($\Delta Z \approx 15$) and, thus, cannot be considered specific. After incubation with increasing concentration of PFOS, the change in ΔZ were of the same magnitude of the one observed with blank additions (from 7 to 15) suggesting that PFOS interacts with the layer but without leading to stable conformational changes as for PFOA. Considering the structural similarity of PFOA and PFOS, we could have expected a similar trend in the biosensor response. The behavior observed can be ascribe to their different affinity for HSA and the possible differences in PFOA/PFOS-HSA binding mechanism. Compared to PFOS data, the incubation of HFPO-DA led to a more meaningful change in the ΔZ , with a trend similar to the one observed for PFOA. These findings suggest that also HFPO-DA interacts with the biorecognition layer but its effect is not as evident as for PFOA. This might depend on the HFPO-DA solubility (higher than PFOA one), interaction mechanism, affinity for HSA (lower than PFOA one), etc. Overall, these negative controls experiments confirmed that the biorecognition layer of our impedimetric platform is highly sensitive (undergoes traceable changes even after blank additions) and particularly suitable for

PFOA detection (for other PFAS the ΔZ are not meaningful and/or proportional to the analyte concentration). The reproducibility of the impedimetric biosensors was found to be about 89%, which is considered acceptable for a first proof-of-concept.

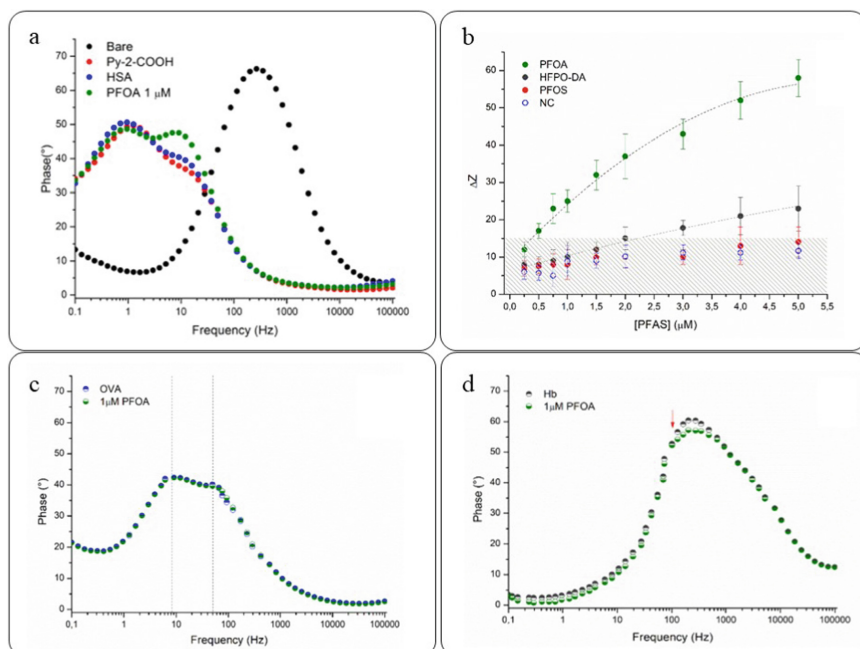


Fig. 5. Example of the changes recorded: (a) Bode phase plot for the HSA-Py-2-COOH-G-SPE recorded in presence of the redox probed, bare (black dots), after Py-2-COOH electropolymerisation (red dots), after HSA immobilisation (blue dots) and after incubation with 1 μM PFOA (green dots); (b) Calibration plot for the HSA-Py-2-COOH-G-SPE biosensors between 100 nM and 5 μM PFOA (green dots), HFPO-DA (grey dots), PFOS (red dots) and buffer solution (white/blue dots), polynomial fitting equation of PFOA calibration plot: $y = 11.20 + 14.97 x - 1.23 x^2$. Error bars calculated on triplicates. **Negative controls experiments:** Bode phase plot for the (c) OVA-Py-2-COOH-G-SPE and (d) Hb-Py-2-COOH-G-SPE. Both biosensors were tested in presence of the redox probe after incubation with 1 μM PFOA (green dots).

In this platform the role of HSA was further evaluated, additional negative controls were performed using other non-delipidated proteins instead of human serum albumin: ovalbumin (OVA) and haemoglobin (Hb). The G-SPE modification protocol was applied without any optimization of the protein concentrations. In this frame, these proteins were selected simply because their MWs are similar to the one of HSA (OVA \approx 45 kD and Hb \approx 64.5 k Da). The results of these tests are exemplified in Fig. 5c–d, where the Bode plot of the modified electrodes prior/after incubation of 1 μM PFOA are compared for both OVA and Hb. The results of OVA-Py-2-COOH-G-SPEs show no changes upon incubation of PFOA. As for HSA, here two processes with different kinetics were observed (dotted lines) even though the frequencies of the Θ_{max} resulted to be shifted towards higher values. For Hb-Py-2-COOH-G-SPEs, the profile of the Bode

plot before PFOA incubation was characterised by a broad peak (overlapped peaks) suggesting the presence of multiple processes with similar kinetics. This difference can be ascribed to the completely different nature of Hb compared to HSA and OVA: Hb is an electroactive protein. In this case, the equilibria of the interfacial region are more complex to follow, but also this second control experiment showed that PFOA incubation do no alter the biorecognition layer in an observable way. Both controls confirm that the possibility to detect increasing PFOA concentrations with protein-Py-2-COOH-G-SPEs depends on the specific changes in the biorecognition layer immobilised at the G-SPE surface. Only HSA, with its high affinity for PFOA and its capacity to undergo a meaningful conformational change when complexed with this compound, is suitable for PFOA biosensing. As for the optic platform, all procedures tested to regenerate the platform after use did not provide successful results, so far.

From these preliminary experiments, we can conclude that HSA can be applied as a PFOA bioreceptor in portable, affordable sensing platforms. The covalent immobilisation of the protein assures a good reproducibility of the biorecognition layer responses and the high sensitivity of impedance outcomes allow to follow HSA-PFOA complex formation.

3.3 Comparison of the Platforms

These preliminary results confirmed the applicability of HSA as a bioreceptor for PFOA recognition both in optical and impedimetric biosensors. The optical LMR-based biosensor presents a high sensitivity compared to the impedimetric portable platform. According to the results obtained so far, we can envisage applying the impedimetric sensor for large-scale, frequent, *in-situ* screening of highly contaminate areas, while the optical platform results to be more suitable for monitoring low PFAS concentration and perform real-time analysis. In this scenario, the two sensing platform show a good complementarity, helping us to answer different analytical questions. The lower sensitivity of the impedimetric platform is counterbalanced by the simplicity and low cost of the sensors. On the contrary, D-shaped FO are more expensive compared to commercial G-SPE and not compatible with portable instrumentation yet. Thanks to the affordable costs and good reproducibility of the EIS-based sensor it was possible to further extend our study testing other PFAS/possible bioreceptor (negative controls), while for the optical platforms the costs resulted to be a limiting factor. To limit the costs, it would be particularly important to regenerate the optical platform assuring the possibility of using it multiple times. Unfortunately, for none of the two sensing platforms it was possible to successfully regenerate the biorecognition layer, mixtures of aqueous/organic solvents need to be further tested. Prior to make these test, we should further improve the design of the biorecognition layer by selecting only the domains hosting the high affinity PFOA binding sites. This step should allow improving the selectivity of both platforms limiting non-specific adsorption phenomena.

4 Conclusions

An optical label-free and a portable impedimetric biosensors are compared. Both sensing platforms are designed to detect PFOA in water matrices by using HSA as a biorecognition layer. The architectures of these sensors are comparable: the transducer surface is functionalised with a polymer rich in free-carboxylic moieties where the protein is immobilised via EDC/NHS chemistry. The preliminary results show the complementarity of these platforms in terms of applicability, sensitivity and costs. The future perspective is to further combine these sensors in a dual signal platform.

References

1. Meegoda, J.N., Kewalramani, J.A., Li, B., Marsh, R.W.: A review of the applications, environmental release, and remediation technologies of per- and polyfluoroalkyl substances. *Int. J. Environ. Res. Public Health* **17**, 1–26 (2020). <https://doi.org/10.3390/ijerph17218117>
2. Sinclair, G.M., Long, S.M., Jones, O.A.H.: What are the effects of PFAS exposure at environmentally relevant concentrations? *Chemosphere* **258**, 127340 (2020). <https://doi.org/10.1016/j.chemosphere.2020.127340>
3. Al Amin, M., et al.: Recent advances in the analysis of per- and polyfluoroalkyl substances (PFAS)—A review. *Environ. Technol. Innov.* **19**, 100879 (2020). <https://doi.org/10.1016/j.eti.2020.100879>
4. Koch, A., Aro, R., Wang, T., Yeung, L.W.Y.: Towards a comprehensive analytical workflow for the chemical characterisation of organofluorine in consumer products and environmental samples. *TrAC - Trends Anal. Chem.* **123**, 115423 (2020). <https://doi.org/10.1016/j.trac.2019.02.024>
5. Feng, H., Ruan, Y., Zhang, K., Lam, P.K.S.: Current analytical methodologies and gaps for per- and polyfluoroalkyl substances determination in the marine environment. *TrAC - Trends Anal. Chem.* **121**, 115372 (2019). <https://doi.org/10.1016/j.trac.2018.12.026>
6. Jia, S., Marques Dos Santos, M., Li, C., Snyder, S.A.: Recent advances in mass spectrometry analytical techniques for per- and polyfluoroalkyl substances (PFAS). *Anal. Bioanal. Chem.* **414**, 2795–2807 (2022). <https://doi.org/10.1007/s00216-022-03905-y>
7. Dodds, J.N., Hopkins, Z.R., Knappe, D.R.U., Baker, E.S.: Rapid characterization of per- and polyfluoroalkyl substances (PFAS) by ion mobility spectrometry–mass spectrometry (IMS-MS). *Anal. Chem.* **92**, 4427–4435 (2020). <https://doi.org/10.1021/acs.analchem.9b05364>
8. Fiedler, H., van der Veen, I., de Boer, J.: Global interlaboratory assessments of perfluoroalkyl substances under the Stockholm Convention on persistent organic pollutants. *TrAC - Trends Anal. Chem.* **124**, 115459 (2020). <https://doi.org/10.1016/j.trac.2019.03.023>
9. Barceló, D., Ruan, T.: Challenges and perspectives on the analysis of traditional perfluoroalkyl substances and emerging alternatives. *TrAC - Trends Anal. Chem.* **121**, 2–3 (2019). <https://doi.org/10.1016/j.trac.2019.07.016>
10. Liu, X., Fang, M., Xu, F., Chen, D.: Characterization of the binding of per- and poly-fluorinated substances to proteins: a methodological review. *TrAC - Trends Anal. Chem.* **116**, 177–185 (2019). <https://doi.org/10.1016/j.trac.2019.05.017>
11. Maso, L., et al.: Unveiling the binding mode of perfluorooctanoic acid to human serum albumin. *Protein Sci.* **30**, 830–841 (2021). <https://doi.org/10.1002/pro.4036>
12. Daems, E., et al.: Native mass spectrometry for the design and selection of protein bioreceptors for perfluorinated compounds. *Analyst* **146**, 2065–2073 (2021). <https://doi.org/10.1039/D0A0N02005B>

13. Han, X., Snow, T.A., Kemper, R.A., Jepson, G.W.: Binding of perfluorooctanoic acid to rat and human plasma proteins. *Chem. Res. Toxicol.* **16**, 775–781 (2003). <https://doi.org/10.1021/tx034005w>
14. Chi, Q., Li, Z., Huang, J., Ma, J., Wang, X.: Interactions of perfluorooctanoic acid and perfluorooctanesulfonic acid with serum albumins by native mass spectrometry, fluorescence and molecular docking. *Chemosphere* **198**, 442–449 (2018). <https://doi.org/10.1016/j.chemosphere.2018.01.152>
15. Chen, Y.M., Guo, L.H.: Fluorescence study on site-specific binding of perfluoroalkyl acids to human serum albumin. *Arch. Toxicol.* **83**, 255–261 (2009). <https://doi.org/10.1007/s00204-008-0359-x>
16. Moro, G., et al.: Covalent immobilization of delipidated human serum albumin on poly (pyrrole-2-carboxylic) acid film for the impedimetric detection of perfluorooctanoic acid. *Bioelectrochemistry* **134**, 107540 (2020). <https://doi.org/10.1016/j.bioelechem.2020.107540>
17. Moro, G., De Wael, K., Moretto, L.M.: Challenges in the electrochemical (bio)sensing of nonelectroactive food and environmental contaminants. *Curr. Opin. Electrochem.* **16**, 57–65 (2019). <https://doi.org/10.1016/j.coelec.2019.04.019>
18. Wu, C.-M., Lin, L.-Y.: Utilization of albumin-based sensor chips for the detection of metal content and characterization of metal–protein interaction by surface plasmon resonance. *Sens. Actuators B Chem.* **110**, 231–238 (2005). <https://doi.org/10.1016/j.snb.2005.01.047>
19. Tang, Z., Fu, Y., Ma, Z.: Bovine serum albumin as an effective sensitivity enhancer for peptide-based amperometric biosensor for ultrasensitive detection of prostate specific antigen. *Biosens. Bioelectron.* **94**, 394–399 (2017). <https://doi.org/10.1016/j.bios.2017.03.030>
20. He, C., et al.: A highly sensitive glucose biosensor based on gold nanoparticles/bovine serum albumin/Fe₃O₄ biocomposite nanoparticles. *Electrochim. Acta* **222**, 1709–1715 (2016). <https://doi.org/10.1016/j.electacta.2016.11.162>
21. Wang, R., Zhou, X., Zhu, X., Yang, C., Liu, L., Shi, H.: Isoelectric bovine serum albumin: robust blocking agent for enhanced performance in optical-fiber based DNA sensing. *ACS Sens.* **2**, 257–262 (2017). <https://doi.org/10.1021/acssensors.6b00746>
22. Riquelme, M.V., Zhao, H., Srinivasaraghavan, V., Pruden, A., Vikesland, P., Agah, M.: Optimizing blocking of nonspecific bacterial attachment to impedimetric biosensors. *Sens. Bio-Sens. Res.* **8**, 47–54 (2016). <https://doi.org/10.1016/j.sbsr.2016.04.003>
23. Liu, Y.-H., Li, H.-N., Chen, W., Liu, A.-L., Lin, X.-H., Chen, Y.-Z.: Bovine serum albumin-based probe carrier platform for electrochemical DNA biosensing. *Anal. Chem.* **85**, 273–277 (2013). <https://doi.org/10.1021/ac303397f>
24. He, Y., et al.: Highly reproducible and sensitive electrochemiluminescence biosensors for HPV detection based on bovine serum albumin carrier platforms and hyperbranched rolling circle amplification. *ACS Appl. Mater. Interf.* **13**, 298–305 (2021). <https://doi.org/10.1021/acsaami.0c20742>
25. Klos-Witkowska, A., Akhmetov, B., Zhumangalieva, N., Karpinskyi, V., Gancarczyk, T.: Bovine Serum Albumin stability in the context of biosensors. In: 2016 16th International Conference on Control, Automation and Systems, pp. 976–980 (2016). <https://doi.org/10.1109/ICCAS.2016.7832427>
26. Daniels, J.S., Pourmand, N.: Label-free impedance biosensors: opportunities and challenges. *Electroanalysis* **19**, 1239–1257 (2007). <https://doi.org/10.1002/elan.200603855>
27. Jiao, L., Zhong, N., Zhao, X., Ma, S., Fu, X., Dong, D.: Recent advances in fiber-optic evanescent wave sensors for monitoring organic and inorganic pollutants in water. *TrAC Trends Anal. Chem.* **127**, 115892 (2020). <https://doi.org/10.1016/j.trac.2020.115892>
28. Shukla, S.K., Kushwaha, C.S., Guner, T., Demir, M.M.: Chemically modified optical fibers in advanced technology: an overview. *Opt. Laser Technol.* **115**, 404–432 (2019). <https://doi.org/10.1016/j.optlastec.2019.02.025>

29. Chiavaioli, F., Janer, D.: Fiber optics sensing with lossy mode resonances: applications and perspectives. *J. Light. Technol.* **8724**, 3855–3870 (2021). <https://doi.org/10.1109/JLT.2021.3052137>
30. Chiavaioli, F.: Recent development of resonance-based optical sensors and biosensors. *Optics* **1**, 255–258 (2020). <https://doi.org/10.3390/opt1030019>
31. Li, Z., Yang, X., Zhu, H., Chiavaioli, F.: Sensing performance of fiber-optic combs tuned by nanometric films: new insights and limits. *IEEE Sens. J.* **21**, 13305–13315 (2021). <https://doi.org/10.1109/JSEN.2021.3068445>
32. Del Villar, I., et al.: Optical sensors based on lossy-mode resonances. *Sens. Actuators B Chem.* **240**, 174–185 (2017). <https://doi.org/10.1016/j.snb.2016.08.126>
33. Del Villar, I., et al.: Design rules for lossy mode resonance based sensors. *Appl. Opt.* **51**, 4298–4307 (2012). <https://doi.org/10.1364/AO.51.004298>
34. Kosiel, K., Koba, M., Masiewicz, M., Śmietana, M.: Tailoring properties of lossy-mode resonance optical fiber sensors with atomic layer deposition technique. *Opt. Laser Technol.* **102**, 213–221 (2018). <https://doi.org/10.1016/j.optlastec.2018.01.002>
35. Chiavaioli, F., et al.: Femtomolar Detection by nanocoated fiber label-free biosensors. *ACS Sens.* **3**, 936–943 (2018). <https://doi.org/10.1021/acssensors.7b00918>
36. Schubert, S.M., et al.: Ultra-sensitive protein detection via Single Molecule Arrays towards early stage cancer monitoring. *Sci. Rep.* **5**, 11034 (2015). <https://doi.org/10.1038/srep11034>
37. Peltomaa, R., Glahn-Martínez, B., Benito-Peña, E., Moreno-Bondi, M.C.: Optical biosensors for label-free detection of small molecules. *Sensors* **18**, 4126 (2018). <https://doi.org/10.3390/s18124126>
38. Guan, J.-G., Miao, Y.-Q., Zhang, Q.-J.: Impedimetric biosensors. *J. Biosci. Bioeng.* **97**, 219–226 (2004). [https://doi.org/10.1016/S1389-1723\(04\)70195-4](https://doi.org/10.1016/S1389-1723(04)70195-4)
39. Yang, L., Guiseppi-Elie, A.: Impedimetric biosensors for nano- and microfluidics. In: Li, D. (ed.) *Encyclopedia of Microfluidics and Nanofluidics*, pp. 811–823. Springer, Boston (2008). https://doi.org/10.1007/978-0-387-48998-8_686
40. VandeVondele, S., Vörös, J., Hubbell, J.A.: RGD-grafted poly-l-lysine-graft-(polyethylene glycol) copolymers block non-specific protein adsorption while promoting cell adhesion. *Biotechnol. Bioeng.* **82**, 784–790 (2003). <https://doi.org/10.1002/bit.10625>
41. Frutiger, A., Tanno, A., Hwu, S., Tiefenauer, R.F., Vörös, J., Nakatsuka, N.: Nonspecific binding—Fundamental concepts and consequences for biosensing applications. *Chem. Rev.* **121**, 8095–8160 (2021). <https://doi.org/10.1021/acs.chemrev.1c00044>
42. Mahato, K., Kumar, A., Maurya, P.K., Chandra, P.: Shifting paradigm of cancer diagnoses in clinically relevant samples based on miniaturized electrochemical nanobiosensors and microfluidic devices. *Biosens. Bioelectron.* **100**, 411–428 (2018). <https://doi.org/10.1016/j.bios.2017.09.003>
43. Zhang, D., Liu, Q.: Biosensors and bioelectronics on smartphone for portable biochemical detection. *Biosens. Bioelectron.* **75**, 273–284 (2016). <https://doi.org/10.1016/j.bios.2015.08.037>
44. Zamfir, L.-G., Puiu, M., Bala, C.: Advances in electrochemical impedance spectroscopy detection of endocrine disruptors. *Sensors* **20**, 6443 (2020). <https://doi.org/10.3390/s20226443>
45. Clark, R.B., Dick, J.E.: Towards deployable electrochemical sensors for per- and polyfluoroalkyl substances (PFAS). *Chem. Commun.* **57**, 8121–8130 (2021). <https://doi.org/10.1039/D1CC02641K>
46. Cheng, Y.H., et al.: Metal–organic framework-based microfluidic impedance sensor platform for ultrasensitive detection of perfluorooctanesulfonate. *ACS Appl. Mater. Interf.* **12**, 10503–10514 (2020). <https://doi.org/10.1021/acsami.9b22445>

47. Moro, G., et al.: Nanocoated fiber label-free biosensing for perfluorooctanoic acid detection by lossy mode resonance. *Results Opt.* **5**, 100123 (2021). <https://doi.org/10.1016/j.rio.2021.100123>
48. Zubiate, P., et al.: Fiber-based early diagnosis of venous thromboembolic disease by label-free D-dimer detection. *Biosens. Bioelectron. X* **2**, 100026 (2019). <https://doi.org/10.1016/j.biosx.2019.100026>
49. Nazri, N.A.A., Azeman, N.H., Luo, Y., Bakar, A.A.A.: Carbon quantum dots for optical sensor applications: a review. *Opt. Laser Technol.* **139**, 106928 (2021). <https://doi.org/10.1016/j.optlastec.2021.106928>
50. Trono, C., Baldini, F., Brenci, M., Chiavaioli, F., Mugnaini, M.: Flow cell for strain- and temperature-compensated refractive index measurements by means of cascaded optical fibre long period and Bragg gratings. *Meas. Sci. Technol.* **22**, 075204 (2011). <https://doi.org/10.1088/0957-0233/22/7/075204>
51. Chiavaioli, F., Gouveia, C.A.J., Jorge, P.A.S., Baldini, F.: Towards a uniform metrological assessment of grating-based optical fiber sensors: from refractometers to biosensors. *Biosensor* **7**, 23 (2017). <https://doi.org/10.3390/bios7020023>
52. Boukamp, B.A.: Practical application of the Kramers-Kronig transformation on impedance measurements in solid state electrochemistry. *Solid State Ionics* **62**, 131–141 (1993). [https://doi.org/10.1016/0167-2738\(93\)90261-Z](https://doi.org/10.1016/0167-2738(93)90261-Z)
53. Agarwal, P.: Application of measurement models to impedance spectroscopy. *J. Electrochem. Soc.* **142**, 4159 (1995). <https://doi.org/10.1149/1.2048479>
54. Casero, E., Parra-Alfambra, A.M., Petit-Domínguez, M.D., Pariente, F., Lorenzo, E., Alonso, C.: Differentiation between graphene oxide and reduced graphene by electrochemical impedance spectroscopy (EIS). *Electrochem. Commun.* **20**, 63–66 (2012). <https://doi.org/10.1016/j.elecom.2012.04.002>



Coronavirus Label-Free Immunosensor: Preliminary Results

R. Cancelliere¹, Laura Micheli¹ (✉), E. Suffredini², S. Bellucci³, G. Betta⁴,
L. Ferrigno⁴, A. Maffucci⁴, and G. Miele⁴

¹ Department of Chemical Science and Technologies, University of Rome “Tor Vergata”, Rome, Italy

laura.micheli@uniroma2.it

² Department of Food Safety, Nutrition and Veterinary Public Health, Istituto Superiore di Sanità, Rome, Italy

³ Istituto Nazionale di Fisica Nucleare–Laboratori Nazionali di Frascati (INFN-LNF), Frascati, Italy

⁴ Department of Electrical and Information Engineering, University of Cassino and Southern Lazio, Cassino, Italy

Abstract. Real-time detection of airborne infection agents present in human breath and environmental airways, such as the human respiratory Coronavirus, is important for public health. For this, a model label-free immunosensor, based on multi-walled nanotubes (MWNT)-based screen-printed graphite electrodes (SPEs), was proposed and studied. For sensing applications, MWNTs have many advantages such as small size with larger surface area, excellent electron transfer promoting ability when used for antibody immobilization, with retention of its selectivity for potential immunosensors development. In order to verify the selectivity of the selected primary antibody (anti-CoV 229E antibody) and the effective immunocomplex formation (antigen-antibody), an in-depth voltammetric characterization of MWNT-SPEs interface was carried out during the multistep fabrication of CoV immunosensor using $[\text{Fe}(\text{CN})_6]^{3-/4-}$ as an electroactive probe. After that, the analytical robustness of the performances of these immunosensing platforms was estimated and verified. Indeed, a nanomolar range detection limit (180 TCID₅₀/mL)g/mL) with excellent reproducibility (RSD% = 8%) was obtained.

Keywords: Label-free immunosensor · Nanomaterials · MWNT · Coronavirus · Voltammetric detection · Screen-printed platforms

1 Introduction

Food quality and safety monitoring together with the clinical diagnosis are issues of utmost importance for human health [1].

In modern livestock production, veterinary drugs, pesticides, hormones and other additives are used on a large scale. The massive use of these compounds may leave

residues in edible products negatively affecting human health [2]. In addition, inadequate storage conditions could lead to the formation of various toxins and the diffusion of pathogens [3]. For the detection and quantification of these analytes, several conventional methods such as chromatography coupled to mass spectrometry, ultraviolet, or fluorescence spectroscopy, among others, are utilized [4]. These methods are laborious, expensive, time-consuming, and require large sample volumes and highly trained personnel. To overcome these limitations, electrochemical, and in particular label-free biosensing platforms, offer a complementary alternative by allowing fast screening of samples on-site [5]. The combination between immunochemistry and electrochemistry offers the possibility to develop a huge number of simple-to-use devices with a low-cost, high selectivity, fast and sensitive response [6]. These characteristics make them especially well-suited for on-field screening analyses, as they are easily coupled to portable devices, especially when screen-printed electrodes (SPEs) are used as a cost-effective alternative to traditional solid electrodes.

In this work, developed in the frame of the project “SFIDE”, we developed a label-free immunosensor for the real-time detection of Coronaviridae (CoV) presence in the aerosol. The family Coronaviridae is part of the order *Nidovirales* [7] and includes a substantial number of pathogens of mammals and birds that individually cause a remarkable variety of diseases (i.e. pneumonia, enteritis, polyserositis, hepatitis, encephalomyelitis, nephritis, and various other disorders). Coronavirus-like infections have been described in different animals (i.e. swine, cattle, horses, cats, dogs, etc.) and in humans. In the last case, coronaviruses may induce pathologies in the spectrum between the common cold and severe acute respiratory syndrome (SARS) [7].

Herein, we report on an immunosensor assembled on multiwall (MWNT)-modified platforms able to detect the presence of coronaviruses in the nanomolar range. The nanomaterials employed are among the most versatile and customizable enabling surface coatings with a plethora of bio/materials for the construction of a wide variety of electrochemical sensing platforms [8]. A carefully voltammetric characterization was conducted in order to study the layer-by-layer construction of the immunosensor.

2 Experimental Section

2.1 Materials and Reagents

All chemicals were of analytical grade. Anti-mouse IgG antibody was purchased from Sigma-Aldrich (Steinheim, Germany). Rabbit anti-CoV-229E spike S1 was purchased from DBA SRL (Milano, Italy), whereas inactivated CoV-229E was provided by Istituto Superiore di Sanità (Roma, Italy). Potassium ferricyanide and potassium ferrocyanide were purchased from Sigma-Aldrich (Steinheim, Germany). Buffers: a) 0.05 M phosphate buffer saline + 0.1 M KCl, pH = 7.4 (PBS); b) 0.05 M phosphate buffer saline (PBS-T), 0.05% Tw20 (v/v).

2.2 Apparatus and Techniques

In-house produced screen-printed devices were used as transducing platforms for our immunosensors developments. A PalmSens 4.0 potentiostat (PalmSens, Netherlands)

was employed for the electrochemical measurements (cyclic voltammetry, CV, and square wave voltammetry, SWV).

2.3 Theoretical Methods

The heterogeneous electron transfer constant (k_0), the standard curves (using non-linear 4 parameter logistic calibration plots), the limit of detection (LOD), and the limit of quantification (LOQ) were calculated as reported in our previous work [5].

2.4 Fabrication of CoV-229E Label-Free Electrochemical Immunosensor

Initially, screen printed electrodes (SPEs) were modified via drop-casting with a dispersion of MWNT [8]. After that, 6 μL of IgG (10 $\mu\text{g}/\text{ml}$) prepared in PBS was drop-casted onto the working electrode (WE) and stored overnight at 4 $^\circ\text{C}$. 6 μL of 5% polyvinyl alcohol (PVA) (incubation of 20 min) was used to block the surface of WE remained free, and after that 6 μL of anti-CoV-229E antibody (5 $\mu\text{g}/\text{ml}$) in PBS was deposited onto the WE. This binding procedure lasted 120 min at room temperature using an orbital shaker. At this point, 6 μL of CoV (several concentrations) was added and left reacting for 60 min. The immunological complex formation was monitored using 0.01 M $[\text{Fe}(\text{CN})_6]^{4-/3-}$ solution as an electroactive probe and square wave voltammetry (SWV) as analytical techniques (Fig. 1).

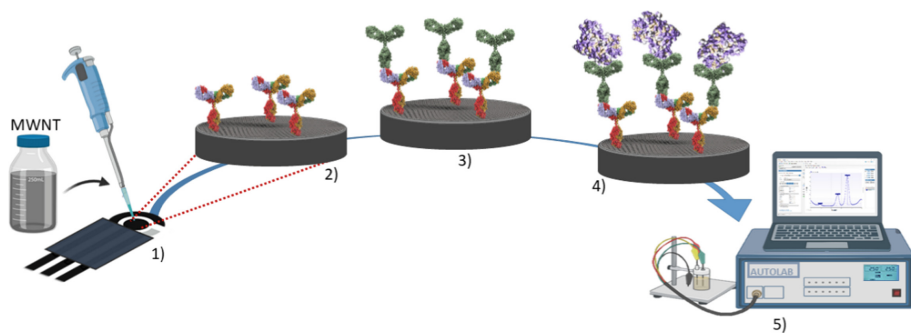


Fig. 1. Schematic representation of MWNT-SPE based immunosensor assembly for CoV detection.

3 Results and Discussion

3.1 Electrochemical Characterization of the Immunosensor Build-Up

Initially, an in-depth electrochemical characterization of the layer-by-layer construction (Fig. 1) of our CoV-immunosensor was undertaken. In particular, the Cyclic Voltammetry (CV) was used to study the fabrication of the immunological chain and thus the effect of the layer coating on the electrodic surface. A visual inspection of the voltammograms

reported in Fig. 2 reveals the effects of the different chemical and biological layers over the electrical conductivity of the electrode/electrolyte interface, influencing the SPE performance. In particular, the construction of the immunological chain, first with mAb-IgG and then with mAb-CoV, produces a significant decrease in the magnitude of voltammetric peaks, as reported in Table 1. This is confirmed by the increase of the peak-to-peak separation, with a consequent deflection of $[\text{Fe}(\text{CN})_6]^{3-/4-}$ to its ideal reversible electrochemical behavior. These phenomena are ascribable to the layer coating of the electrode surface, which became thicker with the assembly procedure, whereby reducing $[\text{Fe}(\text{CN})_6]^{3-/4-}$ permeability through the immobilization of the layers on the WE [9].

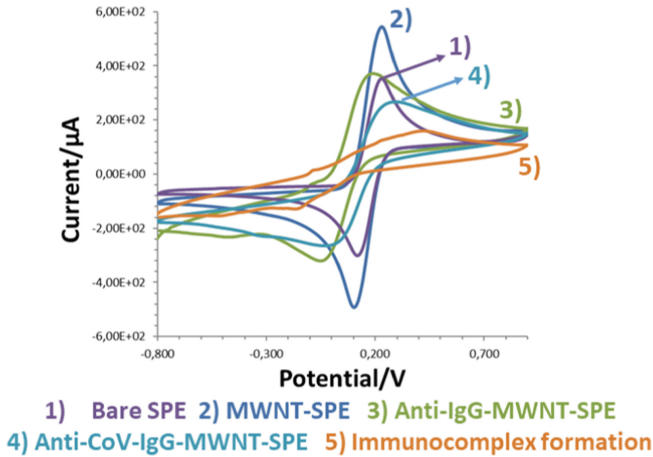


Fig. 2. Electrochemical characterization of electrode interfaces during the multistep biosensor build-up. Cyclic voltammograms recorded in 0.005 M $[\text{Fe}(\text{CN})_6]^{4-/3-}$ in 0.05 M PBS.

Table 1. Anodic and cathodic peak ratio (I_{pa}/I_{pc}), peak-to-peak separation (ΔE), effective surface area (A) and heterogeneous electron transfer rate constant (k^0) estimated for MWNT-SPE using CV in 0.005 M $[\text{Fe}(\text{CN})_6]^{4-/3-}$, in PBS pH 7.4, during CoV-immunosensor fabrication.

Layer	I_{pa}/I_{pc}	ΔE (mV)	A (cm^2)	k^0 (cm/s)
MWNT	1.0 ± 0.2	110 ± 14	0.36 ± 0.05	$(3.5 \pm 0.4) \cdot 10^{-3}$
Anti IgG	1.2 ± 0.2	200 ± 25	0.28 ± 0.02	$(3.3 \pm 0.5) \cdot 10^{-4}$
Anti CoV	1.4 ± 0.4	293 ± 33	0.05 ± 0.01	/
NoV	/	525 ± 39	0.020 ± 0.002	/

3.2 Preliminary Analytical Performances

Once anti-IgG was immobilized, the ideal anti-CoV Ab concentration to be immobilized were investigated. To this purpose, the electrochemical response (SWV faradic current) of different anti-CoV Ab concentrations (0, 0.5, 1, 2, 5, 10 $\mu\text{g/mL}$), incubated for 1 h on anti-IgG-MWNT-modified SPE (Fig. 3a) were tested. By increasing the antibody concentration, a decrease in the recorded faradic current values is observed that can be explained by the following mechanism: the higher the antibody concentration, the higher the molecular crowding on the electrode surface due to the antibody molecular complementarity. The proper antibody concentration to be applied can be obtained considering the 75–80% of the maximum value of the association curve that for anti-CoV Ab is equal to 5 $\mu\text{g/mL}$. From the dose-response curve reported in Fig. 3b a LoD of 180 TCID₅₀/mL [5] with a good reproducibility of 13% (RSD%) are observed.

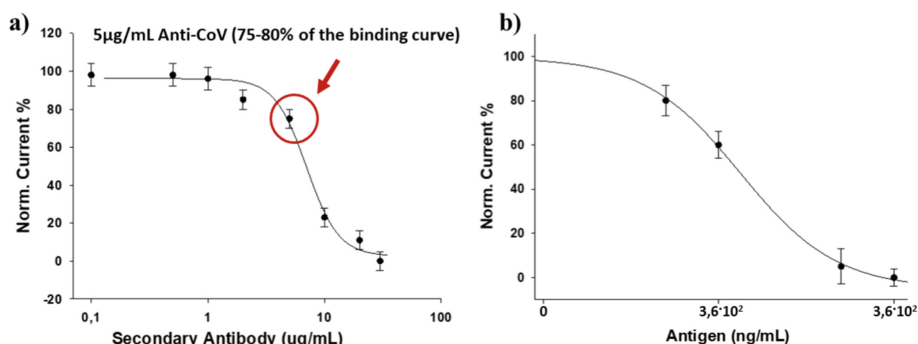


Fig. 3. a) Binding curves (dilution of antibody solution) obtained using different concentrations of anti-CoV Ab and b) the dose-response curve, obtained incubating different antigen concentrations. The results were obtained by making use of SWV and 0.05 M $[\text{Fe}(\text{CN})_6]^{4-/3-}$ solution, in 0.05 M PBS + 0.01 M KCl, pH 7.4.

4 Conclusion

In this work, a disposable, simple, low-cost, label-free voltammetric immunosensor for the determination of 229E CoV was successfully preliminary characterized. The serigraphic sensor, modified with MWNTs, exhibited a low detection limit and good sensitivity paving the way to its potential exploitation for the detection of 229E CoV in aerosol and environment airways.

Funding. This work was partially supported by the Project “SFIDE A SMART FRAMEWORK FOR VIRUS DETECTION”, funded by Italian Ministry of University and Research FISR DD 562/2020 - FONDO INTEGRATIVO SPECIALE PER LA RICERCA, grant # FISR2020IP_02585.

References

1. Fung, F., Wang, H.-S., Menon, S.: Food safety in the 21st century. *Biomed. J.* **41**, 88–95 (2018). <https://doi.org/10.1016/j.bj.2018.03.003>
2. Patel, M., Kumar, R., Kishor, K., Mlsna, T., Pittman, C.U., Mohan, D.: Pharmaceuticals of emerging concern in aquatic systems: chemistry, occurrence, effects, and removal methods. *Chem. Rev.* **119**, 3510–3673 (2019). <https://doi.org/10.1021/acs.chemrev.8b00299>
3. Mitchell, M.J., Billingsley, M.M., Haley, R.M., Wechsler, M.E., Peppas, N.A., Langer, R.: Engineering precision nanoparticles for drug delivery. *Nat. Rev. Drug Discov.* **20**, 101–124 (2021). <https://doi.org/10.1038/s41573-020-0090-8>
4. Alahi, M., Mukhopadhyay, S.: Detection methodologies for pathogen and toxins: a review. *Sensors* **17**, 1885 (2017). <https://doi.org/10.3390/s17081885>
5. Cancelliere, R., et al.: Electrochemical and morphological layer-by-layer characterization of electrode interfaces during a label-free impedimetric immunosensor build-up: the case of ochratoxin A. *Appl. Surf. Sci.* **567**, 150791 (2021). <https://doi.org/10.1016/j.apsusc.2021.150791>
6. Zhang, Y., et al.: Label-free electrochemical immunosensor based on enhanced signal amplification between Au@Pd and CoFe₂O₄/graphene nanohybrid. *Sci. Rep.* **6**, 23391 (2016). <https://doi.org/10.1038/srep23391>
7. Coronaviridae. In: Fenner's Veterinary Virology, pp. 393–413. Elsevier (2011). <https://doi.org/10.1016/B978-0-12-375158-4.00024-9>
8. Cancelliere, R., Tinno, A.D., Cataldo, A., Bellucci, S., Micheli, L.: Powerful electron-transfer screen-printed platforms as biosensing tools: the case of uric acid biosensor. *Biosensors* **12**, 2 (2021). <https://doi.org/10.3390/bios12010002>
9. Cancelliere, R., Di Tinno, A., Di Lellis, A.M., Contini, G., Micheli, L., Signori, E.: Cost-effective and disposable label-free voltammetric immunosensor for sensitive detection of interleukin-6. *Biosens. Bioelectron.* 114467 (2022). <https://doi.org/10.1016/j.bios.2022.114467>



Characterization of Temperature Distribution in Microfluidic Chip for DNA Amplification

Nicola Lovecchio¹, Francesca Costantini², Martina Orsatti¹, Lorenzo Iannascoli³, Augusto Nascetti³, Giampiero de Cesare¹, and Domenico Caputo¹(✉)

¹ Department of Information Engineering, Electronics and Telecommunications, Sapienza University of Rome, 00184 Rome, Italy

{nicola.lovecchio, domenico.caputo}@uniroma1.it

² CREA-DC Research Centre for Plant Protection and Certification, 00156 Rome, Italy

³ School of Aerospace Engineering, Sapienza University, 00138 Rome, Italy

Abstract. This work focuses on the temperature monitoring inside a polydimethylsiloxane microfluidic chip, suitable for DNA amplification. In order to achieve this aim, the microfluidic chip has been thermally coupled with a lab-on-chip integrating, on a single glass substrate, temperature sensors and thin film heater. The wells of the chip have been filled with thermochromic liquid crystals, that change their optical properties at a precise transition temperature (T_T). Experiments have been performed cycling the chip temperatures between 90 °C and 50 °C, two temperatures very close to the annealing and denaturation steps of the standard Polymerase Chain Reaction (PCR), utilized for DNA amplification. Results state that the temperature distribution inside the wells follows values and spatial uniformity required by the PCR cycles, guaranteeing an effective heat transfer from the thin film resistor to the microfluidic chip. Gel electrophoresis of amplified samples showed the presence of the amplifications and thus the successful implementation of the PCR in our lab-on-chip.

Keywords: Lab-on-chip · DNA amplification · Thermochromic liquid crystal · Temperature measurement · Microfluidics · Polydimethylsiloxane

1 Introduction

Lab-on-a-chip (LoC) based on microfluidics [1, 2] have attracted researches attention in the past three decades for diagnostics [3], chemical [4] and biological applications [5, 6]. The major advantages of LoC devices with respect to the traditional methods rely in low volume consumption of both sample and reagents, short assay time, automatized processes, precise and predictable fluid flow regimes [7], portability, and integration with sensors, actuators, controllers [8] to perform on a single chip multiple laboratory analyses.

Among the different functions implemented in the LoC, the integration of DNA amplification through Polymerase Chain Reaction (PCR) or Loop Mediated Isothermal Amplification (LAMP) [9–11] have received a lot attention due to the possibility to reach

superior performances compared to conventional technologies, such as amplification times ten times faster than conventional systems.

RNA/DNA amplification occurs at specific temperatures of the solutions in microfluidic channels or wells. Therefore, a method to precisely monitor and control the temperature has to be implemented [12, 13]. Conventional methods are based on the use of thermocouples [14], resistance temperature probes [15] and laser induced fluorescence (LIF) [16, 17]. However, all of them present some disadvantages. Thermocouples and resistive sensors have a reduced spatial resolution and their presence inside the microfluidic channel can modify the actual temperature due to the low liquid volume inside the microfluidic network. On the other hand, LIF suffers for the variation in the excitation light intensity distribution due to the characteristics of the light source and pathways and for the quenching effects, that can change the relation between the temperature and fluorescence intensity [18].

In order to overcome the abovementioned issues, in this work we measure the temperature inside a microfluidic chip by monitoring the change of the optical properties of thermochromic liquid crystals (TLC) filling the chambers of the chip. These materials, indeed, have a temperature-dependent selective reflectivity property that changes their color as the temperature changes [19]. In particular, they present a transition temperature (T_T) above which they become transparent [20]. Recording the color change during a temperature cycling and processing the acquired images, we were able to monitor the spatial distribution and time evolution of temperature inside the microfluidic chambers, with a non-intrusive method and avoiding at the same time all the instability related to a radiation source.

2 Structure of the System Measurement

The utilized measurement system relies on the combination of a system-on-glass, a microfluidic chip and a commercial mobile phone.

2.1 System-on-Glass (SoG)

The SoG is a single $5 \times 5 \text{ cm}^2$ 1 mm-thick glass substrate, which integrates i) a thin film heater on the bottom side of the glass and ii) temperature and light sensors and an interferential filter on the top side. All the sensors and actuators are fabricated using standard microelectronic technologies.

The heater is a Cr/Al/Cr metal stack, with thickness equal to 100 nm/600 nm/100 nm, respectively. Its double spiral geometry has been optimized in order to get a uniform temperature distribution ($\pm 1.25 \text{ }^\circ\text{C}$ at $90 \text{ }^\circ\text{C}$) over an active area of about 5 cm^2 [21, 22].

The temperature and photo-sensors are p-type/intrinsic/n-type hydrogenated amorphous silicon (a-Si:H) structures grown by Plasma Enhanced Chemical Vapor deposition and patterned through optical photolithography [23]. There are eight photosensors on a radial geometry and six temperature sensors close to the photosensors.

The interferential filter is a stacked structure of $\text{TiO}_2/\text{SiO}_2$ dielectric layers, whose thicknesses have been optimized to reject wavelengths below 510 nm and transit without attenuation (below 5%) wavelengths above 600 nm.

2.2 Microfluidic Chip

The microfluidic chip is a $3 \times 3 \text{ cm}^2$ 5 mm-thick black polydimethylsiloxane (PDMS) layer hosting 4 round wells with diameter equal to 3 mm. The used PDMS is the Sylgard 184 (Dow Corning Corp.) with mixture ratio of curing agent to pre-polymer equal to 1:10. To obtain a black chip, the PDMS was mixed with graphite powder before curing.

The chip has been fabricated bonding the microfluidic chip to a $2.8 \times 3.6 \text{ cm}^2$ 0.1 mm-thick glass substrate following the steps listed below:

- pouring of Sylgard 184 black mixture onto a 3D-printed plastic mold;
- 30 min vacuum treatment to remove air bubbles;
- 10 min baking in oven at $100 \text{ }^\circ\text{C}$;
- spinning of Sylgard 184 transparent mixture on a cleaned $5 \times 5 \text{ cm}^2$ glass substrate;
- laying of the black microfluidic first on the $5 \times 5 \text{ cm}^2$ substrate and then sticking on the thin $2.8 \times 3.6 \text{ cm}^2$ glass substrate;
- 30 min vacuum treatment to promote PDMS chip-glass adhesion and to remove air residues;
- 30 min baking in oven at $100 \text{ }^\circ\text{C}$.

3 Experiments and Results

The experimental set-up is schematically reported in Fig. 1. The experiment aims to determine the temperature inside the microfluidic wells taking advantage of the temperature-dependent optical properties of the TLC. Indeed, the temperature sensors monitor the temperature of the top glass surface of the SoG, which could be different from the temperature of the biological solution.

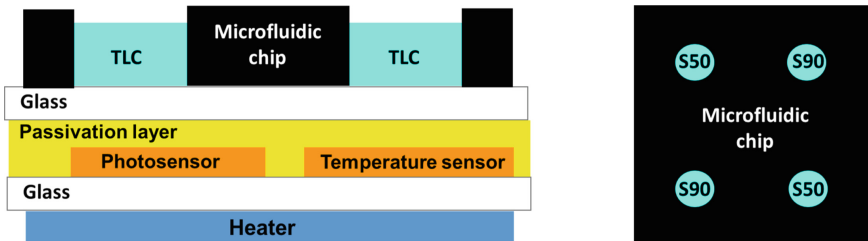


Fig. 1. System-on-Glass platform coupled with the microfluidic chip, whose wells are filled with the thermochromic liquid crystals (TLC).

The microfluidic wells were filled with two formulations of TLC purchased from Hallcrest (Chicago, IL). Two wells were filled with $20 \mu\text{l}$ of S50, which has a $T_T = 50 \pm 1 \text{ }^\circ\text{C}$, while the other two were filled with $20 \mu\text{l}$ of S90, which has a $T_T = 90 \pm 1 \text{ }^\circ\text{C}$. The heater was driven with appropriate current values to execute the following steps:

- temperature increase from 40 °C to 95 °C and then decrease to 40 °C;
- temperature increase from 40 °C to 53 °C and then decrease to 40 °C;
- cycling of steps a and b.

The current values were adjusted, thanks to a PID algorithm, in order to achieve the required set point temperature.

The light from a mobile phone illuminated the microfluidic chip during the temperature cycling and the reflected light was recorded on the same phone. Selected frames of the videos have been processed with Image J software in order to get the color levels. Figures 2 and 3 demonstrate the color change of formulation S90 and S50, respectively. In each figure, blue and green lines are the blue and green components of the color levels of the solutions inside the wells as extracted by ImageJ, the orange curve is the temperature measured by the temperature sensors on the SoG. Figures include pictures of the microfluidic chip during temperature change. The time differences (Δt_1 , Δt_2) between solid and dashed vertical lines represent the delays needed to achieve the set point temperature in the wells.

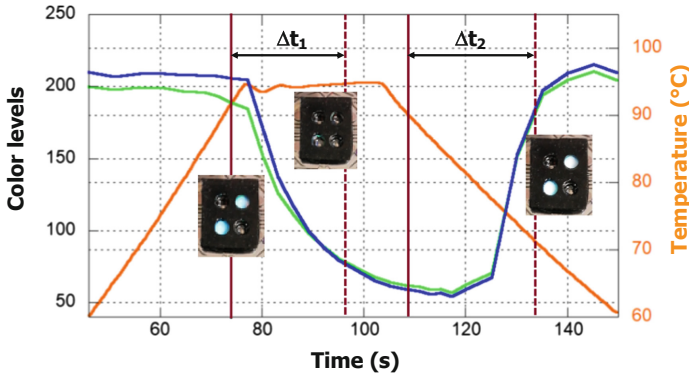


Fig. 2. Blue and green components (color levels) as a function of time in the two wells filled with S90. The right axis is the temperature measured by the temperature sensors. A good uniformity of temperature distribution is achieved for both wells.

Comparing the time evolution of temperature monitored by the sensors and the color/transparency of the microfluidic wells, we observe that, despite a delay time around 20 s between setting temperature on the SoG and on the fluid inside the microfluidic wells, a complete transparency of the TLC is achieved in all the wells above the transition temperature. This behavior has been observed for all the cycles (up to 30) we have implemented in our lab-on-chip. This confirms that the developed system guarantees an effective heat transfer from the thin film resistor to the microfluidic chip and a very uniform temperature distribution inside the wells.

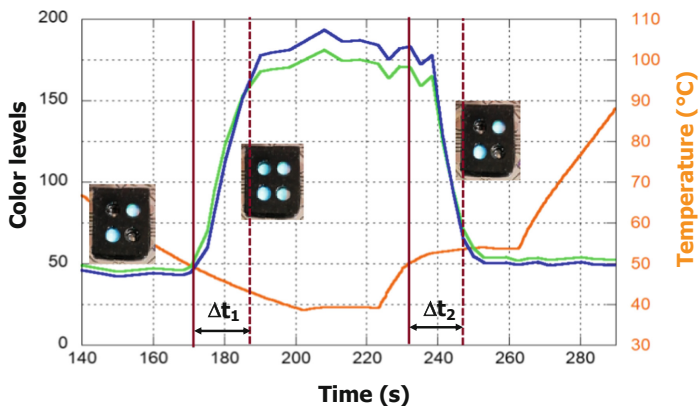


Fig. 3. Blue and green components (color levels) as a function of time in the two wells filled with S50. The right axis is the temperature measured by the temperature sensors. A good uniformity of temperature distribution is achieved for both wells.

4 Conclusions

In this paper we have utilized thermochromic liquid crystals to monitor the temperature distribution inside a microfluidic chip. Experiments have been performed coupling the chip to a SoG, integrating on the same glass substrate a thin film heater, light and temperature sensors and an interferential filter. Data demonstrate that the temperature distribution inside the wells follows the values and spatial uniformity required by the PCR cycles achieving an effective heat transfer from the thin film resistor to the microfluidic chip and enabling this lab-on-chip for practical uses as DNA thermal cycler.

Acknowledgements. Authors wish to thank Italian and Ministry of University (MUR) and Research and Ministry of Foreign Affairs and International Cooperation (MAECI) for the financial supports through the project PGR00843 “Acustofluidic DNA Diagnosis Chip (ADD-Health)”.

References

1. Manz, A., et al.: Planar chips technology for miniaturization and integration of separation techniques into monitoring systems: capillary electrophoresis on a chip. *J. Chromatogr. A* **593**(1–2), 253–258 (1992)
2. Whitesides, G.M.: The origins and the future of microfluidics. *Nature* **442**, 368–373 (2006)
3. Wu, J., Dong, M., Rigatto, C., Liu, Y., Lin, F.: Lab-on-chip technology for chronic disease diagnosis. *NPJ Digit. Med.* **1**(1), 1–11 (2018)
4. Nightingale, A.M., Beaton, A.D., Mowlem, M.C.: Trends in microfluidic systems for in situ chemical analysis of natural waters. *Sens. Actuators B: Chem.* **221**, 1398–1405 (2015)
5. Conde, J.P., et al.: Lab-on-chip systems for integrated bioanalyses. *Essays Biochem.* **60**(1), 121–131 (2016)
6. Nandimandalam, M., et al.: Split aptamers immobilized on polymer brushes integrated in a lab-on-chip system based on an array of amorphous silicon photosensors: a novel sensor assay. *Materials* **14**(23), 7210 (2021)

7. Caputo, D., de Cesare, G., Lovecchio, N., Scipinotti, R., Nascetti, A.: Electrowetting-on-dielectric system based on polydimethylsiloxane. In: 5th IEEE International Workshop on Advances in Sensors and Interfaces IWASI, pp. 99–103. IEEE (2013)
8. Salieb-Beugelaar, G.B., Simone, G., Arora, A., Philippi, A., Manz, A.: Latest developments in microfluidic cell biology and analysis systems. *Anal. Chem.* **82**(12), 4848–4864 (2010)
9. Petralia, S., Verardo, R., Klaric, E., Cavallaro, S., Alessi, E., Schneider, C.: In-Check system: a highly integrated silicon Lab-on-Chip for sample preparation, PCR amplification and microarray detection of nucleic acids directly from biological samples. *Sens. Actuators B: Chem.* **187**, 99–105 (2013)
10. Hung, T.Q., Chin, W.H., Sun, Y., Wolff, A., Bang, D.D.: A novel lab-on-chip platform with integrated solid phase PCR and Supercritical Angle Fluorescence (SAF) microlens array for highly sensitive and multiplexed pathogen detection. *Biosens. Bioelectron.* **90**, 217–223 (2017)
11. Tymm, C., Zhou, J., Tadimety, A., Burklund, A., Zhang, J.X.: Scalable COVID-19 detection enabled by lab-on-chip biosensors. *Cell. Mol. Bioeng.* **13**(4), 313–329 (2020)
12. Sun, K., Yamaguchi, A., Ishida, Y., Matsuo, S., Misawa, H.: A heater-integrated transparent microchannel chip for continuous-flow PCR. *Sens. Actuators B: Chem.* **84**(2–3), 283–289 (2002)
13. Chen, P.C., Nikitopoulos, D.E., Soper, S.A., Murphy, M.C.: Temperature distribution effects on micro-CFPCR performance. *Biomed. Microdev.* **10**(2), 141–152 (2008)
14. Xiang, Q., Xu, B., Fu, R., Li, D.: Real time PCR on disposable PDMS chip with a miniaturized thermal cycler. *Biomed. Microdev.* **7**(4), 273–279 (2005)
15. Norian, H., Field, R.M., Kymissis, I., Shepard, K.L.: An integrated CMOS quantitative-polymerase-chain-reaction lab-on-chip for point-of-care diagnostics. *Lab Chip* **14**(20), 4076–4084 (2014)
16. Ross, D., Gaitan, M., Locascio, L.E.: Temperature measurement in microfluidic systems using a temperature-dependent fluorescent dye. *Anal. Chem.* **73**(17), 4117–4123 (2001)
17. Natrajan, V.K., Christensen, K.T.: Two-color laser-induced fluorescent thermometry for microfluidic systems. *Meas. Sci. Technol.* **20**(1), 015401 (2008)
18. Arik, M., Çelebi, N., Onganer, Y.: Fluorescence quenching of fluorescein with molecular oxygen in solution. *J. Photochem. Photobiol. A: Chem.* **170**(2), 105–111 (2005)
19. Dabiri, D.: Digital particle image thermometry/velocimetry: a review. *Exp. Fluids* **46**(2), 191–241 (2009)
20. Basson, M., Pottebaum, T.S.: Measuring the temperature of fluid in a micro-channel using thermochromic liquid crystals. *Exp. Fluids* **53**(3), 803–814 (2012)
21. Scorzoni, A., et al.: Design and experimental characterization of thin film heaters on glass substrate for Lab-on-Chip applications. *Sens. Actuators A: Phys.* **229**, 203–210 (2015)
22. Lovecchio, N., et al.: Integrated optoelectronic device for detection of fluorescent molecules. *IEEE Trans. Biomed. Circ. Syst.* **12**(6), 1337–1344 (2018)
23. Costantini, F., et al.: Integrated sensor system for DNA amplification and separation based on thin film technology. *IEEE Trans. Compon. Packag. Manuf. Technol.* **8**(7), 1141–1148 (2018)



Compliant Multi-hinge Microgripper for Biomanipulation: Microbeads Grasping Feasibility Study

Alessio Buzzin¹(✉), Andrea Veroli¹, Federica Vurchio², Pietro Ursi³, Andrea Scorza²,
Salvatore Andrea Sciuto², Giampiero de Cesare¹, and Nicola Pio Belfiore²

¹ Department of Information Engineering, Electronics and Telecommunications, “Sapienza”
University of Rome, via Eudossiana 18, 00184 Rome, Italy

alessio.buzzin@uniroma1.it

² Department of Engineering, Università degli studi Roma Tre, via della Vasca Navale 79,
00146 Rome, Italy

³ Department of General Surgery and Surgical Specialties “Paride Stefanini”, “Sapienza”
University of Rome, viale del Policlinico 155, 00161 Rome, Italy

Abstract. A feasibility study on micromanipulation performed by a novel, multi-hinge microgripper with high mechanical dexterity and complex in-plane motion is herein presented. Thanks to design concepts based on selective flexibility, the device is highly compact and easy to be manufactured by means of MEMS technologies. In the presented experimental test case, the microgripper was immersed in a complex mixture, made of saline solution with floating agarose-based microbeads as target objects; direct contact tests were carried out via microscope observation of the jaw-tips operational window. The results highlight the function capability of clamping objects of tens of microns in size, encouraging further developments toward the manipulation of actual cells.

Keywords: Microgripper · MEMS · SOI · Compliant · Microsurgery · Cells · Microbeads · Agarose · Biological manipulation

1 Introduction

Over the years, the progress of microelectronic technologies and micro electro-mechanical systems (MEMS) enabled the development of novel applications, having an impact in everyday life: as an example, medicine welcomed such evolution in fields such as surgery, tissue engineering and microbiology [1]. Moreover, complex operations in biomedical laboratories have been increasingly downscaled and integrated in compact, smart Lab-on-Chip (LoC) systems [2, 3]. Among the possible tasks that can be identified in these fields, the ability of manipulating increasingly smaller objects by MEMS is becoming progressively more valuable, from the microscale down to the nanoscale, thanks to nano electro-mechanical systems (NEMS) [4, 5]. Although in this framework micromanipulation has been extensively explored, for example by optical methods or ultrasonic waves [6, 7], some issues related to potential damage on the target biosample

(i.e. excessive amount of applied energy) can be easily fixed using more versatile end effective contact-based manipulators [8]. The most challenging issue in developing a mechanical manipulator relates to the major trade-off between mechanical complexity, required to improve the motion capabilities, and compactness, needed to implement the device in new and unexplored applications. Indeed, complex motion implies mechanical complexity, which consequently brings to difficulties in scaling down the manipulator's overall footprint [9]. To fix this issue, an equivalent version of the classic mechanical design can be considered to accomplish its prototyping at smaller scales: if traditional hinges are replaced by flexible beams [10], both highly compact and dexterous devices can have a significantly simplified mechanical scheme, allowing for an easier fabrication with MEMS technologies [11]. This approach enables downsizing to extreme extents, encouraging technological challenges in novel applications [12–14].

This work presents a MEMS-technology based manipulator specifically designed to take on these challenges: a double four-bar linkage mirrored structure, with 8 flexible hinges, covers an overall surface of a few square millimetres, while assuring a significantly improved in-plane motion of the tips with respect to state-of-the-art single-hinge grippers [15]. Here we report a feasibility study on the capability of clamping microscaled objects in a complex environment, performing an immersion inside a mixture and carrying out direct geometrical and morphological comparisons and contact tests between microparticles and the clamping window of the mechanism. Agarose-based microbeads were chosen as target objects, floating inside a saline solution to resemble a biomedical scenario. This experimental investigation is intended to support the final stages of longstanding, multidisciplinary efforts in developing highly compact, dexterous, compliant micromanipulators for biomedical applications, involving mechanical design [16], analyses on how scaling affects the physics of the mechanism [17], investigations on materials and prototyping methods [18], determination of potential applications [19, 20], arrangement of test campaigns [21]. The reported results are considered as a preliminary step toward experiments with real tissues or cells, in order to fully validate our device, with the purpose of offering novel solutions in terms of dexterous motion and compactness in the biomedical-surgical field.

2 Design and Operating Principle

The device under test (DUT) is the result of a series of development phases. First, elementary topological and kinematic synthesis have been used to design the pseudo-rigid body equivalent model (PRBM) of a four-bar linkage whose coupler supports the tip that generates a certain path, as illustrated in Fig. 1a. Subsequently, classical revolute joints have been replaced by curved flexible beams: the result is an equivalent mechanism characterized by lumped compliance, but with the same motion capabilities. Furthermore, such a single-layer, single-material structure is easier to fabricate and to downscale with MEMS-based technologies. Figure 1b depicts the final design, with two mirrored mechanisms to model a microgripper. Two couples of interdigitated fingers form electrostatically-actuated rotary comb drives, producing the motion of each four-bar mechanism and, finally, to the displacement of each tip. In this configuration, the actuation causes a shift from the open to the closed state and the clamping action. The tips' operating window is 85 μm -long and 150 μm -wide (Fig. 1b, top right corner).

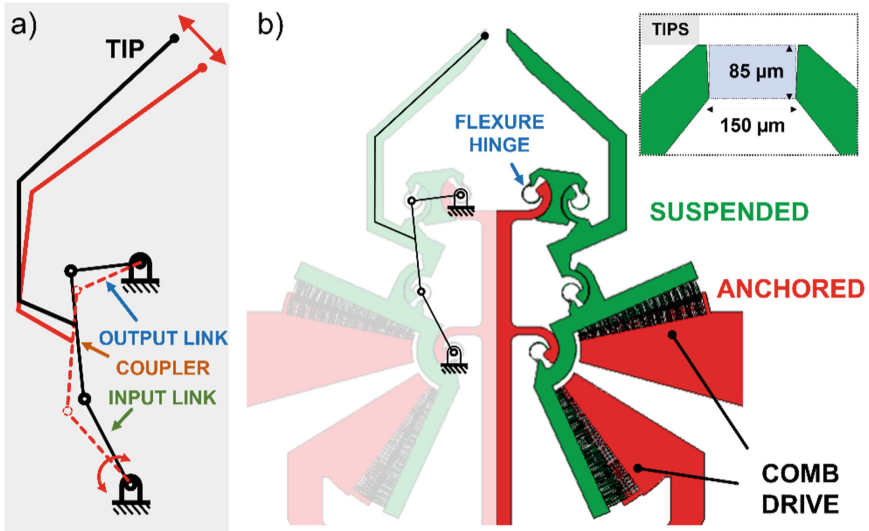


Fig. 1. Device’s design: from pseudo-rigid-body model (a) to its implementation in the final device (b), with a magnified view of the jaw-tips operating area (top right corner).

Subsequently, MEMS-based technologies were employed for the prototyping stage: a silicon-on-insulator (SOI) wafer was chosen as framework, with a 40 μm-thick device layer for the mechanism’s structure, a 2 μm-thick buried oxide acting as sacrificial layer and a 500 μm-thick handle as support-anchor layer. The device fabrication was developed in three main steps: photolithography was performed to define the geometries; deep reactive-ion etching (DRIE) was used to pattern the structure; the sacrificial layer removal was achieved to release the suspended part of the mechanism [11]. Figure 2a shows a

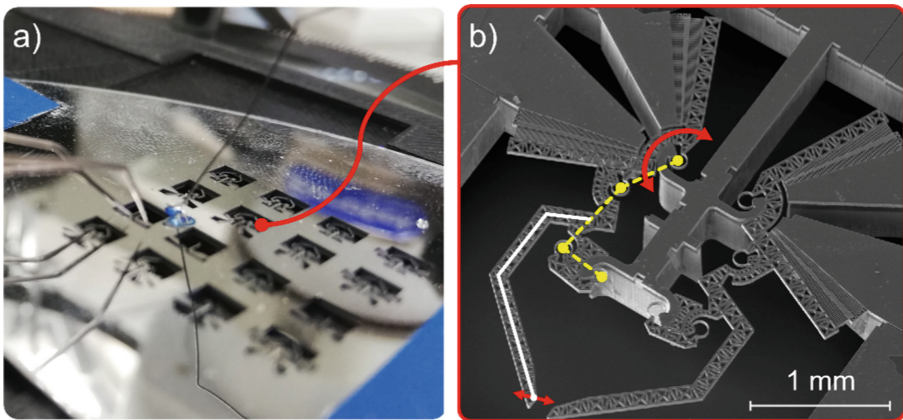


Fig. 2. a) SOI wafer with MEMS-fabricated microgrippers. b) SEM enlargement on the DUT.

6-in. SOI wafer after the fabrication procedures. Figure 2b shows a scanning-electron microscope (SEM) picture of a successfully fabricated device.

3 Microbeads Grasping Feasibility Study

As an important step in the device's overall development before a full implementation in more significant environment applications, we report a study on the gripper's potential capabilities, with the purpose of improving its technology readiness level (TRL). A complex test scenario was arranged, where microparticles were suspended in an aqueous medium with the aim to resemble a biological environment. Direct morphological comparisons of the particles with the device's tips and operating window were carried out via microscope observation. As microparticles, we employed Sepharose® CL-4B agarose-based microbeads. CL-4B present a spheroidal geometry and sponge-like texture, with an average diameter of 20 μm in dry state, and an enlarged wet diameter that span from 45 to 165 μm , at room temperature. These beads were chosen because of their size compatibility with the active area of the device's jaw-tips. Moreover, agarose-based micro-beads have a long history in the biomedical field, as they are composed of inert and biocompatible material, resembling soft tissues in terms of mechanical behavior. Their nanoporous structure has been largely exploited to enhance chemical reactions, such as DNA extraction and purification [22]. For the sample preparation, E-132 blue food coloring was used to color the microbeads for a better visual recognition with respect to the surrounding environment. The blue-dyed beads were then diluted and stirred in saline solution. The experiment was carried out via microscope observation of the device's jaw tips' operational window. The DUT was photographed before (Fig. 3a) and after (Fig. 3b, Fig. 3c, Fig. 3d) its immersion in the microbeads mixture. As a first result, we observed that the mechanical robustness of the fabricated structure is not compromised by its immersion in such a mixture. Most importantly, the technical capability to clamp spheroidal micro-objects of tens of microns in size is here demonstrated, as clearly visible in Fig. 3c–Fig. 3d.

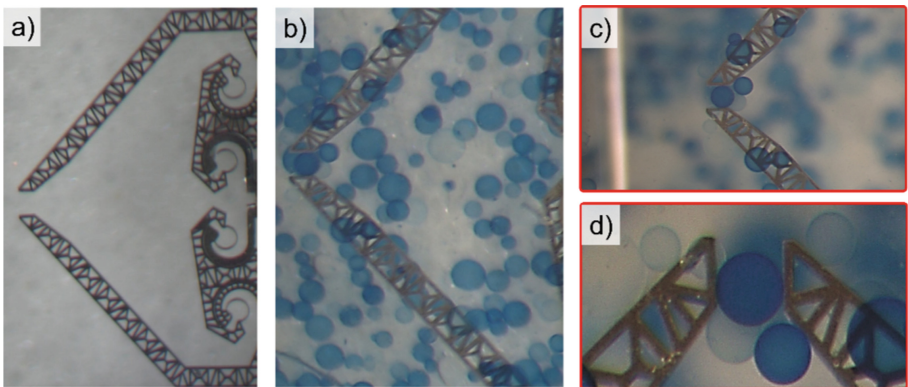


Fig. 3. a) DUT before the immersion. b) DUT after immersion. c) Focused insight on the jaw tips with a 150 μm -sized microbead. d) Rotated enlargement of the DUT's clamping window.

4 Conclusions

This paper reports a feasibility study on the gripping-clamping capabilities of a recently developed microgripper characterized by a complex design, which could be fabricated using MEMS-based technologies on a SOI substrate, thanks to the adoption of selective compliance. Optical microscopy has been applied before and after the device was immersed in a mixture made of microbeads in saline solution. This allowed us to study object-jaws contacts within the device's clamping window. The reported results highlight the function capability of manipulating, grasping and clamping round-shaped objects of around 100 μm in size. This work represents a key step toward a deep and complete validation of our device in actual biomedical-surgical scenarios, as part of a multidisciplinary endeavour. Results point out our device as a promising player in this field, with a reasonable ambition to open new perspectives for compact, effective and dexterous micro-biomanipulation.

References

1. Wang, W., Zhao, Y., Lin, Q.: An integrated MEMS tactile tri-axial micro-force probe sensor for Minimally Invasive Surgery. In: IEEE 3rd International Conference on Nano/Molecular Medicine and Engineering, pp. 71–76. IEEE (2009)
2. Buzzin, A., et al.: Integrated 3D microfluidic device for impedance spectroscopy in lab-on-chip systems. In: 2019 IEEE 8th International Workshop on Advances in Sensors and Interfaces (IWASI), pp. 224–227. IEEE (2019)
3. Buzzin, A., Asquini, R., Caputo, D., de Cesare, G.: On-glass integrated SU-8 waveguide and amorphous silicon photosensor for on-chip detection of biomolecules: feasibility study on hemoglobin sensing. *Sensors* **21**(2), 415 (2021)
4. Bashir, R.: BioMEMS: state-of-the-art in detection, opportunities and prospects. *Adv. Drug Deliv. Rev.* **56**(11), 1565–1586 (2004)
5. Buzzin, A., Veroli, A., de Cesare, G., Belfiore, N.P.: NEMS-technology based nano gripper for mechanic manipulation in space exploration mission. *Adv. Astro. Sci.* **163**, 61–67 (2018)
6. Wiklund, M., et al.: Ultrasound-induced cell–cell interaction studies in a multi-well microplate. *Micromachines* **5**(1), 27–49 (2014)
7. Norregaard, K., Jauffred, L., Berg-Sørensen, K., Oddershede, L.B.: Optical manipulation of single molecules in the living cell. *Phys. Chem. Chem. Phys.* **16**(25), 12614–12624 (2014)
8. Wierzbicki, R., et al.: Design and fabrication of an electrostatically driven microgripper for blood vessel manipulation. *Microelectron. Eng.* **83**(4–9), 1651–1654 (2006)
9. Brouwer, D., de Jong, B., Soemers, H.: Design and modeling of a six DOFs MEMS-based precision manipulator. *Precis. Eng.* **34**(2), 307–319 (2010)
10. Verotti, M., Dochshanov, A., Belfiore, N.P.: Compliance synthesis of CSFH MEMS-based microgrippers. *J. Mech. Des.* **139**(2), 10 (2017)
11. Bagolini, A., Ronchin, S., Bellutti, P., Chistè, M., Verotti, M., Belfiore, N.P.: Fabrication of novel MEMS microgrippers by deep reactive ion etching with metal hard mask. *J. Microelectromech. Syst.* **26**(4), 926–934 (2017)
12. Veroli, A., Buzzin, A., Frezza, F., De Cesare, G., Giovine, E., Belfiore, N.P.: An approach to the extreme miniaturization of rotary comb drives. *Actuators* **7**(4), 70 (2018)
13. Buzzin, A., Cupo, S., Giovine, E., de Cesare, G., Belfiore, N.P.: Compliant nano-pliers as a biomedical tool at the nanoscale: design, simulation and fabrication. *Micromachines* **11**(12), 1087 (2020)

14. Buzzin, A., Veroli, A., de Cesare, G., Giovine, E., Verotti, M., Belfiore, N.P.: A new NEMS based linear-to-rotary displacement-capacity transducer. In: IEEE International Workshop on Advances in Sensors and Interfaces (IWASI), pp. 201–204. IEEE (2019)
15. Velosa-Moncada, L.A., Aguilera-Cortés, L.A., González-Palacios, M.A., Raskin, J.P., Herrera-May, A.L.: Design of a novel MEMS microgripper with rotatory electrostatic comb-drive actuators for biomedical applications. *Sensors* **18**(5), 1664 (2018)
16. Verotti, M., Dochshanov, A., Belfiore, N.P.: A comprehensive survey on microgrippers design: mechanical structure. *J. Mech. Des.* **139**(6), 060801 (2017)
17. Buzzin, A., Rossi, A., Giovine, E., de Cesare, G., Belfiore, N.P.: Downsizing effects on micro and nano comb drives. *Actuators* **11**(3), 71 (2022)
18. Veroli, A., et al.: Development of a NEMS-technology based nano gripper. In: Ferraresi, C., Quaglia, G. (eds.) RAAD 2017. MMS, vol. 49, pp. 601–611. Springer, Cham (2018). https://doi.org/10.1007/978-3-319-61276-8_63
19. Luisetto, I., et al.: An interdisciplinary approach to the nanomanipulation of SiO₂ nanoparticles: design, fabrication and feasibility. *Appl. Sci.* **8**(12), 2645 (2018)
20. Cecchi, R., et al.: Development of micro-grippers for tissue and cell manipulation with direct morphological comparison. *Micromachines* **6**(11), 1710–1728 (2015)
21. Vurchio, F., et al.: Grasping and releasing agarose micro beads in water drops. *Micromachines* **10**(7), 436 (2019)
22. Du, N., Chou, J., Kulla, E., Floriano, P.N., Christodoulides, N., McDevitt, J.T.: A disposable bio-nano-chip using agarose beads for high performance immunoassays. *Biosens. Bioelectron.* **28**(1), 251–256 (2011)



Investigation on the Sensing Properties at Room Temperature of a Graphene/SnO₂ Nanocomposite Towards CO₂

Maria Lucia Miglietta^(✉), Brigida Alfano, Tiziana Polichetti, Ettore Massera, Fausta Loffredo, Fulvia Villani, Anna De Girolamo Del Mauro, and Paola Delli Veneri

ENEA, CR-Portici, P.le E. Fermi 1, 80055 Napoli, Italy
mara.miglietta@enea.it

Abstract. Nanocomposite materials made of graphene and metal oxides are still a hot topic in the scientific research. The huge potential to tune on-demand the physico-chemical properties of these hybrids made them attractive to different research fields as photovoltaics, energy storage and, of course, chemical sensing.

Here, we present the study of a nanocomposite of graphene with SnO₂ prepared through a simple one-step synthesis. A chemiresistor device based on this nanocomposite showed interesting sensing features towards CO₂ with a linear sensitivity curve in the concentration range 1%–10% of CO₂ in dry nitrogen and at room temperature.

Keywords: Graphene · SnO₂ · Metal-oxide composites · Gas sensors · CO₂ · Room-temperature chemical sensing

1 Introduction

Nanocomposite materials made of graphene and metal oxides are still a hot topic in the scientific research. The huge potential to tune on-demand the physico-chemical properties of these hybrids made them attractive to different research fields as photovoltaics, energy storage and, of course, chemical sensing [1–5].

In chemical sensing, the remarkable physico-chemical properties of graphene have soon attracted the interest of researchers that, in the last years, have disclosed its enormous potential in this field [6, 7]. However and despite the noteworthy results achieved, the actual development of a graphene-based gas sensor is still hampered by diverse limitations, such as bad recovery behaviour, lack of selectivity, not to mention that the synthetic processes are not always easily scalable. The hybridization of graphene with metal oxides, which are well-established materials for conductometric gas sensor technology, pursues the goal to complementary enhance the sensing properties, by modulating the chemical sensitivity, tuning the selectivity and generally improving the sensing dynamic [8, 9]. On the other hand, with regard to MOX chemiresistors, one of the most remarkable improvement achieved by this nanocompositing strategy is the reduction of their operating temperature, even gaining room temperature sensitivity depending on the molar ratio MOX:graphene [8].

The present work moves in the wake of these studies and aims to investigate the sensing features of a nanocomposite based on graphene nanoplatelets, prepared through an eco-friendly exfoliation of graphite in hydroalcoholic solution, and SnO₂ nanoparticles, synthesized by a simple sol-gel method [10, 11]. The morphology of the hybrid material (G-SnO₂) was thoroughly characterized by electron microscopy (SEM and TEM), AFM and Raman analysis. Electrical characterizations of the G-SnO₂ nanocomposite in controlled environment disclosed an interesting sensitivity towards CO₂, which was undetectable in the bare components under the same measuring conditions. Responses to increasing CO₂ concentrations were weak but linear in the range 1%–8% of CO₂ in dry nitrogen.

2 Experimental

2.1 Synthesis of the Materials

Graphene nanoplatelets (G) were synthesized according to Fedi et al. [10]. The hydroalcoholic suspension was then freeze-dried to obtain graphene powder. The tin oxide precursor (SnCl₄•5H₂O, AC223691000, 98+%, extra pure) was mixed to graphene powder in a molar ratio 3:1 (C:Sn) and dispersed in ethanol by bath-sonication. This dispersion was casted onto silicon and oxidized silicon substrates, dried for 1 h at 100 °C and then annealed at 180 °C for 2 h in oven in vacuum. Chemiresistor devices were fabricated by drop-casting the SnCl₄/graphene dispersion onto alumina transducers with gold interdigitated electrodes and annealing the films as described above.

2.2 Material Characterization Techniques

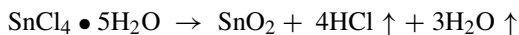
The Raman measurements were collected through a Renishaw inVia Reflex apparatus, using a magnification 100x and the 514.5 nm line of Ar laser as excitation source with an incident power of ~10 mW. Spectra were captured in back-scattering configuration on films casted and annealed onto SiO₂ (250 nm)/Si wafers.

The morphological characterizations of metal-decorated graphenes were performed by Field-Emission Scanning Electron Microscopy (FESEM LEO 1530-2 microscope, acceleration voltage 5 kV) and Atomic Force Microscopy (AFM-Nanoscope IV Veeco, n-doped Si RTESP Veeco tip in tapping mode, scanning rate 1 Hz, 512 scanning lines) on nanocomposite films casted onto Si substrates. TEM images were taken with a FEI TECNAI G12 Spirit-Twin operating at 120 kV. TEM samples were prepared by dipping standard holey carbon grids (400 mesh) into the colloidal suspensions and annealing the films as described in the previous section.

Electrical characterizations in controlled environment were performed on chemiresistor devices placed in an air-tight chamber (40 cl) with electrical feed-through. A fixed bias voltage (1 V) was applied to the electrodes by means of a TTI QL355T Precision Power Supply and the conductance values were recorded by a high resolution Keithley 6485 picoammeter. Relative Humidity value was adjusted humidifying the dry air carrier gas through a water bubbler placed in a thermostatic bath. The measurements were performed setting the total flow at 500 sccm, the temperature at 22 ± 2 °C and at atmospheric pressure.

3 Results and Discussion

The SnO₂ nanoparticles were formed during the annealing process according to the reaction:



The resulting nanocomposite material, G-SnO₂, is shown in Fig. 1a. It shows the characteristic nanoplatelets morphology of graphene (see Fig. 1b) but there is no clear evidence of additional nanostructures; sparse cracks can be observed in the casted film. By comparison with the SEM image of the as-synthesized SnO₂ (Fig. 1c), it stands out that the SnO₂ nanoparticles have an average diameter below 10 nm, with the presence of few small aggregates, and that the resulting layer is a rather thick film. The nanocomposite material seems then composed by graphene nanoplatelets homogeneously covered with nanograins of SnO₂. This morphology seems confirmed by the AFM topography reported in Fig. 1d. The TEM images of the bare components and of the G-SnO₂ nanocomposite further confirm the morphology (Fig. 2). SnO₂ nanoparticles seem partially aggregated, as already observed in wet chemically synthesized nanoparticles, where the presence of OH ions left in samples and/or of the low annealing temperature can cause the aggregation phenomenon [12].

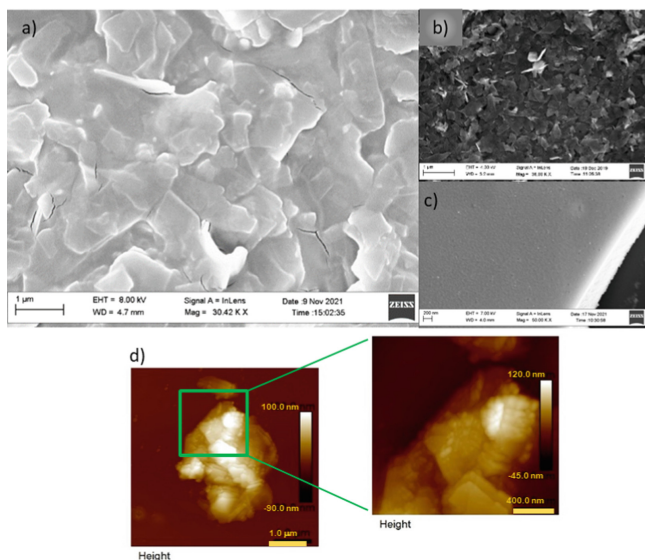


Fig. 1. Morphological and structural characterization of the G-SnO₂ nanocomposite (a) in comparison with those of the bare components: pristine graphene (b), SnO₂ (c). d) AFM image of a graphene nanoplatelet covered with SnO₂ nanograins.

The Raman spectrum of G-SnO₂ is showed in Fig. 3. Besides the three characteristic Raman peaks of pristine graphene - the so-called D, G and 2D bands, at 1350 cm⁻¹,

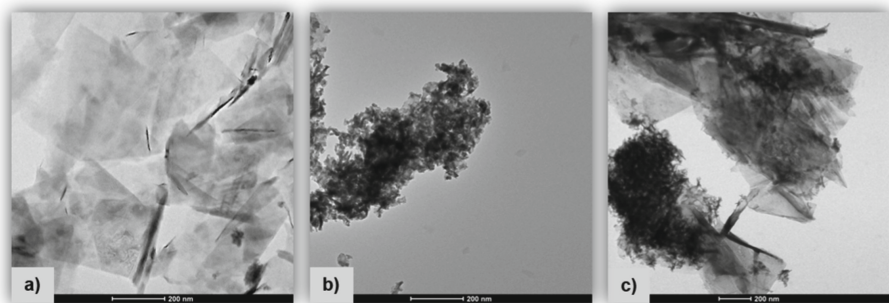


Fig. 2. TEM images of pristine graphene (a), SnO₂ (b) and of the G-SnO₂ nanocomposite (c).

1582 cm⁻¹ and 2700 cm⁻¹ respectively - the spectrum of the composite material displays peaks located at 618 cm⁻¹ and 665 cm⁻¹. These last peaks can be matched with the A_{1g} and S₃ vibration modes of rutile SnO₂.

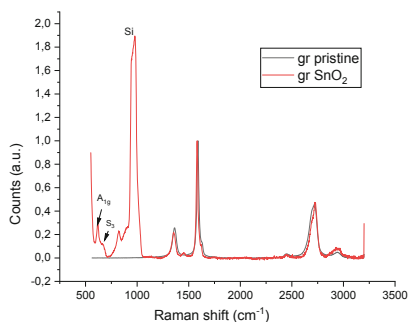


Fig. 3. Raman spectrum of G-SnO₂ (red line) compared to that of pristine graphene (black line). Both spectra were averaged over an area of 10 mm × 10 mm.

The chemoresistive response of the nanocomposite to environmental gases was investigated. An interesting response to CO₂ at room temperature was recorded. While the bare graphene is insensitive to CO₂ and the bare SnO₂ can change its conductance only at high temperatures upon CO₂ exposure [6], the hybrid material prepared herein is able to detect the presence of a 1.5% CO₂ atmosphere in dry environment (Fig. 4) and to follow linearly the CO₂ concentration (Fig. 4b).

This sensitivity towards CO₂ is doubtlessly referable to the interaction of the gas with the SnO₂ nanograins. It has already been reported indeed that CO₂ can effectively release electrons to the SnO₂ when its surface is pre-adsorbed with hydroxyl OH groups, which is consistent with our TEM observation of the SnO₂ film [12, 13]. The electrons gained by SnO₂ from CO₂ afterwards migrate to the depletion layer in the p-n junction between graphene and SnO₂ (Fig. 5). By virtue of the electric field present at the junction, the electrons are transferred to graphene, where according to its p-type nature they determine the decrease of conductivity of the film experimentally observed (Fig. 4a).

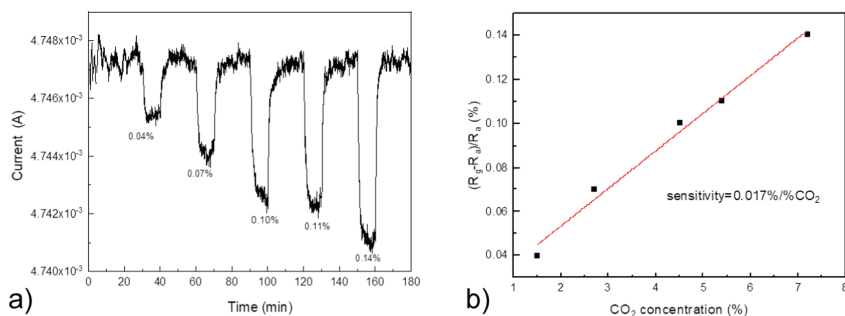


Fig. 4. Electrical response of G-SnO₂ to increasing steps of CO₂ (1.5%, 2.7%, 4.5%, 5.4% and 7.2%): a) dynamic behavior, b) sensitivity curve.

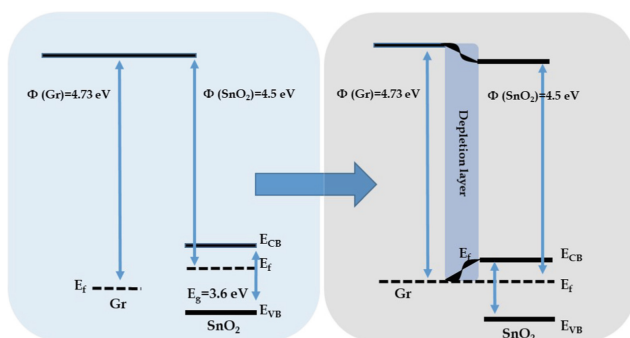


Fig. 5. Band structure of graphene and SnO₂ before (left image) and after (right) the formation of the junction.

The present work shows a new nanocomposite material based on graphene and SnO₂, prepared according to simple solution-based processes, with interesting sensing properties towards an environmentally relevant gas.

Acknowledgments. Research reported in this publication was supported by S.A.L.V.O. project. Funding from the National Programs (PON) of the Italian Ministry of Economic Development (MISE): code B48I20000050005 (Prog n. F/190012/01/X44).

References

1. Li, T., et al.: *Nanomaterials* **12**(6), 982 (2022)
2. Yaqoob, A.A., Ahmad, A., Ibrahim, M.N.M., Karri, R.R., Rashid, M., Ahamd, Z.: Synthesis of metal oxide-based nanocomposites for energy storage application. *Sustain. Nanotechnol. Environ. Remediat.* 611–635 (2022)
3. Ghosh, R., Aslam, M., Kalita, H.: Graphene derivatives for chemiresistive gas sensors: a review. *Mater. Today Commun.* 103182 (2022)
4. Bellani, S., Bartolotta, A., et al.: *Chem. Soc. Rev.* **50**, 11870 (2021)
5. Tale, B., Nemade, K.R., Tekade, P.V.: *Polym.-Plast. Technol. Mater.* **60**(7), 784–797 (2021)

6. Demon, S.Z.N., et al.: Graphene-based materials in gas sensor applications: a review. *Sens. Mater* **32**(2), 759–777 (2020)
7. Wang, C., Wang, Y., Yang, Z., Hu, N.: Review of recent progress on graphene-based composite gas sensors. *Ceram. Int.* **47**(12), 16367–16384 (2021)
8. Sun, D., Luo, Y., Debliquy, M., Zhang, C.: Graphene-enhanced metal oxide gas sensors at room temperature: a review. *Beilstein J. Nanotechnol.* **9**(1), 2832–2844 (2018)
9. Chen, Z., Wang, J., Wang, Y.: Strategies for the performance enhancement of graphene-based gas sensors: a review. *Talanta* **235**, 122745 (2021)
10. Fedi, F., Miglietta, M.L., et al.: *Mater. Res. Express* **2**(3), 035601 (2015)
11. Ganchev, M., Katerski, A., et al.: *J. Phys.: Conf. Ser.* **1186**, 012027 (2019)
12. Das, S., Kar, S., Choudhary, S.: *J. Appl. Phys.* **99**, 114303 (2006)
13. Wang, D., Chen, Y., et al.: *Sens. Actuators B* **227**, 73–84 (2016)



3D-Printed Face Mask with Integrated Sensors as Protective and Monitoring Tool

Silvia Casalinuovo¹(✉), Alessio Buzzin¹, Antonio Mastrandrea¹, Ivan Mazzetta¹, Marcello Barbirotta¹, Lorenzo Iannascoli², Augusto Nascetti², Giampiero de Cesare¹, Donatella Puglisi³, and Domenico Caputo¹

¹ Department of Information Engineering, Electronics and Telecommunications, Sapienza University of Rome, via Eudossiana 18, 00184 Rome, Italy

silvia.casalinuovo@uniroma1.it

² School of Aerospace Engineering, Sapienza University, via Salaria 851, 00138 Rome, Italy

³ Department of Physics, Chemistry and Biology, Sensor and Actuator Systems Division, Linköping University, Campus Valla, 581 83 Linköping, Sweden

Abstract. The outbreak of the recent Covid-19 pandemic changed many aspects of our daily life, such as the constant wearing of face masks as protection from virus transmission risks. Furthermore, it exposed the healthcare system's fragilities, showing the urgent need to design a more inclusive model that takes into account possible future emergencies, together with population's aging and new severe pathologies. In this framework, face masks can be both a physical barrier against viruses and, at the same time, a telemedical diagnostic tool. In this paper, we propose a low-cost, 3D-printed face mask able to protect the wearer from virus transmission, thanks to internal FFP2 filters, and to monitor the air quality (temperature, humidity, CO₂) inside the mask. Acquired data are automatically transmitted to a web terminal, thanks to sensors and electronics embedded in the mask. Our preliminary results encourage more efforts in these regards, towards rapid, inexpensive and smart ways to integrate more sensors into the mask's breathing zone in order to use the patient's breath as a fingerprint for various diseases.

Keywords: Breathing zone · Face mask · 3D-printing · Wearable sensors · CO₂ · Humidity · Temperature · Telemedicine

1 Introduction

In March 2020, the World Health Organization declared the pandemic state due to the SARS-COV-2 rapid spreading [1]. This event forced the general population worldwide to change many aspects of their daily life, such as the constant wearing of face masks as protection from virus transmission risks [2]. At the same time, these events underlined the need for healthcare structures to improve and increase remote-base diagnosis and patients monitoring with the help of modern technology [3]. Growing efforts are being made in this path, especially when dealing with chronic diseases, immunocompromised or handicapped people, who require continuous health-checks, and for communities

living in rural areas [4]. In this framework, face masks can be both a physical barrier against viruses and, at the same time, a telemedicine diagnostic tool. Recently, Xue et al. developed an intelligent face mask for screening breathed coronaviruses aerosol as a diagnostic platform for Covid-19 detection [5].

In this work, we propose a low-cost, custom-made face mask able to protect the wearer from virus transmission, thanks to its FFP2 filters, and to monitor the air quality inside the mask and to automatically transmit the measured data to a web terminal, thanks to integrated sensors and electronics.

2 System Structure

The system structure includes electronic hardware and software components and a 3D-printed face mask.

2.1 Hardware Structure

The hardware structure (Fig. 1) can be divided in two blocks: the “sensing block” that measures temperature/humidity/CO₂ levels inside the breathing zone, and the “processing block” that acts as a computer.

The “sensing block” includes the physical sensor (SDC30 from Sensirion AG), a microcontroller/Wi-Fi module (ESP32 Cam from AI-Thinker), which acquires the data from the sensor and send them wirelessly, a LiPo Battery for power supply and a voltage regulator (MIKROE-2894 from MikroElektronika) that adapts the voltage supplied by the battery to the required voltage of the microcontroller. The “processing block” includes a Raspberry Pi 4, which processes the data received from the microcontroller.

2.2 Software Structure

Arduino was used to program the microcontroller to transfer sensor data every 2 s to the Raspberry. For data availability, a database was created on it by installing a LAMP Server (Linux Apache, MySQL and PHP) and phpMyAdmin to manage the database through a web interface. In this way, it is possible to visualize data in real-time on graphs and use the database for post processing, such as sending an email if a measured value exceeds a threshold. The Arduino code also includes the possibility to send an alert email if the battery level is too low to avoid an immediate shutdown of the system. In addition, a Python code saves-and-sends the database containing the last 24 h by email. The entire software structure, coupled with devices that automatically transmit information to the medical team, has been designed with a focus on telematic monitoring, enabling access to frequent and closer checks of the patients at home.

2.3 3D-Printed Mask

The custom-made face mask (Fig. 2) was designed to have the double purpose of filtering air and hosting the sensing block. The mask geometry was developed with Autodesk Fusion 360® starting from front and lateral generic pictures of the head. Subsequently,

the mask design was refined by aligning it with a volunteer head, which was generated and meshed by means of photogrammetry and with the help of Autodesk Recap Photo®. The final Fusion 360® project includes a larger cap (white component in the foreground of Fig. 2), located in correspondence of the breathing zone, which captures breath and hosts the sensing device; component touching the wearer's face (black element in Fig. 2) and two symmetrical lateral caps that secure air circulation. The three caps have honeycomb-patterned openings and integrate FFP2 filters, as this mask must also be considered as a protective device.

The manufacturing phase was accomplished by 3D-printing. Polylactic acid (PLA) was used as main 3D-printing material for the three caps, mainly for robustness purposes, while a more elastic material, thermoplastic polyurethane (TPU), was used to print the rest of the mask, for comfort purposes.

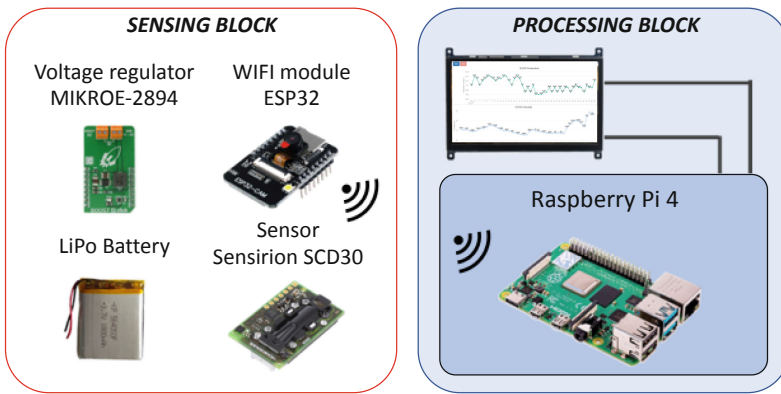


Fig. 1. Schematic overview of the hardware structure.

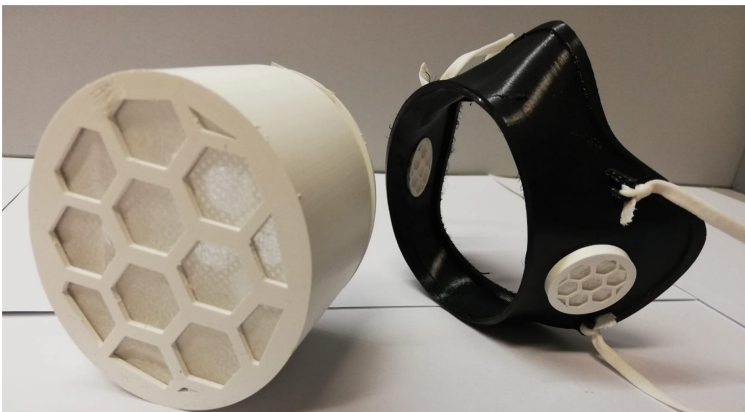


Fig. 2. Picture of the fabricated mask.

3 Measurements

The resulting device was used to analyze exhaled breath over 150 s intervals, starting under the same environmental conditions (temperature of 31 °C, humidity of 56% and CO₂ level of 1600 ppm) to avoid any unwanted fluctuations that were not directly linked to breath. In this setting, we considered the 0-sample coincident with the instant of positioning the mask in correspondence to the breathing zone, while the last sample corresponds to the end of the measurement interval. During the entire breath measurement interval, the mask always keeps the same position with respect to the wearer's face. Measured data show that:

- real-time temperature monitoring displays a constant increase in the observed time range (Fig. 3a)
- humidity reaches values around 90% in about 25 s (Fig. 3b)
- CO₂ sharply increases in the first 25 s (Fig. 3c), then starts to oscillate following the wearer's breathing frequency (see the zoom in Fig. 3d) at around 37500 ppm.

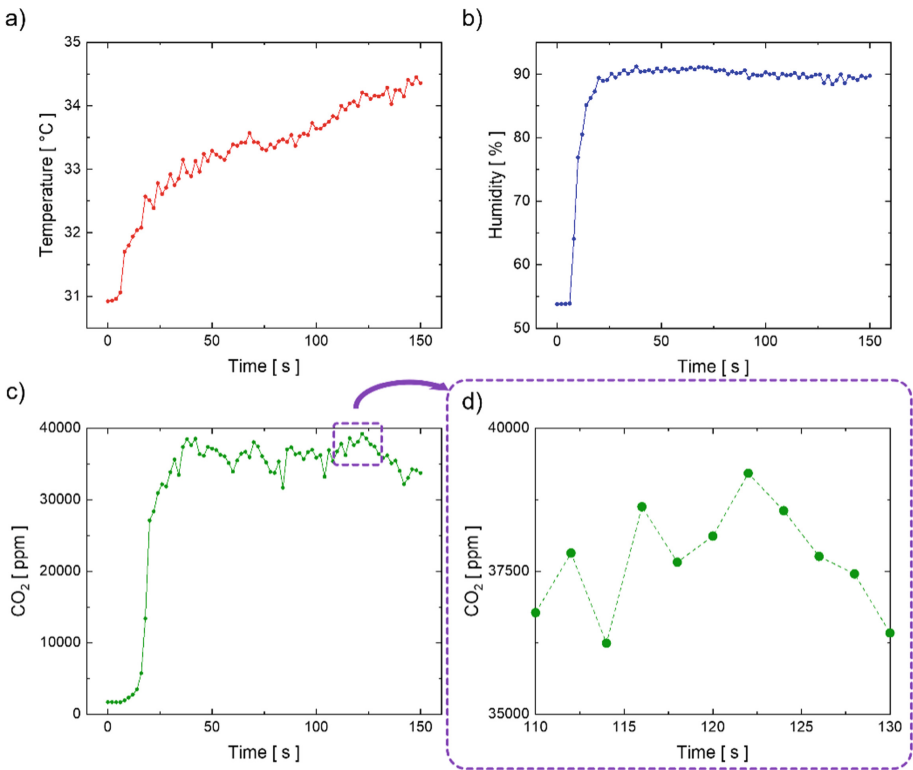


Fig. 3. Simultaneous monitoring of humidity (a), temperature (b) and CO₂ concentration (c) inside the face mask breathing zone over 130 s of wearing, with an insight of the sensed CO₂ concentration inside the 110–130 s range (d).

The reported values are relatively higher with respect to normal breathing values (i.e., without wearing a mask), confirming other literature findings: it has been previously reported that wearing a mask leads to an increase of the dead space volume and consequently to a higher rebreathing of CO₂ [6]. This, also with the higher breathing resistance due to the moist mask, can cause patient's discomfort when using the mask over extended periods of time, together with an increase of respiratory activity and heart rate [7] and effects like headache, asthma or fatigue. In addition, the rise in temperature and humidity in the breathing zone creates a microclimate perfect for pathogens' growth, discomfort sensations and skin-related problems [8].

4 Conclusions

In this work, we developed a custom-made face mask as both a physical barrier against viruses and, at the same time, a telemedicine diagnostic tool. The 3D-printed mask integrates a stand-alone sensing system for breath's CO₂, temperature and humidity monitoring with electronics for wireless data transmission. Preliminary experimental measurements, carried out over a 150 s time range, show a rapid increase of all these three parameters, confirming other literature reports on this topic.

The presented development encourages more efforts in this path, towards rapid, inexpensive and smart ways to integrate more sensors in the mask breathing zone in order to use patient breath as a fingerprint for various diseases. In fact, recent studies highlight the presence (qualitative or quantitative) of volatile organic compounds in the breath profile as biomarkers of a human's health status [9]. In parallel to these promising results, other research projects show the need of alternative technology to the gold standard techniques for breath analysis, and nanomaterial-based sensors seem to be a good choice in terms of sensitivity, specificity, cost and portability [10]. These outcomes reveal a promising frontier in the diagnostic field, allowing an early diagnosis that will be useful especially during emergency management like pandemics or wars.

As the potential behind this diagnostic-telemedicine technology can unlock many challenges, further studies are needed to boost the presented mask as an enabling element for healthcare delivery, allowing for a patient digital experience through a more inclusive health model.

Acknowledgements. Authors thank the financial support of the MUR through the Sapienza University Major Project 2021: "Smart Face-mask For Monitoring Health-related Parameters in The Breathing Zone" - Grant n. RG12117A84C979D3.

References

1. Ghebreyesus, T.A.: World Health Organization. WHO Director-General's opening remarks at the media briefing on COVID-19, 25 May 2020 (2020)
2. Tso, R.V., Cowling, B.J.: Importance of face masks for COVID-19: a call for effective public education. *Clin. Infect. Dis.* **71**(16), 2095–2198 (2020)
3. Smith, A.C., et al.: Telehealth for global emergencies: implications for coronavirus disease 2019 (COVID-19). *J. Telemed. Telecare* **26**(5), 309–313 (2020)

4. Surtel, W., Wójcik, W., Masiak, J., Dzida, G., Horoch, A.: Telemedical systems for home monitoring of patients with chronic conditions in rural environment. *Ann. Agric. Environ. Med.* **21**(1) (2014)
5. Xue, Q., et al.: An intelligent face mask integrated with high density conductive nanowire array for directly exhaled coronavirus aerosols screening. *Biosens. Bioelectron.* **186**, 113286 (2021)
6. Kisielinski, K., et al.: Is a mask that covers the mouth and nose free from undesirable side effects in everyday use and free of potential hazards? *Int. J. Environ. Res. Public Health* **18**(8), 4344 (2021)
7. Geiss, O.: Effect of wearing face masks on the carbon dioxide concentration in the breathing zone. *Aerosol Air Qual. Res.* **21**(2), 200403 (2021)
8. Szepietowski, J.C., Matusiak, Ł., Szepietowska, M., Krajewski, P.K., Białynicki-Birula, R.: Face mask-induced itch: a self-questionnaire study of 2,315 responders during the COVID-19 pandemic. *Acta dermato-venereologica* **100**(5) (2020)
9. Buszewski, B., Kęsy, M., Ligor, T., Amann, A.: Human exhaled air analytics: biomarkers of diseases. *Biomed. Chromatogr.* **21**(6), 553–566 (2007)
10. Broza, Y.Y., Haick, H.: Nanomaterial-based sensors for detection of disease by volatile organic compounds. *Nanomedicine* **8**(5), 785–806 (2013)



Capacitive Gas Sensors with Porphyrinoids Coated SiO₂ Hybrid Nanoparticles

Mounika Mudiganti¹, Gabriele Magna², Lorena Di Zazzo², Roberto Paolesse²,
and Corrado Di Natale¹✉

¹ Dipartimento di Ingegneria Elettronica, Università di Roma Tor Vergata,
Via del Politecnico, 1, 00133 Rome, Italy
dinatale@uniroma2.it

² Dipartimento di Scienze e Tecnologie Chimiche, Università di Roma Tor Vergata,
Via della Ricerca Scientifica, 1, 00133 Rome, Italy

Abstract. This work explores innovative hybrid nanostructured silica materials as chemical gas sensors under volatile compounds (VOCs). For this purpose, porphyrinoids-coated silicon dioxide (SiO₂) nanomaterials have been prepared. A chemical gas sensor based on an impedance array was fabricated using such hybrid SiO₂ NPs on interdigitated electrodes. Experimental investigations on the potential sensing performance were carried out with the produced nano-hybrids using the impedance array.

Keywords: Porphyrinoids · Silica nanoparticles · Capacitive gas sensors

1 Introduction

Nanostructured silica nanoparticles are among the major substrates for widespread utilization in biomedical-drug delivery, imaging, and colorimetric sensor applications, owing to their particular physical, chemical, and optical properties [1]. They have drawn significant attention due to their stability, large-scale synthesis, and ability to be surface functionalized with various molecules and polymers. Porphyrinoids are unique, organic carbon material that offers a tremendous potential in chemical gas sensor applications due to their excellent charge transfer coupling, structure-sensitivity, and photo-activation [2]. Among the applications, porphyrinoids were found suitable for the human volatolome detection [3–6].

Nanostructured silica with unique geometric properties can form improved conjugates with various hybrid nanomaterials, including porphyrinoids [7]. The recent applications of hybridized silica nanomaterials in VOC detection are more beneficial than other sensors [8].

Here, porphyrinoids coated silica nanoparticles have been tested as sensing materials for gas sensors based on the measurement of capacitance changes.

2 Materials and Methods

Three hybrid nanomaterials have been prepared by functionalizing the commercially available pristine SiO₂ nanoparticles (NPs) (Sigma Aldrich SiO₂ nano powder, 10–20 nm) with three different organic dyes: one type of corroles (CuTPC) and two types of porphyrins (MnTPP, CuTPP) - see scheme 1. The functionalized nanoparticles were obtained by post growth coating method. Briefly, a 11 mg of commercial SiO₂ nanoparticles were mixed in a 3 ml of toluene with a 2.4 mg of respective organic dyes (as shown in Fig. 1). The suspension of NPs was then homogenized using a bath ultra-sonication (Fisher scientific, FB 15047, 37 kHz, 30–90 W). Afterwards, hybrid nanoparticles were collected upon centrifugation and the subsequent cleaning procedure. Sensor array was prepared by depositing the hybrid NPs on electrodes using the drop casting method.

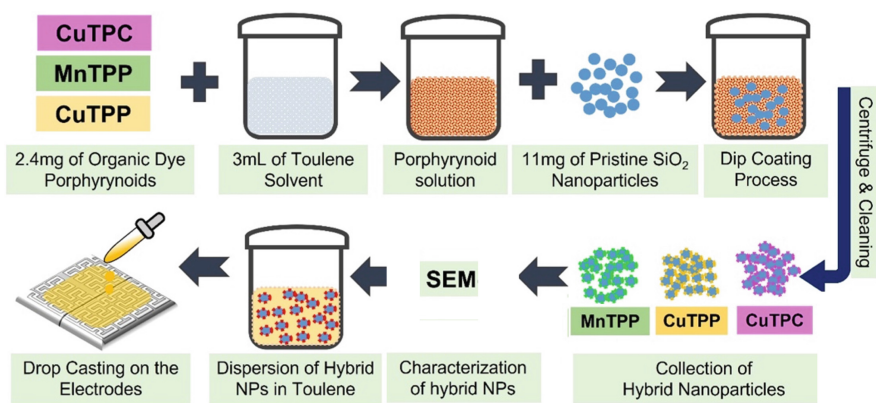


Fig. 1. Schematic illustration of the hybrid NPs preparation process and drop casting on the sensing electrodes.

The colour change of NPs is a preliminary confirmation of the happened functionalization. The morphological characterization was studied using a SEM (SEM, SUPRA 35, Carl Zeiss SMT, Oberkochen, Germany). Samples were directly casted onto the aluminum stubs from the respective toluene stock solutions. Samples were let to dry storing them in an incubator at 25 °C overnight. Bare SiO₂ films have been produced with the same protocol to rule out the presence of residual solvent in the film.

Capacitance Measurements

The three-element sensor array was accommodated in a sealed chamber as shown in Fig. 2. At regular time intervals, the sensors were exposed to vapors from pure compounds, mixtures. Pure compounds were water, acetone, toluene, butanol, and the mixtures were obtained diluting pure compounds with water in the equal ratios. A mass flow controller system (from MKS Instruments, Andover, MA, USA) was used to deliver different concentrations of compounds pressure vapor (30%, 40%, 50%) to the sensor array. References were collected in synthetic air. The total flux was maintained at 200 cm³/min. To measure the capacitance, sensors were connected to a capacitance meter (Siglent SDM3055X-E digital multimeter).

The array was exposed to gases and the relative changes in capacitance were used as a feature/descriptor.

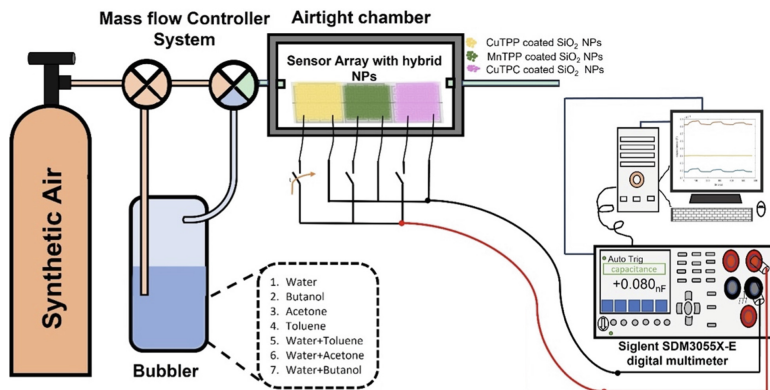


Fig. 2. Schematic illustration of the experimental set-up for the sensing

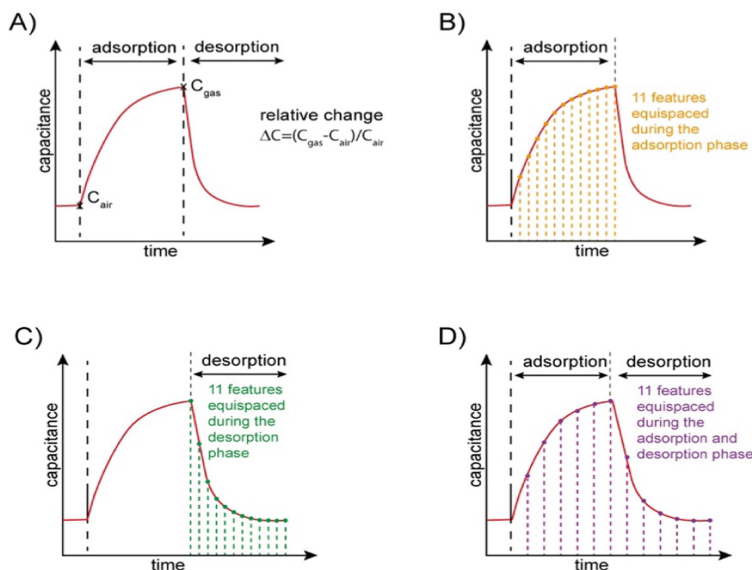


Fig. 3. Pictorial representation of features extracted from sensor responses over time. A) Relative change of capacitance; B) Adsorption phase features; C) Desorption phase features; and D) adsorption and desorption phase features.

Features Selection

Data were collected by a dedicated software developed in Matlab® and features were extracted from time-curves. In order to calculate sensitivity, the relative changes of

capacitance have been considering according to the equation:

$$\Delta C = \frac{C_{gas} - C_{air}}{C_{air}}$$

where C_{gas} is the capacitance at the end of adsorption and C_{air} is the capacitance at the begin as shown in Fig. 3(A).

In the past, evidences have been gained about the importance of the dynamic behavior of sensor responses [9]. In this work we investigated three approaches to compress into a limited number of descriptors the sensors dynamics. The adsorption features are extracted by partitioning the exposure phase into 11 evenly spaced intervals (Fig. 3B); the desorption descriptors are also extracted by partitioning the recovery phase into 11 intervals (Fig. 3C); finally, the adsorption and desorption features are extracted by subdividing the whole experiment into 11 evenly spaced intervals (Fig. 3D).

3 Results and Discussion

The prepared hybrid nanoparticles produced were assessed. Micrographic images obtained by electronic microscope evidence that the functionalization produces a thin external coating without significantly altering neither the shape nor the dimension of the nanoparticles (see Fig. 4).

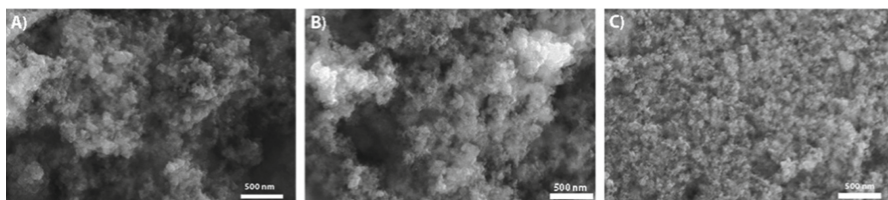


Fig. 4. SEM images of hybrid nanoparticles, A) MnTPP, B) CuTPC and C) CuTPP

The relative change in capacitance ($\Delta C/C$) are calculated for all responses at each different saturated vapor pressures. Figure 5 shows the response curves of sensors with respect to the concentration of pure compounds tested. In case of mixtures, concentrations were estimated considering the diluted vapor pressure.

CuTPP is responding more towards to the mixture of butanol with water. Also, all hybrid nanoparticles show more response in the vapors of acetone and its mixture with water. Especially, corroles coated particles show high response in the acetone than the other vapors.

Response curve are fitted by a linear curve (see Fig. 5). The slope of each curve under all VOCs is considered as the sensitivity of the sensor.

For study the properties of the array to identify the various samples, Principal Component Analysis (PCA) has been calculated on the relative change of capacitance. Data have been autoscaled to zero mean and unitary variance before PCA was calculated. The bi-plot in Fig. 6(A) displays the plot of PC1 vs. PC2 (95% of total variance explained).

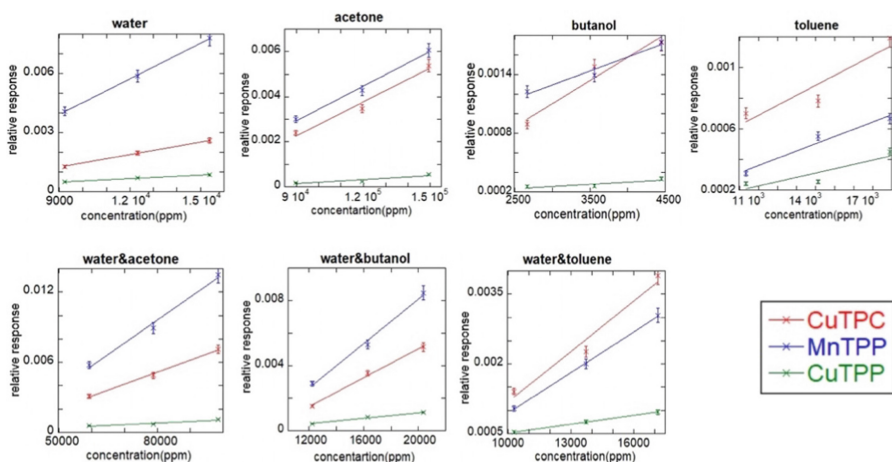


Fig. 5. Response curves of sensors fitted with a linear function.

The plot shows a moderate clustering of classes. The imperfect separation of classes can be ascribed mainly to the confounding effect of concentration that increasing the correlation, tends to distribute all data along PC1. The correlation due to concentration trends and the little number of features (one per sensor) causes that PC1 to explain a high percentage of the total variance. Sometimes, in this situation, the clustering of data can be improved removing the contribution of the first Principal Component, which is associated with quantitative information (concentration) rather than qualitative (e.g. chemical identities).

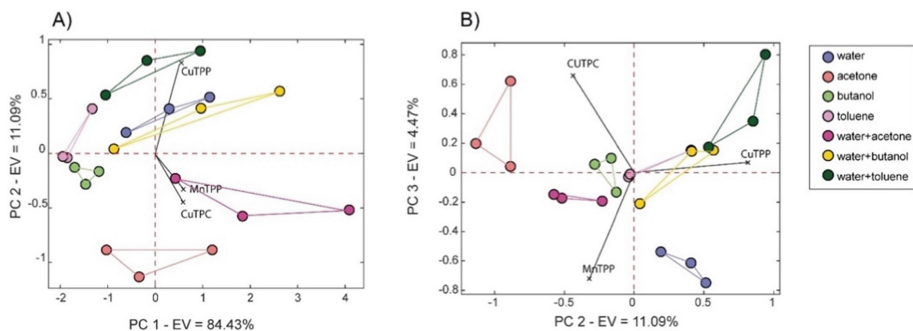


Fig. 6. PCA analysis for relative change in response of all pure compounds

Figure 6(B) shows the projection for the PC2–PC3. This plot carries about 16% of total variance of the data, while the third principal component (PC3) carries 4.47% of the total variance. Since the relation between concentration and scores has been removed, the loadings are less correlated one each other. CuTPP is mostly aligned towards mixtures of butanol and toluene more sensitive to water. MnTPP is aligned towards the mixture of acetone and butanol. CuTPC is aligned towards the acetone. Where toluene is located at

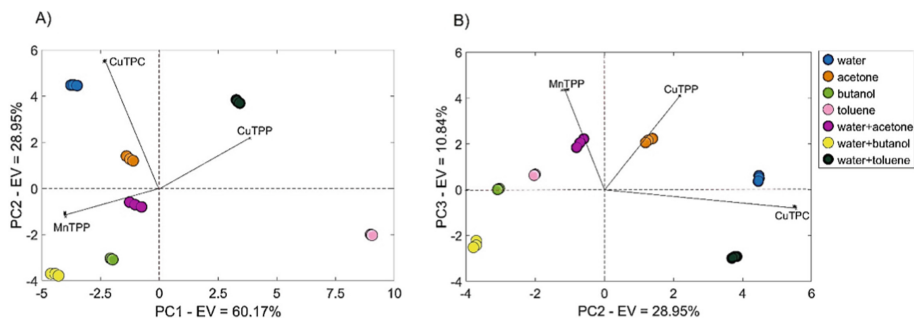


Fig. 7. PCA analysis for all features under VOCs for 11 evenly spaced samples.

the center shows equal contribution for the three sensors. The distinct behavior of water and acetone has observed.

A better classification of sample can be achieved increasing the number of featured per single sensor. For instance, Fig. 7 shows the PCA calculated with the features evaluated during absorption dividing the response curve into 11 spaced samples as mentioned in methods paragraph (see Fig. 3B). Figure 7A shows the biplot projections of along PC1–PC2. Even if this plane still explains about 90% of total variance, this is more evenly distributed into the principal components (60.18% in PC1 and 29.04% in PC2). Remarkably, the data belonging to the same class are plotted in distinct clusters. PC1 discriminates toluene and its mixture from the other compounds. PC2 mainly separates the mixtures from the respective pure compounds (except for the butanol). Different sensors loadings point to different directions, showing the low-correlation occurring. CuTPP aligned towards toluene and its mixture, where MnTPP is aligned towards the acetone, butanol and its mixture. CuTPC aligned towards the water and acetone.

Figure 7B) shows the projection of PC2–PC3. PC3 is discriminating the mixture of butanol from its pure compounds. CuTPC aligned towards the water and mixture of toluene, and CuTPP aligned towards the acetone and water. MnTPP points towards to the mixture of acetone and toluene.

4 Conclusions

In conclusion, hybrid porphyrinoids-coated SiO₂ nanoparticles were successfully produced through a viable solution method and utilized to prepare capacitive array of gas sensors. The normalized impedance measurements indicate the sensitivity towards several species and the lack of selectivity if individual sensors are compensated by the array selectivity shown by the ensemble of sensors. Dynamic features, here simply calculated as the signals at fixed times, shown to be effective to improve the sensor array properties.

References

1. Walcarius, A.: Silica-based electrochemical sensors and biosensors: recent trends. *Curr. Opin. Electrochem.* **10**, 88–97 (2018)
2. Paolesse, R., Nardis, S., Monti, D., Stefanelli, M., Di Natale, C.: Porphyrinoids for chemical sensor applications. *Chem. Rev.* **117**, 2517–2583 (2017)
3. Mougang, Y.K., et al.: Sensor array and gas chromatographic detection of the blood serum volatolomic signature of COVID-19. *IScience* **24**, 102851 (2021)
4. Gasparri, R., et al.: Volatolomic urinary profile analysis for diagnosis of the early stage of lung cancer. *J. Breath Res.* **16** (2022)
5. Murdocca, M., et al.: Targeting LOX-1 inhibits colorectal cancer metastasis in an animal model. *Front. Oncol.* **9** (2019)
6. Zetola, N.M., et al.: Diagnosis of pulmonary tuberculosis and assessment of treatment response through analyses of volatile compound patterns in exhaled breath samples. *J. Infect.* **74**, 367–376 (2017)
7. Montaseri, H., Kruger, C.A., Abrahamse, H.: Recent advances in porphyrin-based inorganic nanoparticles for cancer treatment. *Int. J. Mol. Sci.* **21** (2020)
8. Boudaden, J., Klumpp, A., Endres, H.E., Eisele, I.: Towards low cost and low temperature capacitive CO₂ sensors based on amine functionalized silica nanoparticles. *Nanomaterials* **9** (2019)
9. Yan, J., et al.: Electronic nose feature extraction methods: a review. *Sensors (Switzerland)* **15**, 27804–27831 (2015)



Detection of Volatile Organic Compounds by Using a Nanoporous Zeolite Layer

G. Oliva, A. S. Fiorillo^(✉), and S. A. Pullano

Department of Health Sciences, Magna Græcia University of Catanzaro, Catanzaro, Italy
{giuseppe.oliva,nino,pullano}@unicz.it

Abstract. The selective detection of volatile organic compounds (VOCs) represents a recently investigated approach that could provide information about the alteration of biological processes. As reported in literature, human biological samples (e.g., saliva, urine, breath, etc.) express different VOCs that could provide information on human health status (e.g., drugs therapies, metabolic/biochemical processes, lung cancer, oral squamous cell carcinoma, hepatocarcinoma etc.). In this work we focused on the detection of butanoic, propanoic, and butanedioic acids since they are contained in different biochemical processes. The aim of this work is the fabrication of thin nanoporous films of synthetic zeolite for the selective adsorption/desorption of butyric, propionic, and succinic acids. The detection is performed by the assessment of emission profiles through a photoionization technique. Results evidenced that zeolite layer is highly selective to propionic acid, allowing a higher adsorption. Conversely, butyric acid emissive profile evidenced adsorption levels 5 times less respect to the propionic acid.

Keywords: Nanopores · Synthetic zeolite · Emission profiles · Photoionization system · VOC sensor

1 Introduction

Volatile organic compounds (VOCs) referred to a wide range of compounds, carbon-based chemicals, which can be found both in environmental and biological samples. The latter were recently investigated as biomarkers. An important challenge, in the medical field, concerns with the non-invasive detections of VOCs for the diagnosis and monitoring of health status [1]. Different studies have evidenced that concentrations of specific VOCs in the saliva result over or under-expressed during pathological conditions [2]. Detection of VOCs in biological samples results tricky not only for the wide range of molecules but also for their wide range of concentration [3].

Metabolic processes have been correlated to changes in VOCs concentration, caused by exogen or endogen processes [4]. More specifically, butanoic, propanoic, and butanedioic acids are associated with the alteration of homeostasis correlated to the onset of specific diseases (e.g., colorectal, lung, stomach, and breast cancer). Synthetic zeolites are promising nanoporous materials for the adsorption of specific molecules. Zeolites are aluminosilicate materials, characterized by a porous framework, a high surface/area

ratio, ionic exchange and high adsorption capacity. In addition, thanks to its properties, such as the biocompatibility, the development of a sensor based on thin zeolite layer results a topic of interest in the biomedical field [5]. In this work, zeolite 4A, characterized by a pore size of about 4 Å, was investigated as an adsorptive/desorptive layer [6–9]. The layer, composed of a mixture of zeolite 4A and soybean oil, was spun coated onto a silicon wafer. VOCs emission profiles were performed by using a photoionizer detection (PID) technique [10, 11]. Results were focused on butyric and propionic acids which are involved in anti-inflammatory processes, energy supply, immune regulation, homeostasis [12–14].

2 Materials and Methods

A composite of zeolite 4A powder and soybean oil has been firstly prepared. Zeolite 4A possesses a tetrahedral structure ($[\text{SiO}_4]^{4-}$ and $[\text{AlO}_4]^{5-}$) in which oxygen atoms are shared from adjacent tetrahedral units. It is characterized by sodium mobile cations which can move inside the framework. Pore opening size is about 4 Å with a central cavity of 11.4 Å (α -cage). Vegetable oil, specifically soybean oil, was chosen based on its smoke point, iodine value and viscosity. Firstly, zeolite powder was heated at 250 °C for 2.5 h to remove adsorbed molecules. The composite was made of 65% w/w of zeolite powder 4A and 35% w/w of soybean oil, vigorously stirred by means of a homogenizer at 6400 rpm for 15 min. Subsequently, the mixture was deposited onto a silicon layer at 4000 rpm for 60 s. The layer was then placed on a hot plate at 150 °C for 3 h. The annealing process decomposes the vegetable oil, creating a supporting carbonic matrix. The zeolite layers have an average thickness of 20 μm , and an average roughness of about 1.2 μm . The analysis has been performed in a glass desiccator at 25 °C and 60 °C prior and after acid adsorption. The layers have been placed in contact with 3 ml of butanoic and propanoic acids for 1 h and successively rinsed in water and dried with N_2 . A commercial photoionizer (MiniRae 3000) was used. The photoionizer includes an ultraviolet (UV) source at 10.6 eV capable of ionizing VOC molecules, thus generating a current related to the VOC molecules per unit volume. The UV lamp energy is compatible with the ionization energy of butanoic and propanoic acids [15, 16]. PID is calibrated against isobutylene. Emissive profiles were carried out at two different temperatures (25 °C and 60 °C), using a glass chamber of 7 × 8 × 2 cm for 300 s. Tests were performed using butanoic acid and on propanoic acid using 99% solutions, respectively.

3 Results and Discussion

Figure 1A reports the background emission profile before acid adsorptions, which does not evidence significant emission of molecules.

Subsequently, in Fig. 1b and 1c are indicated the emissive profiles of both acids at temperatures of 25 °C and 60 °C, respectively. At 25 °C, butanoic acid, evidenced a maximum emission of 190 mg/m^3 after approximately 10 s. At 60 °C a maximum emission of 310 mg/m^3 after 15 s was evidenced (Fig. 1b). The increase in temperature leads to an increase of about 40% of the emission profiles, detecting a higher concentration of VOC. The sample with adsorbed propanoic acid evidenced a maximum emission of

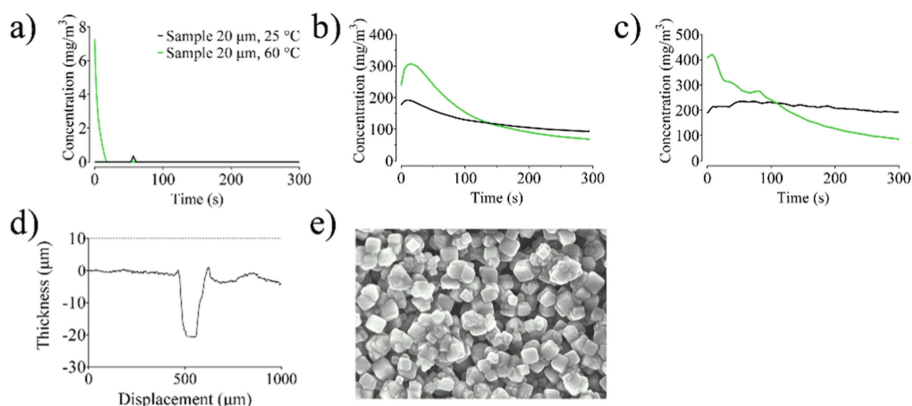


Fig. 1. Desorption profiles of VOCs in a temperature-controlled environment of: a) layer without interaction with acids (background). b) sample with adsorbed butanoic acid. c) sample with adsorbed propanoic acid. d) Profilometric analysis of the zeolite layer. e) SEM image of zeolite 4A layer.

245 mg/m³ after approximately 53 s at 25 °C and a maximum emission of 430 mg/m³ after 20 s at 60 °C (Fig. 1c). Considering the structure of the butanoic acid and the physicochemical properties of zeolite 4A, it was evidenced that the size of the molecule and the pores of zeolite 4A are similar and, as a result, a partial or superficial adsorption takes place. While, if we consider propanoic acid molecule, since their size is smaller than the pore size of zeolite 4A, it is possible a higher adsorption capacity inside the zeolite openings. The adsorption was evaluated through the area under the curve of the emissive profiles (Fig. 1b and 1c). Therefore, the concentrations of molecules of both detected acids were quantified, respectively. Regarding the emission profile of butanoic acid, a desorption of 0.06% w/w and 0.05% w/w (at temperatures of 60 °C and 25 °C, respectively) was evaluated. Similarity, for propanoic acid, a desorption of 0.4% w/w and 0.3% w/w (at temperatures of 60 °C and 25 °C respectively) was evaluated (see Table 1 and 2).

Table 1. Concentrations of butyric acid desorbed respect to the adsorption capacity of zeolite layer.

Thickness (μm)	Temp (°C)	Time (s)	Conc (mg/m ³ ·s)	Desorption (mg)	% w/w
20	60	300	42719	1.70	0.06
20	25	300	37036	1.48	0.05

Results evidenced that the nanoporous layers are highly selective with respect to the propanoic acid rather than butanoic acid. Considering molecules of butanoic acid, the increase of temperature involves an increase of the desorbed molecules of 40% due to the higher energy provided to the system. Referring to the adsorption of propanoic

Table 2. Concentrations of propionic acid desorbed respect to the adsorption capacity of zeolite layer

Thickness (μm)	Temp. ($^{\circ}\text{C}$)	Time (s)	Conc. ($\text{mg}/\text{m}^3\cdot\text{s}$)	Desorption (mg)	% w/w
20	60	300	233441	9.4	0.4
20	25	300	256031	9	0.3

acid, the molecule is smaller than the zeolite openings, allowing a greater adsorption and thus a higher emissive profile. Higher temperature results in a higher desorption rate of molecules, as evidenced by the desorption rate of propionic acid, which is significantly higher than that of butanoic acid.

4 Conclusion

The desorptive properties of a nanoporous layer made of zeolite 4A were investigated, as a selective system, to detect VOCs. Butyric and propionic acids were considered, since they are involved in different biological processes, and their expression may be used to discriminate between physiological or pathological conditions and its monitoring. The selective desorption capacity of the zeolite layer was performed using a photoionization system. Results evidenced that a joint use of a nanoporous layer and a PID can improve the selectivity of the overall device, exploiting the different adsorption of zeolite with respect to butyric and propionic acids.

References

1. Shirasu, M., Touhara, K.: The scent of disease: volatile organic compounds of the human body related to disease and disorder. *J. Biochem.* **150**, 257–266 (2011)
2. Shigeyama, H., Wang, T., Ichinose, M., Ansai, T., Lee, S.-W.: Identification of volatile metabolites in human saliva from patients with oral squamous cell carcinoma via zeolite-based thin-film microextraction coupled with GC–MS. *J. Chromatogr. B Analyt. Technol. Biomed. Life Sci.* **1104**, 49–58 (2019)
3. Arakawa, T., Dao, D.V., Mitsubayashi, K.: Biosensors and chemical sensors for healthcare monitoring: a review. *IEEE Trans. Electr. Electron. Eng.* **17**, 626–636 (2022)
4. Ratcliffe, N., Wieczorek, T., Drabińska, N., Gould, O., Osborne, A., De Lacy Costello, B.: A mechanistic study and review of volatile products from peroxidation of unsaturated fatty acids: an aid to understanding the origins of volatile organic compounds from the human body. *J. Breath Res.* **14** (2020)
5. Tyagi, D., Bhattacharyya, K.: Synthesis of porous materials. In: Tyagi, A.K., Ningthoujam, R.S. (eds.) *Handbook on Synthesis Strategies for Advanced Materials*. IIMS, pp. 189–227. Springer, Singapore (2022). https://doi.org/10.1007/978-981-16-1803-1_6
6. Bacakova, L., Vandrovцова, M., Kopova, I., Jirka, I.: Applications of zeolites in biotechnology and medicine—a review. *Biomater. Sci.* **6**, 974–989 (2018)
7. Stetsenko, M., et al.: Antireflection enhancement by composite nanoporous zeolite 3A–carbon thin film. *Nanomaterials* **9**(11), 1641 (2019)

8. Fiorillo, A.S., Tiriolo, R., Pullano, S.A.: Absorption of Urea into zeolite layer integrated with microelectronic circuits. *IEEE Trans. Nanotechnol.* **14**(2) (2015)
9. Pullano, S.A., et al.: Antireflection properties of composite zeolite gold nanoparticles film. *Electron. Lett.* **54**(6), 370–372 (2018)
10. Szulczyński, B., Gębicki, J.: Currently commercially available chemical sensors employed for detection of volatile organic compounds in outdoor and indoor air. *Environments* **4**(1), 21 (2017)
11. Hsi, P.C.: Photo-ionization detector for detecting volatile organic gases. U.S. Patent No 5,393,979 (1995)
12. Pullano, S.A., Falcone, F., Critello, C.D., Bianco, M.G., Menniti, M., Fiorillo, A.S.: An affordable fabrication of a zeolite-based capacitor for gas sensing. *Sensors* **20**(8) (2020)
13. Li, Y., Chung, T.S., Cao, C., Kulprathipanja, S.: The effects of polymer chain rigidification, zeolite pore size and pore blockage on polyethersulfone (PES)-zeolite a mixed matrix membranes. *J. Membr. Sci.* **260**, 45–55 (2005)
14. de Pietre, M.K., Freitas, J.C.C.: Fundamental studies on zeolite–adsorbate interactions: designing a better aluminosilicate adsorbent for pollutants’ removal. *Environ. Earth Sci.* **81**(1), 1–22 (2021). <https://doi.org/10.1007/s12665-021-10130-w>
15. Weitkamp, J., Ernst, S., Puppe, L. Shape-selective catalysis in zeolites. In: Weitkamp, J., Puppe, L. (eds.) *Catalysis and Zeolites*, pp. 327–376. Springer, Heidelberg (1999). https://doi.org/10.1007/978-3-662-03764-5_5
16. Strieter, F.J., Templeton, D.H., Scheuerman, R.F., Sass, R.L.: The crystal structure of propionic acid. *Acta Cryst.* **15**, 1233–1239 (1962)



Role of IR and UV-Vis Spectroscopies Combined with Electrical Measurements in Materials Relevant for Gas Sensing

Ambra Fioravanti¹ (✉), Sara Morandi², Stefano Lettieri³, Michele Sacerdoti⁴, Pietro Marani¹, and Maria Cristina Carotta¹

¹ Istituto di Scienze e Tecnologie per l'Energia e la Mobilità Sostenibili (CNR-STEMS), 44124 Ferrara, Italy

ambra.fioravanti@stems.cnr.it

² Dipartimento di Chimica, Università di Torino, 10125 Torino, Italy

³ Istituto di Scienze Applicate e Sistemi Intelligenti "E. Caianiello" (CNR-ISASI), 80126 Napoli, Italy

⁴ Dipartimento di Fisica e Scienze della Terra, Università di Ferrara, 44122 Ferrara, Italy

Abstract. Wide band gap semiconductors are extensively used to realize sensors for the detection of a great variety of gases. The study of the sensing mechanism is at the base of the understanding, as well as the tuning, of the sensing properties. In this work, anatase and rutile, polymorphic forms of TiO₂ were considered to be characterized through a combined approach (based on spectroscopic techniques and electrical measurements) finalized to determine the processes involved in the detection mechanism during interaction with carbon monoxide.

Keywords: Thick film gas sensors · UV-Vis-NIR and FT-IR spectroscopies · Sensing mechanisms · Rutile · Anatase · TiO₂

1 Introduction

Today, gas sensors based on semiconducting metal oxides (such as SnO₂, ZnO, TiO₂, WO₃, etc.) are successfully used in many applications (for example in pollutant monitoring, in the control of industrial systems or food quality, in medical diagnosis, etc.) to detect a large number of gaseous compounds (CO, O₃, C₂H₄, NO_x, VOCs, etc.) [1]. They exploit the chemiresistive effect for which the interaction of a gas with their surface can induce a significant change in the electrical resistance/conductance of the oxide. Therefore, the electrical resistance/conductance is the main parameter typically recorded. It is a simple task but this does not provide direct information about the processes that occur during sensing. To describe the sensing mechanism of a specific material toward a specific gas, it is necessary to determine the electronic properties of the oxide during the interaction with the gas.

In this work, our proposed approach is based on the combination of the spectroscopic characterization of the oxide (absorbance FT-IR, diffuse reflectance UV-Vis-NIR) with

the electrical measurements performed on the related thick films. Indeed, the IR and UV-Vis spectroscopies represent a convenient experimental characterization to study the electronic properties and surface chemistry of metal oxides [2, 3]. When there are point defects in these oxides, there are shallow levels in the band gap, with an activation energy typically between 10^{-3} and 10^{-1} eV, being responsible for their semiconducting properties, thus for their gas sensing properties. It is possible to test these defect levels by the absorption of the electromagnetic radiation at specific energies and to detect the changes in level populations and in free carrier concentration by varying the temperature or the atmosphere.

Here, we focused our attention on the titanium oxide both in anatase and rutile phase as functional material. Anatase is a TiO_2 meta-stable phase which irreversibly transforms to rutile phase, that is thermodynamically stable, at temperatures higher than $600\text{ }^\circ\text{C}$ [4]. The pros and cons of using anatase or rutile in gas sensing have been debated since decades and discussion is still open [5]. In the following, the results of the combined approach (based on spectroscopic techniques and electrical measurements) to determine the processes involved in the detection mechanism for TiO_2 in anatase and rutile phase are reported in the case of carbon monoxide (CO) as interacting gas.

2 Materials and Methods

TiO₂ preparation – The anatase powder was synthesized via sol-gel route by dissolving Ti(IV) n-butoxide (Merck, 97%) in absolute ethanol to obtain a 0.23 M solution. Subsequently, an ethanol/water 1:1 vol. Solution was added drop by drop under rapid stirring to the first one. The mixture was filtered by gravity, washed with diethyl ether and dried at $90\text{ }^\circ\text{C}$ for 12 h in air, then calcined at $450\text{ }^\circ\text{C}$ for 2 h. To obtain the rutile sample, the anatase powder was annealed at $850\text{ }^\circ\text{C}$ for 1 h [6].

Morphological characterization – Powder morphology was studied with Field Emission Scanning Electron Microscopy (FE-SEM) by a Carl Zeiss Sigma microscope.

Structural analysis – X-ray diffraction (XRD) analyses were performed by using a Philips PW 1830 vertical diffractometer with Bragg–Brentano geometry. The unit cell parameters were estimated with FullProf software (structure profile refinement), while the crystallite size was calculated by Williamson-Hall method [7].

Spectroscopic characterization – Diffuse reflectance (DR) UV-Vis-NIR spectra were run at RT on a Varian Cary 5 spectrophotometer. For the analysis, the prepared powders were placed in a quartz cell, allowing thermal treatments in controlled atmosphere up to $800\text{ }^\circ\text{C}$. Spectra are reported with the Kubelka–Munk function $[f(R_\infty) = (1 - R_\infty)^2/2R_\infty]$, where R_∞ is the reflectance of an ‘infinitely thick’ layer of the sample] in the ordinate scale [8]. Absorption FT-IR spectra were run on a Perkin-Elmer 2000 FT-IR spectrophotometer equipped with a Hg–Cd–Te cryodetector, working in the range of wavenumbers $7800\text{--}580\text{ cm}^{-1}$. The powders were compressed in self-supporting disks and placed in a commercial heatable stainless steel IR cell (Aabspec) allowing in situ thermal treatments up to $600\text{ }^\circ\text{C}$ and simultaneously spectra recording. For both UV-Vis-NIR and medium IR (MIR) analyses, samples were activated at $550\text{ }^\circ\text{C}$ in vacuum and in dry oxygen, then underwent treatment in CO at $400\text{ }^\circ\text{C}$.

Sensors fabrication – The thick films were deposited on miniaturized alumina substrates provided with Au contacts and heaters by screen printing and fired at 650 °C.

Electrical characterization – Sensors were tested by the flow-through technique with a constant flow rate of 0.5 L/min. Conductance vs. temperature was measured and the surface energy barrier obtained through temperature stimulated conductance measurement [9] both in dry air and in a mixture of dry air and CO. Sensor dynamic responses to CO in dry air were obtained at working temperatures between 350 and 550 °C.

3 Results and Discussion

SEM images showed a homogeneous size distribution of spherical particles both for anatase (Fig. 1A) and rutile (Fig. 1B) powders. As expected, a considerable grain growth occurs when the crystalline phase changes from anatase to rutile [10]. XRD patterns (Fig. 1C) confirm anatase (space group $I4_1/amd$) and rutile (space group $P4_2/mnm$) phases, providing a medium crystallite size of 12 and 101 nm, respectively.

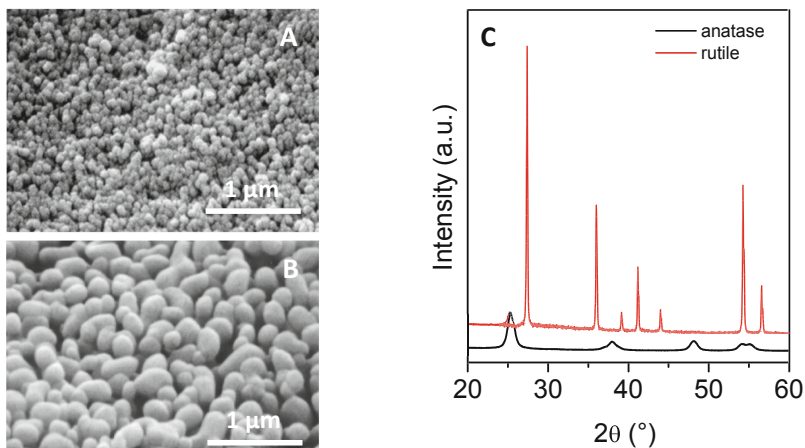


Fig. 1. SEM images of TiO₂ anatase (A) and rutile (B) powders and their XRD patterns (C).

The conductance vs. temperature curves (Arrhenius plots) in air (Fig. 2A) showed for both materials the n-type semiconductor behavior. The shape of the Arrhenius plots and the conductivity are very different for the two TiO₂ phases. At low temperature, anatase exhibits a conductivity about two orders of magnitude lower than the rutile one. On the other hand, the conductivity for the rutile film does not change in the temperature range 100–400 °C. The dry air/CO atmosphere induces an increase in the anatase conductance not observed for rutile sensor, implying better sensing performance for anatase sensor. This is confirmed, as it is shown in Fig. 3, where we report a comparison between the responses in dry air to 50 ppm of CO for TiO₂ anatase and rutile based sensor. Taking into account the surface energy barriers vs. temperature (Fig. 2B), we can observe higher barrier height in presence of reducing atmosphere, in particular for the anatase sensor.

This behavior appears immediately in disagreement with the sensing mechanism based on the Schottky barrier model for n-type semiconductors, already observed for example in ZnO and SnO₂ [11]. Such mechanism consists in a releasing of trapped electrons of ionosorbed oxygen atoms after a surface chemical reaction with a consequent decreasing of the barrier height and the increasing of conductance.

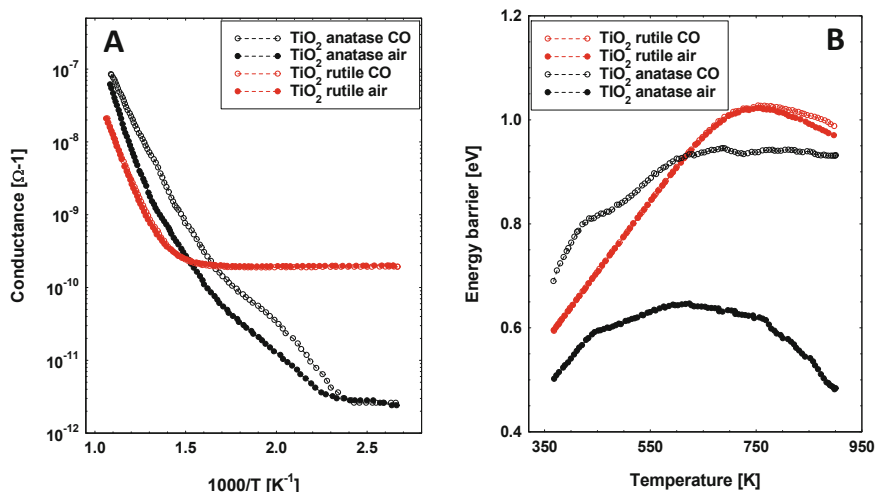


Fig. 2. For the two TiO_2 powders: comparison of conductance vs. temperature in dry air and in a mixture of dry air and CO (100 ppm) (A) and comparison of the energy barrier dependence on temperature in dry air and in a mixture of dry air and CO (100 ppm) (B).

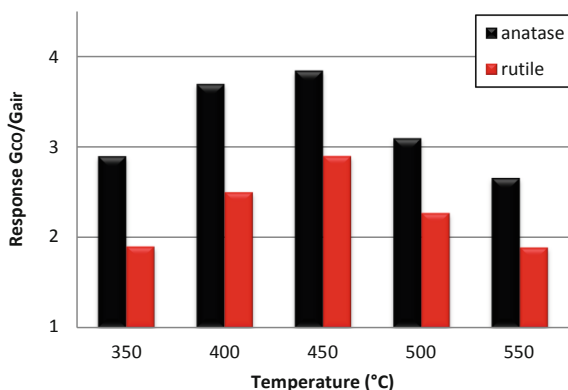


Fig. 3. Responses to 50 ppm of CO reported as G_{CO}/G_{air} obtained at different temperatures for the two TiO_2 powders.

The results of the spectroscopic characterization shed light to this unexpected behavior.

Figure 4 shows both the DR UV-Vis-NIR spectra (section A) and absorption spectra in the MIR region (section B) of anatase (black traces) and rutile (red traces). After

treatment in oxygen at 550 °C (dashed traces), the interaction with CO at 400 °C causes the formation of broad absorptions for both samples (solid traces).

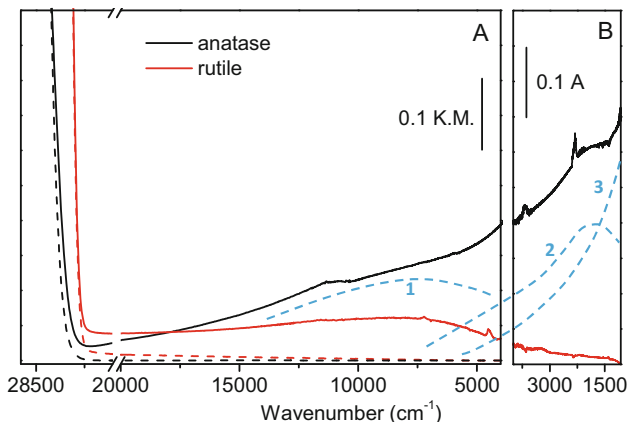


Fig. 4. Diffuse reflectance UV-Vis-NIR spectra (A) and absorption spectra in the MIR region (B) of anatase (black traces) and rutile (red traces) after treatment in oxygen at 550 °C (dotted traces) and after interaction with CO at 400 °C (solid traces).

It is well evident the different spectroscopic behavior of the two samples. In particular, for rutile the interaction with CO causes the formation of a broad band centered in the Vis-NIR spectral region with a weak tail in the medium IR region. This absorption is related to the presence of Ti^{3+} ions and assigned to a metal-metal charge transfer from Ti^{3+} to Ti^{4+} ions, also known as polaronic transition [12–14]. The absorption shown by anatase after interaction with CO at 400 °C is more complex. In this case, at least three contributions can be distinguished, as evidenced by dashed blue curves in the Fig. 4: 1) an absorption related to the polaronic transition already discussed for rutile; 2) an absorption centered in the MIR region and related to the photoionization of mon-ionized oxygen vacancies [15–17] and 3) an absorption that increases in intensity upon decreasing the wavenumbers, a feature characteristic of free electrons in the conduction band [18].

It is clear that an increase in conductance together with an increase in energy barrier height in CO atmosphere means that the electrons which enter the conduction band as a response to CO do not lower the barrier as foreseen by the Schottky barrier model. A similar behavior has been already seen for the mixed $Ti_xSn_{1-x}O_2$ oxides with $x \geq 0.3$, for which CO interacts with the surface lattice oxygen atoms whose bond electrons do not participate to the development of the spatial charge region and thus of the Schottky barrier [19]. Finally, it must be considered that the pure titania in rutile phase is affected by an exaggerated grain coalescence. In this case, the pinning of Fermi level can develop, so hindering the gas response; thereby it is reasonable that the two energy barriers, in air and in CO, do not differ significantly from one another, because very weak sensing process occurs [19].

References

1. Neri, G.: First fifty years of chemoresistive gas sensors. *Chemosensors* **3**, 1–20 (2015)
2. Dey, A.: Semiconductor metal oxide gas sensors: a review. *Mater. Sci. Eng. B Solid-State Mater. Adv. Technol.* **229**, 206–217 (2018)
3. ViterIgor, R., Barhoum, I.: Optical spectroscopy for characterization of metal oxide nanofibers. In: Barhoum, A., Bechelany, M., Makhlof, A. (eds.) *Handbook of Nanofibers*, pp. 523–556. Springer, Cham (2019). https://doi.org/10.1007/978-3-319-53655-2_10
4. Lettieri, S., Pavone, M., Fioravanti, A., Santamaria Amato, L., Maddalena, P.: Charge carrier processes and optical properties in TiO₂ and TiO₂-based heterojunction photocatalysts: a review. *Materials* **14**, 1645 (2021)
5. Zakrzewska, K., Radecka, M.: TiO₂-based nanomaterials for gas sensing—influence of anatase and rutile contributions. *Nanosci. Res. Lett.* **12**, 89 (2017)
6. Carotta, M.C., et al.: Comparison between titania thick films obtained through sol–gel and hydrothermal synthetic processes. *Thin Solid Films* **515**(23), 8339–8344 (2007)
7. Suryanarayana, C., Norton, M.G.: *X-Ray Diffraction: A Practical Approach*. Springer, New York (1998). ISBN 9781489901507
8. Kubelka, P.: New contributions to the optics of intensely light-scattering materials, part I. *J. Opt. Soc. Am.* **38**, 448–457 (1948)
9. Clifford, P.K., Tuma, D.T.: Characteristics of semiconductor gas sensors – II. Transient response to temperature change. *Sens. Actuat. B Chem.* **3**(83), 255–282 (1982)
10. Byrne, C., Fagan, R., Hinder, S., McCormack, D.E., Pillai, S.C.: New approach of modifying the anatase to rutile transition temperature in TiO₂ photocatalysts. *RSC Adv.* **6**, 95232–95238 (2016)
11. Fioravanti, A., Morandi, S., Carotta, M.C.: Spectroscopic–electrical combined analysis to assess the conduction mechanisms and the performances of metal oxide gas sensors. *Chemosensors* **10**, 447 (2022)
12. Cox, P.A.: *Transition Metal Oxides*. Clarendon Press Ed. (1992)
13. Mestl, G., Verbruggen, N.F.D., Knozinger, H.: Mechanically activated MoO₃. 2. Characterization of defect structures. *Langmuir* **11**, 3035 (1995)
14. Dieterle, M., Weinberg, G., Mestl, G.: Raman spectroscopy of molybdenum oxides part I. Structural characterization of oxygen defects in MoO_{3–x} by DR UV/VIS, Raman spectroscopy and X-ray diffraction. *PCCP* **4**, 812–821 (2002)
15. Özgür, Ü., et al.: A comprehensive review of ZnO materials and devices. *J. Appl. Phys.* **98**, 1–103 (2005)
16. Göpel, W., Lampe, U.: Influence of defects on the electronic structure of zinc oxide surfaces. *Phys. Rev. B: Condens. Matter Mater. Phys.* **22**, 6447–6462 (1980)
17. Carotta, M.C., et al.: (Ti, Sn)O₂ binary solid solutions for gas sensing: spectroscopic, optical and transport properties. *Sens. Actuat. B Chem.* **130**, 38–45 (2008)
18. Faglia, G., Baratto, C., Sberveglieri, G., Zha, M., Zappettini, A.: Adsorption effects of NO₂ at ppm level on visible photoluminescence response of SnO₂ nanobelts. *Appl. Phys. Lett.* **86**, 011923 (2005)
19. Carotta, M.C., et al.: (Ti, Sn) solid solutions as functional materials for gas sensing. *Sens. Actuat. B Chem.* **194**, 195–205 (2014)



A High Accuracy QCM Based Sensing System for in Water Ammonia Monitoring

Ada Fort¹, Anna Lo Grasso¹, Elia Landi¹, Marco Mugnaini¹, Enza Panzardi¹ (✉), Valerio Vignoli¹, Luigi Talarico^{2,3}, Marco Consumi^{2,3}, and Agnese Magnani^{2,3}

¹ Department of Information Engineering and Mathematics, University of Siena, Via Roma 56, Siena, Italy

enza.panzardi@unisi.it

² Department of Biotechnology, Chemistry and Pharmacy, University of Siena, Via Aldo Moro 2, Siena, Italy

³ National Interuniversity Consortium of Materials Science and Technology (INSTM) – Siena Research Unit, Via G. Giusti 9, 50121 Florence, Italy

Abstract. Ammonia is among the most popular nutrients for plants and water ecosystems although in, it is also one of the most common water pollutants such that it is used as an important indicator of its quality and, more general, of the health of the global marine ecosystem. In this regards, monitoring of ammonia in water, even in low concentration, arouses ever increasing interest in scientific community, increasingly involved in the environmental protection. In this paper we investigate the feasibility of an in-liquid ammonia detection system based on a quartz crystal microbalance (QCM) and an oscillator circuit. The QCM surfaces have been functionalized with a self-assembled monolayer (SAM) of 3-mercaptopropionic acid in order to exploit the electrostatic attraction between the gold (Au) quartz electrodes surface, covered by the deprotonated carboxylic groups, and the NH_4^+ ions in aqueous solution. Preliminary measurements have been performed and the quartz resonance frequency and the motional resistance have been simultaneously acquired in real time when the quartz surface is exposed to liquid solutions of ammonia at different concentrations. Experimental results show satisfactory ammonia sensing properties proving the formation of a strong bond between the functionalizing layer and the NH_4^+ ions even at the lower tested concentration with an effective change of the physical properties of the sensing layer related to the molecular bond.

Keywords: QCM · Water ammonia monitoring · QCM in liquid measurements · Water quality monitoring

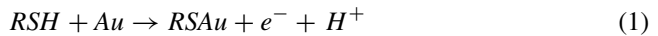
1 Introduction

Ammonia (NH_3) is a nitrogen chemical compound naturally present in ground and surface water due to biological or organic decomposition processes, as well as released in ambient by industrial waste processes or farms with uncontrolled concentrations. As a direct source of nitrogen, ammonia represents one of the most popular nutrients for

plants and water ecosystems although, it is also one of the most common water pollutants due to its high level of toxicity such that it is used as an important indicator of its quality and, more general, of the health of the global marine ecosystem [1]. Therefore, the monitoring of ammonia in water, even in low concentration, arouses ever increasing interest in scientific community and in the organizations responsible for the environmental protection. In this work we investigate the feasibility of an in liquid ammonia detection system based on a quartz crystal microbalance (QCM) and an oscillator circuit. The quartz surfaces, embedding gold electrodes, have been properly functionalized by means of a Self-Assembled Monolayer (SAM) of 3-mercaptopropionic acid (3MPA) solution aiming to exploits the energies attraction between the deprotonated carboxylic groups (COO^-) and the NH_4^+ ions for the detection of ammonia traces in water. Moreover, the developed measurement setup has been conceived to overcome the problems related to the use of QCM in in-liquid applications for mass measurements [2].

2 Sensing Material and Principle

The formation of self-assembled monolayer on gold surfaces is among the most commonly used functionalization methods in QCM-based sensing applications [3, 4]. Basically, the aforementioned reaction involves the formation of a covalent bond between sulfur (S) and gold (Au) molecules followed by a self-organization step driven by electrostatic interactions and weak forces [5, 6]. The coverage, the reproducibility, and the effective formation of SAMs are influenced by many key factors, among which, the concentration of the thiol derivative solution and the cleanliness of the gold surface to functionalize [7]. The use of thiol compounds (RSH) aims to tune the specificity of QCM measurements since the SAM could provide different functionalization surfaces that may react with various kinds of analytes. Moreover, it has to be noted that the time required to the formation of the monolayer, strongly depends on the hydrophobic interactions between the involved carbon chains. Indeed, the formation of the covalent bond between Au and S happens in the first minutes of the reaction according to an exothermic process, described as follows:



Meanwhile, the organization into an ordered monolayer is a process that relies only on weak forces and so it requires longer times to be completed [8].

In this work, the gold QCM electrodes were chemically cleaned and successively functionalized with self-assembled monolayers of 3-mercaptopropionic acid, aiming at realizing an ammonia detection system by exploiting the electrostatic attraction between the deprotonated carboxylic groups (COO^-) and the NH_4^+ ions in aqueous solutions (Fig. 1b).

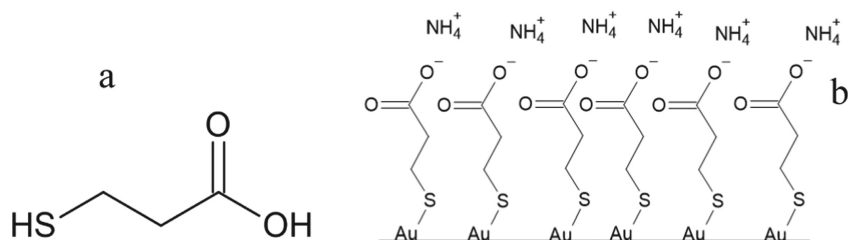


Fig. 1. a) 3-Mercaptopropionic acid structure; b) interaction between ammonium ions and 3-mercaptopropionate in aqueous solution

3 Materials and Methods

3.1 Materials

The chemical cleaning and functionalization of the QCM was realized using: Sulfuric Acid (H₂SO₄, 95–97%), Hydrogen Peroxide Solution (H₂O₂, 30% v/v), Ethanol (absolute) and 3-Mercaptopropionic acid $\geq 99\%$ (3MPA), purchased from Sigma-Aldrich (Milano, IT).

The quartz used for tests is an AT-cut quartz crystal with a nominal resonance frequency f_r of approximately 10 MHz and gold electrodes with 11.5 mm diameter.

Quartz impedance spectra were measured using an impedance analyzer by Wayner Kerr (6500B).

QCM measurements in transient conditions were performed by simultaneously acquiring, in real time (1 s sampling time) the quartz resonance frequency and its motional resistance exploiting a measurement system based on a Mecham oscillator circuit performing an automatic adaptive strategy for gain adjustment [2]. This feature allows to maintain the oscillator frequency close to the series resonance frequency of the quartz to monitor the physical parameters of interest, involving the quartz surface.

3.2 Methods

QCM Surface Cleaning. To obtain a clean gold electrodes surface, the QCM were immersed in a hot piranha solution (3:1 v/v H₂SO₄ 97% /H₂O₂ 30%) for 5 min and then rinsed with ultrapure water. Crystals were dried under nitrogen gas flow and stored under vacuum until the next step was performed.

Self-assembled Monolayer Formation. Clean and dry QCM crystals were immersed in a 1 mM ethanolic solution of 3MPA for 12 h to allow the chemical absorption and formation of the SAM on the gold electrodes. The functionalized crystals were rinsed with ethanol to remove the excess thiol compounds on the surface and then stored in a vacuum box.

Time of Flight Secondary Ions Mass Spectrometry (ToF-SIMS). ToF-SIMS experiments were conducted on a TRIFT III spectrometer (Physical Electronics, Chanhassen, MN, USA) equipped with a 22 keV Au⁺ liquid metal primary ion source with a beam current of 600 pA and a 45° incident angle. Clean (pristine) and functionalized (3MPA) samples were analyzed after storage in a vacuum box. Positive and negative ion spectra were acquired with a pulsed, bunched primary ion beam by rastering over 100 × 100 μm and maintaining the primary ion dose below 10¹² ions/cm². Negative polarization spectra were recorded and calibrated with ions [CH]⁻ (m/z 13.0078) [O]⁻ (m/z 15.995) [C₂H]⁻ (m/z 25.007) [S]⁻ (m/z 31.972) [Au]⁻ (m/z 196.966). The resolution (m/Δm) was 4160 at m/z 27.024.

4 Results and Discussions

4.1 Surface Cleaning and Self Assembled Monolayer Formation

The presence of a SAM consisting of 3-mercaptopropionic acid was evaluated and confirmed by Time-of-Flight Secondary Ions Mass spectrometry. In particular, the results reported in Table 1, concerning the measured ions are consistent with the functionalization of the gold surface of the electrodes. In Fig. 2, the negative ions spectra in the range m/z 200–500 for both the samples: the pristine quartz in Fig. 2a and functionalized in Fig. 2b, are reported. The comparison between the obtained spectra confirms the efficiency of the cleaning procedure described above, since the main ions present in pristine QCM spectra are all attributable to a clean gold surface. The presence of peaks at m/z 228.939 (AuS⁻, dev 3.58 mAMU), 425.905 (Au₂S⁻, dev -0.5 mAMU), and 457.877 (Au₂S₂⁻, dev 5.09 mAMU) are consistent with 3-mercaptopropionic acid bound to the gold surface.

Table 1. Main fragments observed in ToF-SIMS experiments

m/z	Negative fragments	m/z	Negative fragments	m/z	Negative fragments
31.972	[S] ⁻	245.941	[HOAuS] ⁻	457.877	[Au ₂ S ₂] ⁻
105.001	[C ₃ H ₅ O ₂ S] ⁻	254.954	[C ₂ H ₂ AuS] ⁻	498.916	[C ₃ H ₅ Au ₂ S ₂] ⁻
228.938	[AuS] ⁻	425.905	[Au ₂ S] ⁻	622.859	[C ₄ H ₅ O ₅ Au ₂ S ₃] ⁻

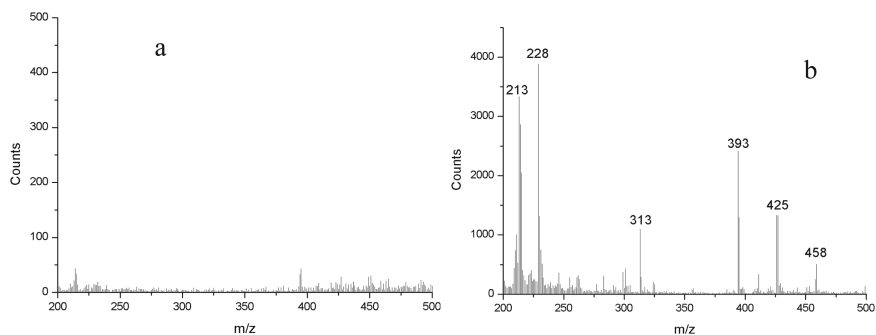


Fig. 2. Negative ToF-SIMS spectra of the pristine QCM (a) and of the 3MPA functionalized QCM (b) samples. Spectral range m/z 200–500

4.2 QCM Measurements

Figure 2a reports the measured impedance quartz amplitude, $|Z|$, and phase, ϕ , spectra before and after the functionalization procedure as a proof of the 3MPA monolayer formation on the quartz surface.

Transient measurements were performed by exposing one of the functionalized quartz surfaces to liquid solutions of NH_3 at different concentrations. The quartz crystal is housed in a measurement chamber suitable for in-liquid applications. At first, $150 \mu\text{L}$ of ultrapure water (UW) are injected into the measurement chamber, to homogeneously cover the quartz surface and such that the liquid can be seen as a semi-infinite layer. Subsequently amounts of $30 \mu\text{l}$ of NH_3 with 30% (v/v) concentration are added to cover the range: $30 \mu\text{l}$ – $150 \mu\text{l}$.

As reported in Fig. 2b a negative resonance frequency shift (Δf_r) can be observed by increasing the NH_3 concentration, until a saturation is reached due to the full coverage of the sensing layer, proving the formation of a strong bond between the functionalizing layer and the NH_4^+ ions even at the lower concentration [9]. On the other hand, the quartz motional resistance shows an opposite trend with respect to f_r , showing an effective change of the properties of the sensing layer related to the molecular bond (Fig. 3).

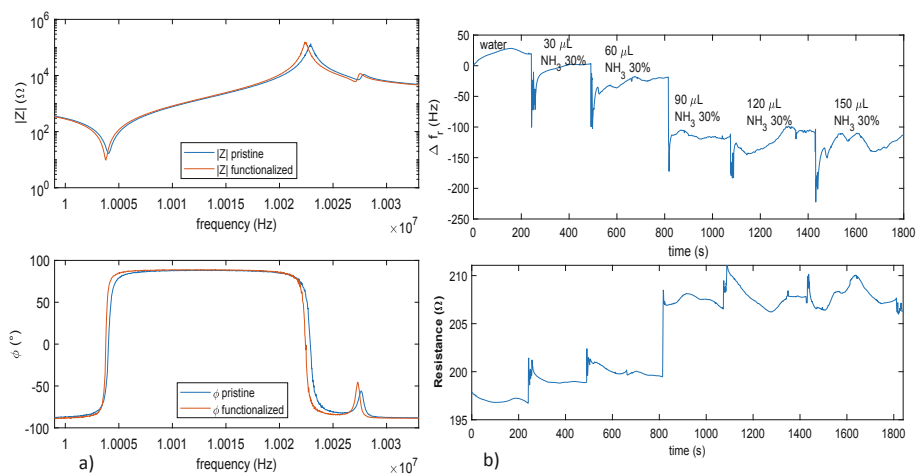


Fig. 3. a-Measured quartz impedance amplitude, $|Z|$, and phases, spectra before and after the functionalization procedure. b-Measured quartz resonance frequency shift and motional resistance variation in time. Measurements starts by adding 150 μ L of water on the QC surface, followed by subsequent additions of 30 μ L of NH_3 with 30% concentration (v/v) in the range 30 μ L–150 μ L.

5 Conclusions

In this work the feasibility of an ammonia detecting system in water has been presented. The sensing system is realized using QCMs which surfaces have been properly functionalized with a self-assembled monolayer of 3-mercaptopropionic for ammonia detection in water. Both the system resonance frequency and motional resistance have been acquired in real time showing appreciable results in terms of ammonia trace detection.

References

- Li, D., Xu, X., Li, Z., Wang, T., Wang, C.: Detection methods of ammonia nitrogen in water: a review. *TrAC Trends Anal. Chem.* **127**, 115890 (2020)
- Fort, A., et al.: An adaptive measurement system for the simultaneous evaluation of frequency shift and series resistance of QCM in liquid. *Sens. (Switz.)* **21**(3), 1–23 (2021). art. no. 678
- Wang, Y., et al.: Potentiometric sensors based on surface molecular imprinting: detection of cancer biomarkers and viruses. *Sens. Actuat. B Chem.* **146**, 381–387 (2010)
- Li, H., Wu, J., Doost, A.S., Su, J., Van der Meeren, P.: Electrostatic interaction between whey proteins and low methoxy pectin studied by quartz crystal microbalance with dissipation monitoring. *Food Hydrocolloids* **113**, 106489 (2021)
- Wang, T., Li, Z., Zong, R., Li, J.: Studies on thiol etching of gold by using QCM-D sensor as the sacrificial probe. *ChemPhysChem* **23**, 1–7 (2022)
- Bain, C.D., Whitesides, G.M.: Molecular-level control over surface order in self-assembled monolayer films of thiols on gold. *Science* **240**, 62–63 (1988)
- Min, H., Park, J.W., Shon, H.K., Moon, D.W., Lee, T.G.: ToF-SIMS study on the cleaning methods of Au surface and their effects on the reproducibility of self-assembled monolayers. *Appl. Surf. Sci.* **255**, 1025–1028 (2008)

8. Kokkoli, E., Zukoski, C.F.: Effect of solvents on interactions between hydrophobic self-assembled monolayers. *J. Colloid Interface Sci.* **209**, 60–65 (1999)
9. Cappelli, I., Fort, A., Grasso, A.L., Panzardi, E., Mugnaini, M., Vignoli, V.: RH sensing by means of TiO₂ nanoparticles: a comparison among different sensing techniques based on modeling and chemical/physical interpretation. *Chemosensors* **8**(4), 1–19 (2020). art. no. 89



A Portable Electrochemical Platform for Cobalt Detection In-Field

Giulia Selvolini¹, Matteo Nuzzo¹, Bianca Melean², Magdolna Casian², Oana Hosu², Cecilia Cristea², and Giovanna Marrazza¹(✉)

¹ Department of Chemistry “Ugo Schiff”, University of Florence, Via della Lastruccia 3, 50019 Sesto Fiorentino, FI, Italy
giovanna.marrazza@unifi.it

² Analytical Chemistry Department, “Iuliu Hațieganu” University of Medicine and Pharmacy, Strada Louis Pasteur 4, 400349 Cluj-Napoca, Romania

Abstract. The presented work shows the preparation of screen-printed electrodes modified with a lead (PbF-SPE) film for adsorptive stripping voltammetric determination of cobalt ions in real samples. The metallic film was deposited *in situ* on the surface of the graphite SPE (GSPE). The conditions for the determination of cobalt in the form of dimethylglyoximate complexes, including the concentration of the complexing agent and the instrumental parameters, were optimized. The limit of detection for cobalt determination was 3.8 ng/mL. These studies were complemented with a voltammetric characterization by using the reversible redox couple ferrocyanide/ferricyanide, to assess for the investigation of each step of the analytical procedure for the metal-based platform.

Keywords: Screen-printed electrodes · Cobalt · Adsorptive stripping voltammetry · Metal film

1 Introduction

Screen-printed electrodes (SPEs) are electrochemical sensors that are expected to be widely used in numerous real-life applications such as biology, medicine, environmental protection, and electronics [1]. Thanks to mass production and relatively low costs SPEs can be disposed of after a single use. The application of SPEs as sensors in the stripping voltammetry of metal ions usually requires the modification of the carbon surface in SPEs with a thin metal film consisting of mercury, gold, silver, bismuth or other materials, which can improve selectivity and sensitivity of the determination. Solutions of mercury ions or mercury oxides were the first ones that were used to obtain *in situ*, *ex situ* or bulk-modified SPEs [2]. However, the storage and utilization of SPEs modified with mercury is hazardous due to the toxicity of mercury and its salts, and consequently poses a significant threat to human and animal health and the environment. These problems were avoided by using electrodes modified with films composed of other, less volatile and less hazardous metals, mainly bismuth [3], antimony and tin. These metals are less toxic than mercury, and their toxicity to a large degree depends on the target organism, elements'

speciation, route of exposure, and chronic or acute poisoning. Most recently, the lead film SPE modified *ex situ* and *in situ* has been proposed for the anodic stripping voltammetric determination of zinc, nickel and cobalt ions [4, 5]. It had earlier been shown that lead film electrodes deposited on glassy carbon, carbon paste or gold supports could successfully be used for the determination of selected heavy metals including cobalt [6].

2 Materials and Methods

2.1 Chemicals

Ammonium chloride (NH_4Cl); ammonium hydroxide (NH_4OH); Co(II) and Pb(II) atomic absorption standards – 1000 mg/L in nitric acid, diluted as required in 10 mM hydrochloric acid; dimethylglyoxime ($\text{C}_4\text{H}_8\text{N}_2\text{O}_2$, DMG) – 10 mM solution in 0.1 M sodium hydroxide; sodium hydroxide (NaOH); hydrochloric acid (HCl); potassium ferrocyanide ($\text{K}_4[\text{Fe}(\text{CN})_6]$); potassium ferricyanide ($\text{K}_3[\text{Fe}(\text{CN})_6]$); potassium chloride (KCl). All reagents were purchased from Merck (Darmstadt, Germany). Deionized water (resistivity: 18 $\text{M}\Omega$) was used for all solutions.

2.2 Apparatus

All experiments were carried out using the PalmSens2 portable potentiostat/galvanostat (PalmSens BV, Houten, The Netherlands) controlled by PStTrace 5.9 software for data acquisition and elaboration. Screen-printed electrochemical cells based on a graphite working electrode, a graphite counter electrode, and a silver pseudo-reference electrode (EcoBioServices srl, Sesto Fiorentino, Italy) were used for the electrochemical experiments. All the reported potentials refer to the pseudo-reference silver screen-printed electrode and all the measurements were carried out at room temperature.

2.3 Cyclic Voltammetry Characterization

The surface of the SPEs was characterized by means of cyclic voltammetry for each modification step of the analytical procedure by dropping onto the SPEs 50 μL of 5 mM $[\text{Fe}(\text{CN})_6]^{-4/-3}$ redox probe (equimolar solution in 0.1 M KCl) and by scanning the potential from -0.8 V to $+0.8$ V at 0.1 V/s.

2.4 Cobalt Detection

Co(II) calibration curve at *in situ* modified PbF-SPEs was performed by means of adsorptive stripping voltammetry in ammonia/ammonium buffer solution, containing Pb(II) in the form of its complex with dimethylglyoxime. Square wave adsorptive stripping voltammetry (SWAdSV) measurements were carried out by following a two-step accumulation protocol under stirring conditions with a successive cathodic stripping scan between -0.8 V and -1.3 V.

Further details are reported in Table 1.

Table 1. Experimental parameters for cobalt determination.

Buffer concentration	0.2 M
Buffer pH	8.2
Lead concentration	40 μ M
DMG concentration	500 μ M
Deposition potential	−1.3 V
Deposition time	20 s
Adsorption potential	−0.8 V
Adsorption time	60 s
Step potential	2 mV
Amplitude	50 mV
Frequency	50 Hz

Each determination is reported as the average of at least three consecutive measurements. The sensitivity of the method was established from the slope of the calibration curve and the limit of detection (LOD) was computed as three times the standard deviation of the blank over the slope of the calibration curve.

3 Results and Discussion

3.1 Electrochemical Sensor Surface Characterization

The modified surface of the working electrode was characterized by means of cyclic voltammetry using the reversible redox couple $[\text{Fe}(\text{CN})_6]^{-4/-3}$ to monitor the whole analytical procedure. The anodic and cathodic peak potentials (E_{pa} , E_{pc}) and currents (i_{pa} , i_{pc}) extracted from the obtained voltammograms are shown in Table 2.

Table 2. CV characterization of the lead film-based platforms in presence of 5 mM $[\text{Fe}(\text{CN})_6]^{-4/-3}$ in 0.1 M KCl for each step of the analytical procedure: A) bare SPE; B) lead film-modified SPE (PbF-SPE); C) PbF-SPE after the accumulation of cobalt dimethylglyoximate; D) PbF-SPE after the accumulation of cobalt complex and a successive stripping scan.

	E_{pa} (V)	E_{pc} (V)	i_{pa} (μ A)	i_{pc} (μ A)
A	0.401	−0.104	81.8	−64.8
B	0.387	−0.009	88.6	−75.3
C	0.394	−0.041	81.6	−68.6
D	0.396	−0.058	81.8	−66.1

It can be observed that lead deposition increases the conductivity of the bare GSPE and the reversibility of the process, while the complex adsorption decreases the conductivity and the reversibility; moreover, the stripping scan seems not to desorb completely the cobalt complex.

3.2 Lead and DMG Concentration Optimization

With the aim of obtaining the best analytical response for cobalt determination, the concentration of lead and DMG were optimized by analyzing solutions containing 30 $\mu\text{g/L}$ of Co(II) and different concentrations of Pb(II) under the already shown experimental parameters. The results are displayed in Table 3.

Table 3. Lead and dimethylglyoxime concentration optimization in presence of 30 $\mu\text{g/L}$ of cobalt.

	Concentration (μM)	i (μA)	%RSD
Pb(II)	10	-6.953	16
	40	-10.271	13
	80	-9.413	11
	100	-8.814	10
DMG	100	-8.567	10
	300	-10.026	12
	500	-10.046	10
	900	-8.959	25

Cobalt stripping peak increased with increasing Pb(II) concentration up to 40 μM and DMG concentration up to 500 μM , which were selected as the value to be used in the subsequent experiments because they resulted in the highest stripping peak current for cobalt detection.

3.3 Cobalt Detection in Standard Solutions

A calibration curve was performed under the optimized conditions in the range from 5 $\mu\text{g/L}$ to 50 $\mu\text{g/L}$: the cathodic peaks of the cobalt dimethylglyoximate increased linearly with Co(II) concentration, reaching almost a plateau (Fig. 1).

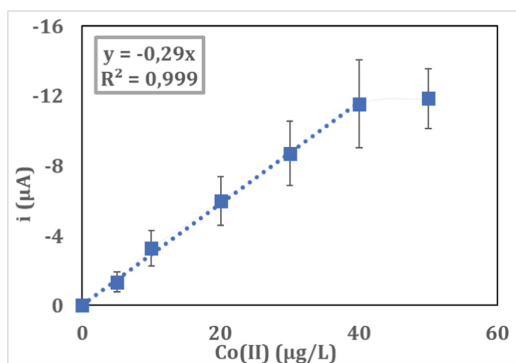


Fig. 1. Calibration curve for cobalt in standard solutions. The signal is reported as the stripping peak current obtained for each platform by varying cobalt concentration up to 50 µg/L.

The detection limit was calculated as three times the standard deviation of the blank over the slope of the calibration curve, retrieving a value of 3.8 µg/L with a high correlation coefficient (R^2) of 0.999. The reproducibility of the method was assessed by testing ten different sensors in the analysis of a fixed concentration of Co(II) of 30 µg/L under the same experimental conditions used for the calibration curve, retrieving a relative standard deviation (RSD) in the corresponding peak current value of 26%.

3.4 Cobalt Detection in Real Samples

To assess the applicability of the method, a calibration curve was performed in an industrial waste deriving from an industrial process of recycling automotive batteries, already containing cobalt and other metals, by adding Co(II) standard solution up to a concentration of 30 µg/L (Fig. 2).

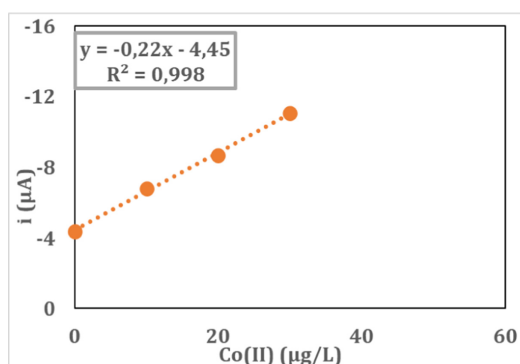


Fig. 2. Calibration curve for cobalt in an industrial waste sample. The signal is reported as the stripping peak current obtained for each platform by varying cobalt concentration up to 30 µg/L.

A linear correlation was retrieved in the tested range with only a slight decrease of the sensitivity in this case. Moreover, the Co(II) concentration in the sample was calculated from the x-intercept of the curve in Fig. 2 and resulted to be of 61 mg/L, which is in good accord with that obtained from inductively coupled plasma (ICP) of 75 mg/L. This demonstrated that the PbF-SPEs could be successfully applied in the analysis of cobalt both in standard solutions and in complex matrices.

4 Conclusions

This work reports the performance of graphite screen-printed electrodes (GSPEs) modified with a lead film in detecting cobalt (II) ions. The platform was electrochemically characterized with $[\text{Fe}(\text{CN})_6]^{-4/-3}$ redox probe and an increase of the performance of the SPEs were observed by the electrodeposition of the metal film. A linear correlation between the stripping peak current and cobalt concentration were retrieved with a high correlation coefficient. Cobalt was successfully detected also in complex matrices, demonstrating the applicability of the PbF-SPEs.

Acknowledgements. This research was funded by Regione Toscana within the project RI.B.AT (Riciclo Integrato Batterie AutoTrazione) in the framework of POR FESR 2014/2020.

References

1. Li, M., Li, Y.-T., Li, D.-W., Long, Y.-T.: Recent developments and applications of screen-printed electrodes in environmental assays – a review. *Anal. Chim. Acta* **734**, 31–44 (2012)
2. Domínguez Renedo, O., Alonso-Lomillo, M.A., Arcos Martínez, M.J.: Recent developments in the field of screen-printed electrodes and their related applications. *Talanta* **73**(2), 202–219 (2007)
3. Serrano, N., Alberich, A., Díaz-Cruz, J.M., Ariño, C., Esteban, M.: Coating methods, modifiers and applications of bismuth screen-printed electrodes. *Trends Anal. Chem.* **46**, 15–29 (2013)
4. Tyszczyk-Rotko, K., Metelka, R., Vytřas, K.: Screen-printed carbon electrodes modified with lead film deposited using different plating methods as sensors in anodic stripping voltammetry. *Electrochim. Acta* **92**, 335–340 (2013)
5. Bobrowski, A., Królicka, A., Maczuga, M., Zarębski, J.: A novel screen-printed electrode modified with lead film for adsorptive stripping voltammetric determination of cobalt and nickel. *Sens. Actuat. B Chem.* **191**, 291–297 (2014)
6. Bobrowski, A., Kalcher, K., Kurowska, K.: Microscopic and electrochemical characterization of lead film electrode applied in adsorptive stripping analysis. *Electrochim. Acta* **54**(28), 7214–7221 (2009)



Ethanol and Glucose Determination by DCFC Working in Batch or Flow Mode

Mauro Tomassetti^{1,2}(✉), Mauro Castrucci², Emanuele Dell'Aglio²,
Luigi Campanella², Riccardo Pezzilli³, and Corrado Di Natale¹

¹ Department of Electronic Engineering, Tor Vergata University, Via Politecnico 1, Rome, Italy
mauro.tomassetti@uniroma1.it

² Department of Chemistry, La Sapienza University, P.le A. Moro 5, Rome, Italy

³ Department of Industrial Engineering, Tor Vergata University, Via Politecnico 1, Rome, Italy

Abstract. In this note, it has been shown that it is possible to realize a very simple batch, or flow system, which can be used to study and evaluate the conversion of chemical energy into electrical energy, using ethanol, or glucose as fuel and particularly highlighting how the use of ethanol as liquid, or glucose, as solid fuel, can have considerable theoretical importance as well as a significant analytical advantage.

Keywords: Direct catalytic ethanol fuel cell · Direct glucose-DCFC-system · Glucose or ethanol flow analytical measurements · Yeast *saccharomyces cerevisiae* · Energy conversion possibility study

1 Introduction

Several studies have been reported in the literature concerning fuel cells of different types and configurations which carry out the conversion of chemical energy into electrical energy, using hydrogen or more complex compounds as fuel, such as methanol and ethanol, thus realizing direct methanol, or ethanol, fuel cells (DMFC and DEFC, respectively) [1, 2]. Despite liquid fuels, as methanol or ethanol, can be used, transported and stored with relative ease, although these fuels are not without dangers. However, the massive use of these liquid fuels can also produce many drawbacks, both because these fuels are easily flammable, and for the possible environmental damage, which can derive from their massive use, due to the emission of carbon dioxide deriving from its catalytic oxidation, for the production of electricity. So also solid fuels as carbohydrates have been proposed [3]. Therefore, several types of carbohydrates-based fuel cells have been reported in the literature, such as direct abiotic fuel cells which use gold-platinum as a catalyst [4–6]. Among fuel cells, those based on biological processes, are particularly appealing for their inherent sustainability. Enzymatic glucose biofuel cells were for instance fabricated [7, 8], using enzymes such as glucose oxidase and laccase as

electrocatalysts, however they have limited stability [9], moreover because their construction is often not a little complex. Lastly microbial fuel cells have been studied, where the different systems of a whole electroactive micro-organism were used [10, 11]. In these devices, microorganisms are used as the primary engine of biological processes for energy production.

2 Experimental

To carry out the measurements for ethanol, or glucose, the experimental apparatus used are illustrated in detail in the figures shown in the following paragraph, depending on whether ethanol, or glucose is determined and whether it is used in batch, or in flow. In the case glucose was used as fuel, a small 50 mL incubator reactor, containing 30 mL of yeast (0.6 g)-glucose-glycine solution, was kept in a thermostatable apparatus at 28.5 ± 1 °C, for 12 h [12], under cautious agitation. At the end of this time, the solution was aspirated and carefully filtered and let to flow from the reactor, by means of a peristaltic pump (at flux rate 4.0 mL min^{-1}) in the DCFC fuel cell.

The DMFC used fuel cell, HTEC Model F111 (From Fuel Cell Store, TX. USA) was used, Measurements were carried out in Potentiostat mode [13, 14], using a Palmsens mod. EmStat potentiostat (Houten, The Netherlands) and a PStace Software ver. 4.6 data interface to a Compaq Presario. For measurement, the anode potential was automatically set to a value of the Optimized Applied Potential (OAP) [13]. Lastly, the fuel cell current was recorded, reading its value at the steady state.

3 Results and Discussion

Our research group has recently studied and developed ethanol fuel cells, by operating first of all in batch mode (See Fig. 1, upper left). In the present research, however, we have been developed a flow apparatus to operate with these fuel cells also in flow mode (See Fig. 1, lower left).

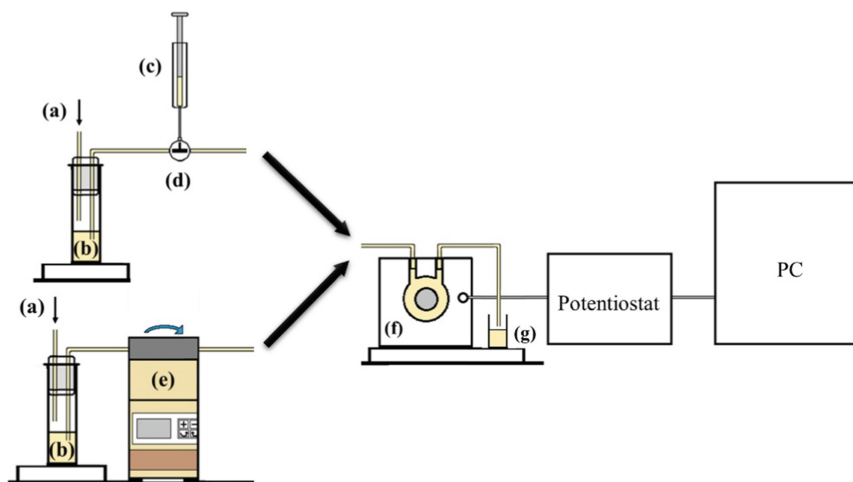


Fig. 1. Ethanol fuel cell, on the right common apparatus, on the upper left: batch experimental apparatus and on the lower left: flow experimental apparatus: (a) inner hydroalcoholic solution; (b) hydroalcoholic solution; (c) graduated syringe; (d) turning tap; (e) peristaltic pump, (f) catalytic fuel cell; (g) draining.

Calibration curves, for ethanol, obtained operating in batch, or flow mode, are reported in Fig. 2.

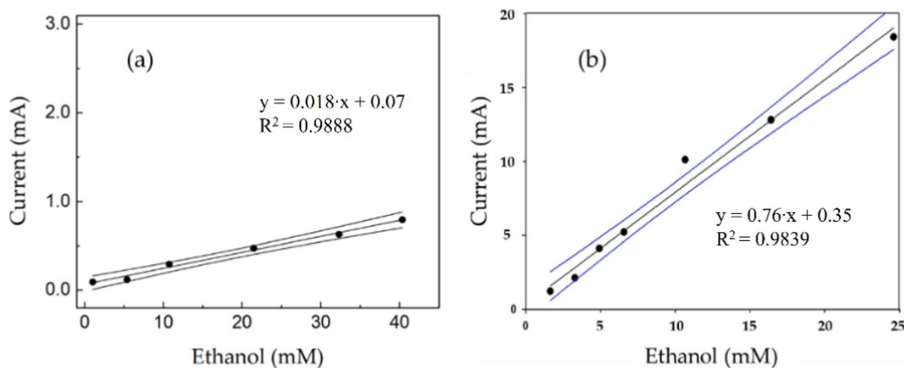
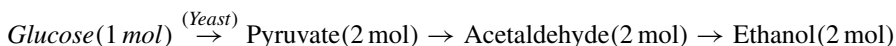


Fig. 2. Ethanol calibration curve, obtained by operating (a) in batch and (b) in flow (4.0 mL min^{-1}) conditions, for increasing ethanol concentrations of the hydroalcoholic solution. Each point is the mean of at least three different determinations.

In addition, in the present research authors investigated the Direct Catalytic Fuel Cell (DCFC) using glucose as fuel for glucose determination (i.e., for analytical purposes), not neglecting also to evaluate the energy production from glucose solution, having the latter a large inherent chemical energy (2.87 MJ mol^{-1}) [4]. For this purpose, glucose fuel cells appeared to be ideal devices, since their introduction, to directly convert chemical energy into electrical energy [9, 15] without generating a relevant pollution.

To this aim, we emphasized the use of a simple commercial DCFC device, coupled with *Saccharomyces Cerevisiae* cells, for analytical purpose, i.e., for glucose determination, and to investigate energy production. We opted for a simpler, more practical, and above all more durable device. The device described in our work involves the use of yeast placed in an external thermostated vessel, in addition to an efficient filtering system that does not allow the penetration of any yeast cells (or other particles) in the anodic compartment of the fuel cell (see Fig. 3, left part).

This makes measures much more repeatable, especially for analytical purposes, and increases the use of the same fuel cell, practically for an unlimited time. In addition, the latter configuration allows to use also simple inexpensive fuel cell available on the market (as in our case). In practice, the system exploited the fermentation reaction induced by yeast cells (*Saccharomyces Cerevisiae* in our case) by converting glucose into ethanol through the following reaction:



The produced ethanol was then used as the actual fuel for the DCFC device, resulting in electric energy. Present note shows that the system can be used both for glucose detection and to estimate the energy production, by working with fuel cell operating both in batch, or in flow mode (see Fig. 3).

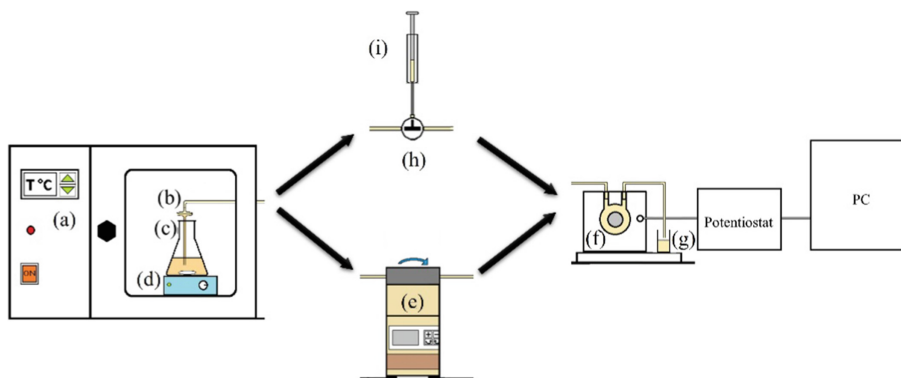


Fig. 3. Yeast-fuel cell left and right common parts of the experimental apparatus. In central part: upper batch and lower flow apparatus, (a) thermostatic apparatus (b) small filter (c) flask containing glucose solution and yeast; (d) magnetic stirrer; (e) peristaltic pump; (f) catalytic fuel cell; (g) draining. (h) turning tap; (i) graduated syringe.

Calibration curves, for glucose, obtained operating in batch, or flow mode, are reported in Fig. 4.

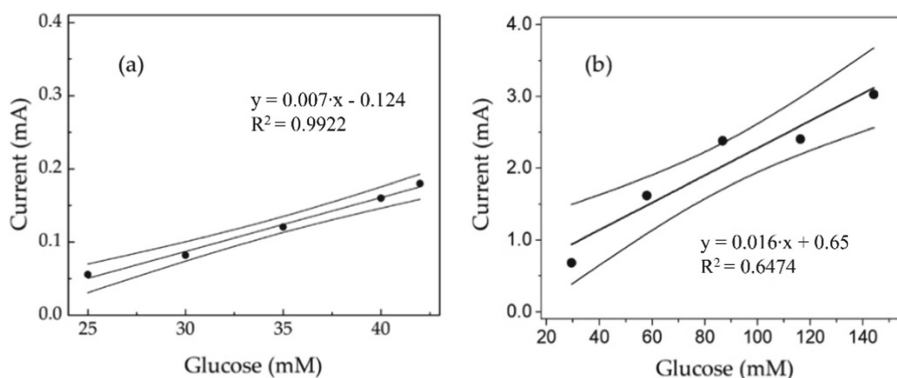


Fig. 4. Glucose calibration curve, obtained by operating (a) in batch and (b) in flow (4.0 mL min^{-1}) conditions, for increasing glucose concentrations. Each point is the mean of at least three different determinations.

Of course, in order to obtain results of a certain interest, it was necessary to optimize a whole series of operating parameters. Moreover, we have shown how the determination of ethanol, but also of glucose, can be performed also in flow, using an apparatus, which allowed to increase the calibration sensitivity of the respective straight lines, if compared with the same ones obtained by operating in batch mode [12, 13], see comparison in Figs. 2 and 4. Finally, it was verified that the system responds, albeit in a different way, also to other carbohydrates, such as sucrose for example; what is of considerable interest, both from an analytic and an energetic point of view. Lastly, from the energy point of view, a rough estimate, based on the measurements carried out, leads to the conclusion that, operating under flow conditions is obtaining a conversion efficiency (\mathcal{E}) about 25% for ethanol fuel and 0.71% for glucose.

4 Conclusion

In conclusion this research has shown how, by operating in flow mode, rather than in batch, it is also possible to have a great advantage, from an analytical point of view, since a considerable increase in the sensitivity of the method can be obtained, probably attributable to a reduction in the effects of poisoning, which, as known [16], can be produced during the operation of the fuel cell, especially when it is desired to carry out the determination of carbohydrates.

References

1. Dillon, R., Srinivasan, S., Aricò, A.S., Antonucci, V.: International activities in DMFC R&D: status of technologies and potential applications. *J. Power Sour.* **127**, 112–126 (2004). <https://doi.org/10.1016/j.jpowsour.2003.09.032>
2. Kirubakaran, A., Jain, S., Nema, R.K.: A review on fuel cell technologies and power electronic interface. *Renew. Sustain. Energy Rev.* **13**, 2430–2440 (2009). <https://doi.org/10.1016/j.rser.2009.04.004>

3. Scott, K., Murano, C.: Microbial fuel cells utilising carbohydrates. *J. Chem. Technol. Biotechnol.* **82**, 92–100 (2007). <https://doi.org/10.1002/jctb.1641>
4. Torigoe, K., et al.: High-power abiotic direct glucose fuel cell using a gold-platinum bimetallic anode catalyst. *ACS Omega* **3**, 18323–18333 (2018). <https://doi.org/10.1021/acsomega.8b02739>
5. Basu, D., Basu, S.: Synthesis and characterization of Pt–Au/C catalyst for glucose electro-oxidation for the application in direct glucose fuel cell. *Int. J. Hydrog. Energy* **36**, 14923–14929 (2011). <https://doi.org/10.1016/j.ijhydene.2011.03.042>
6. Basu, D., Basu, S.: Performance studies of Pd–Pt and Pt–Pd–Au catalyst for electro-oxidation of glucose in direct glucose fuel cell. *Int. J. Hydrog. Energy* **37**, 4678–4684 (2012). <https://doi.org/10.1016/j.ijhydene.2011.04.158>
7. Barelli, L., et al.: Enzymatic fuel cell technology for energy production from bio-sources. Erode, India, p. 020014 (2019)
8. Kizling, M., et al.: Multi-substrate biofuel cell utilizing glucose, fructose and sucrose as the anode fuels. *Nanomaterials* **10**, 1534 (2020). <https://doi.org/10.3390/nano10081534>
9. Brouzgou, A., Tsiakaras, P.: Electrocatalysts for glucose electrooxidation reaction: a review. *Top. Catal.* **58**(18–20), 1311–1327 (2015). <https://doi.org/10.1007/s11244-015-0499-1>
10. Capodaglio, A.G., et al.: Microbial fuel cells for direct electrical energy recovery from urban wastewaters. *Sci. World J.* **2013**, 1–8 (2013). <https://doi.org/10.1155/2013/634738>
11. Slate, A.J., Whitehead, K.A., Brownson, D.A.C., Banks, C.E.: Microbial fuel cells: an overview of current technology. *Renew. Sustain. Energy Rev.* **101**, 60–81 (2019). <https://doi.org/10.1016/j.rser.2018.09.044>
12. Tomassetti, M., Dell’Aglia, E., Castrucci, M., Sammartino, M.P., Campanella, L., Di Natale, C.: Simple yeast-direct catalytic fuel cell bio-device: analytical results and energetic properties. *Biosensors* **11**, 45 (2021). <https://doi.org/10.3390/bios11020045>
13. Tomassetti, M., Angeloni, R., Merola, G., Castrucci, M., Campanella, L.: Catalytic fuel cell used as an analytical tool for methanol and ethanol determination. Application to ethanol determination in alcoholic beverages. *Electrochimica Acta* **191**, 1001–1009 (2016). <https://doi.org/10.1016/j.electacta.2015.12.171>
14. Tomassetti, M., Merola, G., Angeloni, R., Marchiandi, S., Campanella, L.: Further development on DMFC device used for analytical purpose: real applications in the pharmaceutical field and possible in biological fluids. *Anal. Bioanal. Chem.* **408**(26), 7311–7319 (2016). <https://doi.org/10.1007/s00216-016-9795-2>
15. Oncescu, V., Erickson, D.: High volumetric power density, non-enzymatic. Glucose Fuel Cells. *Sci. Rep.* **3**, 1226 (2013). <https://doi.org/10.1038/srep01226>
16. Seiler, T., Savinova, E.R., Friedrich, K.A., Stimming, U.: Poisoning of PtRu/C catalysts in the anode of a direct methanol fuel cell: a DEMS study. *Electrochim. Acta* **49**, 3927–3936 (2004). <https://doi.org/10.1016/j.electacta.2004.01.081>



Voltammetric Determination of H₂O₂ Using a GC-LDH-Proline Catalytic Sensor

Mauro Tomassetti^{1,2}(✉), Riccardo Pezzilli³, Giuseppe Prestopino³, Pier Gianni Medaglia³, and Corrado Di Natale¹

¹ Department of Electronic Engineering, Tor Vergata University, Via Politecnico 1, Rome, Italy
mauro.tomassetti@uniroma1.it

² Department of Chemistry, La Sapienza University, P.le A. Moro 5, Rome, Italy

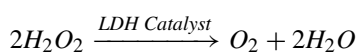
³ Department of Industrial Engineering, Tor Vergata University, Via Politecnico 1, Rome, Italy

Abstract. In our recent work, we built a new catalytic sensor for the determination of hydrogen peroxide, consisting of a glassy carbon (GC) electrode, on which it was glued, by means of a layer of silver paste, a nanomaterial of the type “Layered Double Hydroxide” (LDH), with formula that can be briefly expressed as [Zn^{II}Al^{III}(OH)₂]⁺NO₃⁻ · n H₂O. We have ascertained experimentally that the response of this sensor can be improved if proline is present in the buffer solution.

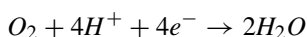
Keywords: LDH catalytic sensor · Cyclic voltametric sensor · Hydrogen peroxide determination · Improvement response using proline

1 Introduction

LDH compounds exhibit a certain catalytic property, towards H₂O₂ [1, 2], according to the following reaction:



which made it possible to build an amperometric electrode, that was recently described by us using this kind [Zn^{II}Al^{III}(OH)₂]⁺NO₃⁻ · n H₂O [3] (see Fig. 1). In fact, the oxygen produced by the catalytic reaction was reduced to cathode, according to the following reaction:



The previous published electrochemical amperometric system [3], from the analytical point of view, showed LOD of the order of about one mmol L⁻¹, a linearity range between about 145 and 1195 mmol L⁻¹, and a rather modest calibration sensitivity, approximately equal to 0.001 mA/mmol L⁻¹.

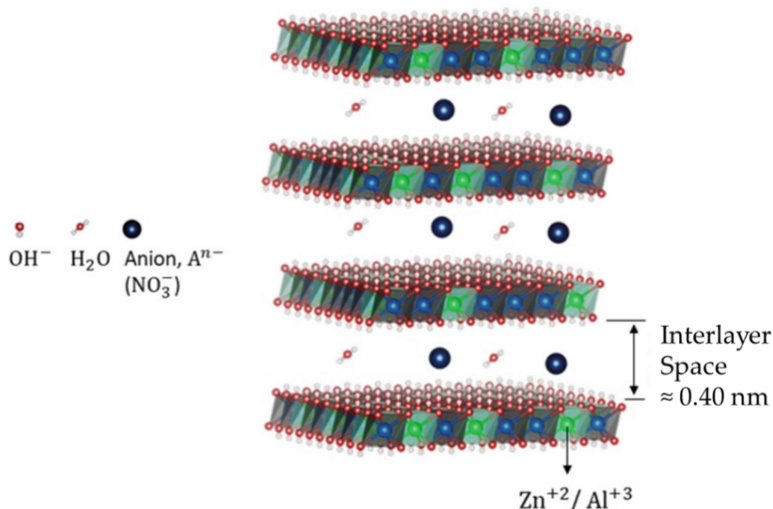


Fig. 1. LDH structure that we used in this research.

Since in a recent article by F. Zhao et al. [4] it has been shown that, in a voltammetric electrode for the determination of hydrogen peroxide, made by means of a system of Ag particles supported by glassy carbon, an increase in sensitivity is obtained following a scan between -0.8 V and $+1.5$ V, performed in a solution of phosphate buffer at pH 7, containing the amino acid proline. It was therefore hypothesized that our GC-Ag paste-LDH sensor, we previously built [3], could also benefit from the presence of this amino acid in solution, i.e., when a similar cyclic voltammetry is carried out, using our sensor, in a phosphate buffer solution (PBS), containing proline, for the determination of H₂O₂ (see Fig. 2).

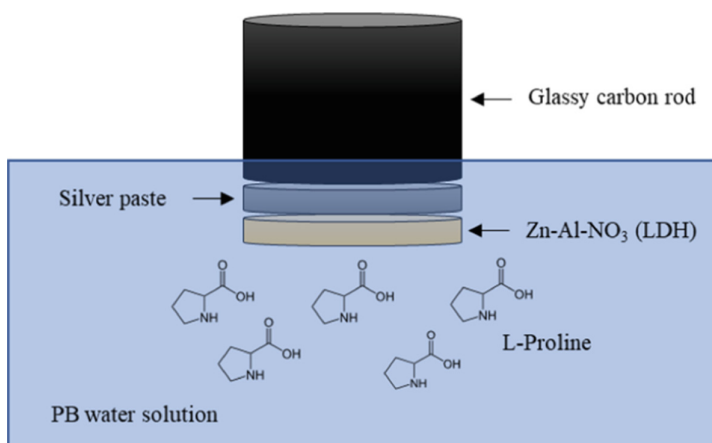


Fig. 2. Construction scheme of GC-Ag (paste)-LDH-proline (in solution).

2 Experimental

The cyclic voltammeteries were conducted in phosphate buffer, at pH 7, and carried out by means of a VersaSTAT3 Potentiostat (AMETEK Scientific Instruments, Princeton, USA), using three electrodes, i.e., a working electrode (modified glassy carbon with silver paste and LDH), an ($\text{Ag}/\text{AgCl}/\text{Cl}^-$) reference electrode and a platinum counter electrode.

3 Results and discussion

To verify the hypothesis above formulated, we carried out cyclic voltammetric experiments with three electrodes system described in the “experimental” section, (see cyclic voltammetric (CV) curves in Fig. 3). From the results of these voltammetries, performed by us, the hypothesis we formulated seems to be confirmed.

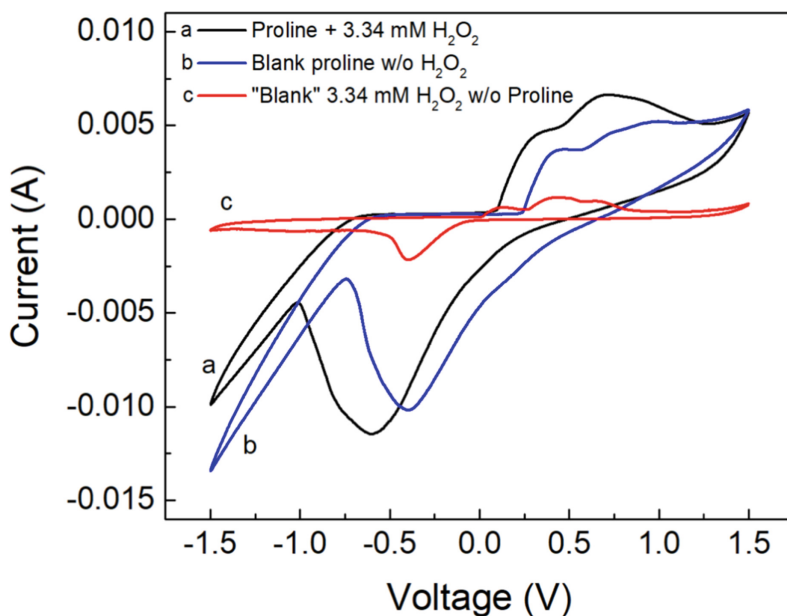


Fig. 3. Cyclic voltammetry of: (a) using GC-Ag(paste)-LDH-Proline (in sol. 20 mM), by H_2O_2 in phosphate buffer with final concentration of 3.34 mM, (b) Blank, with proline, without H_2O_2 in buffer solution, (c) “Blank” CV of 3.34 mM H_2O_2 in buffer solution, without the use of proline, respectively.

We, therefore, after having optimized the quantity of proline to be used, which was found to be 20 mM, have built a calibration curve vs H_2O_2 increasing concentration, obtained by cyclic voltammetry and carried out in the presence of a fixed concentration of proline 20 mM, in phosphate buffer at pH 7, then compared it with the analogous “blank” curve, built in the absence of proline in solution, so obtaining, a curve with a much more pronounced calibration sensitivity (Fig. 4). If compared with the one obtained without the use of proline in solution.

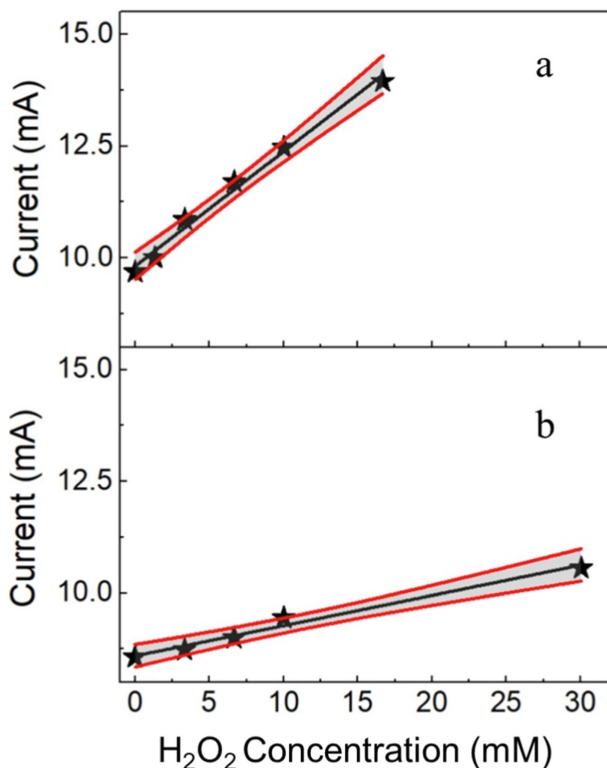


Fig. 4. (a) Straight line interval of CV calibration curve, with 20 mM proline in PBS, increasing H_2O_2 concentration; (b) “Blank” curve in the same condition, without the use of proline in solution.

The calibration curves were obtained by reading the peak current in the cyclic voltammetries, at approximately -0.58 V, i.e., practically the same potential identified by Zhao et al. [4]. Table 1 compares the main analytical data of straight line of the built calibration curve and those of the “Blank” calibration curve, without proline.

Table 1. Comparison of main analytical data of CV calibration curve using 20 mM proline in solution and “Blank” curve.

	Linear regression (y = mA; x = mM)	Linearity range (mM)	R ²	LOD (mM)
CV calibration curve	y = (0.256 ± 0.013)·x + (9.819 ± 0.111)	0-17	0.9899	0.5
“Blank” w/o Proline	y = (0.0676 ± 0.0046)·x + (8.597 ± 0.068)	0-30	0.9822	0.5

4 Conclusion

In conclusion, the hypothesis we formulated seems has been verified, i.e., working in the presence of proline, there are analytical advantages in the determination of H₂O₂, with respect to the determination that it is possible to make with the catalytic-amperometric sensor developed in the previous work without proline in solution [3]; in fact, this allows analytical determinations of hydrogen peroxide concentrations with higher sensitivity and with LOD that is much lower than that of the previous amperometric system, developed in the absence of proline [3]. This is certainly a considerable advantage since, in many real samples, it is often necessary to perform hydrogen peroxide determinations, at low cost and at extremely low concentrations of H₂O₂, without employing, for instance, an enzymatic system, which use is often very valid, but also much more expensive [3, 5].

As regards the mechanism of action of proline, it could be the very simple one already suggested by Zhao et al. [4], but perhaps even more complex [6]. This will have to be verified with running suitable experimental tests.

References

- Xu, L., Lian, M., Chen, X., Lu, Y., Yang, W.: Amperometric sensing of hydrogen peroxide via an ITO electrode modified with gold nanoparticles electrodeposited on a CoMn-layered double hydroxide. *Microchim. Acta* **184**(10), 3989–3996 (2017). <https://doi.org/10.1007/s00604-017-2428-4>
- Heli, H., Pishahang, J., Amiri, H.B.: *J. Electroanal. Chem.* **768**, 134–144 (2016). <https://doi.org/10.1016/j.jelechem.2016.01.042>
- Tomassetti, M., Pezzilli, R., Prestopino, G., Di Natale, C., Medaglia, P.G.: *Microchem. J.* **170**, 106700 (2021). <https://doi.org/10.1016/j.microc.2021.106700>
- Zhao, F., Zhou, M., Wang, L., Huang, Z., Chu, Y.: *J. Electroanal. Chem.* **833**, 205–212 (2019). <https://doi.org/10.1016/j.jelechem.2018.11.050>
- Tomassetti, M., Pezzilli, R., Prestopino, G., Di Biagio, F., Di Natale, C., Medaglia, P.G.: *Processes* **9**, 1878 (2021). <https://doi.org/10.3390/pr9111878>
- Asif, M., et al.: *Biosens. Bioelectron.* **97**, 352–359 (2017). <https://doi.org/10.1016/j.bios.2017.05.057>



Colorimetry by a Smartphone

Leonardo Ciaccheri^(✉), Barbara Adinolfi, Andrea A. Mencaglia,
and Anna G. Mignani

CNR-Istituto di Fisica Applicata “Nello Carrara”, Sesto Fiorentino, FI, Italy
l.ciaccheri@ifac.cnr.it

Abstract. A smartphone has been used for colorimetry, both by means of the built-in camera and by means of a clip-on dispersive grating. Certified colorimetric samples provided by Labsphere® and several samples of cloth fabrics with a palette of the most common colors were considered as test samples. Color measurements directly performed by means of the smartphone camera alone were obtained using the “RGB Detector” App, downloaded from the Google Play Store. More precise measurements were obtained by means of the commercially-available GoSpectro grating and related App. In both cases, in order to quantify the reliability of smartphone-based color measurements, the CIELab color difference ΔE between the certified and smartphone-measured colors were calculated, and are reported in the paper.

Keywords: Colorimetry · Spectroscopy · Smartphone

1 Introduction

A smartphone has a built-in white LED light and a camera. Consequently, it can be conveniently used as a colorimeter. Indeed, simply shining the LED light on a sample and detecting the reflected light it is possible to achieve a good colorimetric assessment. More precise colorimetric measurements can be achieved by adding in front of the camera a dispersive grating while using the smartphone camera as a detector.

There are many applications where color measurements performed by a highly portable and lightweight device such as a smartphone are considered an asset, in [1, 2]:

- Production systems: for quality control, for example in the textile dyeing industry, or for the online condition monitoring of lubricant oils in turbines, compressors and large machinery;
- Food control: for example, fruit ripening, and the detection of nutraceutical indicators (polyphenols, lycopene, fatty acids...) for online labelling the antioxidant capacity of food;
- Large pools of artisans and consumers who need to obtain information on the composition or nature of various materials: varnishes, dyes, bricolage, etc.;
- Environmental sector: for interrogating sensors of pollutants that make use of transducers with color response;

- Reading of test-strips used as indicators of various chemical parameters of environmental interest or for biomedical applications [3, 4].

This paper shows the results achieved when the smartphone is used as a colorimeter in two cases: 1) by means of the built-in white LED and camera as source and detector, respectively, and 2) by using a dispersive grating clipped on the camera for more precise measurements.

2 Samples and Smartphone Setups

Eight certified colorimetric tiles provided by Labsphere® and twelve samples of cloth fabrics with a palette of the most common colors were considered as test samples. These samples are shown in Fig. 1, together with the codes for their identification. Also, the colors of fabrics were previously certified by means of conventional spectrophotometric measurements. In practice, for all samples, the reference tristimulus coordinates were available, so that it was possible to compare the measured values with the reference ones.



Fig. 1. Test samples: LabSphere® color standards (left) and cloth fabrics (right) – tables of codes.

Reflection measurements were performed either by using the smartphone camera alone, and by clipping on the camera the commercially available GoSpectro grating, shown in Fig. 2-left [5]. A Spectralon sample was used as reference.

Figure 2 shows both setups, making use of the smartphone camera alone, and equipped by the grating tool, respectively. A 3D-printed plastic holder was used to hold the smartphone while keeping the same sample-smartphone distance during the color measurements, also allowing to use the touch screen for operation.

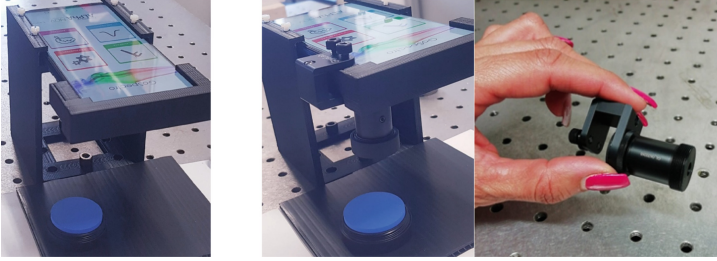


Fig. 2. Setups for color measurements by means of the smartphone alone (left) and of the clip-on grating (center) – the GoSpectro clip-on grating (right).

3 Results of Colorimetric Measurements

Reflection measurements were performed either by using the smartphone camera alone, or by clipping on the camera the GoSpectro grating. In the former case the red, green, and blue outputs of the video camera were converted into RGB coordinates by the “RGB Detector” App, downloaded from the Google Play Store. They were then transformed into tristimulus XYZ coordinates by means of a conversion matrix shown in Eq. 1 (conversion coefficients rounded at the 3rd decimal digit) [6]:

$$\begin{bmatrix} X \\ Y \\ Z \end{bmatrix} = \begin{bmatrix} 0.412 & 0.358 & 0.180 \\ 0.213 & 0.715 & 0.072 \\ 0.019 & 0.119 & 0.950 \end{bmatrix} \begin{bmatrix} R \\ G \\ B \end{bmatrix} \quad (1)$$

With GoSpectro instead, the color functionality of the camera was not used: it was the column of CCD array on which the light was focused that determined the wavelength. The wavelength scale was calibrated by using the spectral lines of a fluorescent lamp, and the red, green, and blue outputs of the whole CCD column were summed up to get the corresponding intensity. The XYZ tristimulus coordinates were obtained by the Eq. (2):

$$X = K \int_{780}^{380} L(\lambda)x(\lambda)d\lambda \quad Y = K \int_{780}^{380} L(\lambda)y(\lambda)d\lambda \quad (2)$$

$$Z = K \int_{780}^{380} L(\lambda)z(\lambda)d\lambda$$

where L is the luminance spectrum given by Eq. (3):

$$L(\lambda) = T(\lambda)L_{D65}(\lambda) \quad (3)$$

being T the transmittance (reflectance) spectrum, and L_{D65} the luminance spectrum of D65 standard illuminance, which is downloadable from CIE website [7]. Finally, in both cases, the CIELab coordinates L^* (clarity), a^* (red-green balance), b^* (blue-yellow balance), and the color difference ΔE were computed by the Eqs. (4) and (5), respectively:

$$L^* = 116 \left(\frac{Y}{Y_n} \right)^{1/3} - 16$$

$$a^* = 500 \left[\left(\frac{X}{X_n} \right)^{1/3} - \left(\frac{Y}{Y_n} \right)^{1/3} \right] \quad b^* = 500 \left[\left(\frac{Y}{Y_n} \right)^{1/3} - \left(\frac{Z}{Z_n} \right)^{1/3} \right] \quad (4)$$

$$\Delta E^* = \left(\Delta L^{*2} + \Delta a^{*2} + \Delta b^{*2} \right)^{1/2} \quad (5)$$

where $\Delta L^* = L_2^* - L_1^*$, $\Delta a^* = a_2^* - a_1^*$, $\Delta b^* = b_2^* - b_1^*$ were the CIELab vectors (L_1^*, a_1^*, b_1^*) and (L_2^*, a_2^*, b_2^*) of the reference and measured colors, respectively.

Table 1 summarizes the results achieved. As expected, the best results were obtained by using the grating. However, also using the smartphone camera alone, acceptable results were obtained, especially considering that simply using the smartphone is a very basic measurement, and that in many cases a quick color evaluation is more than enough.

Table 1. Differences between certified and smartphone-based color measurements.

Codes	ΔE^* RGB	ΔE^* GoSpectro	Codes	ΔE^* RGB	ΔE^* GoSpectro
Red	62	11	BK	79	26
Green	45	22	BL	75	38
Blue	40	19	BR	77	43
Yellow	35	12	BW	65	36
Cyan	39	16	DP	70	41
Orange	37	5,1	DR	74	39
Purple	47	18	EB	68	46
Violet	44	18	GR	73	43
			LB	67	39
			MU	62	56
			OR	71	53
			TO	73	42
MEAN	44	15		71	42

The main reason why the smartphone camera alone provides worse results is that RGB to XYZ conversion matrix requires the RGB measurement are made by using a standard D65 illuminant, which is usually not the case. On the contrary, the measurements achieved by using the GoSpectro grating do not suffer of this problem, because the reflectance spectrum does not depend on the light source. Multiplying this reflectance spectrum by the spectrum of D65 illuminant, which can be downloaded from CIE website (together with XYZ functions), the correct tristimulus coordinates can be calculated.

A source of error when using the GoSpectro grating comes from the fact that the 380–400 nm and 700–780 nm bands are not adequately covered by our light source. However, this is not the main cause, because these missing bands should affect mainly blue and red colors. Red and orange tablets show the lowest color differences instead.

Another cause or error could be given by the white reference spectrum. If it has not a truly flat spectrum, it could distort the reflectance spectrum. Moreover, an excessive illumination could bring some parts of the CCD array close to saturation, determining a nonlinear response. Further studies are currently ongoing on this point.

4 Conclusions and Perspectives

A smartphone was used for colorimetry, either using the built-in camera, and by means of a commercially-available clip-on grating. Certified color standards and cloth fabrics were measured, and the smartphone-measured tristimulus coordinates were compared with the certified values.

Although measurements with the same precision of a spectrophotometer could not be achieved, surely noteworthy is the importance of having a portable, inexpensive, non-destructive, and easy-to-use sample analysis system that allows to obtain information on a sample in real time. This could be of help in many areas, for example in production systems as well as in the quality control of the textile dyeing industry. Another area where smartphone-based systems could be useful is certainly the agriculture sector. For example, a recurring problem in the oil sector is the need to choose the right time for the olive harvest. This is one of the key elements that plays a decisive role on the quality of the oil, and which so far is left only to the experience of the grower. Indeed, the smartphone could certainly give a significant contribution to this application, thus opening new approaches to a wide class of problems.

As almost everyone has a smartphone in the pocket, colorimetric-based measurements has the potential to open-up new applications in citizen science. Indeed, the participation of the population is expected to grow in the coming years, and simple tools are required by the community for data collection and volunteer mapping. A straightforward example could be the data collection for marine and environmental research addressed to the protection of the ecosystem by means of an integrated and synergic scientists-citizens action.

References

1. Ohta, N., Robertson, A.: Colorimetry: Fundamentals and Applications. John Wiley & Sons Inc., Chichester UK (2006)
2. Malacara, D.: Color Vision and Colorimetry: Theory and Applications. SPIE, Bellingham WA (2011)
3. Balbach, S., et al.: Smartphone-based colorimetric detection system for portable health tracking. *Anal. Methods* **13**, 4361–4369 (2021)
4. Aydindogan, E., Ceylan, A.E., Timur, S.: Paper-based colorimetric spot test utilizing smartphone sensing for detection of biomarkers. *Talanta* **208**, 120446 (2020)
5. GoSpectro Homepage (2022). <https://gospectro.eu/gospectro-2/>. Accessed 10 Oct 2022
6. Ocean Optics Homepage. <https://www.oceanopticsbook.info/view/photometry-and-visibility/from-xyz-to-rgb>. Accessed 10 Oct 2022
7. CIE Homepage. <https://cie.co.at/node/2>. Accessed 10 Oct 2022



Nafion-Based Chipless RFID Humidity Sensor for Smart Tag Applications

Giada Marchi^{1,3}, Viviana Mulloni¹(✉), Massimo Donelli², and Leandro Lorenzelli¹

¹ Sensors and Devices, Fondazione Bruno Kessler, Trento, Italy
mulloni@fbk.eu

² Department of Civil, Environmental and Mechanical Engineering, University of Trento,
Trento, Italy

³ Department of Information Engineering and Computer Science, University of Trento, Trento,
Italy

Abstract. —A humidity sensor based on frequency-domain microwave chipless technology is studied and experimentally characterized in this paper.

The chipless microwave sensor is composed of a microwave resonator coupled with a 50 Ω microstrip transmission line, covered with a 180 μm -thick Nafion layer, which acts as sensitive material. The response of the sensor at 25 $^{\circ}\text{C}$ and for a relative humidity (RH) variation in the range of 0–40% has been experimentally assessed. The sensor shows good sensitivity both in terms of frequency and intensity variations and good linearity. The sensor follows the RH variations in a fully reversible way and the response time is estimated in a few seconds.

Keywords: Chipless RFID sensors · Microwave systems · Humidity sensor · Sensing materials · Nafion

1 Introduction

In the last few years, chipless radio frequency identification (RFID) solutions have been proposed as frontier technologies able to merge the advantages of chipped RFIDs with the low cost of barcodes. Chipless RFID systems are generally composed of a passive tag and a readout architecture that exploit non-line-of-sight wireless principles to communicate. At the same time, the prices of chipless RFID tags are very attractive for the market if compared with those of corresponding chipped counterparts.

Chipless RFIDs are very cheap because the tag manufacturing process can be made compatible with low-cost mass production printing techniques by removing the silicon chip and encoding the identification information directly in the physical structure of the tag [1]. However, to transform this highly-promising technology into marketable applications some open challenges, related to coding capability and limited reading distance still need to be solved [2, 3].

A typical chipless RFID tag is composed of a series of conductive resonators on a dielectric substrate and the information is encoded in the resonance peaks that they generate in the time or frequency domain. This particular structure makes these devices

very good candidates for smart labels by combining their remote identification feature with sensing properties [4, 5]. Encoders in the frequency domain can be turned into sensors by adding a suitable layer of sensing material covering one or more of the metallic resonant structures. This layer interacts with a specific physical parameter or chemical substance present in the environment and modifies accordingly the amplitude and the frequency of the encoding resonance peak.

In this work, we will focus on the realization of a smart chipless sensor for relative humidity (RH) monitoring. Recent works on RH detection have widely investigated the performance of sensitive materials such as polyvinyl-alcohol (PVA), Kapton, or even common paper [6–8]. A demonstration of the humidity sensitivity in chipless solutions has also been reported for graphene oxide [9], silica-gel [10], and silicon nanowires [11].

The sensitive material considered in this work is Nafion 117 [12, 13], an ion-exchange polymer well-known for its consolidated use in fuel cells but seldom investigated for chipless humidity sensing applications. This material is readily available in large quantities, is functionally and mechanically stable, resistant to many chemicals and temperature variations, and, most importantly, shows a very high tendency to absorb water from the environment. All these characteristics make Nafion 117 a very suitable candidate for humidity sensing. In fact, this material not only shows a great affinity to water but is also far more sensitive than Kapton. When compared to PVA and common paper, Nafion 117 shows comparable or better sensitivity, better mechanical properties, and works in a totally reversible way.

In the following, we report the results obtained for a microstripped-ELC resonator that can be used as an efficient humidity sensor when covered with a 180 μm -thick layer of Nafion 117.

2 Sensor Simulation, Fabrication, and Measurement Set-Up

The microwave resonator structure employed in this study is that of a typical ELC resonator, widely used in microwave sensing and metamaterial configurations [12]. The resonator is square-shaped and the lateral dimensions are 1.1 mm. The geometry specifications are detailed in [12]. The resonator is then gap-coupled with a microstrip line, and a picture of the real device is shown in Fig. 1. The insertion loss of the resonator was simulated as a function of RH assuming that the dielectric properties of Nafion (dielectric constant and loss tangent) increase as the absorbed water increases, as reported in the literature [14]. The simulation results showed a marked frequency shift and a broadening of the resonance peak with increasing humidity. The resonator used for the experimental characterization, reported in Fig. 1, is fabricated by Computer Numerical Control (CNC) milling on a standard RO4003C substrate with 17 μm -thick copper metallization. Its bare fundamental resonance frequency is 2.78 GHz, which matches the simulated structure. The measurement setup is composed of the sensor prototype connected through two SubMiniature version A (SMA) coaxial connectors to a Vector Network Analyzer (VNA), which acquires the insertion loss values, and a climatic chamber, which controls the environmental humidity, while the temperature was set to 25 °C.

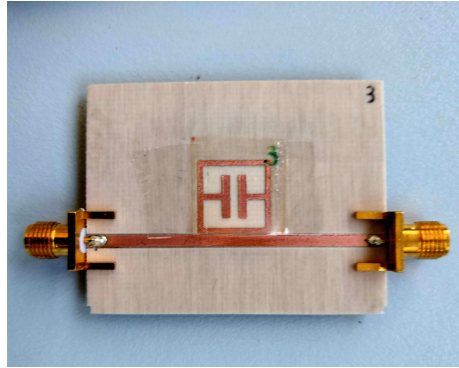


Fig. 1. Microstripped ELC resonator covered with a layer of Nafion 117 and equipped with two SMA connectors.

3 Sensor Experimental Characterization

The results of the measurements at different RH values are shown in Fig. 2. The presence of the Nafion layer above the resonator results in any case in a negative shift compared to the bare frequency of the resonator at 2.78 GHz. As can be seen, as the humidity increases, the negative shift increases and the peaks broadens. The intensity and frequency shift variations for some RH values are reported in Fig. 3.

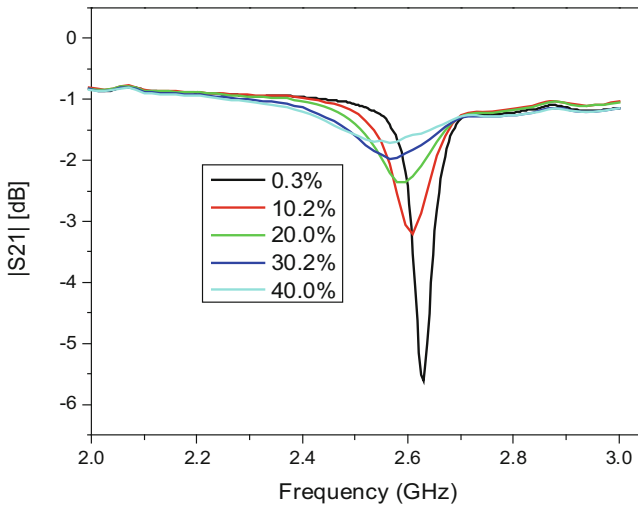


Fig. 2. Resonance peak of the resonator in Fig. 1 at different RH values.

The intensity variations are especially evident at low humidity values, whereas the frequency shift as a function of RH is linear in the range of 0.3–40% RH. Outside this range, the linearity is lost and the peak intensity is quite low (data not shown). Both trends are coherent with the simulation predictions. However, while the bare resonator could be simulated to match perfectly the experimental resonance frequency, the uncertainty of the Nafion dielectric parameters as a function of humidity and the presence of a thin adhesive layer between the resonator and the sensitive layer are probably the reasons why the agreement between simulation and measurements is not quantitatively perfect.

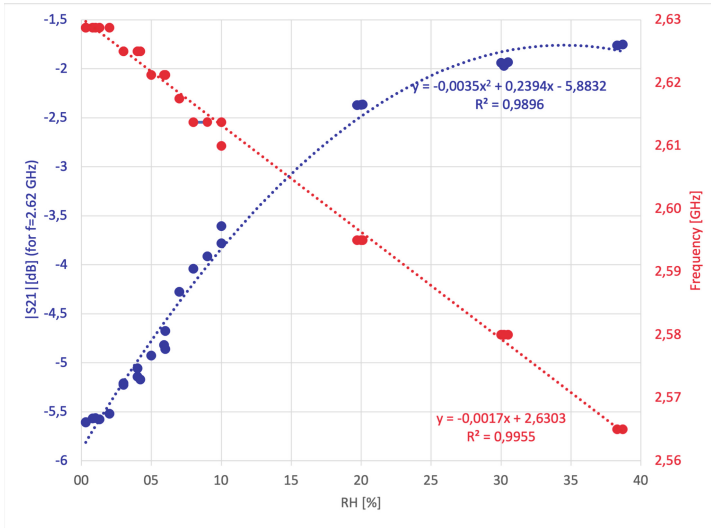


Fig. 3. Frequency (red) and intensity (blue) of the resonance peak of the resonator in Fig. 1 at different RH values. R^2 indicated the square of the Pearson correlation coefficient of the fit.

Cycling measurements in the range of 10–50% were also performed, to verify the response time and the reversibility of the sensor. The results are reported in Fig. 4. The sensor is following perfectly the RH variations of the climatic chamber and the response time is estimated to be around a few seconds, with the desorption phase slower than the absorption phase. No sensitivity degradation was detected after multiple cycles. The noise in the 50% RH plateau is due to the low intensity at 2.625 GHz at this RH value, which is outside the RH range covered in Fig. 3. It should be noted that the data reported in Fig. 3 are the peak intensity and frequency, while in Fig. 4 the intensity at fixed frequency is reported. The sensor can therefore be used in two different ways: as a dual-parameter sensor, requiring a frequency scan in the range of interest, or as a single-parameter sensor, registering the peak intensity at a fixed frequency.

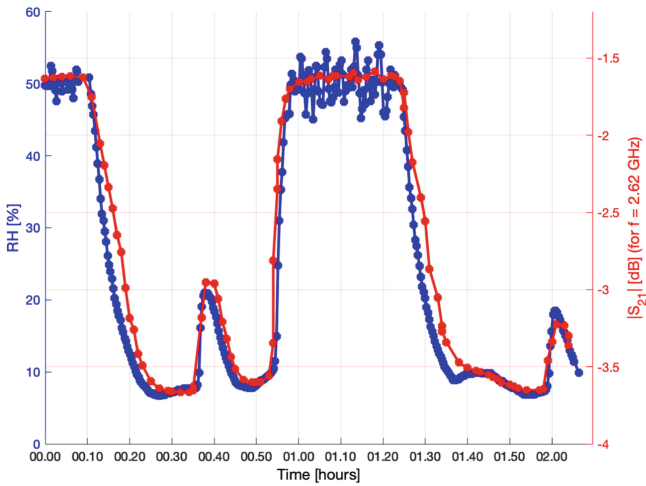


Fig. 4. Sensor signal intensity variation at 2.62 GHz (blue dots) compared with the corresponding RH value obtained by the climatic chamber (red dots).

4 Conclusions

The sensor performances demonstrate the applicability of Nafion membranes for humidity detection using chipless microwave sensors and their suitability for humidity detection in smart packaging applications or wireless multi-parametric sensing, where its low cost compared to more expensive chipped alternatives is a great advantage. Moreover, the design parameters can be easily adjusted to switch from the current resonance frequency range to a working frequency included in an ISM band. This will open the way to simpler integration with standard RFIDs systems or RF operating technologies. The working range can be easily extended outside 0–40% RH varying the Nafion layer thickness. Further investigations to optimize the sensor sensitivity are in progress. Future work will focus on improving the range for remote detection by working on the tag structure surrounding the resonator and on the applicability of this sensing and transduction mechanism to the detection of other environmental parameters.

References

1. Vena, A.: *Chipless RFID Based on RF Encoding Particle: Realization, Coding, Reading System; Remote Identification Beyond RFID*. Elsevier, London (2016)
2. Mulloni, V., Donelli, M.: Chipless RFID sensors for the Internet of Things: challenges and opportunities. *Sensors* **20**, 2135 (2020)
3. Herrojo, P., Mata-Contreras, M.: Chipless-RFID: a review and recent developments. *Sensors* **19**, 3385 (2019)
4. Dey, S., Saha, J.K., Karmakar, N.C.: Smart sensing: chipless RFID solutions for the internet of everything. *IEEE Microwave Mag.* **16**, 26–39 (2015)
5. Karmakar, N.C., Amin, E.M., Saha, J.K.: *Chipless RFID Sensors*. Wiley, New York (2016)
6. Amin, E.M., Karmakar, N.C., Winther-Jensen, B.: Polyvinyl-alcohol (PVA)-based RF humidity sensor in microwave frequency. *PIER B* **54**, 149–166 (2013)

7. Amin, E.M., Karmakar, N.C.: Development of a low cost printable humidity sensor for chipless RFID technology. In: Proceedings of the 2012 IEEE International Conference on RFID-Technologies and Applications (RFID-TA), pp. 165–170 (2012)
8. Feng, Y., Xie, L., Chen, Q., Zheng, L.-R.: Low-cost printed chipless RFID humidity sensor tag for intelligent packaging. *IEEE Sensors J.* **15**, 3201–3208 (2015)
9. Athauda, T., Karmakar, N.: Screen printed chipless RFID resonator design for remote sensing applications. In: Proceedings of the 2018 IEEE Asia-Pacific Microwave Conference (APMC), pp. 1321–1323 (2018)
10. Abbasi, Z., Shariaty, P., Hashisho, Z., Daneshmand, M.: SilicaGel-integrated chipless RF tag for humidity sensing. In: Proceedings of the 2018 IEEE 18th International Symposium on Antenna Technology and Applied Electromagnetics (ANTEM), pp. 1–2 (2018)
11. Vena, A., Perret, E., Kaddour, D., Baron, T.: Toward a reliable chipless RFID humidity sensor tag based on silicon nanowires. *IEEE Trans. Microwave Theory Tech.* **64**, 2977–2985 (2016)
12. Marchi, G., Mulloni, V., Manekiya, M., Donelli, M., Lorenzelli, L.: A preliminary microwave frequency characterization of a nafion-based chipless sensor for humidity monitoring. In: Proceedings of the 2020 IEEE SENSORS, pp. 1–4 (2020)
13. Marchi, G., Mulloni, V., Hammad Ali, O., Lorenzelli, L., Donelli, M.: Improving the sensitivity of chipless RFID sensors: the case of a low-humidity sensor. *Electronics* **10**, 2861 (2021)
14. Paddison, S.J., Bender, G., Kreuer, K.-D., Nicoloso, N., Zawodinski Jr. T.A.: The microwave region of the dielectric spectrum of hydrated Nafion® and other sulfonated membranes. *J. New Mater. Electrochem. Syst.* **3**, 293–302 (2000)



Metal Nanoparticles on Board of Low-Cost Devices for Optical Sensing

Annalisa Scroccarello^(✉), Filippo Silveri, Flavio Della Pelle, and Dario Compagnone

Department of Bioscience and Technology for Food, Agriculture and Environment, University of Teramo, Via Renato Balzarini 1, 64100 Teramo, Italy
ascroccarello@unite.it

Abstract. Nowadays nanomaterials (NMs) have become consolidated building blocks for (bio)sensors and (bio)sensing strategies development. In this contest, the metal nanoparticles (MNPs) offer infinite opportunities since their nano-domain provides unique chemical, physical, electrical, and optical features; the most captivating MNPs' property is the localized surface plasmon resonance (LSPR), which allows them to interact with the electromagnetic radiation, giving rise to typical absorption spectra and naked eye visible colors. Taking advantage of the aforementioned features MNPs have been extensively exploited in the development of optical and colorimetric point-of-need devices.

Herein, device equipped with plasmonic-active thin films of MNPs (gold/Au and silver/Ag nanoparticles/NPs) are presented, suitable for opto-analytical applications. The nanoarchitecture fabrication has been achieved onto ELISA plates. The nano-film was tested as a plasmonic transducer in ELISA plate to evaluate the oxidants capacity of sodium hypochlorite, sodium nitrite, ABTS, H₂O₂, AAPH, DPPH, and ferrous sulfate which are of biological and biochemical interests. Further, life-time studies of the proposed nanoarchitecture were carefully performed with the aim to evaluate the storability of the nano-equipped ELISA plates.

Keywords: AgNPs · AuNPs · Bimetallic nanostructure · Plasmonic-active thin-film · Disposable device · In-situ analysis

1 Introduction

Oxidants represent a wide class of compounds of chemical, biochemical, biomedical, and biological interest [1, 2]. Oxidants enclose radical species and stronger electron acceptors; among the oxidant agents, hydrogen peroxide (H₂O₂) is the most representative compound, belonging to the reactive oxygen species [1]. However, historically known oxidant species are the ABTS, DPPH and AAPH radical species commonly used for in-vitro study and assays [3–5]; further, in the past years, new oxidant species gain increasing interest in the scientific community as the sodium hypochlorite (NaClO) because of its use as disinfectant in the COVID-19 pandemic [2]. Thus, the interest for rapid and easy-to-use methodologies for oxidant species detection is still of primary importance [1, 2]. Nanomaterials (NMs) are widely used to develop analytical strategies

to monitor the oxidants species [1, 2]. Several chemiluminescence, fluorescence, and electrochemical-based approaches have been reported in the literature; anyway, the use of biological components (i.e., cells and enzymes) or external probes (i.e., dyes, etc.) are required [1]. Recently, NMs-based optical/colorimetric sensing strategies represent a great alternative to the previous approaches, because of the simple use and easy signal assessment (i.e., visual assessment). In this field, metal nanoparticles (MNPs) are widely used for optical and colorimetric strategies as nano-indicators because of their outstanding optical features; the MNPs are able to interact with the electromagnetic radiation in the Uv-Visible region giving rise to the localized plasmon resonance phenomena (LSPR), resulting in a visible color dependent on the MNPs composition, size, shape, surface doping/functionalization, and interparticle distance [1–3]. Further, the MNPs are easy to synthesize by simply employing a metal precursor and a natural or chemical reducing agent, making them appealing for the design of new analytical colorimetric strategies.

Herein, different oxidant agents (i.e., H_2O_2 , NaClO , NaNO_2 , FeSO_4 , ABTS, DPPH, and AAPH) have been evaluated by using a plasmonic-active nanostructured thin-film decorated with gold and silver nanoparticles (AuNPs and AgNPs, respectively), fabricated onto a commonly used optical tool, the ELISA plate. The sensing strategy relies on the etching phenomenon, the selective oxidation of AgNPs driven by the oxidant agents returning in a quantitative LSPR variation of the nanostructured thin film.

In addition, the analyzed oxidant agents have been characterized and classified according to their oxidant capacity/reactivity thanks to metrological indexes herein proposed, and further studies have been conducted to define the life-time of the proposed nanocomposite platform. The experimental theme of this work is part of a broader project of characterization of analytical tools user-friendly and suitable for in-field analysis for which it is necessary to still define the horizons and boundaries.

2 Materials and Methods

2.1 Reagents and Apparatus

Dopamine hydrochloride (DA), hydrogen tetrachloroaurate (Au(III)), silver nitrate (Ag(I)), sodium hydroxide, sodium acetate anhydrous, sodium phosphate monobasic monohydrate, sodium phosphate dibasic anhydrous, trizma hydrochloride, hydrogen peroxide solution (H_2O_2 , 30% v/v), sodium hypochlorite (NaClO), sodium nitrite (NaNO_2), Ferrous Sulfate (FeSO_4), 2,2'-azino-bis(3-ethylbenzothiazoline-6-sulphonic acid) (ABTS), 2-difenil-1-piciridrazile (DPPH), 2,2 azobis 2 amidinopropane dihydrochloride (AAPH), and methanol were purchased from Sigma-Aldrich (St Louis, MO, USA). Catechin (CT) was purchased from Extrasynthese (Genay, France). Nunc-Immuno MicroWell MaxiSorp (96-well) solid ELISA plates (EPs) were purchased from Sigma-Aldrich (St Louis, MO, USA). Stock solutions of 10 mM CT was prepared in methanol and stored at $-20\text{ }^\circ\text{C}$ in the dark. The absorbance spectra of the modified ELISA plates were recorded using an EnSpire 2300 Multilabel Reader from PerkinElmer (Turku, FI) with a resolution of 5 nm in the λ range 320–800 nm.

2.2 Nanostructured Plasmonic-Active Film Fabrication

The nanostructured plasmonic-active film synthesis was carried out according to Scroccarello *et al.* [1] as reported below:

- *PDA thin-film formation*: 0.5 g L⁻¹ DA was freshly prepared in Trizma buffer (10 mM, pH 8.5) and promptly used to fill EP microwells (200 μL for well). DA polymerization was carried out under static condition at room temperature for 15 h, in a white incubation chamber, using a warm light source (20 W light bulb), placed at 50 cm of distance. DA polymerization was blocked by emptying the microwells and abundantly washing them with Milli-Q water.
- *AuSD self-formation*: PDA-modified EP wells were filled with 200 μL of 250 μM Au(III) aqueous solution and incubated for 8 h in the dark and at room temperature. The reaction was blocked by emptying the microwells and abundantly washing with Milli-Q water.
- *AuSD functionalization*: PDA@AuSD modified microwells were filled with 150 μL of acetate buffer (10 mM; pH 4.0), 10 μL of 20 mM Au(III) and 40 μL of 1 mM catechin (CT). The reaction was carried out in static condition for 1 h, in the dark and at room temperature. The reaction was blocked by emptying the microwells and abundantly washing them with Milli-Q water.
- *AgNPs-nanonetwork formation*: The PDA@AuNPs-CT modified microwells were filled with 185 μL of Milli-Q water and 10 μL of 20 mM Ag(I), afterward 5 μL of 4 M NaOH was added. The reaction was carried out under stirring condition by orbitally shaking (SSL1, Stuart equipment, Belfast, UK150) at 150 rpm at room temperature, in the dark, for 6 h. The reaction was blocked by emptying the microwells and abundantly washing them with Milli-Q water.

2.3 Oxidants Capacity Evaluation

The oxidant agents H₂O₂, NaClO, NaNO₂, FeSO₄, ABTS, DPPH, and AAPH were freshly prepared in phosphate buffer (PB, 10 mM, pH 7.0) before use. The PDA@AuNPs-CT@AgNPs modified wells were filled with 180 μL of reaction solvent (Table 1) and 20 μL of oxidant agent standard (diluted in the respective reaction solvent) to reach a final assay volume of 200 μL.

The reaction mix was orbitally shaken (60 rpm) for 40 min at controlled temperature (Table 1) in the dark. For FeSO₄ and AAPH different incubation times and temperatures were tested.

The reaction was blocked by emptying the microwells and abundantly washing them with Milli-Q water. The absorbance was recorded at $\lambda = 405$ nm in Milli-Q water before (pre-etching) and after (post-etching) the reaction.

Table 1. Oxidant agents reaction conditions and tested oxidants' concentration ranges.

Oxidants	Reaction solvents	pH	Temperature °C	Time min	[C] μmol L ⁻¹
H ₂ O ₂	PB	7	30	40	10-200
NaClO	PB	7	30	40	50-900
NaNO ₂	PB	7	30	40	5-1500
	AB	4	"	"	"
FeSO ₄	PB	7	30	40	10-5000
	"	"	37	"	"
ABTS ^{•+}	PB 10	7	30	40	50-1000
DPPH [•]	H ₂ O-MeOH 50%		30	40	20-600
	PB-MeOH 10%	7	30	"	"
AAPH	PB	7	30	40	20-1000
	"	"	37	"	"
	"	"	37	150	"

PB: Phosphate Buffer 10 mmol L⁻¹
 AB: Acetate Buffer 10 mmol L⁻¹

2.4 Oxidant Capacity Indexes and Parametrization

The etching phenomenon was monitored by evaluating the absorbance decrease (D%) induced by the etching, mediated by the oxidant agents, according to Eq. 1 (Eq. 1):

$$D\% = \left[\frac{(Abs_{405pre-etching} - Abs_{405post-etching})}{(Abs_{405pre-etching})} \right] \times 100 \quad (1)$$

According to Della Pelle *et al.* [3], for each oxidant agents, indexes to study the oxidants reactivity were extrapolated from the dose-response curve (D% vs. Oxidant agent concentration) and reported below:

- m/X_C^{50} : ratio between the slope (m) of the linear equation ($D\% = mX + q$) and concentration values (X_C^{50}) calculated according to Eq. 2 (Eq. 2) considering the $D\%^{50}$ calculated according to Eq. 3 (Eq. 3).

The X_C^{50} is the oxidant concentration at which the signal (D%) reached its half-value, named ($D\%^{50}$), calculated as the mean value between the highest and lowest signal of the dose-response curve.

$$X_C^{50} = (D\%^{50} - q) / m \quad (2)$$

$$D\%^{50} = (D\%_{\text{lower point}} + D\%_{\text{higher point}}) / 2 \quad (3)$$

- *Relative Oxidant Capacity, ROC*: the m/X_C^{50} ratio of each oxidant normalized against the m/X_C^{50} of H₂O₂ used as a model/reference system and expressed as a percentage according to Eq. 4 (Eq. 4).

$$ROC = \left[\frac{(m/X_C^{50})_{\text{oxidant}}}{(m/X_C^{50})_{H_2O_2}} \right] \times 100 \quad (4)$$

- m/H_2O_2eq : ratio between the slope (m) of H_2O_2 linear equation and the oxidant concentration expressed as H_2O_2 equivalents (H_2O_2eq). The H_2O_2eq of each oxidant agent was calculated from the linear equation of H_2O_2 according to Eq. 5 (Eq. 5):

$$H_2O_2eq = (D\%_{oxidant}^{50} - q_{H_2O_2})/m_{H_2O_2} \quad (5)$$

3 Results and Discussion

3.1 Nanostructured Film Assembling

Figure 1 reports the spectrophotometric characterization in the Visible range of the EP modified with polydopamine (PDA) film (Fig. 1A) and nano-decorated with gold (AuNPs, Fig. 1B and 1C) and silver nanoparticles (AgNPs, Fig. 1D). The NPs formation has been confirmed by the localized surface plasmon resonance (LSPR) phenomenon typically exhibited by nanosized Au and Ag at absorption band of 540 ± 10 nm and 410 ± 10 nm, respectively [1–3].

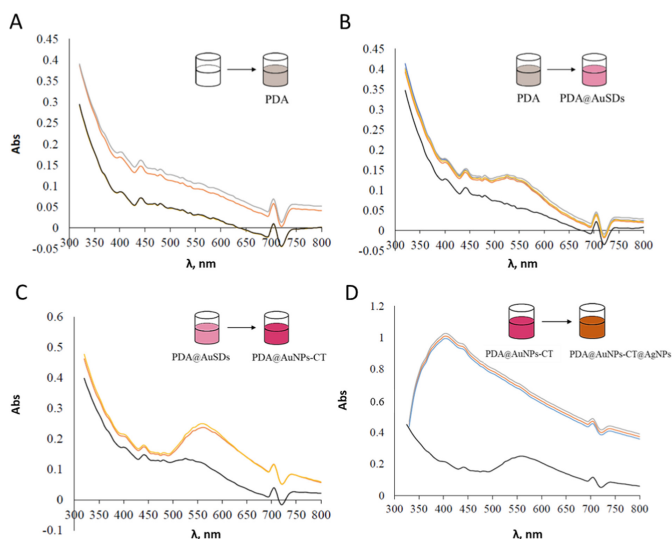


Fig. 1. Visible absorbance spectra of PDA@AuNPs-CT@AgNPs formation steps. (A) *PDA thin-film formation*: EP well before (black line) and after PDA film formation (orange and grey lines); (B) *AuSDs self-formation*: PDA film before (black line) and after AuSDs formation (orange and grey lines); (C) *AuSDs functionalization*: AuSDs before (black line) and after catechin functionalization (yellow and orange lines); (D) *AgNPs-nanonetwork formation*: Au-nanostructured film before (black line) and after AgNPs nanonetwork formation (orange, blue, and grey lines). The inset schematizes the PDA@AuNPs-CT@AgNPs formation steps.

The PDA nano-decoration with gold occurred by a spontaneous self-assembly driven by the reducing free moieties (i.e., catecholic portions) of PDA that are able to reduce the AuSD precursors (Au(III)) from the cationic to the nano-sized and zero-valent state (Au(0)). The AuSDs formation was assessed by the presence of LSPR absorption peak at 550 ± 3 nm (Fig. 1B). Then, the AuSDs were functionalized with catechin (CT) exploiting a seed-growth strategy; the CT acts as a reducing agent inducing an AuSDs growth resulting in an AuSDs enlargement (AuNPs) coupled to the intrinsic surface functionalization [1, 2]. The latter gave rise to an increase in the absorption peak intensity (Fig. 1C). The CT anchoring onto the AuNPs results in a formation of a redox-active corona able to trigger the silver nanonetwork formation. In brief, the CT-shell, thanks to the CT-reducing ability, induces the AgNPs formation onto the PDA@AuNPs-CT film resulting in a bimetallic nanostructured film [1, 2]. The AgNPs formation was confirmed by the LSPR profile that exhibits an absorption band at 405 ± 7 nm, proper of silver nanostructures [1, 2]. The LSPR profile of AgNPs hides the AuNPs absorption peak. Each step of the nanostructure fabrication highlighted great reproducibility with RSD values ($n = 96$ wells) of 6.3% for the PDA film formation, 7.4% and 7.2% for the AuSDs self-formation and CT functionalization, and 8.0% for the AgNPs nanonetwork formation.

3.2 Sensing Strategies, Performances, and Reactivity Indexes

The PDA@AuNPs-Ct@AgNPs thin-film prepared in EP wells is a ready-to-use platform for oxidant agents evaluation without the need for external reagents [1, 2]. The sensing mechanism relies on the ability of external oxidant agents, the analyte, to etch the MNPs; the etching is the chemical oxidation of MNPs resulting in morphological change until their complete dissolution [1, 2]. Among MNPs, the AgNPs are the most used NPs for etching-based strategies development because more prone to donate electrons compared to other noble metals (i.e., gold, platinum, etc.) [1].

Previous works have demonstrated how oxidant agents such as hydrogen peroxide (H_2O_2), peracetic acid, and sodium hypochlorite (NaClO) can selectively and quantitatively oxidize the AgNPs on similar Au/AgNPs-based nanostructured devices, resulting in a proportional LSPR variation used as analytical signal [1, 2]. Table 2 summarizes all the oxidant agents tested (i.e., H_2O_2 , NaClO , NaNO_2 , FeSO_4 , ABTS, DPPH, and AAPH) by using the PDA@AuNPs-Ct@AgNPs platform and exploiting the etching strategy.

Table 2. Oxidant agents dose-response curve parameters and respective oxidant capacity indexes.

Oxidants	Linear Equation	R ²	Linear range $\mu\text{mol L}^{-1}$	RSD %	LOD $\mu\text{mol L}^{-1}$
<i>H₂O₂</i>	$y = 0.148x + 2.5795$	0.9967	1 - 200	< 6.9	0.32
<i>NaClO</i>	$y = 0.0664x + 4.0618$	0.9947	25 - 900	< 12.6	2.94
<i>NaNO₂</i>	/	/	/	/	/
<i>FeSO₄</i>	/	/	/	/	/
<i>ABTS^{•+}</i>	$y = 0.0308x + 3.9136$	0.9929	20 - 1000	< 9.6	6.34
<i>DPPH[•]</i>	/	/	/	/	/
<i>AAPH</i>	/	/	/	/	/

Oxidants	slope/ m % ($\mu\text{mol L}^{-1}$) ⁻¹	D ₅₀ ⁵⁰ %	X _C ⁵⁰ $\mu\text{mol L}^{-1}$	H ₂ O ₂ eq $\mu\text{mol L}^{-1}$	m/ X _C ⁵⁰ % ($\mu\text{mol L}^{-1}$) ⁻²	ROC %	m/ H ₂ O ₂ eq. % ($\mu\text{mol L}^{-1}$) ⁻²
<i>H₂O₂</i>	0.148	17.19	98.70		1.50E-03	/	/
<i>NaClO</i>	0.0664	33.22	439.12		1.51E-04	10.1	3.21E-04
<i>NaNO₂</i>	/	/	/	/	/	/	/
<i>FeSO₄</i>	/	/	/	/	/	/	/
<i>ABTS^{•+}</i>	0.0308	19.77	514.69		5.98E-05	4.0	2.65E-04
<i>DPPH[•]</i>	/	/	/	/	/	/	/
<i>AAPH</i>	/	/	/	/	/	/	/

RSD, n=3

According to previous studies, the AgNPs LSPR peak intensity decrease (D%) induced by the analyte-mediated etching was used as analytical signal. To this aim, the H₂O₂ was employed as a probe to explore and study the AgNPs oxidation progress during the time by monitoring the LSPR absorbance spectra evolution (Fig. 2A). The LSPR absorbance spectra variation along the reaction progress confirms the H₂O₂-mediated AgNPs etching by peak intensity decreases at 405 nm, which is the typical absorption band of AgNPs [1, 2]. Further, the selective etching of AgNPs was proved by the LSPR absorbance spectrum recorded after 40 min of reaction (Fig. 2A, bottom spectrum). Indeed, the LSPR peak of AgNPs completely disappeared due to the full oxidation of AgNPs leading to the AuNPs LSPR profile occurrence with absorption band at 520 nm (Fig. 2A, bottom spectrum).

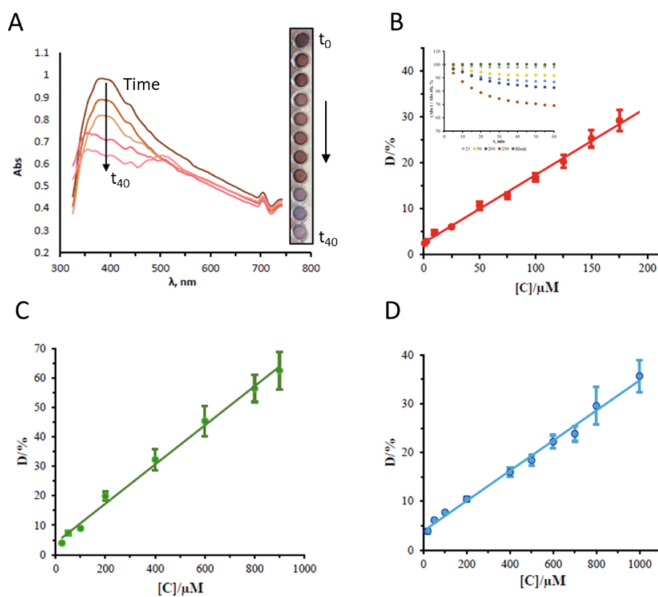


Fig. 2. (A) Absorbance spectra evolution before (brown line) and during the PDA@AuNPs-CT@AgNPs etching mediated by 200 μM H_2O_2 along time; every 10 min for a total reaction time of 40 min. The inset reports the PDA@AuNPs-CT@AgNPs colorimetric progress, the reaction time increase from top (t_0) to bottom (t_{40}). (B) Dose-response curves of H_2O_2 in the range of 1–200 μM , the inset reports the kinetic curves of etching mediated by H_2O_2 . Dose-response curves of (C) NaClO in the range of 25–900 μM ; and (D) ABTS \cdot^+ in the range of 20–1000 μM .

Among the evaluated oxidant only the H_2O_2 , NaClO, and ABTS were able to drive the AgNPs etching (Table 2). H_2O_2 and NaClO are oxidizers, and their mechanism of action relies on the formation of radical species (hydroxyl radical, $OH\cdot$; active chlorine species $OC1^-$, $HOCl$, Cl^- , and Cl_2) responsible for the oxidative processes [1, 2], meanwhile, the ABTS radical activity was confirmed. The ABTS is a radical cation commonly used in a photometric assay for the antioxidant capacity evaluation based ABTS scavenging mediated by the analyte [3].

Dose-response curves, for the quantitative determination of H_2O_2 , NaClO, and ABTS, were built using increasing amounts of H_2O_2 (Fig. 2B), NaClO (Fig. 2C), and ABTS (Fig. 2D) by plotting the signal (D%) against concentration values (μM). Linear ranges from 1 to 200 μM for H_2O_2 , from 25 to 900 μM for NaClO, and from 20 to 1000 μM for ABTS were reported; Table 2 reports parameters of the dose-response curves. No LSPR variation was observed for respective blanks of reaction (reaction medium without analyte). Good determination coefficient ($R^2 \geq 0.9929$) and reproducible signals ($RSD \leq 9.6\%$, $n = 5$) were obtained for the analytes. Remarkable limit of detection (LOD) of 0.3 for H_2O_2 , 2.9 for NaClO, and 6.3 for ABTS were obtained, the LOD was calculated according to the following equation: $LOD = [(3 \times \sigma_{blank}) / \text{linear regression slope}]$ [1].

Despite the NaNO_2 , FeSO_4 , DPPH, and AAPH are oxidant agents (i.e., NaNO_2 , and FeSO_4), and radical species (i.e., DPPH, and AAPH) no AgNPs etching was reported. The ineffectiveness of these species could be attributed to the low oxidation capacity in the experimental reaction conditions; indeed, NaNO_2 exhibits oxidant capacity at acidic pH [6], the FeSO_4 is used as an oxidant stressor for *in-vitro* studies then long reaction times ($t > 48$ h) and physiological conditions are required [7], and DPPH principally retains its radical behaviour in ethanolic/methanolic solution [4]. The AAPH is a strong radical generator, known for its ability to initiate/trigger oxidation processes in living organisms; although the potential oxidant ability of AAPH, no etching phenomenon was observed because of the higher instability of AAPH radicals resulting in short half-life [5].

Eventually, the H_2O_2 , NaClO , and ABTS reactivity were evaluated and compared. To this aim, m/X_C^{50} , ROC , and m/H_2O_2eq parameters with metrological characteristics have been extrapolated by the linear equation (see Sect. 2.4). These parameters allow comparing different oxidants overcoming the partial information given using the single parameters as the m or *linear range* in terms of concentrations and signal reached. In detail, the m/X_C^{50} encloses the dose-response curve slopes (change in response per unit of concentration) and the mean oxidant concentration of the linearity range, allowing to directly assess and compare the oxidant capacity and effectiveness. The higher the value of m/X_C^{50} , the greater the oxidizing activity [3].

The m/X_C^{50} values of H_2O_2 , NaClO , and ABTS are reported in Table 2. As expected, H_2O_2 ($m/X_C^{50} = 1.5 \times 10^{-3}$) is the most reactive chemical species respect with NaClO ($m/X_C^{50} = 1.5 \times 10^{-4}$), and ABTS ($m/X_C^{50} = 6.0 \times 10^{-5}$); for this reason, the H_2O_2 was used as a reference/model system for the calculation of the ROC and m/H_2O_2eq indexes. The ROC and m/H_2O_2eq are relative indexes allowing to relate the oxidant reactivity to the reference standard resulting useful for samples analysis.

As evinced in Table 2, according to m/X_C^{50} , ROC , and m/H_2O_2eq parameters the reactivity order is $\text{H}_2\text{O}_2 > \text{NaClO} > \text{ABTS}$.

3.3 Platform Storability

Eventually, the storability test of PDA@AuNPs-Ct@AgNPs platform to study the lifetime of the proposed platform has been performed. Different storing conditions have been tested: environmental atmosphere/air and nitrogen (N_2)-modified atmosphere, different buffer/solvents (water/ H_2O , methanol/ MeOH , methanolic solution in water, phosphate buffer/ PB , saline solution), and antioxidant/reducing compounds (ascorbic acid/ AA , sodium citrate). Figure 3 report the signal evolution (D%) the PDA@AuNPs-Ct@AgNPs platform stored during time. In all the conditions tested the platform resulted storable for one month, and after 16 days no further signal variation was reported. The most promising results have been obtained with methanolic solution in water (80, 60 and 40% of MeOH) and 10 mM sodium citrate aqueous solution retaining more than the 89% of the starting signal (Fig. 3). In all the storing conditions reproducible signals were highlighted ($\text{RSD} \leq 2.9\%$, $n = 5$) proving the stability of the nanostructured film during the time.

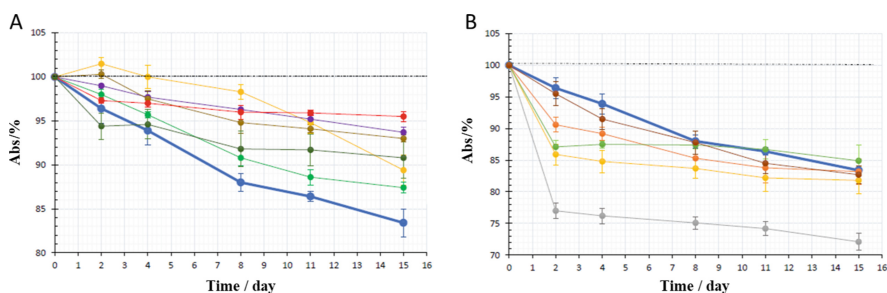


Fig. 3. Solvents screening for PDA@AuNPs-CT@AgNPs storability assessment during time. (A) Solvents and gaseous environments that act better than water (blue line): 10 mM sodium citrate aqueous solution (yellow line), nitrogen (green line), 40% methanolic solution in water (violet line), 60% methanolic solution in water (brown line), 80% methanolic solution in water (red line), 100% methanol (olive line). (B) Solvents and gaseous environments that act worse than water (blue line): 20% methanolic solution in water (brown line), environmental atmosphere/ air (orange line), 10 mM ascorbic acid aqueous solution (green line), 10 mM phosphate buffer (pH 7.0) (yellow line), physiological solution/0.9% saline solution (grey line). The signal was expressed as Storability/% vs. time monitoring the Absorbance intensity retention (Abs%, $\lambda = 405$ nm) during time. The absorbance intensity retention has been reported as % and calculated according to the following equation: $Abs\% = (Abs_t / Abs_{t0}) \times 100$, where Abs_{t0} is the absorbance value before the storability test and Abs_t in the absorbance value recorded after different times of storage.

For the better storing conditions, no aggregation or collapse phenomena are observed, indicating that Ag is well anchored and embedded in the film. Whereas for the worse storing condition the absorbance intensity decrease could be attributed to (i) a slight peak decrease due to AgNPs oxidation driven by the solvents (i.e., MeOH of air), (ii) a shift and/or broadening of the AgNPs LSPR peak induced by AgNPs morphology changes or interaction of solvents with the AgNPs surface (i.e., saline solution).

4 Conclusions

In this study, a nanostructured thin film using polydopamine self-decorated with Au and AgNPs were developed. The nanostructure fabrication can be performed onto any substrate thanks to the use of polydopamine which is able to form ubiquitously adhesive redox-active polymer. Herein, the nanostructured thin film was realized onto ELISA plate to provide easy-to-use systems for the evaluation of oxidant species by using the etching strategy. The developed platform allowed the monitoring and quantification of the H_2O_2 , NaClO, and ABTS which are analytes of and biological interest.

Useful indexes (m/X_C^{50} , ROC, and m/H_2O_2eq) were extrapolated from the oxidants dose-response curves which enable the direct comparison of the oxidant capacity of oxidant species as well as the evaluation of their intrinsic reactivity. The indexes herein proposed are universally exploitable for the comparison of molecules with the same class of reactivity (i.e., oxidant agents, antioxidant agents, etc.).

Finally, the storability of the proposed nanostructured platform in several storing conditions (solvents, modified atmosphere, etc.) has been assessed. Definitely, herein is proposed the realization of ready-to-use kits, potentially useful in different bioanalytical industrial/environmental applications.

References

1. Scroccarello, A., et al.: Plasmonic active film integrating gold/silver nanostructures for H₂O₂ readout. *Talanta* **222**, 121682 (2021)
2. Scroccarello, A., Della Pelle, F., Del Carlo, M., Compagnone, D.: Monitoring disinfection in the Covid-19 era. A reagent-free nanostructured smartphone-based device for the detection of oxidative disinfectants. *Microchem. J.* **175**, 107165 (2022)
3. Della Pelle, F., et al.: Antioxidant capacity index based on gold nanoparticles formation. Application to extra virgin olive oil samples. *Food Chem.* **178**, 70–75 (2015)
4. Huang, D., Ou, B., Prior, R.L.: The chemistry behind antioxidant capacity assays. *J. Agric. Food Chem.* **53**(6), 1841–1856 (2005)
5. Betigeri, S., Thakur, A., Raghavan, K.: Use of 2, 2'-azobis (2-amidinopropane) dihydrochloride as a reagent tool for evaluation of oxidative stability of drugs. *Pharm. Res.* **22**(2), 310–317 (2005). <https://doi.org/10.1007/s11095-004-1199-x>
6. Gladwin, M.T., et al.: The emerging biology of the nitrite anion. *Nat. Chem. Boil.* **1**(6), 308–314 (2005)
7. Park, O.K., Oh, J.M., Choi, M.K., Park, S.T., Chung, Y.T.: Effect of antioxidants on FeSO₄ toxicity in cultured myocardial cells. *Korean J. Phys. Anthropol.* 161–168 (1997)



Soiling Detection Investigation in Solar Irradiance Sensors Systems

Elena Esposito^(✉), Gianni Leanza, and Girolamo Di Francia

ENEA CR-Portici, TERIN-FSD-SAFS, P. le E. Fermi 1, 80055 Portici, Italy
elena.esposito@enea.it

Abstract. Dirt deposition on solar irradiance measurement instruments can lead to errors in radiation measurements and, as a result, in incorrect energy production management issues. Climate and meteorological conditions may affect in different way the deposition process and thus, soiling severity and type are geographical and time-dependent.

To investigate the soiling impact, here we describe a methodology that allows estimating the effect of dirt deposition on solar irradiance measurement systems, e.g., pyrheliometer. The methodology relies on the evaluation of a soiling index, based on pyranometer data measurements and it has been in field validated, using a solar irradiance measurement system deployed at ENEA Research Center of Portici. The results show that, under suitable assumptions, the computed index may be used to obtain a reasonable estimation of soiling effect.

Keywords: Solar irradiance · Weather data · Soiling detection · Satellite data

1 Introduction

The increasing use of sensor technologies in several application fields, such as Air Quality, Health, Energy, Photovoltaic (PV) systems, led to an increasing interest in the scientific and technical communities over the sensor devices accuracy in in-field operation and in the reliability of the corresponding generated datasets.

As far as PV systems are concerned, several authors have investigated the soiling effect on photovoltaic modules, in order to estimate and predict the efficiency loss in the energy production [1, 2]. However, only a few studies have investigated the effect of soiling on solar irradiance sensors, e.g., pyranometer and pyrheliometer [3–6]. Specifically, in [3] the authors provided a set of measurements, performed using pyranometer and pyrheliometer instruments at several locations in southern Spain and Morocco. They found that pyranometers may be assumed to be as only poorly sensitive to soiling, with a resulting error in Global Horizontal Irradiance (GHI) estimation never larger than 5%. On the contrary, pyrheliometers are much more affected by soiling and errors as large as 10% can be detected in only a few days since the last cleaning event reaching values even larger than 15% or more in a few weeks. In [4] the soiling effect has been investigated, in the composite climatic zone of India. The study has been performed using test pyranometer and pyrheliometer never cleaned during the soiling test period lasting nearly

two months, while reference instruments were cleaned on daily basis. Also in [5–7], the authors have investigated soiling impact and proposed correction formulas, highlighting the higher sensitivity to soiling of pyrhemometers with respect to pyranometers. These kind of instruments seem to be strongly affected by dust deposition that results in a marked decrease in the sensors signal and, consequently, in errors on the photovoltaic plant energy product estimation.

Studying the soiling effect on the solar irradiance measurement systems means to find a way to quantify the signal loss and to identify the environmental factors affecting soil accumulation. In this respect, the optimal experimental set-up should have reference instruments (pyranometer and pyrhemometer) regularly cleaned and timely compared to similar test instruments uncleaned, to detect possible anomalies with respect to the reference sensors [4].

If such an equipment is not available, soiling indices can be nevertheless defined, based on suitable assumptions. In this work, we study the soiling effect on a solar radiation measuring system based on pyrhemometers and pyranometers assuming that the latter's are slightly affected by soiling. We try, moreover, to search specific pattern in weather data, in order to identify the environmental factors that mostly contribute to soiling deposition. Specifically, the historical data, recorded by the weather station located in the city of Portici (Fig. 1), have been employed to quantify the soiling deposition on the pyrhemometer surface, assuming that data recorded by the pyranometer are unaffected by soiling and therefore here assumed as a reference. A 5-year long dataset has been used for this analysis.

2 Experimental Background

2.1 Site and Instrumentation Description

The sensors system is deployed in the ENEA Research Center in Portici (NA), located close to the sea on the Gulf of Naples.



Fig. 1. Map of Portici city located on the Gulf of Naples (left); map of ENEA Research Center and local dominant wind configuration (right).

Portici is a densely populated area whose microclimate is mostly determined by its geographical position and by the sea proximity, which affects Temperature and Relative Humidity as a result of local winds. The sensors system is housed on a Solar Tracker (mod. STR-22 with Shadow Ball MB 12) and in a special facility nearby located, connected via suitable converters to a data acquisition unit (Fig. 2).



Fig. 2. Solar Tracker with Diffuse Pyranometer, Normal Global Pyranometer EKO mod. MS-802 F and Pyrheliometer HUKSEFLUX DR01-10 (right); Global Horizontal Pyranometer (left).

2.2 Methodologies

In order to obtain an estimation of soiling deposition, we have computed Direct Normal Irradiance (DNI) according to Eq. 1

$$DNI_{comp} = \frac{GHI - DHI}{\sin \alpha} \quad (1)$$

where GHI is the Global Horizontal Irradiance, DHI is the Direct Horizontal Irradiance and α is the solar elevation angle, computed with high precision (1/100 degree), using SOLPOS calculation algorithm provided by NREL [8]. In Fig. 3, DNI_{comp} is reported together with the measured DNI_{meas} , GHI and DHI , during a day when the sensors cleaning has been performed. It is worth to note that, while pyranometer measurements are practically unaffected by the cleaning action, the pyrheliometer data exhibit an abrupt change and a marked increase in DNI , from 630 W/m^2 to almost 800 W/m^2 is observed.

Assuming, therefore, that pyranometers are mostly unaffected by soiling, a soiling index, SI_1 , has been defined as:

$$SI_1 = \frac{|DNI_{comp} - DNI_{meas}|}{DNI_{comp}} \quad (2)$$

where DNI_{meas} is measured by pyrheliometer and DNI_{comp} is computed according to Eq. 1.

A second possible approach to estimate a soiling index is to compare DNI data measured on earth with DNI data obtained by using COPERNICUS solar irradiance data. This approach has the advantage to avoid any indirect measurement by means of pyranometers but, on the other hand, can be affected by the intrinsic differences among surface and satellite data. The European Earth Observation Program Copernicus and specifically, the Copernicus Atmosphere Monitoring Service (CAMS) uses atmospheric modeling combined with Earth observation data, to provide information on air quality, global atmospheric composition, climate, solar and UV energy [9]. In particular, one of the CAMS services provides solar radiation values at ground level using data from different sources to cross-referencing cloud information obtained from the satellite with the optical state of the atmosphere and soil properties.

The tested dataset consists of a 5 years long daily dataset containing solar irradiance values outputted by pyranometer and pyrhemliometer sensors and Copernicus solar data (see Table 1).

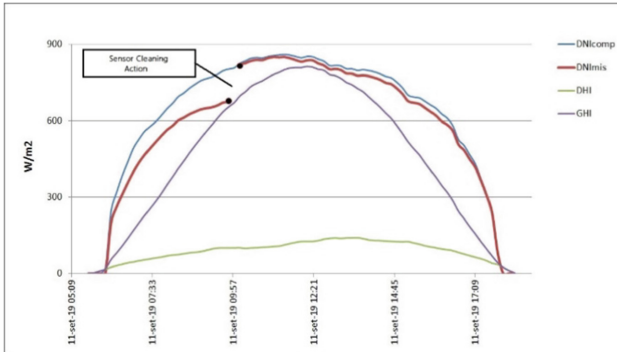


Fig. 3. Cleaning action effects on the pyrhemliometer and pyranometer surface. Red line represents the pyrhemliometer DNI measurement; purple line is GHI and green line is DHI.

Table 1. Dataset description.

Variables	Specifications
Timestamp	10 min. Sampling rate (Jan. 2016–Dec. 2020)
Global Horizontal Radiation (GHI)	W/m^2 (Pyranometer)
Diffuse radiation (DHI)	W/m^2 (Pyranometer)
Measured Direct Normal Radiation (DNI_{meas})	W/m^2 (Pyrhemliometer)
Computed Direct Normal Radiation (DNI_{comp})	W/m^2 (Eq. 1)
Global Horizontal Radiation (GHI_{sat})	W/m^2 (Copernicus)
Diffuse radiation (DHI_{sat})	W/m^2 (Copernicus)
Direct Normal Radiation (DNI_{sat})	W/m^2 (Copernicus)

The first step for the implementation of the described methodology consists in the selection of ad hoc period in the entire dataset. For the sake of clarity it is worth to note here that usually, suitable CAMS data subsets are selected according, for instance, to a Clearness Index Kt , ratio of the horizontal global irradiance to the corresponding irradiance available outside of the atmosphere. On the contrary, all available data will be hereafter considered since, although it is true that low DNI_{sat} values, corresponding in general to bad weather conditions, would result in an artificial increase of the soiling index, the same bad weather conditions could effectively give rise to an effective soiling effect. Therefore, for this first analysis no data will be ruled out. We have used the daily dataset and for each day, we computed DNI_{comp} according to Eq. 1. Then, we have used

Copernicus daily data and computed SI_2 using DNI_{sat} , according to Eq. 3

$$SI_2 = \frac{|DNI_{sat} - DNI_{meas}|}{DNI_{sat}} \quad (3)$$

The indices computed by means of Eq. 2 and Eq. 3 have been evaluated taking care to include the periods in which no cleaning operations have been performed in order to show the soiling effect. Figure 4 clearly shows the increase in the daily soiling index values and the same behavior occurs in the second index computed with Copernicus data, considering the relation between satellite and ground data.

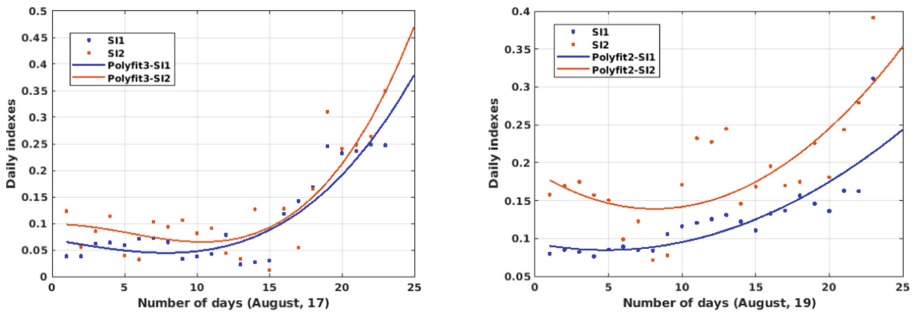


Fig. 4. Soiling indices plots during some of no-cleaning periods. Both indices have the same increasing behavior.

In Fig. 5, SI_2 is reported as a function of SI_1 considering all daily data. It is worth to note that for $SI_1 \geq 0.5$, SI_2 seems to be nicely linearly correlated to SI_1 .

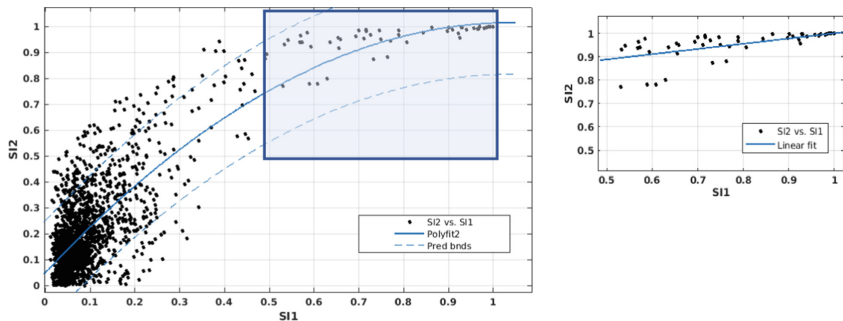


Fig. 5. Scatter plot of SI_2 vs. SI_1 along the entire daily dataset with Polyfit2 at 95% confidence interval bounds.

In Fig. 6 Wind rose pictures obtained using 10 min averaged data, show the differences in the Wind Speed (WS) and Wind Direction (WD) in two range of SI_1 ($SI_1 \geq 0.5$ and $SI_1 < 0.5$).

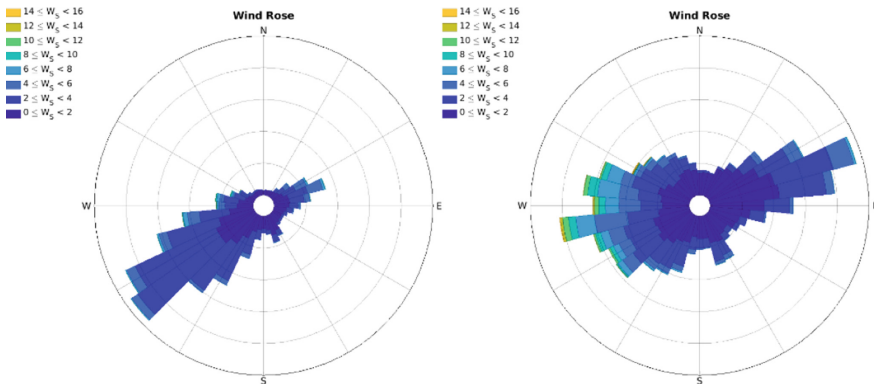


Fig. 6. Wind rose computed in the range $SI_1 \geq 0.5$ (left) and $SI_1 < 0.5$ (right), showing the location characteristics and the differences between them in the considered ranges. The dominant parameter seems to be WD.

It is interesting to stress that, while for $SI_1 \geq 0.5$, a dominant wind direction is revealed, this is not observed at all for $SI_1 < 0.5$. We have computed the wind rose for each year, confirming these behaviours.

In conclusion, we find that the computed soiling indices allow obtaining an estimation of soiling deposition process where no reference instrumentation is available. Specifically, for large values of indices (≥ 0.5), we obtain a high correlation between SI_1 and SI_2 . This implies that, if SI_1 is a good estimator of soiling deposition, then also SI_2 can be used, bypassing ground pyranometer data. Furthermore, the analysed location highlights the weather conditions affecting the instruments, namely wind speed and its direction. The next step will be to install additional solar irradiance systems regularly cleaned co-located together with not cleaned systems and to study the soiling deposition process also using Machine Learning approaches to real time detect the configuration requiring cleaning intervention. The environmental parameters influencing soiling process will be analysed considering their multivariate distribution during the co-location test period, to capture the specific configurations contributing to soiling deposition.

References

1. Shaju, A., Chacko, R.: Soiling of photovoltaic modules-Review. In: IOP Conference Series: Materials Science and Engineering, vol. 396. no. 1. IOP Publishing (2018)
2. Ferlito, S., De Vito, S., Di Francia, G.: Detect anomalies in photovoltaic systems using isolation forest (preliminary results). In: Di Francia, G., Di Natale, C. (eds.) Sensors and Microsystems, vol. 753, pp. 231–238. Springer, Cham (2020). https://doi.org/10.1007/978-3-030-69551-4_31
3. Geuder, N., Quaschnig, V.: Soiling of irradiation sensors and methods for soiling correction. *Sol. Energy* **80**(11), 1402–1409 (2006)
4. Mudike, R., Barbate, I., Tripathi, A.K., Reddy, Y.B.K., Banerjee, C.: Soiling effect on the performance of solar radiometers in composite climatic zone of India. In: 2019 International Conference on Electrical, Electronics and Computer Engineering (UPCON), pp. 1–6 (2019)

5. Pape, B., Batlles, J., Geuder, N., Pinero, R.Z., Adan, F., Pulvermueller, B.: Soiling impact and correction formulas in solar measurements for CSP projects. In: SolarPACES Conference, Berlin, Germany (2009). <https://doi.org/10.13140/2.1.4355.0406>
6. Wolfertstettera, F., et al.: Monitoring of mirror and sensor soiling with TraCS for improved quality of ground-based irradiance measurements. *Energy Procedia* **49**, 2422–2432 (2014)
7. Leanza, G., Zingarelli, M., Pascarella, F., Ferlito, S.: Analisi meteo-radiativa dei siti ENEA di Portici e Manfredonia. Rapporto triennale 2007–2008–2009. ENEA
8. NREL SOLPOS CALCULATOR. <https://midcdmz.nrel.gov/solpos/solpos.html>. Accessed July 2022
9. COPERNICUS, Atmosphere Monitoring Service. <https://atmosphere.copernicus.eu>
10. <https://www.eko-instruments.com/eu/categories/products/pyranometers/ms-80sh-pyranometer>. Accessed July 2022
11. <https://www.huksefluxusa.com/wp-content/uploads/2017/04/DR01-DR02-DR03-manual-v1609-US.pdf>. Accessed July 2022



Actively Controlled Synchronized-Switch Harvesting on Inductor for Piezoelectric Transducers

Laura Landi, Cinzia Tamburini, and Aldo Romani^(✉)

Advanced Research Center on Electronic Systems, University of Bologna, Cesena, Italy
{laura.landi10, cinzia.tamburini3, aldo.romani}@unibo.it

Abstract. Vibrational energy harvesting by means of piezoelectric transducers has been of particular interest in recent years for powering autonomous, wireless devices. In this context, a non-linear treatment of piezoelectric voltage greatly enhances electromechanical conversion. This paper presents an ultra-low power circuit implementation of the technique called Synchronized Switch Harvesting on Inductor (SSHI). The circuit detects the zero-current condition through the rectifier with a series shunt resistor and a nano-power comparator. Simulations show that the maximum power extracted is approximately 6.7 times greater than with a passive rectifier. The estimated overall consumption of the circuit components is 4 μ A. The measured voltage flip efficiency is between 91% and 94%.

Keywords: Piezoelectric transducers · Energy harvesting · SSHI · Micropower · Power conversion

1 Introduction

Energy harvesting is the process by which energy present in the environment is extracted, stored and converted into directly usable electricity. It is necessary to resort to energy harvesting whenever it is not possible to use a battery, e.g. in harsh environmental conditions or due to difficulties in recharging. Another large-scale objective of energy harvesting is to reduce the number of produced batteries, avoiding their environmental impact. In the world of energy harvesting, the problem is that energy sources are intermittent and characterized by low power densities. This creates difficulties in the power conversion optimization process. This is truer for energy harvesting from vibrations. Many transducers used to derive energy from vibrations exploit piezoelectricity, which is a property of some materials that develop a charge partition on their surface when subject to a mechanical stimulus. Conversely, they exhibit a mechanical deformation when a voltage is applied to their terminals. Piezoelectric transducers (PTs) consist of beams, membranes or cantilevers made of piezoelectric materials with metal electrodes. The PT develops an electrical charge proportional to the mechanical deformation applied to it. A mechanically generated electric current charges the capacitance between the electrodes of the PT. Therefore, in a first approximation, the PT can be modeled as a current source with a mainly capacitive impedance in parallel.

The simplest solution to extract energy from PTs is called Standard Interface or Standard Energy Harvester (SEH) and consists in a rectifier connected to the PT, with a storage capacitor and a load connected in parallel to its output. The current flows towards the load only when the voltage of the PT (in module) becomes greater than the rectified voltage. Then, the rectifier is not conducting for a part of the time, although there are still charge displacements following the vibrations of the PT. After the rectifier stops conducting, a voltage inversion driven by vibrations starts, which involves the dissipation of energy that is not transferred to the load. Another disadvantage of a passive rectifier is that the maximum power is extracted from the PT only for a specific load value, which cannot be clearly identified with irregular vibrations and highly variable loads, as is the case in many energy harvesting applications.

An alternative and more efficient solution involves the use of switching power converters triggered in a synchronous way with input vibrations. These non-linear solutions also require dedicated control circuitry that consumes additional power. However, the additional harvested power is typically higher, even in presence of weak and irregular vibrations. This paper elaborates on the specific and well-known technique called Synchronized-Switch Harvesting on Inductor (SSHI), introduced by *Taylor et al.* in [1] and described by *Lefeuvre et al.* in [2]. SSHI solves the drawbacks of the SEH by adding, in parallel to the PT, a switch and an inductor in order to create an RLC resonant circuit operated synchronously with vibrations (Fig. 1a). The switch is closed each time the rectifier stops conducting and must be reopened exactly after a half-period of the RLC circuit in order to fully flip the PT voltage. This brings the PT voltage at the opposite conduction threshold of the rectifier. Since the PT current is crossing zero and changing sign, the rectifier immediately restarts conducting. In this way, the rectifier always conducts. At the same time, it is worth to note that control circuits draw power and losses in the RLC circuit may lead to a partial voltage inversion. Therefore, a tradeoff between voltage flip efficiency, delays and consumption must be pursued.

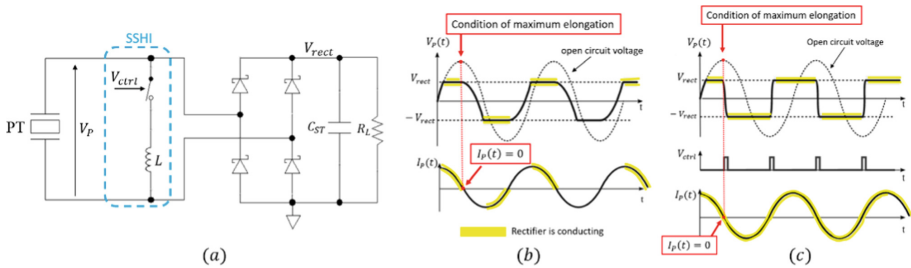


Fig. 1. Energy harvesting interfaces. $I_P(t)$ is the piezoelectric current induced by vibrations. (a) SSHI interface; (b) waveforms when SSHI is disabled, i.e. SEH; (c) waveforms when SSHI is enabled, ideal case with 100% voltage flip efficiency.

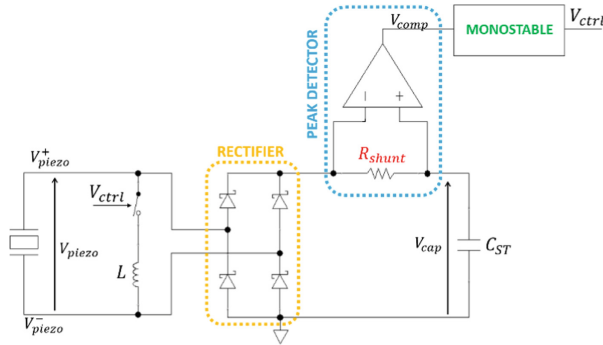


Fig. 2. Implementation of the proposed solution.

2 The Proposed Solution

The goal of the work was to implement an alternative and complete circuit implementation of a power converter based on SSHI that maximizes the voltage flip efficiency and still achieves an ultra-low power consumption. Figure 2 shows the proposed solution. The switching condition is detected by means of a shunt resistor in series between rectifier and storage element. In this way, the difference between the rectified voltage and the voltage across the storage capacitor becomes zero when the current on the shunt resistor is zero. Detecting the zero-crossing of the current on the shunt resistor corresponds to detecting the switching off the rectifier. In this implementation, a nano-power comparator senses the voltage across the resistor. The signal at the output of the comparator is then processed by a subsequent tunable monostable that provides the correct timing for controlling the switch.

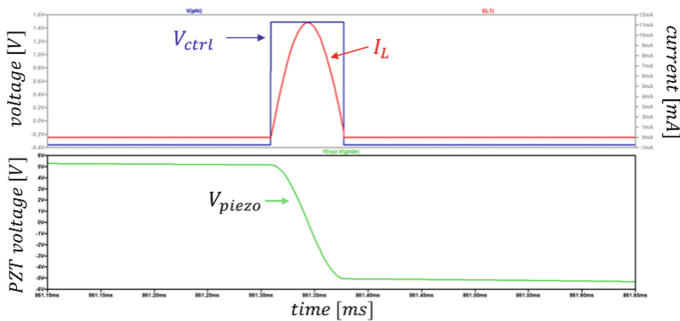


Fig. 3. Detail of one inversion of the voltage across the PT when the SSHI is enabled.

2.1 Simulation Results

Simulation analysis was performed to ensure that the circuit operates correctly. Circuit simulations with available models of components highlight that the voltage inversion occurs correctly and exactly when the PT current is crossing zero. In correspondence with each inversion, the inductor is able to fully charge and discharge itself (Fig. 3). In this way, it allows a complete voltage flipping.

The graphs in Fig. 4 show the extracted average power as a function of the load voltage and as a function of the load resistance. The graphs compare the trend in the case of the rectifier alone (SEH) with the trend obtained with the proposed solution based on SSHI. The maximum power extracted with the proposed solution is approximately 6.7 times greater than with the SEH.

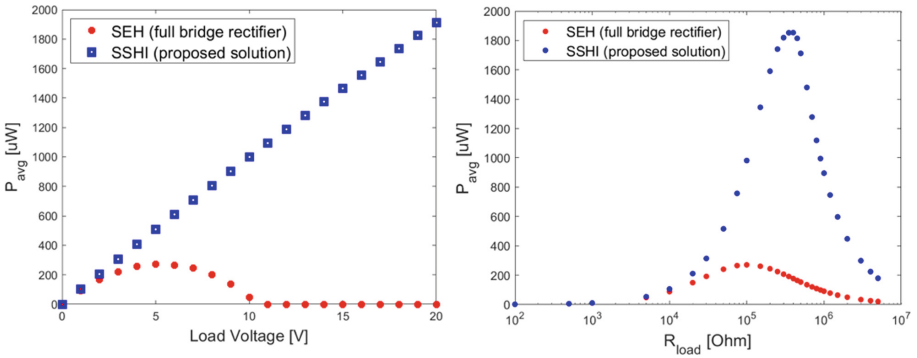


Fig. 4. Simulation results. Operating conditions: $V_{P0} = 10$ V, $f_0 = 53$ Hz, $C_P = 48.6$ nF, $L = 4.7$ mH, $C_{ST} = 10$ μF, $R_{shunt} = 3$ kΩ, real model for diodes and comparator, ideal model for the monostable.

2.2 Experimental Results

The circuit was implemented with off-the-shelf components that were chosen to guarantee adequate performance and low power consumption. While solutions reported in literature [3, 4] typically achieve a maximum voltage inversion efficiency between 80% and 90%, the proposed circuit achieves about 91–94% (Fig. 5). Lower voltage flip efficiencies imply longer times with no conduction through the rectifier until the PT voltage reaches the conduction threshold again. The increase in the extracted power compared to the use of the SEH is evident (Fig. 6). As the voltages approaches the maximum operating voltages of components, some performance degradation is observed. However, power is still higher than with the SEH.

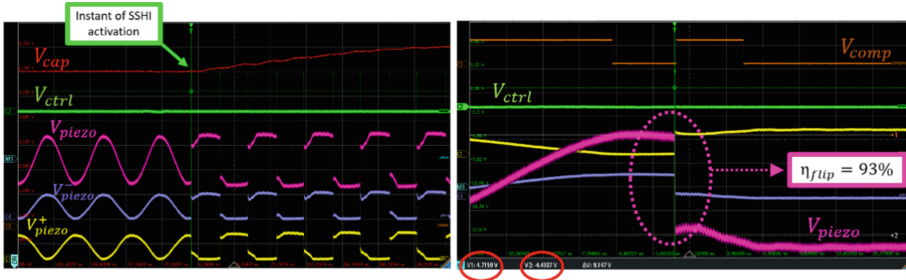


Fig. 5. Oscilloscope waveforms obtained with the proposed solution and detail of the voltage across the PT. The transducers used are the PPA (Piezo Protection Advantage) type, made by Midé Technology. Vibrations are applied with an electrodynamic shaker.

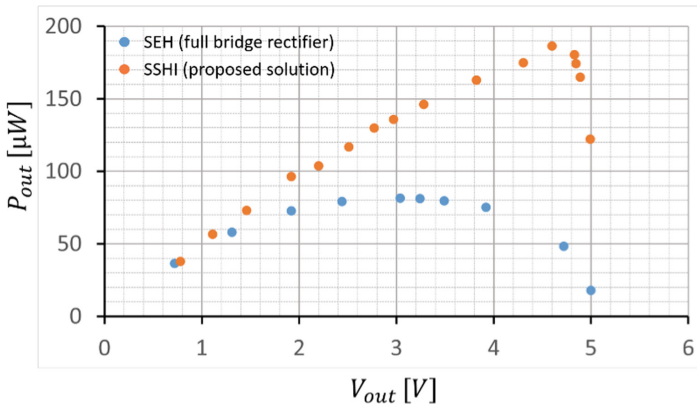


Fig. 6. Experimental characterization of the extracted power.

3 Conclusions

Even if exhaustive energy assessments require further progress, the estimated consumption of the circuit is approximately equal to $4 \mu\text{A}$ of which 210 nA is the typical static consumption of the peak detector, about 50 nA of the switch and $3 \mu\text{A}$ is the maximum consumption of the monostable. The low intrinsic consumption of the implementation and the significantly higher extracted power make it a viable and suitable solution for supplying, with vibrations characterized by low amplitudes, low-power electronic systems, such as personal healthcare devices or sensing nodes.

References

1. Taylor, G.W., Burns, J.R., Kammann, S.A., Powers, W.B., Welsh, T.R.: The energy harvesting eel: a small subsurface ocean/river power generator. *IEEE J. Oceanic Eng.* **26**(4), 539–547 (2001)
2. Lefeuvre, E., Badel, A., Richard, C., Petit, L., Guyomar, D.: A comparison between several vibration-powered piezoelectric generators for standalone systems. *Sens. Actuators A: Phys.* **126**(2), 405–416 (2006)
3. Eltamaly, A.M., Addoweesh, K.E.: A novel self-power SSHI circuit for piezoelectric energy harvesting. *IEEE Trans. Power Electron.* **32**(10), 7663–7673 (2017)
4. Hong, J., Chen, F., He, M., Wang, S., Chen, W., Guan, M.: Study of a low-power-consumption piezoelectric energy harvesting circuit based on synchronized switching technology. *Energies* **12**(16), 3166 (2019)



LoRa-Based Wireless Sensor Network System for Aquatic Elements and Flood Early Warning Monitoring

Mattia Ragnoli¹, Gianluca Barile¹, Alfiero Leoni¹, Giuseppe Ferri¹,
Andrea Pelliccione¹, Vincenzo Stornelli¹(✉), and Dina Del Tosto²

¹ Department of Industrial and Information Engineering, University of L'Aquila, Piazzale Ernesto Pontieri 1, Monteluco di Roio, 67100 L'Aquila, Italy

vincenzo.stornelli@univaq.it

² Environment and Civil Protection Sector, Via XXV Aprile n.5b, 67100 L'Aquila, Italy

Abstract. Wireless Sensor Networks (WSNs) nowadays represent a widespread and continuously evolving scenario. This is possible, in significant manner, thanks to Low Power Wide Area Networks (LPWANs) technologies. In this paper, a LoRa based Wireless Sensor Network (WSN) flood monitoring system is presented. The design, realization and real scenario test results are presented for the reported prototype. The system is composed of a sensor node and a web section for data treatment and alarm implementation. The sensor node is microcontroller based, and communicates towards a LoRaWAN network structure by means of a LoRa transceiver. A remote web section is used for data analysis and flooding alarm. The device uses simple but low cost and robust sensors to monitor the water level. The node is powered by solar energy harvesting using a photovoltaic cell, which, thanks to the employment of a low power standby mode, allows the device to achieve energetic sufficient energy.

Keywords: Wireless sensors networks · LoRa · Environmental monitoring · Flooding · LPWAN

1 Introduction

Safety in urban and extra-urban environments can be jeopardized by natural phenomena linked to the presence of aquatic elements such as rivers, water basins, drainage channels [1, 2]. The causes of flood occurrences can be various: wind and temperature changes, rain conditions, making a forecast based approach complex and possibly not quickly responsive enough. The development of warning systems represents a necessary effort. Low Power Wide Area Network (LPWAN) technologies [3] are particularly suited for monitoring the aforementioned phenomena, including the possibility to achieve inexpensive but effective Internet of Things (IoT) systems. These structures allow the implementation of standalone devices or networks of sensor nodes of various nature, which can synergically be used to enhance safety during critical events, and to acquire large amount of useful data during normal operation.

In literature, there are many different approaches to early warning systems for natural phenomena such as earthquakes [4], forest fires [5], but also networks of sensors used to monitor dangerous situations in industrial environments [6]. This paper presents a LoRa (Long Range) based Wireless Sensor Network (WSN) system for the monitoring of aquatic elements and flood early warning, following the early prototype presented in [7].

The paper is structured as: first, a brief introduction on LoRa and LoRaWAN technologies is reported, then the description of the sensor node and system architecture is presented, along with node obtained data.

1.1 Communication Technology Overview

LoRa modulation technique, by Semtech, [8], is based on chirp spreading spectrum (CSS) modulation technique. This technology allows radio communication in environments characterized by a low signal to noise Ratio (SNR) while maintaining high energetic performances, allowing battery powered devices to enhance the working duration. LoRaWAN Medium Access Control (MAC) [9] level is often used with LoRa physical layer, enabling the possibility to implement various network topologies of sensor nodes. The standard topology is the star network, where a gateway acts as interfacing medium between LoRa radio and Internet, allowing the deployment of thousands of devices per gateway unit, respecting LoRaWAN access policy, with reduced costs. These characteristics make this modulation technique suitable for IoT (Internet of Things) applications in low link budget use cases.

2 System Architecture

The sensory system (Fig. 1) is a SAMD21 microcontroller based device [10]. Analog data sampling and manipulation is executed locally.

A LoRa radio interface, based on Semtech SX1276 transceiver [11] communicates with a LoRaWAN network structure, subsequently, a remote web section is used for information storage, analysis and warning activation. Water level and temperature sensors interfaces, along with an IMU (Inertial Measurement Unit), are equipped onboard, as well as a DS3231 Real Time Clock (RTC) [12] integrated circuit. The aforementioned level sensors are conductive metal forks that allow observing the presence of water by measuring a variation in electrical resistance at the two terminals. The sensor is inserted in a resistive bridge interface for readout using the microcontroller's Analog to Digital Converter (ADC). The device implements energy harvesting from a renewable source such as the solar harvesting, being it not connected to the electrical network. The power management is implemented using a solar cell that charges a high capacity LiPo battery by means of a charge regulator circuit. The system is designed to allow interfacing different kind of sensors without significant hardware architecture changes.

The node is part of a star network structure, where the LoRaWAN gateway represents the star center. It enables forwarding the node-obtained data towards The Things Network [13] support application through TCP/IP protocol. An HTTP integration is used to forward received payloads to Losant IoT [14] service for data analysis and alarm

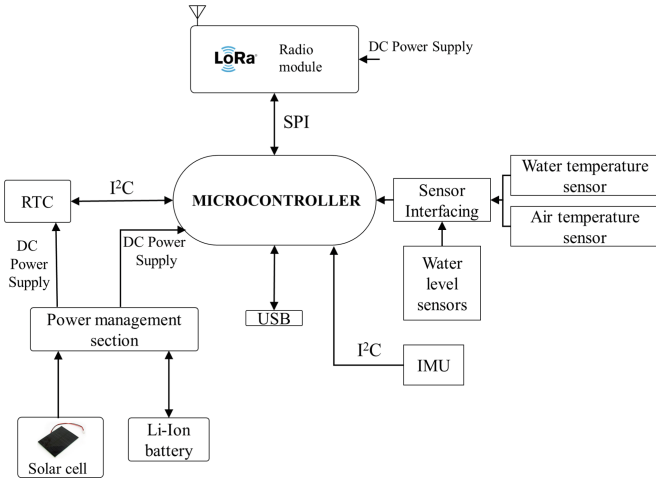


Fig. 1. Sensor node scheme

activation. The flood subjected zone is partitioned into three levels through the presence of sensors and every partition is associated to different alert priority. When water exceeds the first level, a moderate flood risk warning is enabled. If there is an overflow of the second level, a high risk alarm is actuated. If a structural vibration exceeding a determined threshold is sensed by the IMU, an interrupt is sent to the microcontroller and a packet is forwarded through LoRa radio, then an alarm is activated.

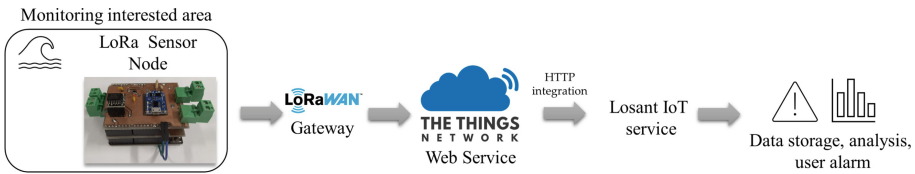


Fig. 2. Monitoring system scheme

Figure 2 shows an application scheme of the monitoring system proposed in this work.

The RTC is used to enable an interrupt-driven firmware architecture as shown in Fig. 3 block diagram. The sensor node is set in low power consumption, by setting all peripherals in standby mode, between each sampling to achieve better energy efficiency. Using this configuration it is possible to achieve full energetic sufficiency in bright days, and possibility of operation for a large interval of time in worst case of full dark or solar cell failure. The time interval between data reading and sending can be modified accordingly to the location specific needs.

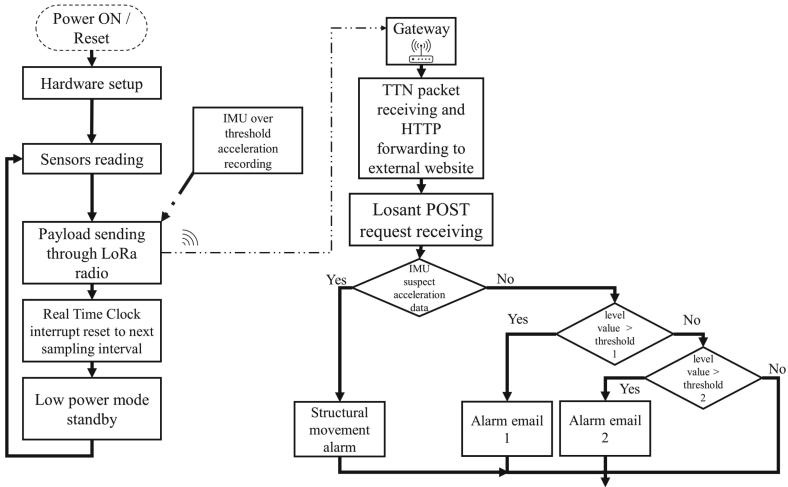


Fig. 3. Operating flow block diagram

In Fig. 4 a real example of water level diagram is reported from sampled data over a time span of 24 h, showing level reaching a warning value where the alarm mechanism is activated. This allows the authorities to be informed of a possible danger, and subsequently to activate safety procedures.

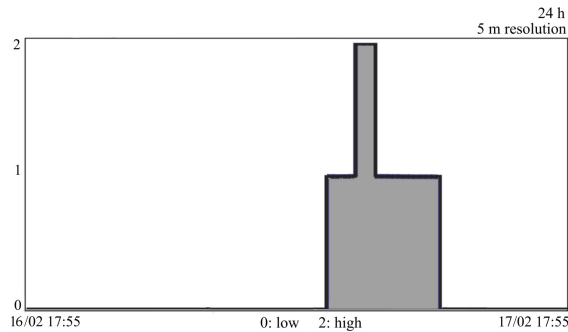


Fig. 4. Water level over 24 h time span

3 Conclusions

This paper has presented a flood monitoring system based on LoRa technology for low power communication and implementation of a LoRaWAN based wireless sensor network. The deployed devices, along with the web data manipulation infrastructure allows the use of early warning mechanisms in case of flood occurrence, while maintaining low realization costs.

Future developments of the proposed system are the deployment of a more populated sensor network, the implementation of additional sensors for a more complete environmental monitoring node and the integration of the available alarm mechanisms with the local authorities interfaces.

References

1. Pregnotato, M., Ford, A., Wilkinson, S.M., Dawson, R.: The impact of flooding on road transport: a depth-disruption function. *Transp. Res. Part D Transp. Environ.* **55**, 67–81 (2017)
2. Daniel, V.E., Florax, R.J.G.M., Rietveld, P.: Flooding risk and housing values: an economic assessment of environmental hazard. *Ecol. Econ.* **69**(2), 355–365 (2009)
3. Gulati, K., et al.: A review paper on wireless sensor network techniques in Internet of Things (IoT). *Mater. Today: Proc.* (2021)
4. Alphonsa, A., Ravi, G.: Earthquake early warning system by IOT using wireless sensor networks. In: 2016 International Conference on Wireless Communications, Signal Processing and Networking (WiSPNET). IEEE (2016)
5. Son, B., Her, Y.-S., Kim, J.-G.: A design and implementation of forest-fires surveillance system based on wireless sensor networks for South Korea mountains. *Int. J. Comput. Sci. Netw. Secur. (IJCSNS)* **6**(9), 124–130 (2006)
6. Salameh, H.A.B., Dhainat, M.F., Benkhelifa, E.: An end-to-end early warning system based on wireless sensor network for gas leakage detection in industrial facilities. *IEEE Syst. J.* (2020)
7. Ragnoli, M., et al.: An autonomous low-power lora-based flood-monitoring system. *J. Low Power Electron. Appl.* **10**(2), 15 (2020)
8. AN1200.22 LoRa™ Modulation Basics. <https://semtech.my.salesforce.com/sfc/p/#E000000JelG/a/2R0000001OJu/xvKUC5w9yjG1q5Pb2IIkpolW54YYqGb.frOZ7HQBcRc>. Accessed 18 Apr 2022
9. LoRa Alliance, What is LoRaWAN Specification. <https://lora-alliance.org/about-lorawan/>. Accessed 18 Apr 2022
10. SAMD21 32-bit ARM-Based Microcontroller. <http://ww1.microchip.com/downloads/en/DeviceDoc/40001884A.pdf>. Accessed 18 Apr 2022
11. Semtech SX1276. <https://www.semtech.com/products/wireless-rf/lora-core/sx1276>. Accessed 18 Apr 2022
12. Extremely Accurate I2C-Integrated RTC/TCXO/Crystal. <https://datasheets.maximintegrated.com/en/ds/DS3231.pdf>. Accessed 18 Apr 2022
13. The Things Network. <https://www.thethingsnetwork.org/>. Accessed 18 Apr 2022
14. Losant IoT. <https://www.losant.com/>. Accessed 18 Apr 2022



Quartz Crystal Microbalance Study in Controlled Environment for Particulate Matter Sensing

Ettore Massera^{1(✉)}, Luigi Barretta², Maria Lucia Miglietta¹, Brigida Alfano¹,
and Tiziana Polichetti¹

¹ ENEA, CR-Portici, P.le E. Fermi 1, 80055 Napoli, Italy
ettore.massera@enea.it

² STMicroelectronics - V.le Remo De Feo 1, 80022 Arzano, NA, Italy

Abstract. Today, air quality sensors miniaturization is a trending topic for industry research. Market demand for wearable devices with “internet of things” capabilities has exponential growth. Particulate matter sensors in consumer electronics are all based on the optical particles counter mechanism and are always too bulky. As an interesting alternative we propose a study on a commercial quartz crystal microbalance showing the correlation between its electronic features and the measurement of the particulate matter present in the air with a reference instrument. We also present preliminary measurements for a quartz crystal microbalance which surface is covered by a layer of graphene nanoplatelets making a comparison with the pristine one.

Keywords: QCM · PMS · PM Sensors · Particulate matter · Aerosol

1 Introduction

Environmental air quality quantification is a fundamental need for public health. Pervasive monitoring and the estimation of the exposure to air pollutants by a single person is the reason that drives research to Internet of Things (IoT) gas sensor systems easy to install and transport [1]. Very ambitious is to get to wear such a system as a pouch bag or even a fitness armlet. The Italian Project S.A.L.V.O. (Creation of a multi-sensor node for monitoring work environments) aims to demonstrate the feasibility to realize a wearable prototype of an IoT sensor system for enhancing worker safety. Among all the sensors, the Particulate Matter Sensor (PMS) needs high research efforts to reduce its size. By definition, the particulate matter measurement is a mass concentration estimation of size-defined particles dispersed in an air volume. Several Low-Cost PM sensors (LCPMS), useful for portable embedded systems, are already present on the market, and research literature is rich in articles discussing their performance [2]. LCPMS sensors' bottleneck is their dimension and accuracy. Typically their smallest volume is about some cube centimeter. Here, we show how micro

electro-mechanical system (MEMS) technology can be a suitable tool to achieve the micro dimension and a MEMS microbalance system [3] could aspire to replace LCPMS for the particulate matter measurement. As a proof of concept, a way to comfortably evaluate on a macroscopic scale the physics of an oscillating membrane is to adopt a commercial Quarz Crystal Micro-balance (QCM). This work illustrates a study of a commercial QCM in a controlled environment exposed to a standard reference material. A comparison between a bare QCM and one QCM with surface covered with graphene nanoplatelets was also conducted in order to investigate the effect of different electrostatic features of the sensing surface.

2 Experimental

The experimental set-up can be outlined by different parts described below.

2.1 The QCM Sensor System

The QCM tested, made by OpenQCM factory [4], is silicone dioxide layer AT-cut piezoelectric quartz crystals (Fig. 1-left). Active diameter is 14 mm; quartz thickness is 160 μm ; electrodes are in gold/titanium; fundamental oscillating frequency is 5 MHz. QCM is installed on a 14 mm QCM quartz holder (Fig. 1-right). The quartz signals are wired using a USB 3.0 male that can be easily connected to a powerful electronic PCB based on a network analyzer. A Python software installed on a PC connected to the USB port, give a useful graphical user interface that allows to change parameters, see the signal's time evolution, and record measurement Logs.

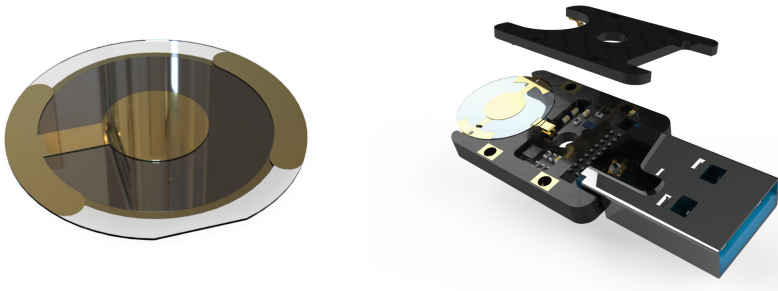


Fig. 1. On the left the Quarz Crystal Microbalance produced by OPENQCM; on the right the QCM holder with the USB connector.

2.2 The PM Chamber for the QCM Study in Controlled Environment

An acrylic trapezoidal box of about 440Lt (PM chamber) is installed in a conditioned environment of a volume of 15 m³. Temperature and humidity variation are mitigated by the conditioned environment. A filtered ventilation system reduces the content of dust, PM and potential volatile organic compounds to ensure a quasi-zero air supply and avoid background interference. Furthermore, inside the PM chamber is installed an accurate temperature and humidity sensor that logs this two environmental parameters during the experiments.

The PM chamber is equipped with a dust injector TOPAS SAG-410 that ensures a continuous, constant PM dosing and homogeneous diffusion with a compressed air injector. For all the experiments, the certified ISO 12103-1 Arizona test dust [5] is dispensed. This dust is composed by particulate with a wide spread of particle dimensions. The gravimetric PM measurement divides particulate in different bins correlated to the particle dimension. As example $PM_{2,5}$ refers to the mass concentration expressed in $\mu\text{g}/\text{m}^3$ of particulate with particles equal or less of 2,5 μm . In the Arizona test dust are present particles ranging from 1 μm to 100 μm .

A certified optical PM sensor “TSI DustTrak 8533” is used as reference instrument for the PM measurement in air. This instrument is certified on the Arizona test dust and is capable to measure PM_1 , $PM_{2,5}$, PM_4 , PM_{10} and the total Particulate Matter PM_{tot} .

2.3 The QCM Exposure to PM

We recorded two sessions of in-air dust-injection, one with a bare QCM (QCM0) and the other one with a QCM (QCMC) functionalized with a graphene nano platelets layer.

This material was prepared by direct exfoliation of natural graphite flakes in hydro-alcoholic solvent [6]. Few microliter of the graphene dispersion were then drop-casted onto the quartz crystal microbalance surface, previously silanized to favour the adhesion.

First overtone resonance frequency at 15 MHz and the dissipation module (S) [7] are chosen as key-features. In each experimental session, membranes are continuously exposed from zero to above 5 mg/m³ of total PM. Sessions are recorded in two different days, dust exposure has different time exposure and intensity injection for the two session. Fig 2-left illustrate the boxplot of the exposure intensity to the total PM for the two QCM during the two sessions. Figure 2-right shows the time resolved PM total injection for the two membrane, black for the QCM0, red for the QCMC. QCM0 is exposed to more intensive PM but for a minor time respect to QCMC. Both the membranes are exposed for more than one hour to the dust injection.

The particle size distribution of the dust changes during measurement, in Table 1 we report the particle size percentage contribution to the total PM in two conditions: during the injection, when the total PM is 5 mg/m³ and 30 min

after the injection stop (the total PM collapse to $0,5 \text{ mg/m}^3$). The table show that particles with larger size decay more quickly. Considering particles with the same size, the characteristic time decay depends principally by the chamber geometry and other environmental parameters.

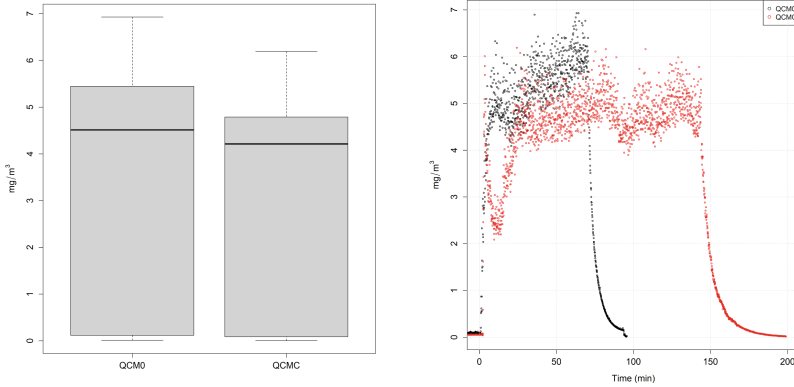


Fig. 2. On the left box plot of intensity distribution related to the PM Total measured during the dust exposure of QCM0 and QCMC in the two sessions; on the right the time resolved PM total exposure for QCM0 (black) and QCMC (red).

Table 1. Particle size (D) percentage contribution to the total PM during the injection (total PM = 5 mg/m^3) and after 30 mins PM decay (PM total = $0,5 \text{ mg/m}^3$)

Particles dimension (μm)	$D < 1$	$1 < D < 2,5$	$2,5 < D < 4$	$4 < D < 10$	$D > 10$
During injection (%)	61,3	8,85	9,8	15,375	4,675
after PM decay (%)	79,3	11,425	7,275	2	0

3 Results and Discussion

During the dust injection first overtone frequency resonance and dissipation module (S) are recorded. As the dust settles on the surface, resonant frequency shift and S increase. The variations of the resonant frequency are strongly dependent on the variation of the membrane temperature. The same does not happen for S , therefore we focused on the S behaviour. in Fig. 3 the plots illustrate the increment of S for the QCM0 (left plot) and QCMC as the integral of the injected total PM increases.

It can be seen that the parameter S is able to follow the integral of the total injected PM quite well, thus suggesting to investigate the correlation between the PM and the time differential of S ($\Delta S/\Delta t$). Adopting a simple linear regression model between $(\Delta S/\Delta t)^\alpha$ and the PM_x measured by the reference instrument

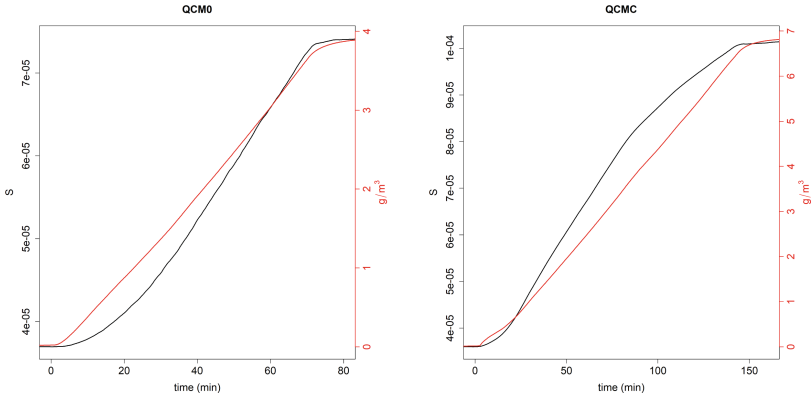


Fig. 3. Dissipation module S increase (black line) due to the increase of the accumulated total PM injected in the PM chamber (red line). On the left the QCM0 plot while on the right is the QCMC plot.

Table 2. Coefficient of determination R^2 and the slope B (expressed in $m^3 * mg^{-1} * sec^{-1}$) for the simple linear regression model between $(\frac{\Delta S}{\Delta t})^\alpha$ and the PM bins value measured by the reference instrument with α that can assume 0, 5; 1; 2

	QCM0						QCMC					
	R^2			B			R^2			B		
	$\sqrt{\frac{\Delta S}{\Delta t}}$	$\frac{\Delta S}{\Delta t}$	$(\frac{\Delta S}{\Delta t})^2$	$\sqrt{\frac{\Delta S}{\Delta t}}$	$\frac{\Delta S}{\Delta t}$	$(\frac{\Delta S}{\Delta t})^2$	$\sqrt{\frac{\Delta S}{\Delta t}}$	$\frac{\Delta S}{\Delta t}$	$(\frac{\Delta S}{\Delta t})^2$	$\sqrt{\frac{\Delta S}{\Delta t}}$	$\frac{\Delta S}{\Delta t}$	$(\frac{\Delta S}{\Delta t})^2$
			10^{-5}	10^{-7}	10^{-11}				10^{-6}	10^{-7}	10^{-11}	
PM_1	0,866	0,852	0,771	1,2	1,8	2,1	0,588	0,711	0,855	9,6	1,6	2,3
$PM_{2,5}$	0,865	0,851	0,770	1,1	1,6	1,83	0,588	0,711	0,854	8,4	1,4	2,0
PM_4	0,861	0,846	0,764	0,93	1,4	1,6	0,591	0,713	0,853	7,4	1,2	1,7
PM_{10}	0,844	0,825	0,739	0,76	1,1	1,3	0,603	0,721	0,850	6,2	1,0	1,4
PM_{tot}	0,836	0,816	0,728	0,71	1,1	1,2	0,605	0,721	0,846	5,9	0,97	1,3

in the different bins with α that can assume 0, 5; 1; 2 we express in Table 2 the capability of S for the two membrane to measure the different PM fractions considering as benchmarks the coefficient of determination R^2 and the slope B estimated in the linear regression.

Both the QCM show values of $R^2 > 0,85$ for PM fractions PM_1 , $PM_{2,5}$ and PM_4 indicating a good correlation that can compete with commercial LCPMS [2]. Even if the sensitivities (the slope B) of the two QCM are quite similar, they show different behaviour with dust exposure: for QCM0 best correlation values are obtained with $\alpha = 0,5$ while for QCMC the same happen with $\alpha = 2$. This different behaviour can be attributed to the surface functionalization of QCMC and is worth to be further investigated in a next work.

4 Conclusion

With this work, we illustrate an experimental methodology to characterize quartz crystal micro-balance exposed to PM dispersed in ambient air. We demonstrate the ability of QCM to measure PM. Besides the good potentiality of the proposed method, this preliminary work showed that QCM surface functionalization could improve selectivity and sensitivity to the different PM fractions and deserves to be further investigated. This work can be then considered a starting point to the development of a PM sensing technology based on oscillating membranes that targets the miniaturization of LCPMSs.

Acknowledgment. Research reported in this publication was supported by S.A.L.V.O. project. Funding from the National Programs (PON) of the Italian Ministry of Economic Development (MISE): code B48I20000050005 (Prog n. F/190012/01/X44).

References

1. De Vito, S., Fattoruso, G., Toscano, D.: An IoT based approach to ultra high resolution air quality mapping thorough field calibrated monitoring devices. No. EGU22-9376. Copernicus Meetings (2022)
2. Alfano, B., et al.: A review of low-cost particulate matter sensors from the developers' perspectives. *Sensors* **20**(23), 6819 (2020)
3. Foncellino, F., Barretta, L., Massera, E., Corigliano, A.: Piezoelectric mems for microparticles detection. *IEEE Sens.* **2021**, 1–4 (2021). <https://doi.org/10.1109/SENSORS47087.2021.9639237>
4. Novaetech, S.R.L.: Spin-off Company of the National Institute for Astrophysics (INAF). <https://openqcm.com/>
5. ISO 12103-1, A2 FINE TEST DUST. <https://www.powdertechinc.com/product/iso-12103-1-a2-fine-test-dust/>
6. Fedi, F., et al.: A study on the physicochemical properties of hydroalcoholic solutions to improve the direct exfoliation of natural graphite down to few-layers graphene. *Mater. Res. Express* **2**(3), 035601 (2015)
7. Dixon, M.C.: Quartz crystal microbalance with dissipation monitoring: enabling real-time characterization of biological materials and their interactions. *J. Biomol. Tech.* **19**(3), 151–8. PMID: 19137101; PMCID: PMC2563918 (2008)



3D-Printed Capacitive Accelerometers

Massimo Scarsella[✉], Gianluca Barile, Laura Iacoboni, Stefano Ricci,
Vincenzo Stornelli, and Giuseppe Ferri

Department of Industrial and Information Engineering and Economics, University of L'Aquila,
67100 L'Aquila, Italy

massimo.scarsella@graduate.univaq.it

Abstract. The aim of this work is to show the possibility to realize accelerometers through 3D-printing technique and to investigate the potentiality of these devices. The feasibility of such accelerometers is studied considering the capability of printers to extrude both insulating and conductive materials. Different types of geometries with different characteristics and performance are carefully analyzed and their advantages and disadvantages are determined. The research focuses mainly on differential capacitive accelerometers, today extremely widespread and that can be realized relatively easily via 3D printing, provided that both insulating and conductive materials can be used with the same printer. The printed sensor has been stimulated on each axis with mechanical oscillations produced by a loudspeaker connected to a signal generator. The output signal from the sensor has been read employing an electronic interface for differential capacitive sensors. The obtained experimental results are in a good accordance with those theoretically predicted.

1 Introduction

In recent years, accelerometers have become extremely widespread devices. Probably, the main reason behind this fact is that the determination of the acceleration to which a system is subjected is fundamental in the monitoring and control of many phenomena, since, through integration, it is possible to obtain also position and speed. For example, through an accelerometer we can measure the acceleration of gravity, or the inclination of the accelerometer itself if it is stationary, being known the direction and the intensity of the force of gravity. Some common applications are control and stabilization of automated mechanical systems, monitoring of vibratory phenomena such as seismic activity and machinery vibrations, blur-free image capture in cameras, and device tilt and motion detection in mobile phones [1, 2].

Today, these instruments have diversified themselves in dozens of different types. In particular, this research focuses mainly on differential capacitive accelerometers. This is done mainly for two important reasons. The first one is that they can be realized relatively easily via 3D printing, provided that both insulating and conductive materials can be used with the same printer. Moreover, 3D printing is becoming accessible to a growing audience, mainly thanks to the reductions in costs of 3D printers. This means that today is it possible to realize prototypes of a great variety of devices in an

economical and rapid way. The second one is that today differential capacitive sensors are extremely widespread; consequently new and improved solutions for the electronic reading interface are continuously developed. For example, solutions that can operate on a full-range sensor variation have been developed in [3, 4]. In addition to this, capacitive accelerometers are typically less prone to problems related to noise and temperature as compared to other types, such as piezoelectric accelerometers. Other advantages regard low power consumption, bias and scale factor stability.

For these reasons, in this paper we show that it is possible to join the benefits of 3D printing and capacitive sensing by presenting the results obtained in the realization of a 3D-printed capacitive accelerometer.

2 3D Printing Technology

2.1 Main Features and Design Flow of 3D Printing

Today, 3D printing technology is a useful tool for rapid prototyping of devices and systems [5]. Thanks to it, a significant reduction in planning times and costs is possible. Moreover, the technology research in the field of 3D printing could lead in the future to the development of new technologies and new materials that can be used in 3D printing, making the realization of printed accelerometers even more interesting in the future. The fact that many modern printers allow the extrusion of more than one material in a single printing process, together with the availability of conductive and insulating materials for 3D printing, make it possible to create printed capacitive accelerometers. Finally, one of the most important opportunities offered by 3D printing technology in the production of 3D printed sensors is the possibility of carrying out an ad-hoc design of the sensor for the specific application.

3 Capacitive Accelerometers

3.1 Basic Operation and Principles

As for other types of accelerometers, a capacitive accelerometer relies on the exploitation of a mobile mass to vary a system of capacitance. Typically, to make the mass mobile and exploit its inertia to detect accelerations, the elastic properties of the materials are exploited, which in the presence of stresses behave in many respects like a spring. This point is further clarified with reference to Fig. 1, which illustrates the operating principle of all capacitive accelerometers.

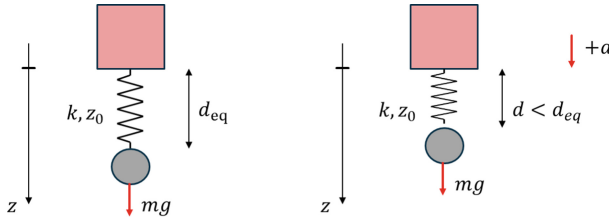


Fig. 1. Basic Operation in absence (left) and presence (right) of an acceleration along z .

As can be seen in Fig. 1, if in absence of acceleration along the z -axis we have a certain distance between the mobile mass and the fixed end, in presence of an acceleration along the positive z direction, the same distance will be smaller, indicating that the system is subject to an acceleration. In this simple approximated example, the spring represents the elastic properties of a solid material.

In capacitive accelerometers, this basic principle is used to vary a system of capacitances. For example, in the biaxial case and neglecting parasitic parameters, a typical equivalent electrical for a capacitive accelerometer is the circuit shown in Fig. 2, where all the capacitances are in general function of the acceleration in both directions x and y .

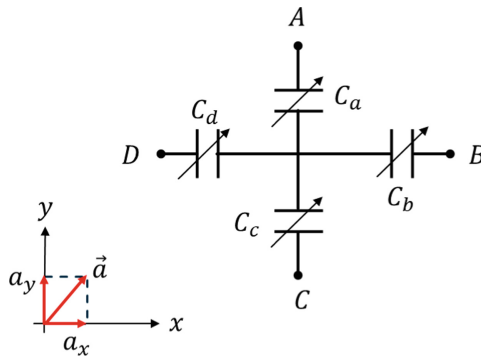
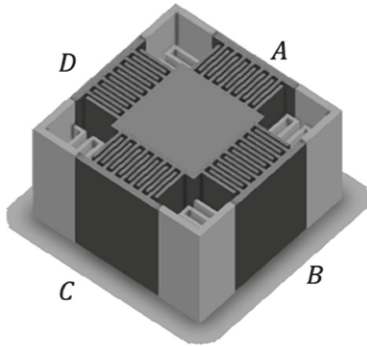


Fig. 2. Equivalent circuit for a biaxial capacitive accelerometer.

3.2 Tested Geometries

Different types of geometries with different characteristics and performance have been carefully tested and analyzed. In this section we describe the main characteristics of the realized geometries.

An example of a 3D-printed capacitive accelerometer is shown in Fig. 3. The black part represents the conductive material, while the white material is the insulator that separates conductive parts and is also used to realize the springs. Neglecting parasitic parameters, the device can be represented with the electrical circuit shown in Fig. 2, where all the capacitance values can sense the acceleration in both directions x and y .



$$C = \sum_{i=1}^N (\epsilon S/d) = (N - 1)(\epsilon S/d)$$

Fig. 3. Example of biaxial accelerometer.

The values of the capacitances can be estimated using simple approximated formulas or, alternatively, through the use of electrostatic simulation tools, and both the approaches have been used in this work. Since the device has been designed symmetrically, at rest (namely, in absence of accelerations) all the capacitances are approximately equal to C where N is the number of fingers for side, d is the distance between adjacent fingers, S is the facing area between adjacent fingers. If instead we have an acceleration along the x direction, the values of the capacitances will change since we will have a displacement of the central conductor from the rest position. The main limits of this geometry are the impossibility to detect acceleration on the z axis, and the fact that the capacitance values are in general function of both the accelerations along x and y axis, which is not a desirable property in general.

Another geometry able to overcome these problems is shown in Fig. 4 together with its equivalent circuit, in which the external conductive planes are not included in order to show the internal detail of the device. Unlike the previous one, this geometry is triaxial, and neglecting undesirable parasitic parameters the value of each capacitance depends only on the accelerations on its axis.

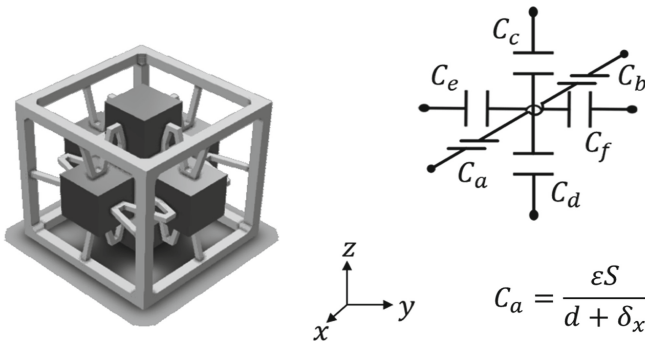


Fig. 4. Example of triaxial accelerometer.

4 Experimental Results

4.1 Experimental Setup and Results

The printed sensor has been stimulated with mechanical oscillations produced by a loudspeaker, connected to a signal generator. This experimental setup is shown schematically in Fig. 5. In this way, the printed sensor has been tested by stimulating it on a single axis and using an electronic reading interface for differential capacitive sensors described in [6]. Figure 6 shows the trend of the output voltages from the interface as the amplitude and frequency of the mechanical oscillations applied to the sensor vary. The results are in excellent agreement with those expected theoretically. As can be seen in Fig. 6, the output voltage increases as the amplitude of the signal applied to the loudspeaker increases and decreases as the frequency increases with a low-pass behavior. The obtained output voltages are of the order of millivolts, as the sensor is rather large to obtain appreciable capacitance values, and consequently the springs are rather robust to support the mass that moves only slightly.

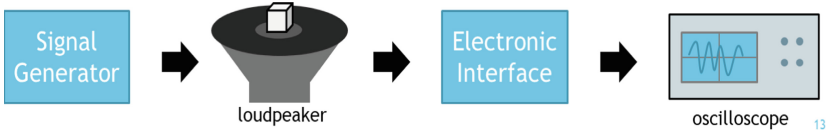


Fig. 5. Experimental setup.

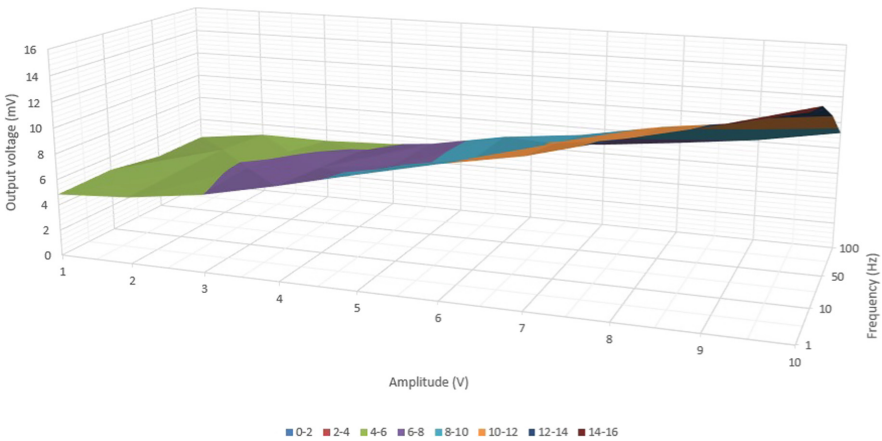


Fig. 6. Output voltage as a function of input oscillation parameters.

5 Conclusion

In this paper, the possibility to realize 3D-printed capacitive accelerometers has been investigated. The study shows that such devices can be realized using a printer able

to extrude both conductive and insulating materials. The technology research in the field of 3D printing could lead in the future to the development of new technologies and new materials that can be used in 3D printing, making the realization of printed accelerometers even more interesting. Moreover, the possibility of carrying out an ad-hoc design of the sensor for the specific application makes the realization of 3D printed sensors extremely interesting.

References

1. Tavakoli, H., Sani, E.A.: A new method for eliminating cross axis sensitivity in two axis capacitive micromachined accelerometers. In: 2013 21st Iranian Conference on Electrical Engineering (ICEE), pp. 1–5 (2013). <https://doi.org/10.1109/IranianCEE.2013.6599678>
2. Sethuramalingam, T.K., Vimalajuliet, A.: Design of MEMS based capacitive accelerometer. In: International Conference on Mechanical and Electrical Technology 2010, pp. 565–568 (2010). <https://doi.org/10.1109/ICMET.2010.5598424>
3. Barile, G., et al.: A CMOS full-range linear integrated interface for differential capacitive sensor readout. *Sens. Actuators A* **281**, 130–140 (2018)
4. Depari, A., et al.: Autobalancing analog front end for full-range differential capacitive sensing. *IEEE Trans. Instrum. Meas.* **67**, 885–893 (2018). <https://doi.org/10.1109/tim.2017.2785160>
5. Macdonald, E., et al.: 3D printing for the rapid prototyping of structural electronics. *IEEE Access* **2**, 234–242 (2014). <https://doi.org/10.1109/ACCESS.2014.2311810>
6. Ferri, G., Stornelli, V., Parente, F., Barile, G.: Full range analog wheatstone bridge-based automatic circuit for differential capacitance sensor evaluation. *Int. J. Circuit Theory Appl.* **45**, 2149–2156 (2016). <https://doi.org/10.1002/cta.2298>



A Novel Sensor Node for Smart Personal Protective Equipment

Fabrizio Formisano¹✉, Antonio Del Giudice¹, Michele Dellutri²,
Girolamo Di Francia¹, Giuseppe Loffredo¹, Armando Picardi⁴, and Stefano Salvatori³

¹ ENEA Portici, Naples, Italy

fabrizio.formisano@enea.it

² STMicroelectronics, Milan, Italy

³ University Niccolò Cusano, Rome, Italy

⁴ University Giustino Fortunato, Benevento, Italy

Abstract. Personal protective equipment (PPE) has been finding interesting opportunities of improvement as a consequence of the rapid diffusion of IOT technologies. PPE devices can provide a valid support in mitigation of hazards at work emanating from production process. In the unfortunate case of imminent risk or work accident a responsive cloud-connected PPE, could dramatically reduce the first aid intervention time.

This work describes a new development system based on the results of S.A.L.V.O. project preliminary device [1]. The hardware architecture has been here upgraded allowing the monitoring of the environmental physical and chemical quantities of interest. A new software has been developed in order to efficiently control the system and the communication protocol. The sensor node exchanges messages by means of cloud connection, with a control software that gives back to the human operator a comprehensive representation of the worker exposure to dangerous gasses, loud noise, free fall event, indoor and outdoor position and Particulate Matter (PM) exposure. Preliminary trials have been conducted and the results will be reported in the last section.

The whole system serves as a test bench to prove the effectiveness of the proposed solution.

Keywords: Smart personal protective equipment · Safety on workplace · Particulate matter (PM) and gas exposure · Sensor networks

1 Introduction

In 1969 in Italy 4.858 people died at workplace [2]. Although working conditions have improved, death at work is still nowadays a significant phenomenon. In 2021, in the period January August, there were 772 deaths [2], more than three a day. The high number of accidents and “white deaths” in workplaces shows the urgent need for us to put in place countermeasures exploiting the recent advances in IOT technologies for health and safety to guarantee, control and maintain the conditions of health and safe workplace for workers. The Legislative Decree 81/08 in Italy provides obligations for the employer which is responsible of the risks assessment within the working environment and also of adopting measures to promptly prevent accidents and manage emergencies.

The employer is also obliged to equip workers with personal protective equipment (PPE). This is a critical aspect especially in case of isolated workers or in particular operating conditions for which it is necessary to equip the worker with appropriate communication systems that allow to promptly cope with risky conditions as: free fall, gas or PM over threshold, temperature or humidity out of thresholds, loud noise and user alarm. The aim of the S.A.L.V.O. project is to create a smart wearable PPE with the capabilities listed above.

Nowadays smart PPE are mostly characterized by systems that typically do not have indoor as well as outdoor location systems integrated on board. They recognize different environments by looking for dedicated wireless tags posed into the place under monitoring [3–5]. Also, there is a lack of systems with integrated physical sensor which importance is underestimated and in general they do not take into account the specificities of particulate transduction [6]. The sensor node described in this work, integrates gas, PM and physical sensors overcoming the limits mentioned before. Moreover, the sensor node has integrated RTLS and GPS modules that give the possibility to the remote operator to locate the worker in both indoor and outdoor working conditions.

The quantities of interest are regularly acquired and checked by algorithm that interprets and recognizes dangerous situations comparing the samples with thresholds. The board has enhanced communication capabilities since an important requirement of the project is the possibility to send messages over the internet to an IOT infrastructure. The last one, among other tasks, decodes the raw data received and correlates them with other measurements so that a hazardous condition can be classified and immediately reported to human operator.

The hardware is divided in Communication Board (CB) and Multi Sensor Node (MSN). The functionalities of the two blocks will be presented in the next paragraph. MSN includes chemical and physical (particulate, temp, Rh, inertial, audio) sensors and exhibits the possibility to transmit over Wireless LORAWAN(R) network. As future development, there is the possibility to communicate alarm conditions to the nearby workers and to enable the implementation of artificial intelligence algorithms to interpret some others dangerous poses or gestures. The sensor node also monitors particulate matter exposure.

The rest of the work is organized as follow: next paragraph describes in detail the prototype, paragraph 3 shows the software logic behind the system and paragraph 4 reports some experimental data obtained during lab trials.

2 Sensor Node

The new sensor node will allow a continuous monitoring of the environment in which a worker is operating and will serve as test platform for both hardware and software components of the whole system for further optimizations. The system is composed by the sensor node and a remote control software. After acquired, the quantities of interest are sent to a LoraWan server (The Things Network Server [7]) which in turn sends data to an application server (TagoIO) [8]. It parses the data and shows relevant information about the status to a human operator. This paragraph describes in detail the prototype also called Sensor Node (SN). In Fig. 1 there is a first look of the SN as block diagram.

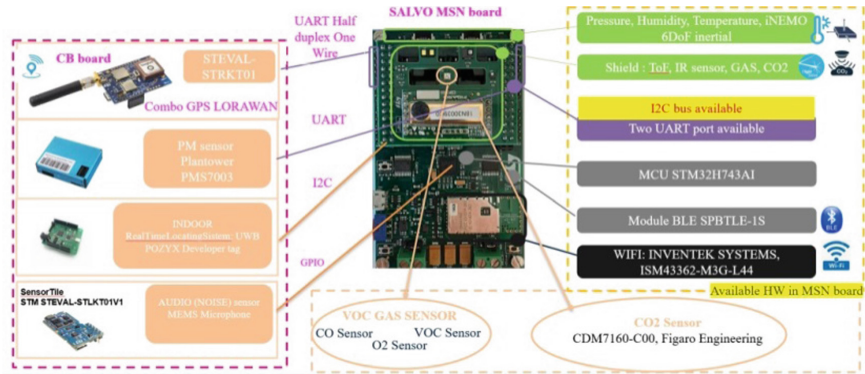


Fig. 1. Block diagram of the Sensor Node with P/N for specific boards and components.

The SN is divided in two main boards: Communication Board (CB) and Multi Sensor Node (MSN). The CB is the master in the architecture, in other words it controls the main tasks of the system e.g.: initiates the communication with the MSN, runs the main algorithm of the board and it is in charge of sending messages to the control center. The CB is the initiator and controller of communication between the two boards. In particular, it supports the following functions and actions: GPS readout, assembling and coding of the transmission data packet, LoraWan endpoint (LoraWan protocol stack management) for data transmission to next element of LoraWan infrastructure (gateway bridge).

The MSN is a slave board and contains the necessary sensors to collect information about the environmental acoustic noise (STMicroelectronics MP34DT05-A), volatile organic compound (P/N not available yet), temperature (STMicroelectronics STTS22H), relative humidity (STMicroelectronics HTS221) and motion (STMicroelectronics LSM6DSOX). The CB and MSN communicate each other by means of a serial half-duplex bus.

The MSN performs the following functions:

- readout from sensors
- acquisition and management of indoor location data through RTLS tag-shield and infrastructure (anchors)
- alarm button sampling (assistance request)
- feedback to the worker (vibration, buzzer and led)

In Fig. 2 a lab version of the system is showed. It's easy to recognize the different devices.

The SN has locating capabilities. It can determine its position both in indoor and outdoor situations. For the indoor position it exploits the functionalities of a RTLS module (UWB pozyx) mounted on the MSN. The position is obtained by triangulation algorithms of the RTLS system that uses anchors installed around in the workplace. The information obtained by the RTLS is then appended to the recorded alarm events. The outdoor position is obtained from the GPS module integrated in the CB. The SN exploits the motion sensor to capture free fall events. This information is acquired by the MSN

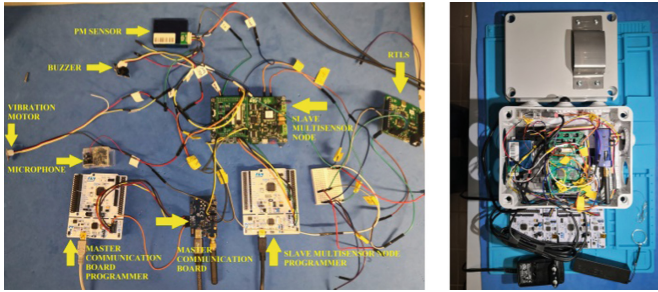


Fig. 2. Lab version of Sensor Node

and if a “free fall condition” is recognized the CB issues an alarm message and send it to the control center.

The SN also monitors the PM exposure to particles with an aerodynamic diameter equal or less than 10 and 2.5 μm by means of a PM sensor (Plantower PMS7003). Particulate matter exposure is monitored by the SN which can issue an over-threshold alarm.

The sensor node can monitor the exposure of the worker to dangerous gasses. Prototypes of VOC sensors have been used in this work while CO₂ is monitored by means of a commercial sensor. The VOC sensor is under assessment for its capability to significantly sense CO and O₂. The algorithm is based on thresholds and once exceeded an alarm is sent to the worker by means of sound and vibration of the sensor node and at the same time, it is sent to the remote operator.

The SN monitors the acoustic noise level by a separate audio board. This audio board elaborates the audio signal and raises a flag when the preset limit is exceeded. In turn, the SN when receives the flag, recognizes an alarm condition and sends a message to the operator.

3 Software

The software has been developed allowing the communication between CB and MSN. The software part that runs on the MSN, controls a loop that periodically, read all the sensors of the board and put the data in a packet ready to be withdrawn by the CB. The MSN evaluates risky situations comparing the data received with thresholds or with related parameters. It catches asynchronous events coming from the user button, the audio board and free fall events. It also manages the alarm register, low priority telemetry, CB master board requests, acknowledge from the LoraWan server and reports an alarm to the worker (buzzer, led and vibration).

The CB software controls the state machine of the node, it initiates the communication with the MSN and picks up the data representing the quantities of interest. The CB is responsible to acquire the outdoor position (GPS) of the SN, handle the LoraWan communication, prepare the transmission packet with the useful information and forward the acknowledge to MSN. The alarm messages sent to the operator are visualized on a PC or portable device with the dashboard showed in Fig. 3.



Fig. 3. Dashboard the GPS outdoor position and the RTLS indoor position

4 Lab Trials

The SN functionalities have been tested in lab. In particular, for a set of functionalities the timing of the measurement chain has been recorded since time is a critical parameter for quick assistance. The times have been measured starting from the issuing of the alarm event from the SN to their visualizations on the dashboard. All the alarms have been received successfully on the dashboard confirming the correct functionality of whole acquisition chain. Table 1 reports the measured latencies.

Table 1. Recorded latencies

Alarm type	Average time (s)
User alarm	41
Audio	20
PM	35
CO2	32
Temperature	18
Free Fall	21

5 Conclusions

A novel prototype of a Sensor Node for safety application on workplaces has been presented. The prototype will serve as a test bench for future improvement of the system and for the development of new functionalities. Wearing the SN, a worker can be monitored during the course of his work; the information sent to the control center are especially important if the worker is operating in an area where gas leaks are possible or if the worker is alone in a rough environment or if he is operating at height. The possibility to monitor PM exposure of the worker is important to prevent long term diseases.

The trial session shows that the whole system (LoraWan communication protocol and acquisition algorithms) reports an alarm condition in terms of tens of seconds.

Future works include power consumption optimization, architecture improvement, in particular, improvement of sensing capabilities and minimization of form factor.

References

1. Del Giudice, A., Dellutri, M., Di Francia, G., Formisano, F., Loffredo, G.: S. A. L. V. O.: Towards a Smart Personal Protective Equipment. In: Di Francia, G., Di Natale, C. (eds.) *Sensors and Microsystems*. AISEM 2021. LNEE, vol 918. Springer, Cham (2023). https://doi.org/10.1007/978-3-031-08136-1_44
2. <https://www.inail.it/cs/internet/home.html>. Accessed 30 Apr 2022
3. Kanan, R., Elhassan, O., Bensalem, R.: An IoT-based autonomous system for workers' safety in construction sites with real-time alarming, monitoring and positioning strategies. *Autom. Constr.* **88**, 73–86 (2018)
4. Wu, F., Wu, T., Yuce, M.R.: An internet-of-things (IoT) network system for connected safety and health monitoring applications. *Sensors* **19**, 21 (2019). <https://doi.org/10.3390/s19010021>
5. Wu, F., Rüdiger, C., Redouté, J.M., Yuce, M.R.: WE-Safe: a wearable IoT sensor node for safety applications via LoRa. *IEEE* (2018). 978-1-4673-9944-9/18/31:00
6. Basodan, R.A., Park, B., Chung, H.J.: Smart personal protective equipment (PPE): current needs, opportunities for nanotechnology and e-textiles. *Flex. Printed Electron.* **6**(4), 043004 (2021). <https://dx.doi.org/10.1088/2058-8585/ac32a9>.
7. <https://www.thethingsnetwork.org/>
8. <https://tago.io/>



Radar Sensor System for Unobtrusive Level Monitoring of Granular Solids Stored in Silos

Marco Zini¹✉, Marco Baù¹, Fabio Scubla², Matteo Loda², Giuseppe Stefini²,
Alessandro Nastro¹, Marco Ferrari¹, and Vittorio Ferrari¹

¹ Department of Information Engineering, University of Brescia, Via Branze 38, 25123 Brescia, Italy

m.zini005@unibs.it

² Invisiblefarm S.r.l., Via Rodolfo Vantini 1, 25126 Brescia, Italy

Abstract. This work explores the possibility of measuring from the outside of a fiberglass silo the level of stored granular solids, such as grains, flour, sand, or feed, by employing an unobtrusive millimeter-wave radar sensor system without the need for a specific hatch. A prototype embedding a frequency-modulated continuous-wave (FMCW) radar sensor system operating at 76–81 GHz, combined with a dedicated electronic board has been developed to acquire and manage data through Wi-Fi connection. The prototype has been installed on the outside of a fiberglass silo containing granular and dusty material with a density of about 800 kg/m³ while employing four load cells as reference measurement system. The proposed prototype has been tested over repeated cycles of load and unload of the silo, during which the level of the stored granular solid has varied between 0.5 and 5.2 m. The measurement repeatability, which defines the equivalent resolution of the sensor system, has been estimated at one standard deviation resulting in 0.037 m. The obtained experimental results show the effectiveness of the proposed radar sensor system in estimating the level of the material stored into the silo, without the need for an opening in the silo.

Keywords: Millimeter-wave radar sensor · FMCW radar · Level monitoring

1 Introduction

Level monitoring of granular solids stored in silos, such as grains, flour, sand, or feed is often required in industrial and agricultural applications [1]. Typically, mechanical sensors, such as load cells, are employed for these purposes. Even though these types of sensors are relatively cheap, tailored container designs and demanding installation procedures are typically needed. Furthermore, the density of the material stored in the silo must be known to define the filling level [1]. Alternatively, optical sensors can be used, but with the drawback of being ineffective in dusty environments or with poorly-reflective materials [2]. Similarly, ultrasound sensors can be used, yet they are unavailing with sound-absorbing materials and are affected by the speed of sound which depends largely on the propagation medium composition and on the environmental pressure and temperature [3].

Frequency-modulated continuous-wave (FMCW) millimeter-wave radar sensor systems have proven to be a viable alternative to overcome such issues [4, 5]. Compact systems are nowadays available thanks to the recent progresses in the fabrication of fully-integrated radar microchips, promoted by the intensive use in the automotive field that has made available this technology at low cost [6, 7].

In this context, the possibility of measuring unobtrusively the level of granular material stored inside a fiberglass silo by means of a millimeter-wave radar sensor system has been explored. A prototype embedding a FMCW radar sensor system operating at 76–81 GHz, and an electronic board to acquire the data and manage a remote communication through Wi-Fi connection has been developed and experimentally verified.

2 System Description

A FMCW radar system continuously transmits frequency-modulated electromagnetic waves, named chirp, and detects signal reflections due to the presence of one or more objects in its field of view (FOV).

Typically, a FMCW radar is composed of a synthesizer that generates the chirp signal x_{TX} , one or more transmitting (TX) and receiving (RX) antennas and a mixer that combines the received signal x_{RX} with the transmitted one x_{TX} generating the signal x_{IF} , as shown in Fig. 1a. The signal x_{IF} is fed to the low-pass filter (LPF) to reject high-frequency spectral components, thus leading to x_{LP} . Figure 1b shows the typical trend over time of the frequencies f_{TX} and f_{RX} of x_{TX} and x_{RX} , respectively. Specifically, f_{TX} is assumed to vary linearly from the starting frequency f_c and span the bandwidth B during the chirp time T_c .

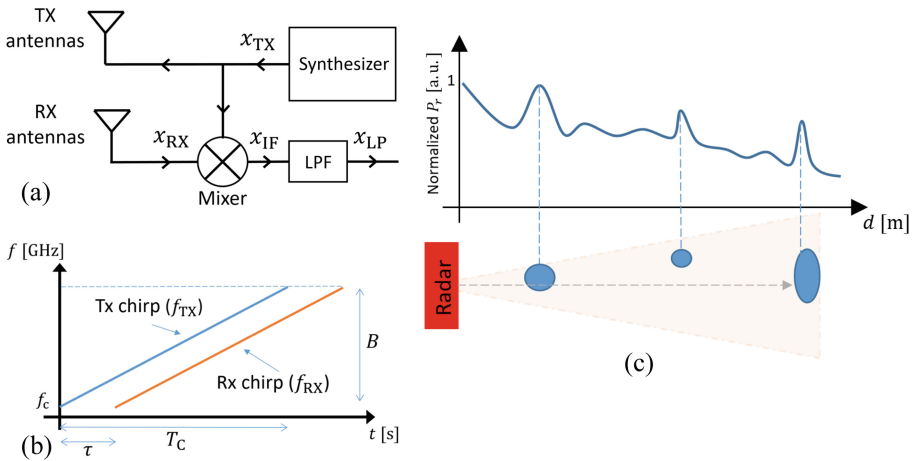


Fig. 1. a) FMCW radar block diagram. b) Frequency of the transmitted and received signals over time. c) Normalized reflected power P_r as a function of d showing peaks corresponding to three objects within the FOV of the antennas.

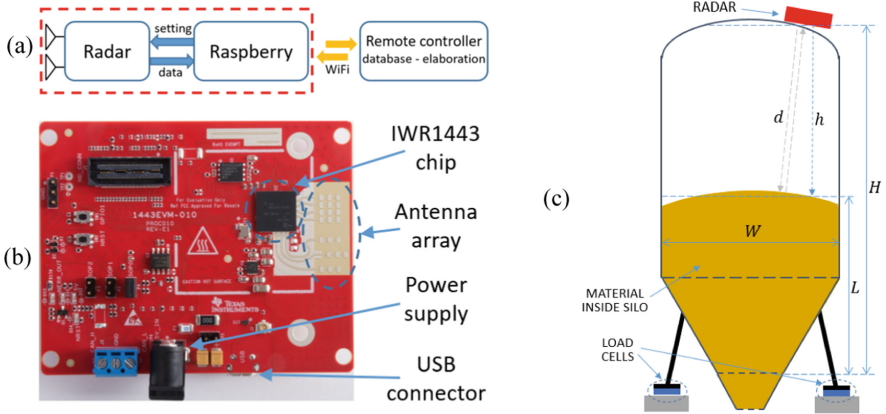


Fig. 2. a) Block diagram of the developed radar system. b) Picture of the Texas Instruments IWR1443BOOST board. c) Schematic diagram of the silo structure and radar positioning.

Considering a single object placed within the FOV at a fixed distance d from the radar, which causes the reflection of the transmitted signal, f_{RX} is expected to have the same trend of frequency variation over time as f_{TX} but delayed by a time $\tau = 2d/c$, where c is the speed of light. Figure 1c shows how the presence of one or more objects in the FOV induces peaks in the normalized reflected power P_r of x_{LP} , thus allowing to estimate the distances between the objects and the radar.

Figure 2a shows the block diagram of the developed prototype. The radar sensor is based on the Texas Instruments IWR1443BOOST development board featuring a 76–81 GHz FMCW radar sensor fabricated in TI’s 45-nm RFCMOS process, as shown in Fig. 2b. The chip is equipped with built-in electronics that also comprises hardware supporting front-end configuration, calibration, and complex operations. The board provides an antenna array composed of 3 transmitting (TX) and 4 receiving (RX) antennas with a maximum transmission power of 12 dBm, allowing for a theoretical detection range of up to 50 m. A Raspberry PI board interfaces the radar sensor, acquires data and manages the remote communication through a Wi-Fi connection.

3 Experimental Results

The prototype has been installed on the top and outside of a fiberglass silo containing sound-absorbing, granular and dusty material with a density of about 800 kg/m^3 , as shown in Fig. 2c. The silo has a total height H of 6.1 m and presents a cylindrical section with diameter W of 2.48 m in the upper part, and a conical shape in the lower part. The radar sensor has been mounted tilted to accommodate for the curved cover of the silo as shown in Fig. 3a. Given the silo dimensions, the radar board has been set with a detection range of 10 m and configured with one transmitting and two receiving antennas. The silo embeds four load cells under the feet anchors that allow for real-time measurements of the weight of the stored granular material. Considering the weight, the geometry of the silo, and the mass density of the material, the level L_w of material stored in the silo has been estimated and used as the reference value.

The level of the material L inside the silo is determined as $L = H - h$, with the assumption of $h \approx d$, as the tilt of the radar has been considered negligible. Moreover, since granular solids tend to build up a heap with non-planar surface, h has to be considered as an average value [1]. The distance h is determined from the reflected power P_r normalized to its maximum amplitude, as shown in Fig. 3b. Each peak of P_r corresponds to an object within the FOV of the antenna array. Excluding peaks located at $h < 0.5$ m, corresponding to the reflections between the radar and the top cover of the silo, no distinct peaks are evident in the raw reflected power. Therefore, to improve the signal-to-noise ratio and to estimate the average distance h , an algorithm based on consecutive acquisitions of P_r and linear filtering techniques has been devised [8]. A measurement campaign of 15 consecutive days during which the silo has been loaded and progressively unloaded has been performed. Figure 4 compares the experimental values of L and L_w measured every minute, when the level has been varied between 0.5 and 5.2 m.

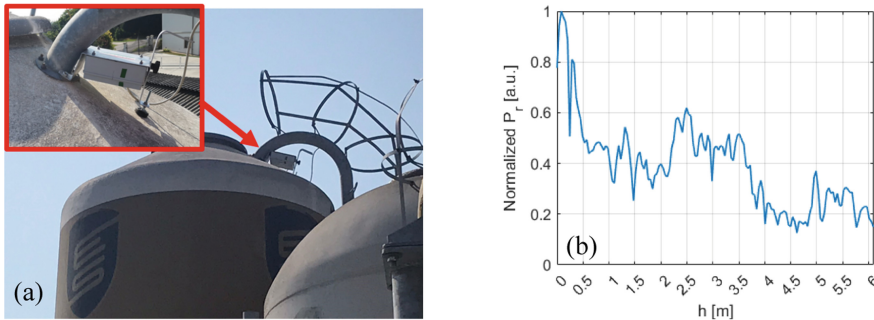


Fig. 3. a) Image of the prototype installed outside the circular fiberglass silo. b) Measured normalized reflected power P_r as a function of h .

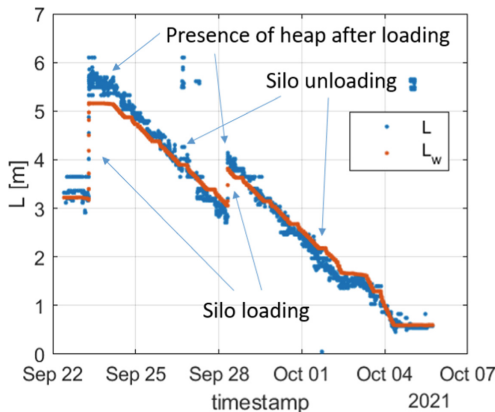


Fig. 4. Estimated and reference levels L and L_w obtained employing the radar and load cells systems, respectively, for a measurement campaign of 15 days, measured every minute.

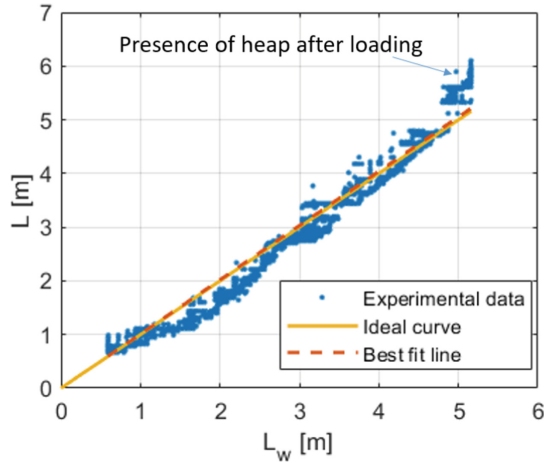


Fig. 5. Comparison between the radar estimated level L and reference level L_w .

The discrepancy between L and L_w after the first silo loading is probably related to the formation of heap due to the loading process from the top. This discrepancy is also present after the second loading even if less accentuated, probably due to a lower amount of loaded material. Minor deviations between L and L_w can be observed for $L < 2$ m, i.e. in correspondence of the beginning of the conical part of the silo. Such deviations can be attributed to inaccuracies in the estimation of the material level from the load cells system.

As shown in Fig. 5, the best fit line of L against L_w has a slope of 1.06, i.e. close to the ideal line, showing the effectiveness of the radar sensor system to estimate from the outside the level of the material stored into the silo, within the explored range. The discrepancy that can be observed for L around 5 m has been ascribed to the formation of a heap in the loading process. The measurement repeatability, which defines the equivalent resolution of the sensor system, has been estimated at one standard deviation over 100 repeated measurements at the fixed level $L_w = 3.63$ m, resulting in 0.037 m.

4 Conclusions

A radar system for unobtrusive level monitoring of granular solids, such as grains, flour, sand, or feed stored in silos has been presented. The proposed system is based on a commercial 76–81 GHz FMCW radar sensor and a Raspberry PI board to acquire the data and manage a remote communication through Wi-Fi connection. A tailored algorithm has been devised to elaborate the reflected power returned by the system, improving the signal-to-noise ratio and the estimation of the material level inside the silo. The developed prototype has been installed outside the top face of a cylindrical fiberglass silo containing sound-absorbing, granular and dusty material. The system has been tested for 15 consecutive days during which the silo has been loaded and progressively unloaded in the level range between 0.5 and 5.2 m. The effectiveness of the system has been verified comparing the estimated level of the material obtained exploiting the radar and the load cells




system. Performing 100 repeated measurements of P_r at the fixed level $L_w = 3.63$ m, the resolution has been estimated as 0.037 m.

References

1. Vogt, M., Michael, G.: Silo and tank vision: applications, challenges, and technical solutions for radar measurement of liquids and bulk solids in tanks and silos. *IEEE Microw. Mag.* **18**(6), 38–51 (2017)
2. Ryde, J., Hillier, N.: Performance of laser and radar ranging devices in adverse environmental conditions. *J. Field Robot.* **26**(9), 712–727 (2009)
3. Panda, K.G., Agrawal, D., Nshimiyimana, A., Hossain, A.: Effects of environment on accuracy of ultrasonic sensor operates in millimetre range. *Perspect. Sci. Recent Trends Eng. Mater. Sci.* **8**(September), 574–576 (2016)
4. Lin, J., Li, C., Chang, C.-C., Tsai, T.-H., Zito, D., Chang, S.-F.: Review —semiconductor integrated radar for sensing applications. *ECS J. Solid State Sci. Technol.* **7**(7), Q3126–Q3142 (2018)
5. Edvardsson, O.: An FMCW radar for accurate level measurements. In: 1979 9th European Microwave Conference, pp. 712–715 (1979)
6. Parra, Y.G., et al.: Development of a low-cost, short-range radar system to measure speed and distance. *Tecciencia* **12**(22), 99–106 (2017)
7. Jeong, S.H., Lee, J.E., Choi, S.U., Oh, J.N., Lee, K.H.: Technology analysis and low-cost design of automotive radar for adaptive cruise control system. *Int. J. Automot. Technol.* **13**(7), 1133–1140 (2012)
8. Hsiao, T.-W., et al.: A novel moving average method of vehicle detection in the fmcw radar using antennas with different beamwidths at k-band. In: 2015 IEEE 6th International Symposium on Microwave, Antenna, Propagation, and EMC Technologies (MAPE), pp. 136–139 (2015)



Fusion Analysis of a Palmprint-Hand Geometry Multimodal Ultrasound Recognition System

Monica Micucci  and Antonio Iula  

University of Basilicata, 85100 Potenza, Italy
antonio.iula@unibas.it

Abstract. Multimodal biometric systems are employed in several application fields due to series of advantages in terms of universality and recognition rate. Compared to other technologies, Ultrasound has many advantages, because it allows to obtain 3D images of human body and to verify liveness. In this work, a multimodal ultrasound recognition system based on the fusion of palmprint and hand geometry is proposed and experimentally evaluated. Volumetric hand images are acquired by using water as coupling medium and 2D rendering are obtained at various depth levels. Successively, 2D and 3D features are extracted both for palmprint and hand-geometry. Recognition performances are evaluated through verification experiments by employing a homemade database, first by considering the single characteristics and successively by fusing them. Results demonstrated a drastic improving of results with the fusion but not necessarily the best fusion result is obtained by considering the best palmprint and hand geometry.

Keywords: Multimodal systems · 3D Hand Geometry · 3D Palmprint

1 Introduction

The increasing demand for major security has led to the emergence of multimodal biometric systems, which consist of a combination of two or more biometric characteristics. Their peculiarity makes such systems employed in an increasing number of applications. Multimodal systems show a series of benefits compared to biometric systems based on a single characteristic improving universality, recognition rate, security [1, 2]. Furthermore, they provide the possibility of authenticating users for which one of the single biometric cannot be detected. Multimodal systems based on the use of a single sensor for image acquisition are increasingly investigated because allow to achieve cost-effectiveness and improved acceptability from users [3]. This singularity is mostly valid for hand-based characteristics, such as fingerprint, palmprint, hand vein, hand geometry whose features can be extracted from a single image. Among various acquisition technologies experimented with for collecting hand images, Ultrasound results very attractive and interesting due to the peculiarity of acquiring volumetric images of the human body allowing more accurate features and the capability to verify liveness and making the system insensible to eventual contaminations on the skin such as grease, ink, and humidity [4, 5].

In the present work, fusion performances of an ultrasound palmprint-hand geometry multimodal system are experimentally analyzed and evaluated.

2 Experimental Set-Up

The system employed for acquisition of 3D hand images consists of an ultrasonic scanner (ULA-OP - ULtrasound Advanced Open Platform) [6], a numeric controlled pantograph employed as system for automatic movement of the probe (LA435 by Esaote S.P.a., Genova, Italy) consisting in a linear commercial array of 192 elements with frequency of 12 MHz [7–9]. Due to Ultrasound reflection in presence of air, a coupling medium is essential between the probe and the hand. In this work, a good acoustic coupling is guaranteed by submerging the hand and the probe in a tank full of water, with the palm directed upwards. A 3D hand image can be acquired by moving the probe along elevation direction, while several B-mode are collected and stored. In order to collect the whole hand, several parallel scans are performed. These images are combined to achieve a volume of $166 \times 200 \times 27 \text{ mm}^3$, successively post-processed to achieve the 8-bit grayscale 3D matrix of $416 \times 500 \times 68$ voxels. From hand volume, fourteen 2D images are extracted at varying under skin depth by performing a projection of the external surface of the hand along the xy plane and a translation of this surface along z inside the skin. Figure 1 reports an example of 3D hand rendering.

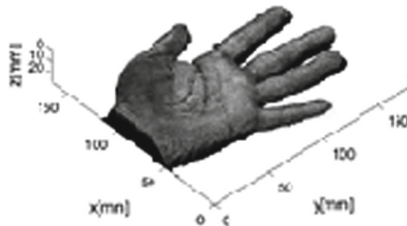


Fig. 1. Example of 3D hand rendering

3 Feature Extraction

2D and 3D features for both hand geometry and palmprint have been extracted from all fourteen 2D renderings. For hand geometry, the procedure mainly consists in defining a number of key points by defining the middle point on the wrist boundary as a reference point and calculating the distance from this point to each other point on the contour of the hand through Euclidean distance [10, 11]. Then, several points including finger peaks, middle point, valleys between fingers, other fingers base point and extra point are extracted and shown in Fig. 2a with different colors.

From such point, 26 distances, are calculated in order to define a 2D template. Such distances, as those shown in Fig. 2a include hand length, palm length and fingers' width and length.

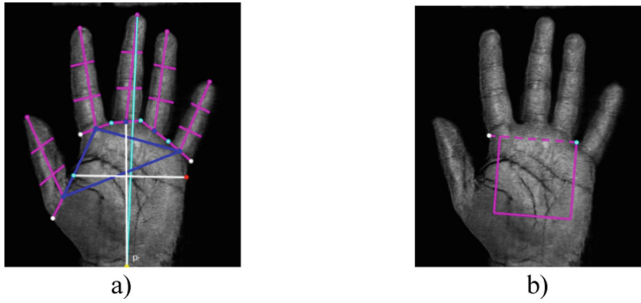


Fig. 2. a) 2D hand geometry template defined as 26 distances calculated from a number of key points; b) Palmprint ROI defined as a square from two key points of Fig. 1a.

Successively, 2D templates are combined in different ways in order to obtain three kinds of 3D template:

- Mean Features (MF): length as mean of lengths at various depths;
- Weighted Mean Features (WMF): length as weighted mean of lengths at various depths;
- Global Features (GF): lengths computed at various depths.

As regards palmprint, the Region of Interest (ROI) is extracted from human hand image by defining a square in an automatic way by exploiting two of the key points as shown in Fig. 2a. Successively, after a bicubic resize from 133×133 to 266×266 of palm image, a classical line-based procedure is performed in order to obtain 2D template [12, 13]. The algorithm mainly consists of scanning and processing the image along four directions (0° , 90° , 180° , 270°) and then summing the four binary images obtained. 2D templates are then combined through an ad hoc algorithm generating a 3D template that takes into account the principal lines' depth [13].

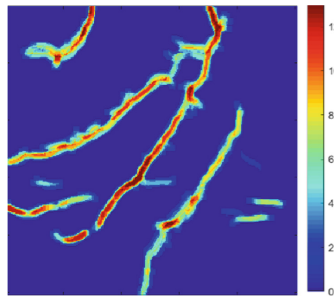


Fig. 3. Example of 3D template in a color scale representation.

This algorithm basically consists of two operations repeated 14 times: dilatation of current template with structuring element of β dimension and logical AND between

pixels of current dilated template and next depth template. Final result is represented by a color scale matrix where the value of each pixel varies from 0 to 13 (see Fig. 3).

4 Experimental Results

In order to evaluate the recognition capability of the proposed system, verification experiments are carried out by exploiting a home-made database containing 110 samples acquired from 50 volunteers [14]. Initially, experiments are carried out for each single biometrics. For both cases, verification involves a series of matching between each template for all others contained in the database, obtaining for each comparison a score that represents the distance between two templates. For hand geometry, the matching score is defined through the computation of absolute distance both for 2D and 3D templates:

$$AD = \sum_{i=1}^{26} |Q_i - R_i| \quad (1)$$

where Q is query template and R is the reference template.

For palmprint, the matching formula for 2D templates is based on a classic pixel-to-area approach consisting in a logical AND operation between the corresponding pixels of the two templates:

$$2Dscore = \frac{2}{M_R + M_Q} \sum_{i=1}^n \sum_{j=1}^n R(i, j) \oplus Q(i, j) \quad (2)$$

where Q is query template and R is the reference template, respectively, M_R and M_Q are the sum of white pixels in R and Q, respectively.

As regards 3D templates, the above formula is modified by inserting an additional term that accounts for the difference of depth between the two 3D matching templates through a parameter α :

$$3Dscore = \frac{2}{M_R + M_Q} \sum_{i=1}^n \sum_{j=1}^n R(i, j, 1) \oplus Q(i, j, 1) \\ \oplus |O_R(i, j) - O_Q(i, j)| < \alpha \quad (3)$$

where Q is query template and R is the reference template, respectively, M_R and M_Q are the sum of white pixels in R and Q, respectively, $O_R(i, j)$ and $O_Q(i, j)$ are the occurrences of value “1” in R(i, j, k) and Q(i, j, k) and α is an integer which values varies from 0 to the number N of 3D template levels.

If score results from comparison between two templates belonging to the same user, it is called genuine; instead, if it results from a comparison between templates of different user, it is an impostor score.

Successively, two biometric systems are combined at matching-score level by through a method called matcher weighting (MW) [15, 16]:

$$R_{MW} = w_i R_i \quad w_i = \frac{\frac{1}{e_i}}{\sum_{i=1}^n \frac{1}{e_i}} \quad (4)$$

where w_i is the weight of R_i , e_i is the corresponding EER, and n is the number of the characteristics.

In a previous work [14], it was assumed that the best recognition performance would be achieved by combining the best hand geometry and palmprint cases, obtained by using Global Features (GF) and $\alpha = 6$, respectively. In this work, several other fusion experiments are performed by evaluating various α values for palmprint and different 3D templates for hand geometry. Figure 4 shows DET curves, which plot False Rejection Rate (FRR) versus False Acceptance Rate (FAR), for three fusion results obtained by varying α and 3D hand geometry template. As can be seen, in any case the fusion dramatically improves recognition performances. EER values, which are computed by the intersection of the first bisector with the curves, are summarized in Table 1. The data demonstrate that the best fusion result is not obtained by considering the best cases of the two single characteristics.

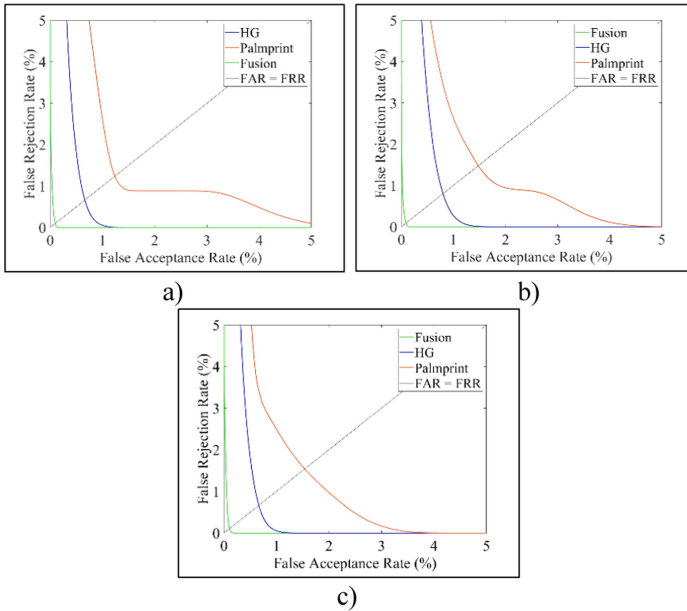


Fig. 4. DET curves reporting three fusion results: a) HG (GF)-Palmprint ($\alpha = 6$); b) HG (GF)-Palmprint ($\alpha = 4$); c) HG (MF)-Palmprint ($\alpha = 5$).

Table 1. EER values obtained for fusion experimentations

	EER		
Method	GF - $\alpha = 6$	GF - $\alpha = 4$	MF - $\alpha = 5$
HG	0.63%	0.63%	0.74%
Palm	1.18%	1.54%	1.48%
Fusion	0.08%	0.08%	0.07%

5 Conclusions and Discussion

A 3D Multimodal biometric system based on the fusion between hand geometry and palmprint is experimentally tested. 3D hand images are acquired by using water as coupling medium. Recognition performances are evaluated through verification experiments carried out on a home-made database, first by considering single modalities, successively by fusing them. Experimental results demonstrated that the fusion dramatically improves the recognition performances of the system compared to the single biometrics. Furthermore, the best fusion result is not obtained by considering the best cases of the two single characteristics. Ongoing work is dedicated to a systematic application of the fusion by varying all the parameters to maximize recognition performances of the multimodal system. Also, a more reliable acquisition system, which uses gel as coupling medium [17–19] instead of water, will be experimented.

References

1. Jaswal, G., Kaul, A., Nath, R.: Multimodal biometric authentication system using hand shape, palm print, and hand geometry. In: Verma, N., Ghosh, A. (eds.) *Computational Intelligence: Theories, Applications and Future Directions - Volume II. Advances in Intelligent Systems and Computing*, vol. 799. Springer, Singapore (2019). https://doi.org/10.1007/978-981-13-1135-2_42
2. Oldal, L.G., Kovacs, A.: Hand geometry and palmprint-based authentication using image processing. In: *Proceedings of the IEEE 18th International Symposium on Intelligent Systems and Informatics (SISY)* (2020)
3. Dai, J., Zhou, J.: Multifeature-based high-resolution palmprint recognition. *IEEE Trans. Pattern Anal. Mach. Intell.* **33**, 945–957 (2011)
4. Iula, A.: Ultrasound systems for biometric recognition. *Sensors* **19**(10) (2019)
5. Jiang, X., et al.: Ultrasonic fingerprint sensor with transmit beamforming based on a PMUT array bonded to CMOS circuitry. *IEEE Trans. UFFC* **64**, 1401–1408 (2017)
6. Tortoli, P., et al.: ULA-OP: an advanced open platform for ultrasound research. *IEEE Trans. UFFC* **56**, 2207–2216 (2009)
7. Iula, A., et al.: An enhanced ultrasound technique for 3D palmprint recognition. In: *2013 IEEE International Ultrasonics Symposium (IUS)*, pp. 978–981 (2013)
8. Iula, A., Savoia, A.S., Caliano, G.: An ultrasound technique for 3D palmprint extraction. *Sens. Actuators A* **212**, 18–24 (2014)
9. Iula, A., Nardiello, D.: Three-dimensional ultrasound palmprint recognition using curvature methods. *J. Electron. Imaging* **25**(3) (2016)

10. Sharma, S., et al.: Identity verification using shape and geometry of human hands. *Expert Syst. Appl.* **42**, 821–832 (2015)
11. Iula, A.: Biometric recognition through 3D ultrasound hand geometry. *Ultrasonics* **111** (2021)
12. Huang, D.S., Jia, W., Zhang, D.: Palmprint verification based on principal lines. *Pattern Recognit.* **41**, 1316–1328 (2008)
13. Iula, A., Nardiello, D.: 3D ultrasound palmprint recognition system based on principal lines extracted at several under skin depths. *IEEE Trans. Instrum. Meas.* **68**(12), 4653–4662 (2019)
14. Iula, A., Micucci, M.: Multimodal biometric recognition based on 3D ultrasound palmprint-hand geometry fusion. *IEEE Access* **10**, 7914–7925 (2022)
15. Dass, S.C., et al.: A principled approach to score level fusion in multimodal biometric system. In: *Proceedings of the International Conference on Audio-Video-Based Biometric Person Authentication* (2005)
16. Nandakumar, K., Chen, Y., Dass, S.C., Jain, A.K.: Likelihood ratio based biometric score fusion. *IEEE Trans. Pattern Anal. Mach. Intell.* **30**(2), 342–347 (2008)
17. Nardiello, D., Iula, A.: A new recognition procedure for Palmprint features extraction from ultrasound images. In: De Gloria, A. (eds.) *Applications in Electronics Pervading Industry, Environment and Society*. ApplePies 2017. LNEE, vol. 512, pp. 113–118. Springer, Cham (2019). https://doi.org/10.1007/978-3-319-93082-4_15
18. Iula, A., Micucci, M.: Experimental validation of a reliable palmprint recognition system based on 2D ultrasound images. *Electronics* **8**(12) (2019)
19. Iula, A., Micucci, M.: A feasible 3D ultrasound Palmprint recognition system for secure access control applications. *IEEE Access* **9**, 39746–39756 (2021)



Algorithm for Velocity Estimation in a Multivariable Motion Sensor

Federico Mazzoli¹✉, Davide Alghisi², and Vittorio Ferrari¹

¹ Department of Information Engineering, University of Brescia, Via Branze 38, Brescia, Italy
f.mazzoli002@unibs.it

² Gefran SpA, Via Cave 11, Provaglio d'Iseo, BS, Italy

Abstract. This paper proposes an algorithm for velocity estimation using the position and acceleration signals obtained respectively from a resistive potentiometric displacement sensor and a MEMS accelerometer. The algorithm is composed of two processing chains that independently estimate velocity starting from position and acceleration signals. Velocity estimation from position is obtained through an adaptive windowing differentiator while the estimation from acceleration is based on a leaky integrator low-pass filter. Such two estimations are fused together by means of a tailored weighted average. The proposed algorithm is first simulated in MATLAB and then experimentally implemented and tested. Both simulations and experimental results show that velocity estimation given by the fusion of the outputs of the two processing chains has a lower estimation error compared to the output of each single chain.

Keywords: Real-time velocity estimation · Multivariable sensor · Motion control · Embedded systems

1 Introduction

Velocity estimation obtained from signals provided by motion sensors, without specifically using velocity sensors, plays a crucial role within the industrial field e.g., for servomotor controllers in closed-loop control systems and motion control of mechanical machines, including robot manipulators [1]. A basic approach involves differentiating the signal from a position sensor to obtain a velocity signal. Nevertheless, the high-frequency noise included in such position signal is amplified by the differentiation [2]. The width of the differentiation window rules the trade-off between the estimation noise and its delay. Several methods have been developed to estimate velocity from position data while reducing estimation errors and minimizing delay. For example, adaptive algorithms can be exploited to dynamically adjust the differentiation window [3].

Within the scopes of multivariable sensor and data fusion, there are techniques and methods that allow to estimate velocity by combining position and acceleration data coming from different sensing elements [4]. In this context, this work investigates a new technique for velocity estimation designed for a custom multivariable motion sensor, suitable for implementation in embedded systems based on simple microcontrollers

thanks to its low computational complexity. This paper is organized as follows: Sect. 2 presents the working principle and the block diagram of the proposed algorithm; Sect. 3 discusses the blocks and the simulation results, experimental results are shown in Sect. 4, while conclusions are reported in Sect. 5.

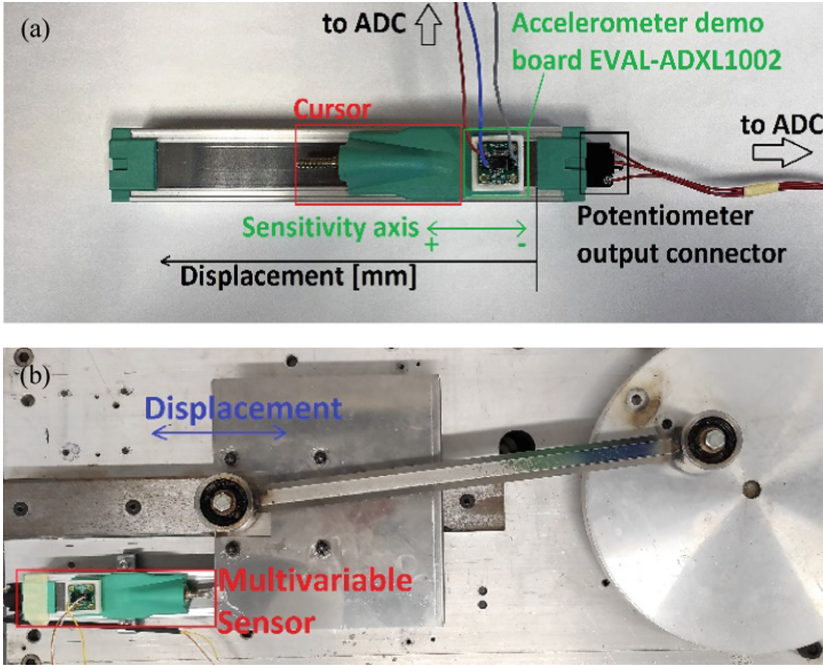


Fig. 1. (a) Multivariable motion sensor: resistive potentiometric displacement sensor (Gefran PK) equipped with an accelerometer (Analog Devices ADXL1002) mounted on the cursor. (b) Multivariable sensor linked to the rod-crank mechanism.

2 Multivariable Motion Sensor and Proposed Estimation Algorithm

A multivariable motion sensor prototype has been realized by combining a resistive rod-less potentiometric displacement sensor (Gefran PK) with electrical stroke length of 100 mm and a single-axis MEMS accelerometer (Analog Devices ADXL1002) with measurement range of $\pm 50 g$ coupled to the respective evaluation board EVAL-ADXL1002 fixed on the cursor. A mechanical adapter ensures the alignment of the accelerometer sensitive axis with the direction of the cursor displacement. A picture of the assembled multivariable sensor and the motion testing equipment is shown in Fig. 1.

The proposed estimation algorithm is composed of two processing chains acting on the position and acceleration signals coming from the two sensors, respectively, as shown in Fig. 2. The first chain is composed of a preprocessing section, consisting of the

series of a median filter and a low-pass filter to reduce noise on the position signal pos . In this chain, velocity estimation is based on the differentiation of two position samples whose relative distance is dynamically adjusted according to the trend of the position signal. The block *End-Fit FOAW* implements an adaptive windowing differentiation to estimate velocity vel as shown in Eq. (1). The term T indicates the sampling period; y_k and y_{k-N} represent two generic position samples while N indicates the number of samples in the differentiation window. The regulation criterion of N , as reported in [3], is based on searching the maximum value assumed by N such that the straight line $L_{y_{k-i}}$ passing through y_k and y_{k-N} intersects each of the uncertainty bands d associated to the position samples inside the window as shown in Eq. (2). The straight line $L_{y_{k-i}}$ is defined in Eq. (3) while its parameters are reported in Eqs. (4) and (5).

$$vel = (y_k - y_{k-N})/NT \tag{1}$$

$$\left| y_{k-i} - L_{y_{k-i}} \right| \leq d \forall i \in \{1, \dots, N\} \tag{2}$$

$$L_{y_{k-i}} = a_n + b_n(k - i)T \tag{3}$$

$$a_n = (ky_{k-N} + (N - k)y_k)/N \tag{4}$$

$$b_n = (y_k - y_{k-N})/NT \tag{5}$$

The estimated velocity vel is median- and low-pass filtered in the postprocessing section to output velocity estimation vel_p .

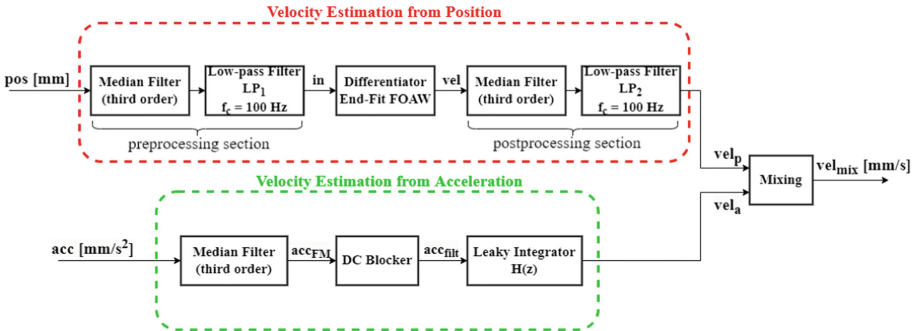


Fig. 2. Block diagram of the velocity estimation algorithm.

The second processing chain acts on the acceleration signal acc . First, the acceleration is preprocessed by a median filter to remove spikes. Then, the *DC Blocker* block removes the DC component of acceleration due to the 0-g offset of the accelerometer and to any residual misalignment between its sensitive axis and the cursor direction.

The DC component is recursively estimated by a third-order elliptical low-pass filter. Finally, the leaky integrator with transfer function $H(z)$ reported in Eq. (6) integrates the

acceleration acc_{fit} to obtain velocity estimation vel_a . The pole in $H(z)$ is determined by the stability factor α . In order to obtain asymptotical stability, it must be $0 < \alpha < 1$. The term T stands for the sampling period of the acceleration signal acc .

$$H(z) = zT/(z - \alpha) \quad (6)$$

The overall velocity estimation vel_{mix} is obtained by the weighted average of vel_p and vel_a , calculated according to Eq. (7). To minimize the estimation error and its delay, two different pairs of weights are designed: the first pair is named *exponential weights* and is indicated as $[w_{1e}, w_{2e}]$ in Eq. (8), while the second pair is named *linear weights* and is indicated as $[w_{1l}, w_{2l}]$ in Eq. (9). From the rod-crank mechanism kinematics of Fig. 1b, the motion law is sinusoidal with fundamental frequency f_{rd} which can be set. Weights are calculated for a given frequency f_{rd} , depending on the tuning parameters A , B , m , q .

$$vel_{\text{mix}} = (w_1 vel_p + w_2 vel_a)/2 \quad (7)$$

$$[w_{1e} = 2e^{-f_{\text{rd}}d+A}/(e^{-f_{\text{rd}}d+A} + e^{f_{\text{rd}}d-B}), w_{2e} = 2e^{f_{\text{rd}}d-B}/(e^{-f_{\text{rd}}d+A} + e^{f_{\text{rd}}d-B})] \quad (8)$$

$$[w_{1l} = 2(-mf_{\text{rd}} + q)/q, w_{2l} = 2mf_{\text{rd}}/q] \quad (9)$$

3 Simulation Results

The proposed algorithm has been simulated in MATLAB by supplying position pos_{ref} and acceleration acc_{ref} input signals, both generated numerically according to the kinematic model of the rod-crank mechanism, as reported in Eqs. (10), (11), (12).

$$pos_{\text{ref}} = r(1 - \cos(2\pi f_{\text{rd}}t) + \mu - (\mu^2 - \sin^2(2\pi f_{\text{rd}}t))^{1/2}) \quad (10)$$

$$vel_{\text{ref}} = 2\pi f_{\text{rd}}r(\sin(2\pi f_{\text{rd}}t) + \sin(4\pi f_{\text{rd}}t)/2(\mu^2 - \sin^2(2\pi f_{\text{rd}}t))^{1/2})^{1/2} \quad (11)$$

$$acc_{\text{ref}} = (r(2\pi f_{\text{rd}})^2)(\cos(2\pi f_{\text{rd}}t) + \cos(4\pi f_{\text{rd}}t)/\mu) \quad (12)$$

The block parameters adopted in the algorithm are listed below. The cut-off frequency of the low-pass filters LP_1 and LP_2 is $f_c=100$ Hz; the uncertainty band of *End-Fit FOAW* differentiator is set to $d = 30 \mu\text{m}$; the third-order elliptic low-pass filter relative to *DC Blocker* has a normalized bandwidth equal to 10^{-4} and the leaky integrator stability factor is $\alpha = 0.999$. For the two weighted averaging methods, Fig. 3 compares the maximum relative errors of velocity estimations for different signal frequencies f_{rd} in the range [1, 10] Hz. The estimation errors of vel_p and vel_a respectively increase and decrease with f_{rd} because of the frequency responses of the differentiator *End-Fit FOAW* and the leaky integrator block. For each value of the test frequency f_{rd} , the error of the velocity estimation vel_{mix} is the lowest between those of vel_p and vel_a . In particular, the weighted average with *linear weights* typically produces the lower estimation error.

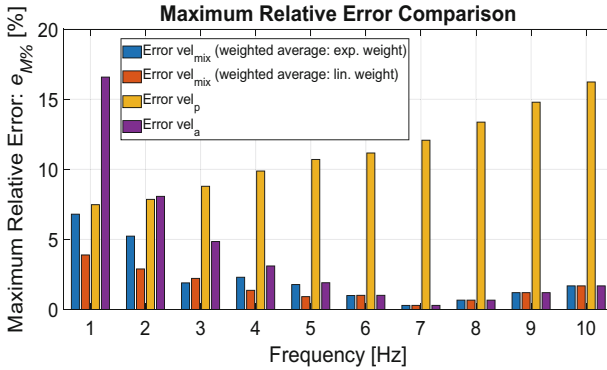


Fig. 3. Maximum relative error for different velocity estimations versus test frequency f_{rd} in the range [1, 10] Hz.

4 Experimental Results

Experimental results have been obtained by fixing the multivariable motion sensor to the rod-crank mechanism as shown in Fig. 1b. The instrumentation setup is reported in Fig. 4. Sensors are powered at 5 V by PL303-P Power Supply and the position and acceleration signals are sampled by means of a NI USB-6212 DAQ with sampling frequency $f_s = 1$ kHz and a resolution of 16 bits. The algorithm has been implemented in MATLAB, using the same block parameters used in simulation.

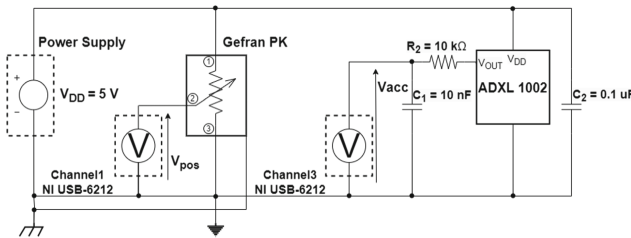


Fig. 4. Schematic instrumental setup, adopted to acquire position and acceleration signals.

Figure 5 shows the position and acceleration signals obtained when the multivariable sensor cursor is linked to the rod-crank mechanism, rotating at $f_{rd} = 2.8$ Hz. From these two signals the algorithm computes the velocity estimations vel_p , vel_a and vel_{mix} . The corresponding estimation errors, calculated as $|vel_{ref} - vel|$, are shown in Fig. 6.

5 Conclusions

An algorithm for velocity estimation from position and acceleration signals composed of two parallel processing chains producing respectively two velocity estimations, vel_p and vel_a was presented. Such estimations are fused through a weighted average operation to produce a single combined velocity estimation vel_{mix} . Both simulations and experimental results show the effectiveness of the proposed algorithm whereby the combined estimated velocity vel_{mix} has lower errors with respect to both single estimations vel_p and vel_a .

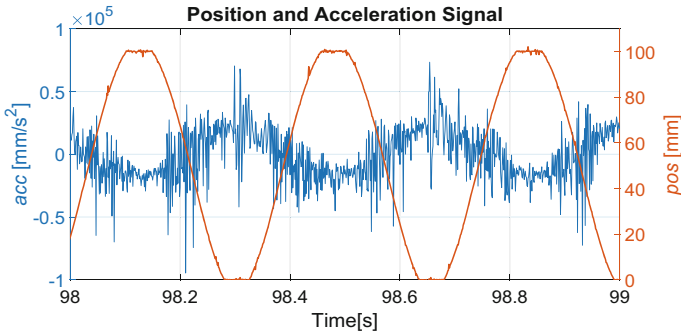


Fig. 5. Measured position and acceleration signals obtained from the multivariable motion sensor linked to the rod-crank mechanism at rotation frequency $f_{rd} = 2.8$ Hz.

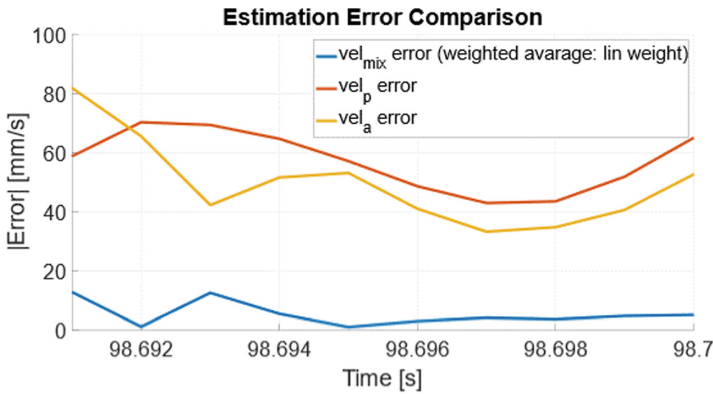


Fig. 6. Experimentally obtained estimation error of vel_{mix} compared with those of vel_p and vel_a .

References

1. Liu, G.: On velocity estimation using position measurements. In: Proceedings of the 2002 American Control Conference, pp. 1115–1120 (2002)
2. Brown, R.H., Schneider, S.C., Mulligan, M.G.: Analysis of algorithms for velocity estimation from discrete position versus time data. In: IEEE Transactions on Industrial Electronics, vol. 39, no.1, pp. 11–19 (1992)
3. Janabi-Sharifi, F., Hayward, V., Chen, C.J.: Discrete-time adaptive windowing for velocity estimation. In: IEEE Transactions on Control Systems Technology, vol. 8, no.6, pp. 1003–1009 (2000)
4. Zhu, W., Lamarche, T.: Velocity estimation by using position and acceleration sensors. In: IEEE Transactions on Industrial Electronics, vol. 54, no.5, pp. 2706–2715 (2007)



Analysis of Logic Schemes for the Optical Implementation of Pointwise Operations in Gated Recurrent Unit Cells

Badrul Alam, Andrea Ceschini, Antonello Rosato, Massimo Panella,
and Rita Asquini^(✉)

Department of Information Engineering, Electronics and Telecommunications,
University of Rome “La Sapienza”, Via Eudossiana 18, 00184 Rome, Italy
rita.asquini@uniroma1.it

Abstract. In this work, we present and analyse some possible schemes for the implementation through all-optical logic gates of a complete Gated Recurrent Unit that is adopted in deep neural networks. We start by defining the mathematical operations required in a GRU cell and their corresponding optical circuit. A key role in those schemes is given to Semiconductor Optical Amplifiers, whose active operations are modelled in the paper. They are employed in a Cross-Phase Modulation configuration, which was used to analyse a XOR gate. Our analysis considers noisy input signals and nonidealities caused by band-pass filters in the optical channels. The models investigated also include the delays of signals in transition through the amplifiers, with the aim of estimating actual constraints to be considered in real implementations.

Keywords: Optical logic gate · Photonic circuits · Semiconductor optical amplifier · Gated recurrent unit · Deep neural network

1 Introduction

In Deep Learning, recurrent layers including also feedback connections are used in stacked architectures for implementing Deep Recurrent Neural Networks (DRNNs) that deal with very complex tasks such as nonlinear system identification, time series analysis, speech and video classification, and so forth [1]. Nonetheless, DRNNs are also useful in distributed/federated learning environments, where large quantities of data are processed even using high-speed optical communication systems [2].

Long Short-Term Memory (LSTM) and Gated Recurrent Unit (GRU) layers, introduced in [3] and [4] respectively, are two of the most popular recurrent layers adopted to this end. They have established as a *de facto* standard in sequential data modelling being well-suited to deal with long-term dependencies in many applications, from time series forecasting to anomaly detection [5]. In particular, GRU layers imply a reduced amount of processing elements while maintaining the capability to capture long-term dependencies in the processed data [6].

However, the employment of such recurrent models is highly demanding in terms of computational power and processing time. Therefore, optical implementation of LSTM and GRU architectures, especially all-optical solutions, are highly pursued due to the possibility to improve the clock speed beyond the limits of classical computing and to reduce power dissipation [7–9]; to this end, some arrangements are well established in literature [10] although with some scalability issues. The recent introduction of an optical activation function [7] and the scalable approach to optical cross-phase-modulation (XPM) [11] enable new pathways for a larger scale deployment of existing devices and schemes. LSTM-based recurrent layers are also implemented by using quantum gates and quantum gate arrays, which can be based in turn on optical technologies [12].

In this work, we present and analyse possible schemes for the implementation through all-optical logic gates of the pointwise operations necessary for a complete all-optical GRU cell. After defining the mathematical operations required in a cell, and their corresponding optical circuit, we proceed with the numerical modelling of the relevant issues. A key role in those circuits is given to Semiconductor Optical Amplifiers (SOAs) [13], which are employed in a Cross-Phase Modulation configuration in order to analyse the actual behaviour of a XOR gate [14]. In the simulations, the data is represented by a 10 Gbit/s stream of NRZ signal propagating in the waveguides/fibers, where the pulses represent a bit ‘1’. The schemes presented in this work can be implemented through optical fiber technology or other optical integrated platforms as well [15–19].

2 Equivalent Circuits for Pointwise Operations

The mathematical representation of a GRU cell is shown in Fig. 1a, where the previous state h_{t-1} is one of the inputs for the computation of the current state and layer’s output h_t . As it can be seen in Fig. 1b, the actions of vector transfer, concatenation and duplication can be directly implemented through optical signals transition through waveguides and Y-splitters/combiners, as well as directional couplers.

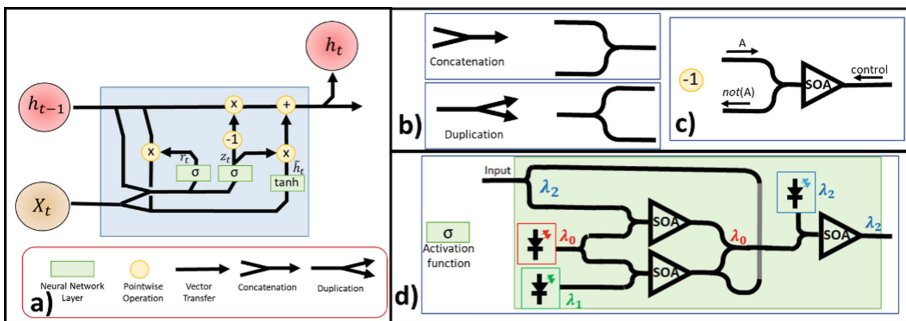


Fig. 1. Basic implementation of a GRU cell: a) mathematical arrangement of a GRU cell; b) GRU optical implementation for concatenation, duplication, NOT operations; c) scheme of the activation function in the proposed model.

On the other hand, in order to obtain pointwise operations, it is necessary to employ more complex optical elements, often achieved through the use of active elements. In

continuity with the approach in [11], our suggested arrangements for the pointwise operations make use of SOAs in their non-linear states. As an example, a Cross-Gain-Modulation scheme [14] can be used as a NOT gate through the signal arrangement shown in Fig. 1c.

An experimental demonstration for implementing both sigmoid $\sigma(\cdot)$ and hyperbolic tangent $\tanh(\cdot)$ activation functions in a fiber wave circuit is reported in [7], represented in Fig. 1d in a more general fashion accordingly to the approach proposed herein. Pointwise operations such as adders and multipliers are more complex to implement, since they are obtained through a concatenation of multiple optical gates [8, 9]. A half adder (HA) can be built through the combination of XOR and AND optical gates as shown in Fig. 2a, while a full adder (multiple bits) is a cascade of HAs. The same blocks can be used for the development of an optical multiplier, as illustrated in Fig. 2b.

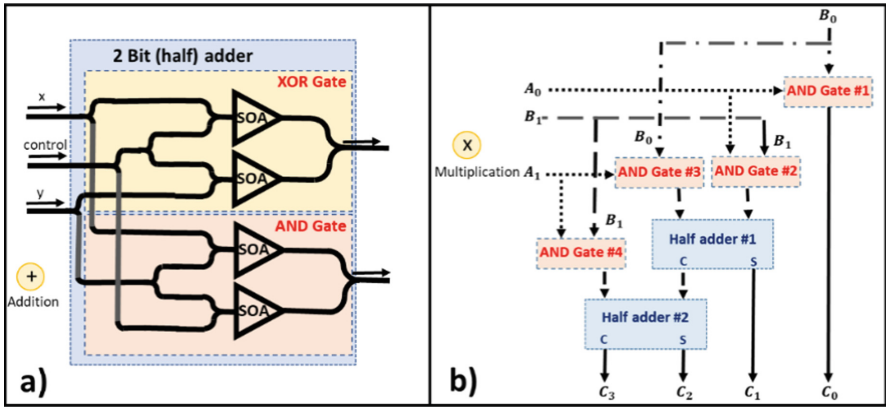


Fig. 2. GRU optical implementation for addition and multiplication operations, which are obtained through the concatenation of multiple blocks: a) half adder built by combining a XOR gate with an AND gate; b) multiplication between two-bits-long-operands.

3 Simulation Settings

All the suggested arrangements for the pointwise operations make use of SOAs in their non-linear states, which require particular attention to produce simulation results close to experimental values [13, 20]. Our model of SOA was obtained by combining parameters of existing commercial devices (“SOA-1550-BP” from Optilab[®]) with the main parameters obtained by datasheets (i.e., saturation power 14 dB, unsaturated gain 100 at 350 mA) or by estimation with comparison to literature (i.e., alpha factor 3, gamma factor 0.1, active zone cross-section area $6 \cdot 2 \cdot 10^{-13} \text{ m}^2$, waveguide length 1000 m, effective index 3.390). The performance characteristics of the numerical model, which was obtained by following the calculation method reported in [13] by employing product-log functions, are shown in Fig. 3.

Simulations and models were carried out through the use of Simulink[™] and Matlab[®], in particular considering the schematics shown in Fig. 2. The optical signals were streams

of 10 Gbit/s (period 0.1 ns) NRZ modulated signals, with carrier frequency of 193.1 THz ($\lambda_0 = 1550$ nm) and input power at 1 mW (0 dBm). In order to be closer to experimental situations, we have introduced a white noise (SNR = 20 dB) and a distortion of the signal due to phase noise of the carrier and non-ideal filtering. The filter characteristics are: passband 80 GHz; stopband -20 dB at 100 GHz; Gaussian shape of the transfer function in the passband. For the sake of better readability, the signal was represented after an envelope detection, as illustrated in Fig. 4.

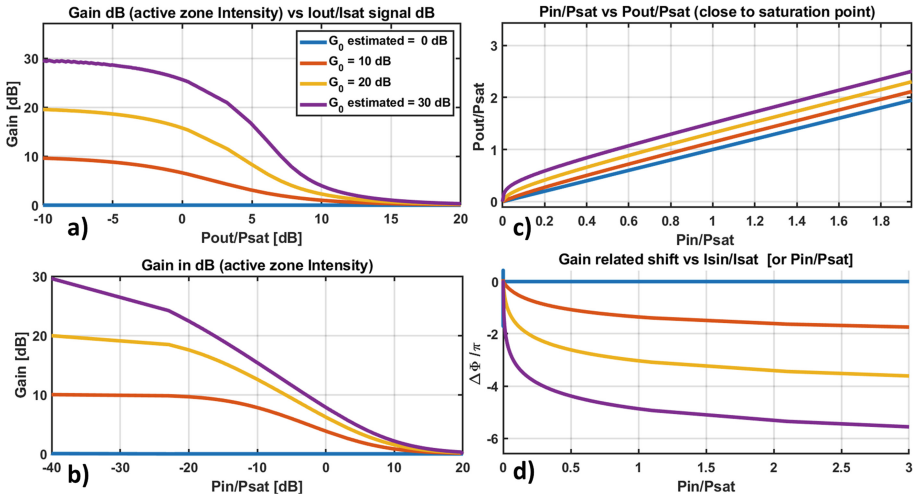


Fig. 3. Characteristics of the adopted SOA, where power is normalized with saturation power (high values for gain have been estimated): a) gain of the active zone vs output power b) gain of the active zone vs input power, c) output power vs input power, d) phase shift deriving from input power (due to charge and refractive index variation).

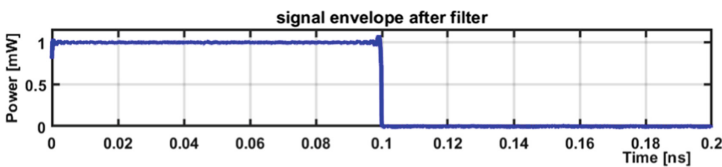


Fig. 4. Signal 1–0 envelope of the modulated signal after transition through an 80 GHz filter.

4 Results

The signal evolution of the XOR gate is represented in Fig. 5, as taken from the XPM scheme in Fig. 2. The input signal's bit has the profile reported in Fig. 4. By comparing the two figures, the signal level at the output of the single SOAs, which is shown in Figs. 5a and 5b, is unsurprisingly higher than the input for the given amplification. The

signal transiting through the SOAs are subject to phase shift, as per the adopted model. The SOAs were tuned close to the previously presented values, in order to impose a π phase shift. For a signal transition $\{x = 1, y = 1\}$, this default value induces a destructive effect on the output, while for $\{x = 0, y = 1\}$ and $\{x = 1, y = 0\}$ the phase shift is not π and thus, the signal amplitude is different than 0.

The delay of the transition through the SOA was also computed and revealed to be reasonably low, as reported in Fig. 6. Since the delay is referred to the sole active zone, this small value is justified but it is also reassuring information for scalability in multistage operations: the required delay compensation is limited.

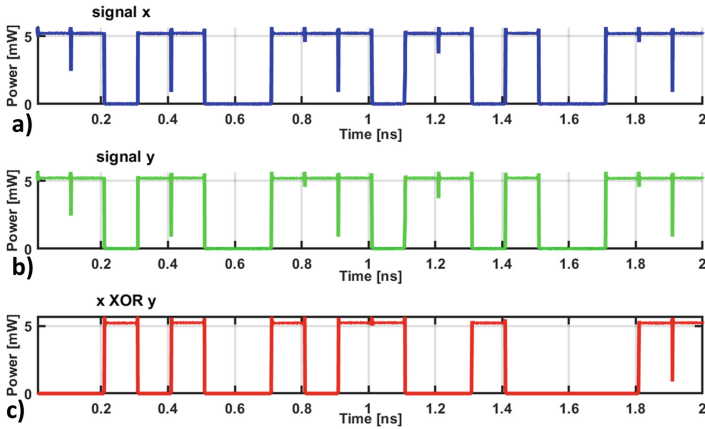


Fig. 5. XOR gate signal evolution, with 1 mW amplitude input signal: a) output from SOA connected to “x”; b) output from SOA connected to “y”; c) output from the combination of the two SOA output signals, due to their respective phase shift.

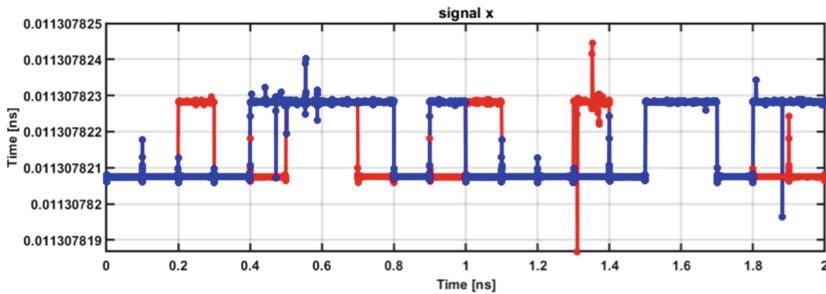


Fig. 6. Delay variations of the two SOAs corresponding to the signal transitions.

5 Conclusions

In this work, we have presented all-optical circuits schemes allowing the implementation of pointwise operations in a GRU cell. We have also shown the critical aspects in the

modelling of such systems, included the analysis of some critical sections. Actually, hardware implementations of deep neural networks require high computational power and long times for the training and inference phases, with particular reference to real-time applications. The results of this preliminary study are very promising, as they prove the potentiality of the proposed approach to develop scalable all-optical multi-bit operations for high-speed data processing in Deep Learning applications.

References

1. Yu, Y., Si, X., Hu, C., Zhang, J.: A review of recurrent neural networks: LSTM cells and network architectures. *Neural Comput.* **31**, 1235–1270 (2019)
2. Rosato, A., Panella, M., Araneo, R., Andreotti, A.: A neural network based prediction system of distributed generation for the management of microgrids. *IEEE Trans. Industry Appl.* **55**, 7092–7102 (2019)
3. Hochreiter, S., Schmidhuber, J.: Long short-term memory. *Neural Comput.* **9**, 1735–1780 (1997)
4. Cho, K., Van Merriënboer, B., Bahdanau, D., Bengio, Y.: On the properties of neural machine translation: encoder-decoder approaches. arXiv preprint [arXiv:1409.1259](https://arxiv.org/abs/1409.1259) (2014)
5. Nguyen, H.D., Tran, K.P., Thomassey, S., Hamad, M.: Forecasting and anomaly detection approaches using LSTM and LSTM autoencoder techniques with the applications in supply chain management. *Int. J. Inf. Manag.* **57**, 102282 (2021)
6. Chung, J., Gulcehre, C., Cho, K., Bengio, Y.: Empirical evaluation of gated recurrent neural networks on sequence modeling. arXiv preprint [arXiv:1412.3555](https://arxiv.org/abs/1412.3555) (2014)
7. Gayen, D.K., Chattopadhyay, T., Pal, R.K., Roy, J.N.: All-optical multiplication with the help of semiconductor optical amplifier—assisted sagnac switch. *J. Comput. Electron.* **9**(2), 57–67 (2010)
8. Mourgiyas-Alexandris, G., et al.: An all-optical neuron with sigmoid activation function. *Opt. Express* **27**, 9620–9630 (2019)
9. Ramachandran, M., Prince, S., Verma, D.: Design and performance analysis of all-optical cascaded adder using SOA-based MZI. *J. Comput. Electron.* **17**(2), 845–856 (2018)
10. Agrawal, G.P.: *Nonlinear Fiber Optics*, 6th edn. Elsevier, Amsterdam (2019)
11. Porzi, C., et al.: Review on SOA-MZI-based photonic add/drop and switching operations. *Front. Optoelectron.* **6**(1), 67–77 (2013)
12. Ceschini, A., Rosato, A., Panella, M.: Design of an LSTM cell on a quantum hardware. *IEEE Trans. Circuits Syst. II: Express Briefs* **69**, 1822–1826 (2022)
13. Connelly, M. J.: *Semiconductor Optical Amplifiers*. Chapter 3, pp. 21–41. Springer, Cham (2002)
14. Durhuus, T., et al.: All-optical wavelength conversion by semiconductor optical amplifiers. *J. Lightwave Technol.* **14**, 942–954 (1996)
15. Bogaerts, W., et al.: Programmable photonic circuits. *Nature* **586**, 207–216 (2020)
16. Buzzin, A., Asquini, R., Caputo, D., de Cesare, G.: On-glass integrated SU-8 waveguide and amorphous silicon photosensor for on-chip detection of biomolecules: feasibility study on hemoglobin sensing. *Sensors* **21**, 415 (2021)
17. Asquini, R., Buzzin, A., Caputo, D., de Cesare, G.: Integrated evanescent waveguide detector for optical sensing. *IEEE Trans. Compon. Packag. Manuf. Technol.* **8**, 1180–1186 (2018)

18. Alam, B., et al.: Numerical and experimental analysis of on-chip optical wireless links in presence of obstacles. *IEEE Photonics J.* **13**(1), 16600411 (2021)
19. Alam, B., Veroli, A., Caló, G., Petruzzelli, V., Benedetti, A.: Multilayer optical routing by means of vertical directional coupler with long range surface plasmons. *AIP Conf. Proc.* **2145**, 020017 (2019)
20. Kapoor, A., et al.: Saturation characteristics of InGaAsP-InP bulk SOA. In: *Proceedings SPIE, Physics and Simulation of Optoelectronic Devices XVIII*, vol. 7597 (2010)



Deep Learning for a Comprehensive Transformer Fault Detection Through Vibrational Data

Valerio Rucconi¹(✉), Letizia De Maria¹(✉), Daniele Bartalesi¹, Bau Valecillos², Simone Garatti³, and Sergio Bittanti³

¹ RSE S.p.A., Technologies for Transmission & Distribution Department, Milan, Italy
valerio.rucconi@gmail.com, letizia.demaria@rse-web.it

² Trafoexpert GmbH, 8610 Uster, Switzerland

³ Dipartimento di Elettronica, Informazione e Bioingegneria, Politecnico di Milano, Milan, Italy

Abstract. This paper presents a comprehensive view of the vibrational analysis performed on a three-phase oil-immersed transformer by expanding and deepening our previous research works. The aim is to show the virtue of deep neural networks in transformer fault detection, as well as to study the vibrational behavior of the transformer tank, a topic that, in literature, has not yet been thoroughly studied. This analysis, which focuses on transformer windings failures, is based on real vibration data recorded by optical sensors located on the transformer tank. The failure of the windings was reproduced by their loosening in a laboratory environment. The measured vibrational spectra were used to develop a classifier capable of detecting winding loosening. Compared to the literature, the robustness of the obtained classifier against possible sensor misplacement was also investigated, which led to an analysis of the tank locations most relevant to this type of analysis. This analysis proved that neural networks were able to detect fault with a high accuracy, robustly to possible misplacements in the positioning of the sensor, and that the *no-load* condition performed better the *load* condition.

Keywords: Oil-insulated transformer · Winding fault detection · Vibration sensor · Machine learning · Feedforward neural networks

1 Introduction

A transformer with loose windings has a reduced ability to withstand external short-circuit events, exposing itself to permanent damage and dangerous failures [1]. To prevent these types of failure, it is necessary to have a classifier capable of evaluating the state of the windings in real time, so that any looseness can be monitored. Among the various possible methods that can be implemented to build this classifier, vibrational analysis of the transformer tank is considered an excellent on-line and non-invasive technique to monitor internal faults. That's because changes in the mechanical characteristics of the windings and core influences the vibration pattern of the transformer tank and thus, by analyzing the tank vibrations, the state of the device can be inferred [2].

The purpose of this research work is to present a comprehensive view of the vibrational analysis performed on a three-phase oil-immersed transformer by means of data analysis techniques [3]. In particular, we explore the virtue of deep neural networks for fault detection in transformers by merging, deepening, and inferring general conclusions, built on our previous work [4, 5]. This time we refer to neural network algorithms built with Keras, an open-source library for neural networks written in Python.

1.1 Experimental Set-Up

This analysis was performed on all the four walls of the transformer under investigation (42 kV/580 V, 750 kVA, ONAN cooling): the Low-Voltage (LV) side, the High-Voltage (HV) side, and both side walls (Side A and Side B), as depicted in Fig. 1.

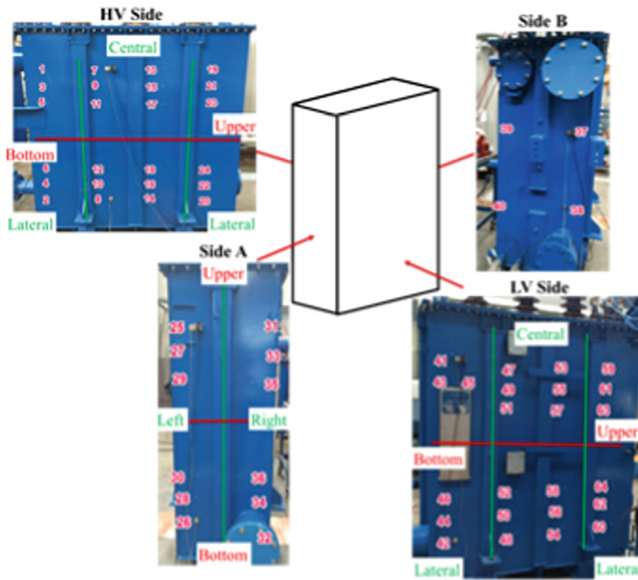


Fig. 1. The four sides of the transformer: each number represents the position of the corresponding sensor; the divisions shown in the pictures are indicative of the sensor clusters considered for the analysis

The vibration sensing system employed is based on optical MEMS accelerometers (flat frequency response up to 1000 Hz), an Electro-Optical Unit (EOU), and a conditioning and recording unit. Under the *load* condition, the main vibration content is found at frequencies between 50 Hz and 500 Hz, while a transformer operated under the *no-load* condition exhibits its main vibration content at frequencies between 50 Hz and 1000 Hz. A 2-min time series was recorded for each position on the transformer tank for both tight and loose windings at a sampling rate of 44 kHz. Each of the recorded time signals was partitioned into 100 time-subsets, then averaged, filtered, and FFT transformed in the frequency domain. The final data set consists of the magnitudes of the main harmonics

of the spectrum, represented with a vector of real numbers, with the addition of a label representing “tight” or “loose” windings.

1.2 Outline of the Analysis

The analysis of the effectiveness of neural networks in classifying winding faults is analyzed through the following four conceptually consecutive sections.

- Individual sensor locations were considered and a neural network for each location was trained so to analyze the ability to predict each individual sensor.
- A more complete classifier was introduced by considering a training dataset formed by vibrational data corresponding to all sensor positions present on a specific area of the transformer tank.
- To check the robustness against unseen sensor positions, all data points corresponding to a given position were removed from the training dataset and tested the so-obtained classifier on the data corresponding to the removed position.
- Putting together the results obtained so far, a neural network trained with the smallest possible number of sensors but capable of successfully performing a robust fault detection was derived.

The reliability of the neural networks obtained at each stage of our investigation is expressed by its accuracy. The threshold values of accuracy are expressed in Table 1.

Table 1. Accuracy ranges

Color	Accuracy	Interpretation
Green	Accuracy > 90 %	Satisfactory prediction
Orange	90 % > Accuracy > 60 %	Unsatisfactory prediction
Red	Accuracy < 60 %	Unpredictable

2 Analysis

To foretell the state of windings based on the vibrations of a single sensor, a properly tuned neural network based on data referring to the same sensor gave almost always a 100% accuracy for each sensor position (except for one position on HV side and one on the lateral side). However, when a classifier built for one position is tested against data measured in another location, the prediction accuracy can deteriorate significantly. As expected, classifiers constructed with data referring to one single sensor position are not robust against possible sensor misplacements in the test phase.

To solve this robustness problem, the learning process is enhanced by merging data of a wide range of sensor positions according to the clusters of sensors indicated in Fig. 1. In this way, the neural networks can take into account all patterns arising on a

specific area of the transformer tank, thus providing more robustness against possible sensor misplacements. The following Table 2 reports the accuracy obtained on the test dataset of a properly tuned neural networks for the clusters taken into consideration.

Table 2. Reliability of the classifier for the low voltage, high voltage, and side clusters

LV	Load	No-Load	HV	Load	No-Load	Side	Load	No-Load
Central	94.81 %	100.00 %	Central	98.33 %	100.00 %	Side A	48.41 %	98.67 %
Lateral	99.79 %	100.00 %	Lateral	97.26 %	100.00 %	Side B	78.62 %	100.00 %
Upper	96.42 %	99.68 %	Upper	99.25 %	100.00 %			
Bottom	94.14 %	100.00 %	Bottom	95.60 %	100.00 %			

As can be seen from Table 2, the *no-load* condition yields a more accurate classification of the winding state than the *load* condition. Since these neural networks exploit data of all the sampled positions of the transformer, their robustness against possible sensor misplacements in the test phase is expected to be higher than the one previously obtained. However, in a real scenario, it is not always possible to set up such a large number of measurement positions. Therefore, it is necessary to identify the most informative positions for diagnostic purposes so to reduce the number of sensors needed to obtain an accurate and robust classifier.

For this reason, the analysis continues by analyzing if there are positions that can be predicted even without the employment of data coming from their location so as to reduce the number of sensors used to construct these classifiers while keeping the robustness property. This is assessed by removing from the training dataset all data of a specific location and keeping them aside as a holdout test set, while data of all other sensors of the cluster form the training and validation dataset. In this way, the unused position can be interpreted as vibration data totally unobserved during the design of the classifier and the reliability of the trained classifier indicates its robustness against this unobserved position. Table 3 shows the accuracy of a properly tuned neural network in predicting each removed position of the lateral HV and LV clusters.

Since some sensor measurements can be ignored during the training phase without harming the resulting classifier, it is possible to obtain a neural network able to correctly classify all the vibration data using a reduced number of sensors. With a trial-and-error process, the least number of sensors sufficient to obtain a classifier with a high enough accuracy was obtained. Once again, the *no-load* condition proved to be consistently better than the *load* one. In fact, if an unloaded transformer is analyzed, it is possible to predict the state of the windings with an excellent accuracy and robustness against possible mispositioning of the sensor with only a reduced number of sensors for each side of the transformer tank considered. Table 4 below shows the accuracy results achieved on the HV and LV lateral clusters for illustrative purposes: the sensor positions reported refer to those positions that have been omitted during the training and validation phase and therefore the accuracy in classifying these positions indicates the robustness of the resulting neural networks against possible sensor misplacements (from the previous

Table 3. Reliability of the classifier over the LV and HV lateral drawn-out positions

Removed Position LV-Lateral	Load	No-Load	Removed Position HV-Lateral	Load	No-Load
41	98.86 %	100.00 %	1	86.62 %	26.42 %
42	97.96 %	50.00 %	2	54.80 %	50.00 %
43	97.49 %	100.00 %	3	52.66 %	87.25 %
44	64.12 %	100.00 %	4	71.91 %	50.25 %
45	91.60 %	63.74 %	5	20.80 %	49.75 %
46	99.90 %	49.75 %	6	84.35 %	49.75 %
59	61.25 %	100.00 %	19	64.34 %	91.31 %
60	55.25 %	62.71 %	20	54.30 %	50.25 %
61	100.00 %	100.00 %	21	68.90 %	100.00 %
62	99.10 %	50.00 %	22	53.74 %	100.00 %
63	56.31 %	100.00 %	23	54.70 %	99.50 %
64	99.00 %	100.00 %	24	98.71 %	100.00 %

results it is reasonable to suppose that the positions employed for the construction of these classifiers are predicted with almost 100% accuracy).

Table 4. Reliability of the classifier trained with the fewest lateral LV and HV sensors

LV- Lateral	Load	LV- Lateral	No-Load	HV- Lateral	Load	HV- Lateral	No-Load
41	99.50 %	43	100.00 %	24	98.71 %	3	100.00 %
42	98.99 %	44	100.00 %			19	100.00 %
43	96.98 %	61	100.00 %			21	100.00 %
45	97.50 %	63	100.00 %			22	100.00 %
61	100.00 %	64	97.27 %			24	100.00 %
62	99.50 %						
64	99.00 %						

3 Conclusions

The first and most important conclusion that can be drawn from this research work is that neural networks have shown to be able to classify the state of transformer windings based on vibration measurements obtained on its transformer tank: they were able to correctly classify the state of the windings based on both measurements obtained from a single sensor and measurements obtained from clusters of sensors, and, ultimately, they also proved to be robust against possible sensor misplacement because they were able to perform fault detection based only on measurements obtained from a selected and reduced number of sensors in the cluster. This is because the measured vibrations on the

transformer tank revealed a common pattern that allowed a generalization to unexplored positions and thus a reduction in the sensors employed. Second, the *no-load* condition outperformed the *load* condition in classifying the state of the windings based on the vibrations obtained on the transformer tank in each step of our analysis.

Acknowledgments. This work has been financed by the Research Fund for the Italian Electrical System in compliance with the Decree of Minister of Economic Development; April 16 2018.

References

1. García, B., Burgos, J.C., Alonso, Á.M.: Transformer tank vibration modelling as a method of detecting winding deformations-part I: theoretical foundation. *IEEE Trans. Power Delivery* **21**(1), 157–163 (2005)
2. Hu, Y., Zheng, J., Huang, H.: Experimental research on power transformer vibration distribution under different winding defect conditions. *Electronics* **8**(8), 842 (2019)
3. Bittanti, S.: *Model Identification and Data Analysis*. John Wiley & Sons (2019)
4. Rucconi, V., De Maria, L., Garatti, S., Bartalesi, D., Valecillos, B., Bittanti, S.: Deep learning for fault detection in transformers using vibration data. *IFAC-PapersOnLine* **54**(7), 262–267 (2021)
5. Rucconi, V., De Maria, L., Garatti, S., Bartalesi, D., Valecillos, B., Bittanti, S.: No-load transformers: vibration spectra analysis by deep learning methods for loose windings deterioration. In: Di Francia, G., Di Natale, C. (eds.) *Sensors and Microsystems*. AISEM (2021). Lecture Notes in Electrical Engineering, vol. 918, pp. 251–257. Springer, Cham (2021). https://doi.org/10.1007/978-3-031-08136-1_39



PM Sensor Based on Piezoelectric MEMS: Mock Up

L. Barretta^(✉) and F. Foncellino

Analog, MEMS and Sensors Group- STMicroelectronics, Via Remo De Feo,1, 80022 Arzano, Italy

luigi.barretta@st.com

Abstract. In this work is presented the first realization of a mock up for particulate detection, based on piezoelectric material.

The sensing element of this object is a circular membrane of PZT (lead-titanium zirconate), which has a resonant frequency around 250 kHz.

It is shown the composition of the parts and the principles that allow its operation, from the system of fluxing of the area inside the sensor to the heating system that allows by thermo-phoretic effect the reaching of the particles to the sensitive surface up to the reading electronics that allow the measurement of dust concentration, and that make this mock up self-sufficient.

For the characterization is used a special test chamber for particulate matter, where in a controlled environment (both temperature and humidity) can generate and monitor concentrations of particulate matter made from specific certified PM₁₀-like dust.

Keywords: Particulate matter · Particle sensor · Mass sensor · MEMS resonator · Piezoelectric material

1 Introduction

One of the most studied pollutants in recent years is certainly particulate matter. Many studies in fact evaluate the effects of exposure to high rates of particulate matter on human health and whether there is a correlation between these and respiratory diseases. Informing people of their surroundings and the rate of pollutants in which they are immersed through portable particulate and gas sensors, or even better wearables has become a goal for electronics manufacturers [1].

The mock up that we are going to present is based on the gravimetric method [2], i.e. we expect an accumulation of particles on the surface of the sensing element and then measure their mass. Being able to measure the flow through the sensor we are then able to obtain a measure of particulate matter concentration. The sensing body is made of a circular membrane of piezoelectric material, of PZT [3, 4] (lead-titanium zirconate), which vibrates at a resonance frequency around 250 kHz.

The particulate matter, which enters the chamber via a controlled flushing system, is deposited on the sensing element which decreases its resonant frequency [5, 6]. The

shift in the recorded resonant frequency can then be related to the deposited mass [7] and thus to the concentration of particulate matter present in the environment where the sensor is inserted.

In this work, after presenting the parts that make up the mock up, from the fluxing system to the central body that allows the deposition of particles on the sensing element and the reading electronics, will be shown characterization in a particle test chamber of the ENEA center of Portici, which we will briefly describe.

2 Materials and Methods

The mock up under study consists of various parts that allow the measurement of particulate matter. In Fig. 1(a) you can see a picture of all the parts that compose it.

For the air fluxing inside the central element, formed by PM cells (Fig. 1(c)) of which we can see a CAD schematization in Fig. 1(b), a piezoelectric micropump is used. The pump together with the heater is controlled by a sensor board piloted by an Arduino that allows us to choose the frequency and voltage of driving the pump and consequently choose the flow.

The heater, inserted in the PM cell represents a crucial part because through the heat generated by it in a perpendicular way to the sensing element the deposition efficiency is maximized [8] exploiting the thermo-phoretic effect (see Fig. 2).

The impedance analyzer allows you to record the impedance spectrum as it varies with frequency and then to identify the value of the resonant frequency as it varies with time. This allows, as said, to identify the mass that is deposited on the sensitive element (Fig. 3).

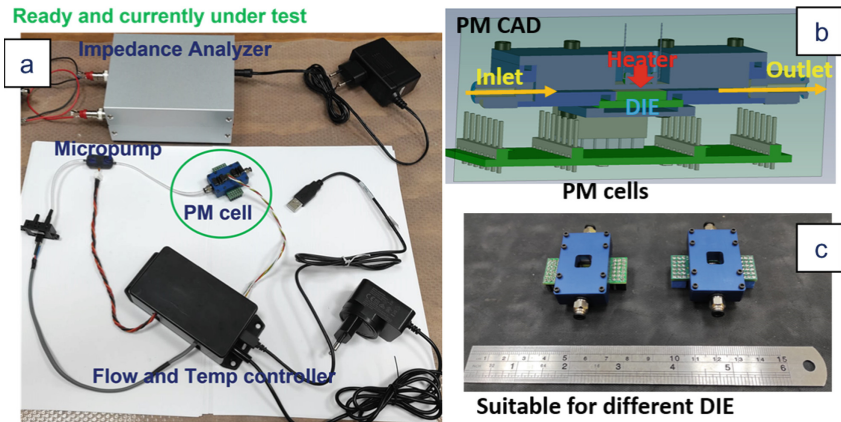


Fig. 1. PM mock up. (a) components that make up the sensor (b) CAD of the PM cell and the driver board, (c) a picture of the PM cells.

The tests are carried out inside the PM chamber of the ENEA research center in Portici. This characterization chamber consists of a box of about 500 L inside which we find a PM generator, Topas Sag 410, with which certified PM10-like powders are injected.

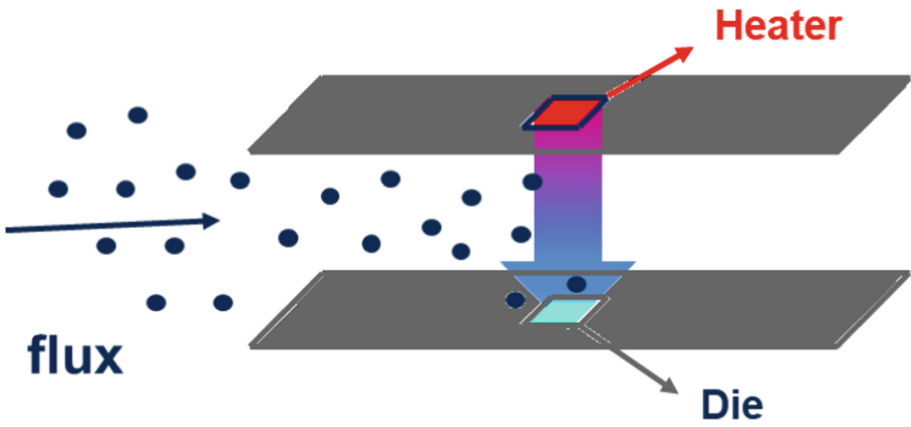


Fig. 2. Schematization of the thermophoretic effect.

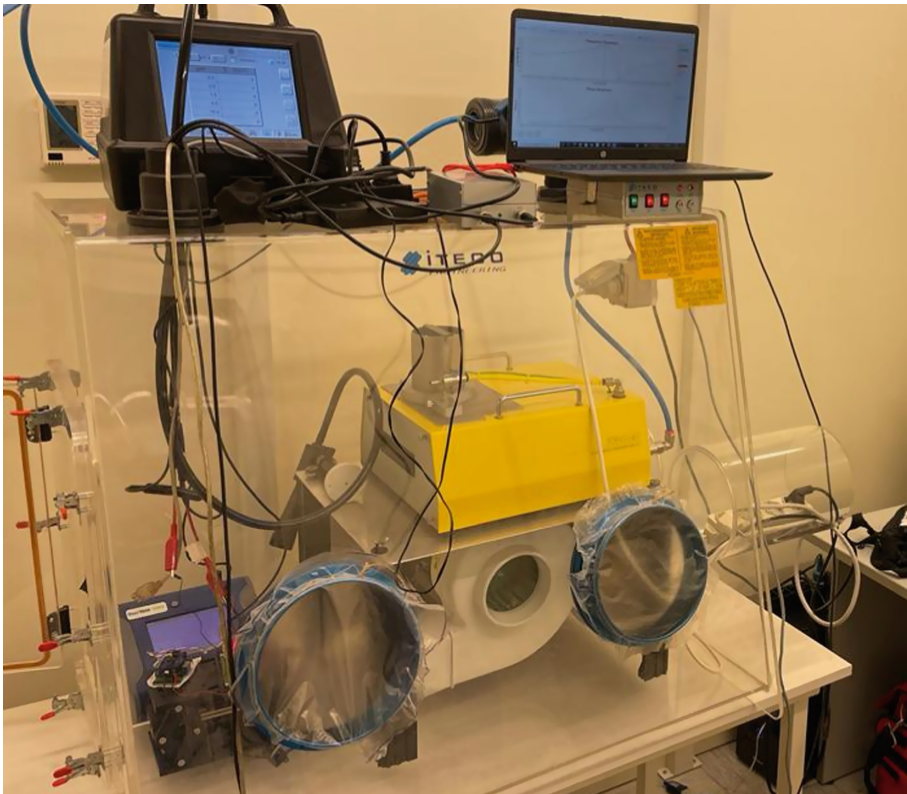


Fig. 3. ENEA PM chamber.

A ventilation system provides to homogenize the particulate matter in the chamber so as not to have systematic errors in the comparison between the concentrations measured by

the mock up and the reference instruments. The reference instruments are a Dusttrack DRX aerosol monitor 8533 and a Lasair III particle measuring systems, the first one is an OPC (optical particle counter) used for PM_{10} , $PM_{2.5}$ and PM_{10} measurements, the second one is a particle counter for cleanroom class control capable of counting particles from 0.3 to 25 μm in 6 different channels. In addition, temperature and humidity are constantly monitored to check that the environmental parameters do not change during the measurement.

3 Results

The mock up was subjected to injections of $10 \mu\text{m}/\text{m}^3$ for several sensitive elements by varying the flow and piezo pump and heater temperature.

In Fig. 4 it is possible to see how the resonance frequency changes during particulate injection, it is possible to see that there are frequency shifts of about 1 kHz for elements subjected to a temperature of 100°C and flows of 1.2 and 1.5 sscm.

Optical inspection images of the elements subjected to particulate deposition are shown in Fig. 5. Figure 5(a) shows the clean membrane before particulate injection, Fig. 5(b) shows the same membrane after PM chamber deposition. Figure 5(c) shows an underpasted membrane at the same concentration of particulate but keeping the heater off. As it is possible to see in the latter case the particulate deposition is negligible as well as the recorded frequency shift. This confirms, as anticipated that the use of therewinder and thus the action of the thermophoretic effect is necessary to maximize particulate deposition on the sensing element.

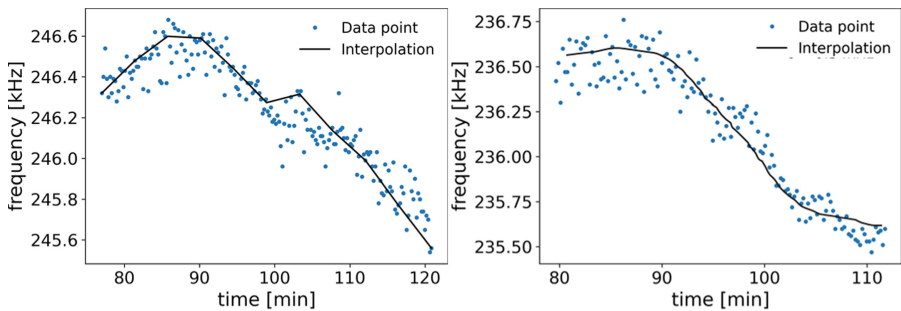


Fig. 4. Frequency shifts obtained for two different membranes by injecting into the chamber concentrations of PM_{10} equal to $10 \mu\text{m}/\text{m}^3$

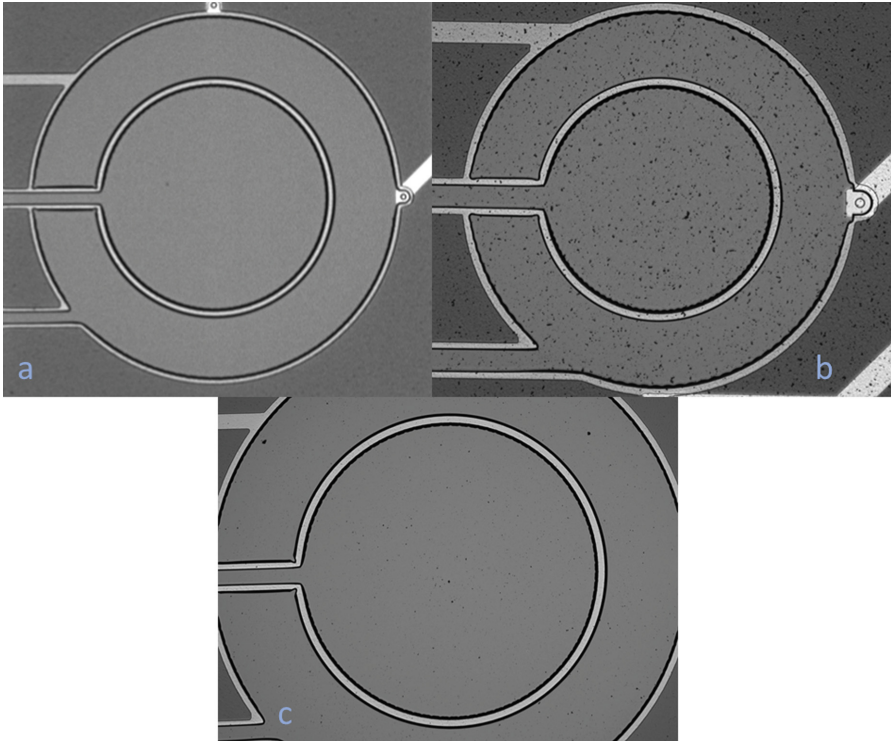


Fig. 5. (a) clean membrane before injection, (b) particulate-covered membrane after particulate iniezione in PM ENEA chamber. (c) membrane subjected to injection without the use of the heater.

4 Conclusion

In this work a first prototypical mock up based on piezoelectric elements, in particular circular diaphragms (membranes), which have the ability to shift their resonant frequency when mass is added on their surface, has been presented.

It has been investigated the role of the heater that drives the thermo-phoretic effect which is necessary to maximize the deposition of particulate matter on the sensing element.

The results showed a shift of about 1 kHz for elements subjected to particulate concentrations of 10 $\mu\text{g}/\text{m}^3$ when the heater temperature is set to 100 °C. Tests with the same concentrations but without the use of the heater showed negligible deposition and frequency shifts, which confirms to us that the use of the heater and thus the action of the thermophoretic effect is necessary.

Responses to different concentrations and different flow and temperature settings of the heater will be investigated in the future before fabrication of a new optimized mock up.

Acknowledgments. Research reported in this publication was supported by SALVO project that has received funding from the National Programs (PON) of the Italian Ministry of Economical Development (MISE): code B48I20000050005 (Prog n. F/190012/01/X44).

References

1. Alfano, B., et al.: A review of low-cost particulate matter sensors from the developers' perspectives. *Sensors* **20**(23), 6819 (2020)
2. Tasić, V., et al.: Comparative assessment of a real-time particle monitor against the reference gravimetric method for PM10 and PM2.5 in indoor air. *Atmos. Environ.* **54**, 358–364 (2012)
3. Ismail, A.K., et al.: The principle of a MEMS circular diaphragm mass sensor. *J. Micromech. Microeng.* **16**(8), 1487 (2006)
4. Foncellino, F., Barretta, L., Massera, E.: Concept of MEMS vibrating membrane as particulate matter (PM) sensor. In: Di Francia, G., Di Natale, C. (eds.) *AISEM 2020. LNEE*, vol. 753, pp. 119–123. Springer, Cham (2021). https://doi.org/10.1007/978-3-030-69551-4_17
5. Nazemi, H., et al.: Mass sensors based on capacitive and piezoelectric micromachined ultrasonic transducers—CMUT and PMUT. *Sensors* **20**(7), 2010 (2020)
6. Zhihong, W., et al.: Biosensors based on flexural mode piezo-diaphragm. In: 2008 3rd IEEE International Conference on Nano/Micro Engineered and Molecular Systems. IEEE (2008)
7. Foncellino, F., Barretta, L., Massera, E., Corigliano, A.: Piezoelectric mems for microparticles detection. In: 2021 IEEE Sensors, pp. 1–4. IEEE (2021)
8. Fahimi, D., et al.: Vertically-stacked MEMS PM2.5 sensor for wearable applications. *Sens. Actuators Phys.* **299**, 111569 (2019)



Assessment of Piezoelectric Properties on Prototype BZT-BCT Devices

Rossana Scaldaferrì¹, Luigi Barretta¹, Paolo Aprea², Valeria Casuscelli¹, Paola Sabrina Barbato¹(✉), and Domenico Caputo²

¹ Analog, MEMS & Sensors Group- STMicroelectronics, Via Remo De Feo, 1, 80022 Arzano, Italy

paolasabrina.barbato@st.com

² DICMaPI- Università degli Studi di Napoli Federico II, P.Le V. Tecchio, 80125 Naples, Italy

Abstract. The aim of this contribution is to assess the ferroelectric and piezoelectric properties of Barium Zirconate Titanate- Barium Calcium Titanate (BZT-BCT) sol-gel thin films. 400 nm-thick films with a randomly oriented perovskitic crystal structure have been grown on platinum coated silicon wafer by means of repeated deposition by spin coating and subsequent heat treatments (350 °C and 750 °C). Hence, Pt top electrode have been sputtered through shadow mask. The main results are here summarized: Maximum Polarization (P_{\max}) value equal to 41.3 $\mu\text{C}/\text{cm}^2$ obtained in a PE curve (@15 V and 1 kHz) and a calculated value of relative dielectric constant equal to 582 has been estimated from the CV curves (@ 10 V and 1 kHz). Trough displacement measurements it has been possible to estimate an $e_{31,f}$, (transversal piezoelectric coefficient) equal to 7.99 C/m^2 by applying a sine signal at 12.375 kHz (the first vibration mode) and a maximum amplitude of 20 V.

Keywords: BZT-BCT · Lead-free · Sol-gel · Thin films · Piezo MEMS

1 Introduction

Barium Zirconate Titanate-Barium Calcium Titanate $(1-x)\text{BaZr}_{0.2}\text{Ti}_{0.8}\text{O}_3-x\text{Ba}_{0.7}\text{Ca}_{0.3}\text{TiO}_3$ (BZT-BCT) ceramic has attracted a lot of attention since the work of Liu and Ren [1] that reported a large value of piezoelectric coefficient comparable to the PZT system, with a maximum d_{33} value of 620 pC/N at $x = 0.5$. In the last years, several groups [2–5] work on the development of BZT-BCT sol-gel thin films since, with respect to bulk ceramics, the integration of thin films in MEMS devices is essential to have a series of advantages such as small weight and inertia, low power consumption and short response time [6]. The piezoelectric properties of these BZT-BCT thin films have been addressed in few papers, such as in the work of Huang and coworkers [3], Chi and coworkers [4] and Li et al. [2]. Up to date, the highest of d_{33} equal to 250 pm/V has been reported by Huang for BCZT sol gel thin films annealed at 800°C. Chi and coworkers obtained a (100) oriented $\text{Pb}_{0.8}\text{Ca}_{0.2}\text{TiO}_3$ (PCT) seeding layer in order to induce a (100) preferential orientation in BCZT sol gel thin films. These authors reported a value of d_{33} ,

evaluated by PFM measurements, equal to 104 pm/V. Similarly, Li et al. [2] reported a d_{33} value respectively of ~110 pm/V and 130 pm/V for (1-x) BZT-xBCT with $x = 0.5$ and 0.55 respectively deposited over a LNO seed layer, estimated by using the PFM method at a frequency far from the resonant frequency of the cantilever.

Recently, Mazzalai and coworkers [7] developed “a cheap, versatile, and easy to use setup, based on cantilever tip displacement detection and a charge amplifier allowing for simultaneous measurements of polarization and in plane piezoelectric stress”. Following this approach is possible to estimate directly $e_{31,f}$ as a function of the electric field.

In this article, we report about the production, morphological and electrical characterization of 0.5BZT-0.5BCT prototype devices whose piezoelectric properties have been assessed on cantilevers structures following the Mazzalai measurement principle. Moreover, by using square capacitors structures of different area, we also performed ferroelectric characterization.

2 Materials and Methods

2.1 Prototype Device Fabrication

The prototype cantilevers have been produced by 5 repeated deposition routes. Each deposition route is made up of the following steps:

- spin-coating by dispensing a 0.35 M precursor solution over a platinum-coated silicon wafer of 700 μm . The time of spin coating has been extended to accomplish the solvent evaporation
- pyrolysis on a hotplate @ 350 °C for 5 min to remove the organic matter
- annealing in a muffle @ 750 °C for 30 min to obtain the desired crystalline phase.

Finally, a 400 nm- thick film made of BZT-BCT has been obtained whose ferroelectric, dielectric and piezoelectric properties have been completely assessed by sputtering a Pt top electrode through a suitable shadow mask and by manually etching the BZT-BCT with 1 N HCl @ 100 °C to provide the contact to the bottom electrode.

2.2 BZT-BCT Thin Films Crystal Structure and Morphological Characterization

The final layer thickness was measured by means of a profilometer AMBIOS Technology XP-1 in four different positions. Scanning Electron Microscopy without any metal coating was performed at an accelerating voltage of 10 kV with a working distance of 5–7 mm and aperture of 30 μm to assess the deposited oxide morphology. The crystal structure was checked by X-ray powder diffraction (XRPD, PANalytical X’Pert Pro automated diffractometer equipped with a XCelerator PIXCEL 1D detector) in grazing incident diffraction ($\omega = 1^\circ$) over a 2θ range from 20 to 60°, with the following operating conditions: CuK α radiation, 40 kV, 40 mA, step size 0.0131° 2θ , counting time 18.87 s per step.

2.3 Prototype Ferroelectric and Piezoelectric Characterization

The dielectric and ferroelectric characteristics of BZT-BCT prototypal devices were measured at room temperature by Aixact TFAalyzer 2000E applying a triangular bipolar signal at fixed frequency. Current-Voltage characteristic curves were measured by B1500A Semiconductor Device Analyzer. Piezoelectric measurements on a clamped cantilever structure have been performed by Polytec MSA500 Micro System Analyzer by means of an appositely designed fixture. The deflection of the cantilever subject to an opportune amplified tension signal is revealed by a laser on the square structure close to the cantilever. To find the opportune sine signal, a periodic Chirp function with amplitude 20 V has been used to observe the velocity as a function of frequency in the 10 kHz-100 kHz range allowing to determine the first vibration mode. Then a sine signal at frequency of the first vibration mode and a maximum amplitude of 20 V has been applied to measure the displacement of the cantilever as a function of time.

3 Results

3.1 Thin Layer Morphology and Crystal Structure

The 400 nm-thick BZT-BCT layer shows a non-oriented perovskitic structure, as confirmed by the XRD pattern (Fig. 1). SEM imaging evidenced many defectivities of the BZT-BCT surface more likely attributable to the non-standardized and manual process (Fig. 2). The Fig. 2 b exhibits a homogeneous structure at the micrometric scale.

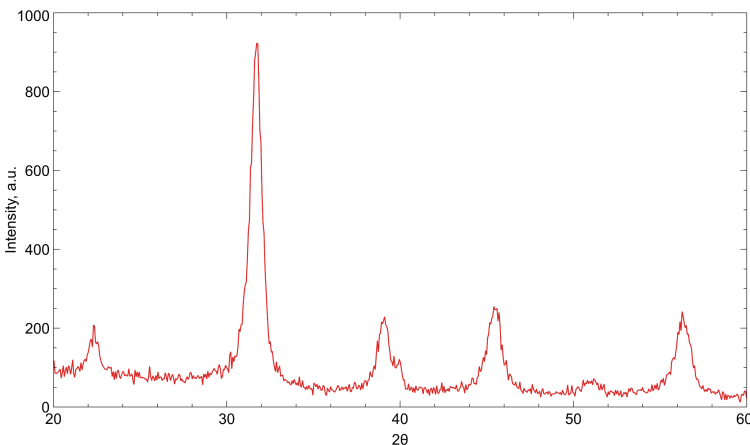


Fig. 1. XRD pattern of the final layer in grazing incidence ($\omega = 1^\circ$)

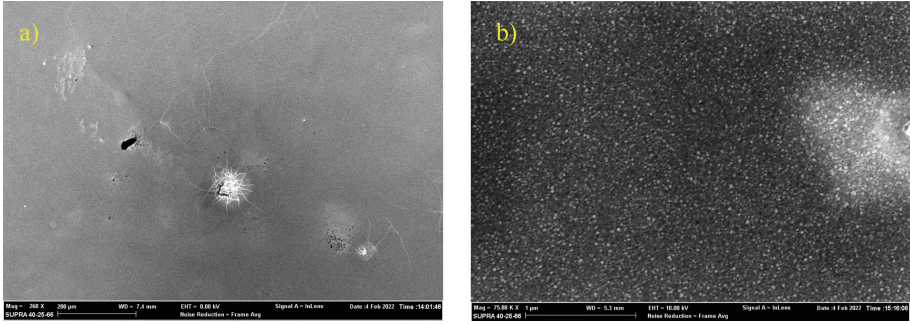


Fig. 2. SEM images of BZT-BCT surface: a) general view at 250 X; b) higher magnification at 80 kX.

3.2 Dielectric, Ferroelectric, Resistive and Piezoelectric Properties

Figure 3 shows the hysteresis loops obtained by applying a signal amplitude of 15 V at 1 kHz measuring two capacitors of different area: 0.25 mm^2 (blue line) and 1 mm^2 (red lines). Moreover, the results of P-E curves are tabularly reported in Table 1.

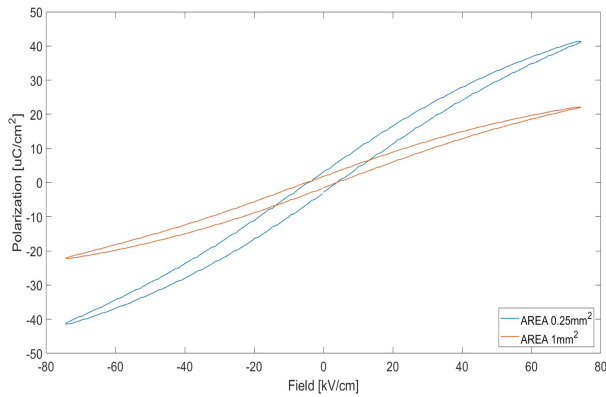


Fig. 3. *P-E*: 0.25 mm^2 (blue line) and 1 mm^2 (red lines)

Table 1. Ferroelectric results

Device area	P_{\max} [$\mu\text{C}/\text{cm}^2$]	ΔE_C [kV/cm]
0.25 mm^2	41.3	54.33
1 mm^2	22.13	57.9

It appears that, even though the curves are normalized by the device areas, the polarization decreases with increasing the device area due to the defectivities present in the film, whose contribution increases with the area of the device negatively affecting the material properties. Further characterizations in terms of Capacitance-Voltage and Current-Voltage characteristics (not shown) confirm that presence of defectivities affects both ferroelectric and dielectric characteristics. In particular 1 mm² area devices exhibits an extrapolated value of the relative dielectric constant of 582, while in the same conditions for 0.25 mm² device $\epsilon_r = 1024$ has been recorded. Finally, from Current-Voltage measurements BZT-BCT thin film behaves as a dielectric with a good resistance, and breakdown voltage about 60 MV/m has been measured.

In Fig. 4 a) it is reported the modal analysis of the clamped cantilever excited with a p-Chirp function. Even though the measure is noisy, it is possible to distinguish the different vibrational mode, the first vibration mode has been detected at 12.375 kHz, which corresponds to a pumping mode (see Fig. 4 a)). Afterwards, the cantilever was excited with a sine signal (20 V and 12.375 kHz) and the displacement as a function of time has been measured (Fig. 4 b)). Finally, by means of Eq. 1, which relates the stress generated in the plane and the electric field applied to a thin-film capacitor stuck on an elastic plate and free to move perpendicular to the plate at the same time, it was possible to estimate the $e_{31,f}$, (transversal piezoelectric coefficient) equal to 7.99 C/m²

$$e_{31,f} = \frac{Y \cdot t_{si}^2 \cdot w(x_2)}{3 \cdot V \cdot (1 - \nu) \cdot c_f \cdot x_1 \cdot (2 \cdot x_2 - x_1)} \quad (1)$$

where Y is the Young's Module ($1.69 \cdot 10^{11}$ Pa); t_{si} is the substrates thickness 700 μ m); ν is Poisson's ratio (0.064), c_f electrode coverage factor (0.094); $w(x_2)$ is the deflection function (55 nm); x_1 and x_2 are respectively the length of the piezo active area (9 mm) and that of the laser incidence (10.5 mm).

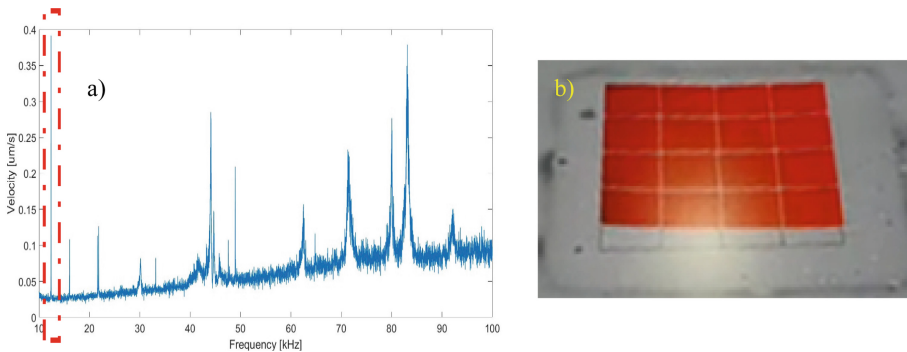


Fig. 4. Piezoelectric Characterizations: a) velocity in the FFT b) Out of plane measurement through MSA500 on Cantilever.

4 Conclusions

400 nm thick, thin films with randomly oriented perovskitic nanograins were produced by non-standardized processes resulting in some defectivities as shown by SEM. Material deposition should yet be optimized but obtained data are very encouraging. A maximum Polarization (P_{max}) value equal to 41.3 $\mu\text{C}/\text{cm}^2$ has been obtained @ 15 V and $f = 1$ kHz with an estimated value of relative dielectric constant equal to 1024 @ 1kHz on low area devices. Finally, an estimated $e_{31,f}$, (transversal piezoelectric coefficient) equal to 8 C/m² have been found.

References

1. Liu, W.F., Ren, X.B.: Large piezoelectric effect in Pb-free ceramics. *Phys. Rev. Lett.* **103**(25), 257602 (2009)
2. Li, W.L., Zhang, T.D., Xu, D., Hou, Y.F., Cao, W.P., Fei, W.D.: LaNiO₃ seed layer induced enhancement of piezoelectric properties in (100)-oriented (1-x)BZT-BCT thin films. *J. Eur. Ceram. Soc.* **35**(7), 2041–2049 (2015)
3. Huang, L., Dai, Y., Wu, Y., Pei, X., Chen, W.: Enhanced ferroelectric and piezoelectric properties of (1-x)BaZr_{0.2}Ti_{0.8}O₃-xBa_{0.7}Ca_{0.3}TiO₃ thin films by sol-gel process. *Appl. Surf. Sci.* **388**, 35–39 (2016)
4. Chi, Q.G., Zhang, C.H., Sun, J., Yang, F.Y., Wang, X., Lei, Q.Q.: Interface optimization and electrical properties of 0.5BaZr_{0.2}Ti_{0.8}O₃-0.5Ba_{0.7}Ca_{0.3}TiO₃ thin films prepared by a sol-gel process. *J. Phys. Chem. C.* **118**(28), 15220–15225 (2014)
5. Barbato, P.S., Aprea, P., Caputo, D., Casuscelli, V., Scaldasferri, R., Di Matteo, A.: 0.5(BaZr_{0.2}Ti_{0.8}O₃)-0.5(Ba_{0.7}Ca_{0.3}O₃) thin films deriving from green sol-gel routes. In: 8th International Workshop on Advances in Sensors and Interfaces, IWASI 2019 2019, pp.139–142 (2019). Article number 8791305
6. Hu, P.: Study on high precision mems inertial sensor with increased detection capacitance driven by electromagnetism. *Chem. Eng. Trans.* **66**, 1273–1278 (2018)
7. Mazzalai, A., Balma, D., Chidambaram, N., Jin, L., Muralt, P.: Simultaneous piezoelectric and ferroelectric characterization of thin films for MEMS actuators. In: 2013 Joint IEEE International Symposium on Applications of Ferroelectric and Workshop on Piezoresponse Force Microscopy (ISAF/PFM), pp. 363–366 (2013)



Smart Internet of Things (IoT) System for Construction Sites Monitoring

Davide Colaiuda¹✉, Gianluca Barile¹, Eleonora Laurini², Andrea Pelliccione¹,
Pierluigi De Berardinis², Vincenzo Stornelli¹, and Giuseppe Ferri¹

¹ Department of Industrial and Information Engineering and Economics,
University of L'Aquila, 67100 L'Aquila, Italy
davide.colaiuda1@graduate.univaq.it

² Department of Civil, Construction-Architectural and Environmental Engineering,
University of L'Aquila, 67100 L'Aquila, Italy

Abstract. Construction sites are risky places for work-related injuries. Constant monitoring of workers and people within the site is particularly important, and this can be achieved by using smart devices. This work proposes a system based on UHF RFID technology, which uses tags to monitor workers and gear access to the site. It also communicates detected data on a remote server using MQTT protocol, that ensure high scalability of the system, allowing the use of several nodes to also in different areas and so making it possible to evaluate workers position.

Keywords: Industry 4.0 · RFID · Construction site · Remote monitoring

1 Introduction

In recent years there have been a wide diffusion of the so-called “Smart Systems”, which are electronic devices with embedded sensors capable to collect, process and transmit data to servers or other systems. This possibility allowed the automation of several processes as industrial or construction ones, using these systems in a transparent way and without interfering with the normal operations. Thanks to these devices, manipulation of the process-associated data got easier and faster. In particular, a lot of popularity has been gained from remote monitoring systems, with one or more electronic devices that collect information about work-related parameters transmitting them through a certain protocol (such as WiFi), and making them consultable remotely. Recently, there are studies on the importance of these smart systems in management and monitoring of construction sites [1].

This kind of device is usually referred to as “Internet of Things” (or IoT), and is widely diffused for a lot of different applications, such as home automation, surveillance or smart power grids [2]. IoT systems are particularly useful for the aforementioned monitoring applications, also due to their easy applicability, for example, in construction industries and sites: this in fact results as the working areas with the higher rate of work-related injuries and fatalities [3]. In this work, an IoT smart system for construction monitoring is proposed. This is based on several nodes located within the monitored site, that can

collect data using UHF RFID (Ultra-High Frequency Radio-Frequency Identification) technology, because of its long distance of operation. Nodes collect data from tags, that are applied on gear and helmets of the workers and send them to a remote server using MQTT protocol.

This paper is structured as follows: in the first section, the UHF RFID technology is introduced, followed by an explanation on chosen communication protocol. Second section describes the system in its component blocks and explain its functionality. At last, in third section some collected data obtained from a demo scenario are presented together with future developments.

2 Technology Overview

2.1 UHF Radio-Frequency Identification

RFID is one of the most diffused close-range data transmission technologies, and obtained an increasing interest for a lot of different applications over the years. Differently from other technologies as barcode or magnetic cards, it does not need contact or visibility for its operation. It requires two main components: a reader and one or more tags that stores data. Reader consists of a CPU, an encoder/decoder and an antenna and can receive and transmit data at a certain frequency; tags instead consist only of a non-volatile memory with a decoder/encoder and an antenna working at the same frequency [4]. Tags are usually built as cards (like credit cards), with a built-in antenna and a silicon chip with the memory. Figure 1 shows the typical architecture, at block scheme, of both a RFID reader and a RFID tag.

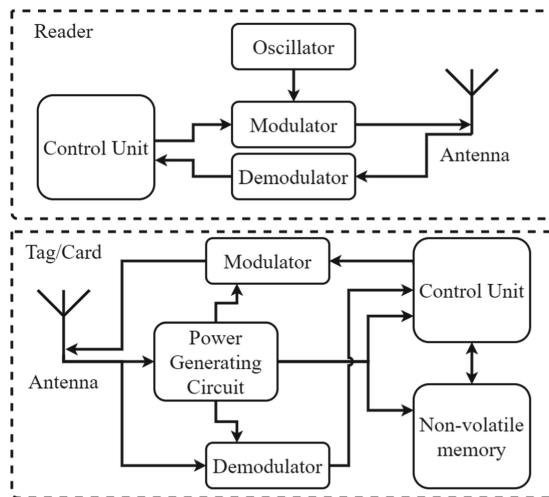


Fig. 1. Block diagrams of a RFID reader and a generic RFID tag (or card).

Depending on the operative frequencies of these devices, 3 types of RFID can be individuated: Low Frequency (LF), at 125 kHz and 134 kHz; High Frequency (HF), at 13,56 MHz; Ultra-High Frequency (UHF), at different frequencies above 856 MHz. The last one allows the greatest ranging of them, since signals are transmitted as effective RF waves, while LF and HF works with Near Field Communication (NFC); together with this, higher frequency means smaller antennas, so an easier integration, that reduces the cost of the tags. However, readers must work at a higher frequency, so that UHF readers are more expansive and complex with respect to LF and HF ones. This property makes UHF RFID suitable for different applications in several areas, that includes tracking and localization systems [5] and monitoring applications with nodes or gateways [6]. Since it uses RF waves, UHF RFID readers typically can measure distance of tag objects evaluating the Received Signal Strength Indicator (RSSI), making it suitable especially for inventory or warehouse applications.

2.2 MQTT Communication Protocol

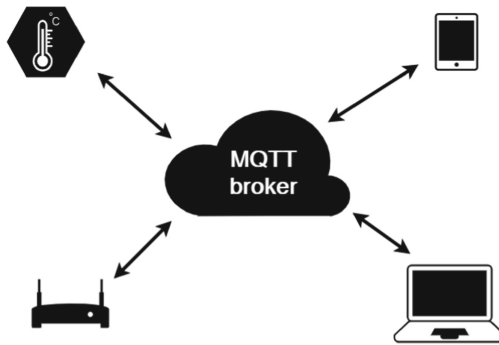


Fig. 2. MQTT communication architecture.

Since wireless connection can be really tough in construction sites, especially in outdoor ones, a protocol with a reduce band consumption is required. Due to this, for the cited application the MQTT protocol has been chosen. It is a lightweight protocol in which a device, called broker, acts as a container and message dealer for other devices, called clients, which can either publish or subscribe messages to/from a certain topic, as shown in Fig. 2. This allows a really easy scalability of the system, since communication happens directly from client to broker, without considering other different clients.

Also, for huge servers, there can be more brokers that share the same data content, so to serve different clients more efficiently. Hence, the issue of latency in this protocol can interfere with time-critical applications, since device-to-device transmission requires publishing on the broker from a device and subscribe to it by the other one.

3 System Design

3.1 Working Principles

The proposed system is based on several nodes, which consist of a microcontroller that manages a UHF RFID reader and a WiFi module; its functionality is shown in Fig. 3. These nodes are placed at the access gate of different areas of the site to detect the passage of gears and workers. Gear has a tag applied on it, while workers have a tag applied under the helmet. In this way, when the reader detects the tag presence, it is possible to monitor who and what enters or leaves the site.

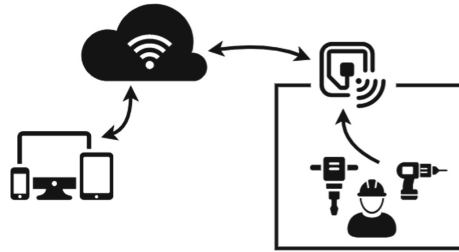


Fig. 3. Working principles of the proposed system.

Then, collected data are published on a proper MQTT topic via WiFi, at a desired transmission rate. Here, a server shows these collected data that can hence be consulted remotely from any device with an internet connection.

The node can also include warnings and alerts: since there can be constraints on parameters, such as the maximum number of workmen in a specific area, it can be required to send a message or alert someone of the issue. This is achieved from the system publishing a message and specifying a context within it, that can be shown as a string remotely. The server also can use the error code to establish if it's needed to alert some other person or device. Other warnings, such as a person standing still beneath the gate, can be communicated to the server as a string, without requiring a specific alert.

4 Demo Scenario

4.1 Remote Server

The platform used to develop a server is Ubidots, which allows to create simple interfaces (called dashboards) to display data related to a specific topic. Data can be displayed with different graphic styles to improve their readability. The demo dashboard realized for this application is shown in Fig. 4.

A single node of the system has been mounted at the entrance of a room to test its behavior, and data of a working have been registered. In Fig. 5 are reported the data of people entering and living the test room within several hours; since just one gate is mounted, data are only relative to the value of "Room 1" in Fig. 4.

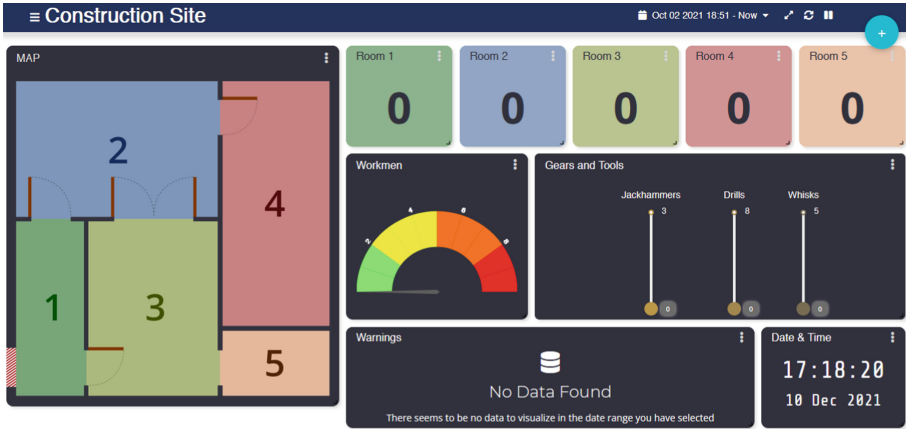


Fig. 4. Server dashboard realized on Ubidots for the application: some demo data has been inserted.

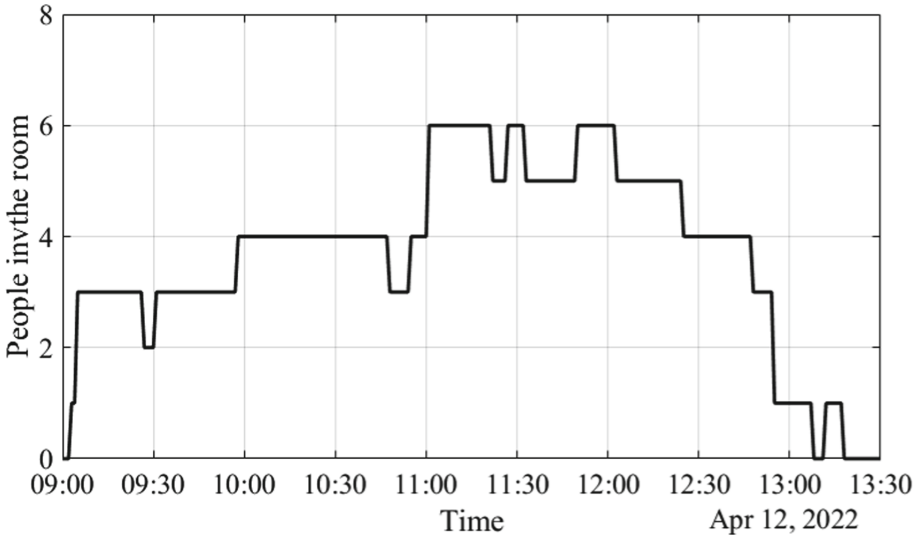


Fig. 5. Transit of people inside and outside a demo room in a morning work.

5 Conclusions

In this paper we presented a node system to monitor construction sites and working areas. The use of multiple nodes allows to distinguish different areas of the site, and data of every node is shared on the same remote server. Together with access data, information on gear and eventual warnings are sent to ensure a complete supervision from remote.

As a future development, it is possible to implement a localization method based on RSSI, which is possible to evaluate using UHF RFID. Also, nodes can be embedded with other sensors to evaluate different parameters, as safety conditions like air pollution. The whole system is low-cost and easily re-configurable to add features and making it fully customizable.

References

1. Liu, T., Hou, J., Xiong, G., et al.: Smart cloud-based platform for construction sites. In: 2016 IEEE International Conference on Service Operations and Logistics, and Informatics (SOLI), pp 168–173. IEEE (2016)
2. Kour, K., Kour, J., Singh, P.: Smart Applications of Internet of Things. In: 2018 First International Conference on Secure Cyber Computing and Communication (ICSCCC), pp 143–146. IEEE (2018)
3. Jeong, B.Y.: Occupational deaths and injuries in the construction industry. *Appl Ergon* **29**, 355–360 (1998). [https://doi.org/10.1016/S0003-6870\(97\)00077-X](https://doi.org/10.1016/S0003-6870(97)00077-X)
4. Nath, B., Reynolds, F., Want, R.: RFID technology and applications. *IEEE Pervasive Comput* **5**, 22–24 (2006). <https://doi.org/10.1109/MPRV.2006.13>
5. Brennan, D., Kolaja, J.: Real time location system using passive UHF RFID. In: Proceedings of the 2014 15th International Carpathian Control Conference (ICCC), pp 58–62. IEEE (2014)
6. Nadzir, N.M., Rahim, M.K.A., Zubir, F.: Wireless sensor node with UHF RFID for monitoring system. In: 2017 International Symposium on Antennas and Propagation (ISAP), pp 1–2. IEEE (2017)

Author Index

A

Adinolfi, Barbara, 88
Alam, Badrul, 167
Alfano, Brigida, 34, 129
Alghisi, Davide, 160
Aprea, Paolo, 186
Asquini, Rita, 167

B

Baldini, F., 1
Barbato, Paola Sabrina, 186
Barbirotta, Marcello, 40
Barile, Gianluca, 124, 135, 192
Barretta, L., 180
Barretta, Luigi, 129, 186
Bartalesi, Daniele, 174
Baù, Marco, 147
Belfiore, Nicola Pio, 28
Bellucci, S., 16
Betta, G., 16
Bittanti, Sergio, 174
Buzzin, Alessio, 28, 40

C

Campanella, Luigi, 77
Cancelliere, R., 16
Caputo, Domenico, 22, 40, 186
Carotta, Maria Cristina, 58
Casalinuovo, Silvia, 40
Casian, Magdolna, 71
Castrucci, Mauro, 77
Casuscelli, Valeria, 186
Ceschini, Andrea, 167
Chiavaioli, F., 1

Ciaccheri, Leonardo, 88
Colaiuda, Davide, 192
Compagnone, Dario, 100
Consumi, Marco, 64
Costantini, Francesca, 22
Cristea, Cecilia, 71

D

De Berardinis, Pierluigi, 192
de Cesare, Giampiero, 22, 28, 40
De Girolamo Del Mauro, Anna, 34
De Maria, Letizia, 174
De Wael, K., 1
Del Giudice, Antonio, 141
Del Tosto, Dina, 124
Del Villar, I., 1
Dell'Aglio, Emanuele, 77
Della Pelle, Flavio, 100
Delli Veneri, Paola, 34
Dellutri, Michele, 141
Di Francia, Girolamo, 111, 141
Di Natale, Corrado, 46, 77, 83
Di Zazzo, Lorena, 46
Donelli, Massimo, 94

E

Esposito, Elena, 111

F

Ferrari, Marco, 147
Ferrari, Vittorio, 147, 160
Ferri, Giuseppe, 124, 135, 192
Ferrigno, L., 16
Fioravanti, Ambra, 58

Fiorillo, A. S., 53
 Foncellino, F., 180
 Formisano, Fabrizio, 141
 Fort, Ada, 64

G

Garatti, Simone, 174
 Giannetti, A., 1

H

Hosu, Oana, 71

I

Iacoboni, Laura, 135
 Iannascoli, Lorenzo, 22, 40
 Iula, Antonio, 153

L

Landi, Elia, 64
 Landi, Laura, 118
 Laurini, Eleonora, 192
 Leanza, Gianni, 111
 Leoni, Alfiero, 124
 Lettieri, Stefano, 58
 Lo Grasso, Anna, 64
 Loda, Matteo, 147
 Loffredo, Fausta, 34
 Loffredo, Giuseppe, 141
 Lorenzelli, Leandro, 94
 Lovecchio, Nicola, 22

M

Maffucci, A., 16
 Magna, Gabriele, 46
 Magnani, Agnese, 64
 Marani, Pietro, 58
 Marchi, Giada, 94
 Marrazza, Giovanna, 71
 Massera, Ettore, 34, 129
 Mastrandrea, Antonio, 40
 Mazzetta, Ivan, 40
 Mazzoli, Federico, 160
 Medaglia, Pier Gianni, 83
 Melean, Bianca, 71
 Mencaglia, Andrea A., 88
 Micheli, Laura, 16
 Micucci, Monica, 153
 Miele, G., 16
 Miglietta, Maria Lucia, 34, 129
 Mignani, Anna G., 88
 Morandi, Sara, 58
 Moretto, L. M., 1
 Moro, G., 1
 Mudiganti, Mounika, 46

Mugnaini, Marco, 64
 Mulloni, Viviana, 94

N

Nascetti, Augusto, 22, 40
 Nastro, Alessandro, 147
 Nuzzo, Matteo, 71

O

Oliva, G., 53
 Orsatti, Martina, 22

P

Panella, Massimo, 167
 Panzardi, Enza, 64
 Paolesse, Roberto, 46
 Pelliccione, Andrea, 124, 192
 Pezzilli, Riccardo, 77, 83
 Picardi, Armando, 141
 Polichetti, Tiziana, 34, 129
 Prestopino, Giuseppe, 83
 Puglisi, Donatella, 40
 Pullano, S. A., 53

R

Ragnoli, Mattia, 124
 Ricci, Stefano, 135
 Romani, Aldo, 118
 Rosato, Antonello, 167
 Rucconi, Valerio, 174

S

Sacerdoti, Michele, 58
 Salvatori, Stefano, 141
 Scaldaferrì, Rossana, 186
 Scarsella, Massimo, 135
 Sciuto, Salvatore Andrea, 28
 Scorza, Andrea, 28
 Scroccarello, Annalisa, 100
 Scubla, Fabio, 147
 Selvolini, Giulia, 71
 Silveri, Filippo, 100
 Stefani, Giuseppe, 147
 Stornelli, Vincenzo, 124, 135, 192
 Suffredini, E., 16

T

Talarico, Luigi, 64
 Tamburini, Cinzia, 118
 Tomassetti, Mauro, 77, 83

U

Ursi, Pietro, 28

V

Valecillos, Bau, 174
 Veroli, Andrea, 28

Vignoli, Valerio, [64](#)
Villani, Fulvia, [34](#)
Vurchio, Federica, [28](#)

Z
Zini, Marco, [147](#)
Zubiate, P., [1](#)